PhD-FSTC-2014-17
The Faculty of Sciences, Technology and Communication

# DISSERTATION

Presented on 30/06/2014 in Luxembourg

to obtain the degree of

# DOCTEUR DE L'UNIVERSITÉ DU LUXEMBOURG

# EN SCIENCES DE L'INGENIEUR

by

Mark MICHAEL
Born on 10 August 1982 in Stralsund (Germany)

# A DISCRETE APPROACH TO DESCRIBE THE KINEMATICS BETWEEN SNOW AND A TIRE TREAD

## Dissertation defense committee

Dr.-Ing. Bernhard Peters, dissertation supervisor
*Professor, Université du Luxembourg*

Dr. Algis Džiugys
*Lithuanian Energy Institute*

Dr.-Ing. Stefan Van Baars, Chairman
*Professor, Université du Luxembourg*

Dr. Tibor Fülöp
*Goodyear S.A. Luxembourg*

Dr. sc. tech. Martin Schneebeli
*WSL, Institute SLF*

Prof. François Nicot, Vice Chairman
*IRSTEA - Grenoble*

# A Discrete Approach to Describe the Kinematics between Snow and a Tire Tread






**Mark Michael**

Faculty of Science, Technology and Communication

University of Luxembourg

A thesis submitted for the degree of

***DOCTOR OF ENGINEERING SCIENCE***

June 2014

I dedicate this work to
*my indescribable*
*Laura.*

# Acknowledgements

I would like to acknowledge that the presented research project is financed by the National Research Fund of Luxembourg (FNR). Therefore, I am very thankful to the FNR for giving me the opportunity to conduct my research work independently.

The successful developments of this project were undertaken at the University of Luxembourg. Therefore, I like to acknowledge my thankfulness to Prof. Bernhard Peters.

This work is conducted in collaboration with the IRSTEA, the French National Research Institute of Science and Technology for Environment and Agriculture, and Goodyear Innovation Centre Luxembourg, the Innovation Center of one of the world largest tire manufacturer. I like to thank both institutes for the valuable support provided over the project period. In particular, I am thanking Prof. Francois Nicot and Dr. Tibor Fülöp for the successful engineering work conducted together over the span of this project.

Further, I like to acknowledge the great work conducted together with the entire LuXDEM and Inutech Team of whom I like to thank Dr. Florian Hoffmann in particular.

Simulations presented in this study were carried out using the High-Performance-Computing facility (HPC) of the University of Luxembourg, see Varrette et al. (2014), whose staff and administrators I hereby like to thank gratefully. According to the UL HPC platform the simulations of this project used CPU hours of total 20 year and 300 days in 2013 only, which are a cost of 12854.42 Euro by the public EC2 computing environment of Amazon.

# Abstract

The objective of this study is to develop a simulation technique that enables to describe the interactions between snow and a moving surface. The developments of this study are focused on the application of the interactions between a tire tread and a snow-covered road.
Contrary to a continuum mechanics approach snow is considered to exist of discrete grains which are allowed to bond and collide with each other. Therefore, a discrete approach based on the extended Discrete Element Method is applied to the snow. Micro-mechanical models are developed to describe the deformational behaviour of snow. The micro-mechanical models describe the deformation and growth of the bonds between grains as well as the contact behaviour of snow grains on the grain-scale. Further, the age of a snow sample, the temperature and deformation rate applied are taken into account by the developed models. The deformational behaviour of snow under brittle and ductile loading rates is validated with experimental data of common measurements in the field of snow mechanics. The simulation results successfully recapture the macro- and micro-scale deformation behaviour of snow and enable to identify the primary deformation mechanism in charge at the different loading rates, densities and temperatures.
However, this approach allows treating individual snow grains during loading due to a rolling tire and predicting both position and orientation of grains. The micro-mechanical response of each snow grain in contact with the structure of the tire surface generates a global impact that defines the interaction forces between the snow and the tire surface, which simultaneously indicate the strength of traction. In order to predict the elastic deformation of the tire surface the Finite Element Method is employed.
A coupling method is developed between the discrete approach to characterise snow and the finite element description of the tire tread. The coupling method compensates quite naturally the shortages of both numerical methods. Further, a fast contact detection algorithm has been developed to spare valuable computation time. The coupling approach was successfully tested and validated with a small scale application but also with the large scale application of tire - soil interaction. The large-scale simulation results of tire - soil interactions showed to be accurate in comparison to similar traction measurements.
Finally, the interaction of snow with rigid and deformable tread parts has been studied in accordance to friction measurements of the field of tire mechanics. The results show the ability of the simulation technique to describe the targeted interactions and give valuable insight into the underlying mechanisms.

# Nomenclature

| | |
|---|---|
| $_{\alpha\ \beta\ \gamma}$ | The Greek indices identify the three spatial components of a physical quantity. $\alpha\ =\ (1,2,3)$ |
| $\vec{B}$ | Three component vector / Tensor first rank. |
| $\overline{B}$ | Dyad / Tensor second rank. |
| $B_\alpha$ | Components of a first rank Tensor. |
| $B_{\alpha\beta}$ | Components of a dyad. |
| | |
| $_{i\ j\ k}$ | The roman indices identify one item within a number of entities, e.g. $i^{th}$ grain of $n$ grains $i\ =\ (1,2,...,n)$ |
| $\underline{B}$ | $n$ - Component vectors are single underlined symbols. |
| $\underline{\underline{B}}$ | Matrices are double underlined symbols. |
| $B_i$ | Components of $n$ - component vector. |
| $B_{ij}$ | Components of a matrix. |
| | |
| $R$ | Gas constant. |
| $\lambda$ | Material porosity. |
| $\sigma_{bcs}$ | Brittle compression strength of ice. |
| $\sigma_{dcs}$ | Ductile compression strength of ice. |
| $\sigma_{ts}$ | Tensile strength of ice. |
| $E$ | Young's elasticity modulus. |
| $G$ | Shear modulus. |
| $H$ | Material hardness. |

| | |
|---|---|
| $\mu$ | Coefficient of friction. |
| $\nu$ | Poisson's ratio. |
| $\rho$ | Material density. |
| $\theta$ | Rotational Stiffness. |
| $e_{ice}$ | Coefficient of restitution of ice. |
| $e$ | Coefficient of restitution. |
| $k$ | Material Stiffness. |
| | |
| $\vec{v}_{ij}$ | Relative velocity at contact point. |
| $\vec{\phi}$ | Particle orientation in Euler angles. |
| $\vec{F}_b$ | Particle bond force. |
| $\vec{F}_c$ | Particle collision force. |
| $\vec{F}$ | Particle force. |
| $\vec{M}_b$ | Particle moment/torque due to bonding. |
| $\vec{M}_c$ | Particle moment/torque due to collision. |
| $\vec{M}$ | Particle moment/torque. |
| $\vec{a}$ , $\dot{\vec{v}}$ , $\ddot{\vec{x}}$ | Particle acceleration. |
| $\vec{b}$ | Unit vector of the bending axis of a bended bond. |
| $\vec{d}_b$ | Distance vector between the center of the bond and the particle. |
| $\vec{d}_c$ | Distance vector between the collision point and the particle center. |
| $\vec{n}_b, \vec{t}_b$ | Normal unit vector of the bond and its orthogonal tangential unit vector, respectively. |
| $\vec{n}_c, \vec{t}_c$ | Normal unit vector of the collision point and its orthogonal tangential unit vector, respectively. |
| $\vec{n}, \vec{t}$ | Normal unit vector of the point of contact and its orthogonal tangential unit vector, respectively. |
| $\vec{v}_{ij}$ | Relative velocity between particle $i$ and $j$. |
| $\vec{x}$ | Particle position. |

| | |
|---|---|
| $\vec{v}$ , $\dot{\vec{x}}$ | Particle velocity. |
| $d\vec{\omega}$ , $d\dot{\vec{\omega}}$ | Angular velocity of a particle. |
| $d\vec{\phi}$ | Relative angular displacement. |
| $d\vec{u}$ | Relative displacement. |
| $A_b$ | Bond area. |
| $N_b$ | Coordination number, i.e. number of bonds per grains. |
| $N_g$ | Number of grains. |
| $R_{ij}$ | Effective particle radius. |
| $T$ | Particle temperature. |
| $\delta_n$ | Normal particle overlap. |
| $\delta_t$ | Tangential particle overlap. |
| $\vec{\omega}_{ij}$ | Relative angular velocity between particle $i$ and $j$. |
| $dt$ | Time difference or timestep length. |
| $m$ | Particle mass. |
| $r_b$ | Bond radius. |
| $r$ | Particle radius. |
| $t_b$ | Bonding time or age of a bond. |
| $t_c$ | Contact time or duration of a collision. |
| $t$ | Time or a particular timestep. |
| | |
| $\vec{u}$ | Nodal displacement vector. |
| $\sigma, \tau$ | Stress |
| $\varepsilon_l$ | Loading rate |
| $\varepsilon$ | Strain |
| $\dot{\varepsilon}$ | Strain rate or creep rate. |
| $\underline{\underline{M}}$ | Mass matrix of meshed structure. |

| | |
|---|---|
| RVE | Representative Volume Element |
| CCDM | Combined Continuum and Discrete Model |
| DEM | Distinct/Discrete Element Method |
| DPM | Discrete Particle Method |
| FEM | Finite Element Method |
| MPM | Material Point Method |
| XDEM | Extended Discrete Element Method |

# Contents

# Chapter 1

# Introduction

The research in snow mechanics is mainly driven by three major fields of applications. The first larger portion of investigations comes from the field of snow avalanche studies where the forecast of the release of inclined snow covers and the construction of protective structures is of principal interest. The winter sport industry delivers the second larger portion of research knowledge which is concerned with the improvement of security, comfort and efficiency of their equipment. The third major effort is undertaken by the tire industry in order to understand the mechanisms of tire - snow traction and thus improve their products in relation driving safety.

Despite the larger progress in research of natural hazards over the last decades, heavy snowfalls and resulting avalanches are still the major risk to the population and tourism of mountain regions. To design protective structures and devices the load developing under a snow cover has to be predicted. Also the stress developing in the inclined layer of a snow cover needs to be predicted to estimate the release of an avalanche. Therefore, a larger effort is put into the development of novel material models and methods able to determine those quantities.

Ski sport activities increased tremendously over the last century due to the everlasting competition in the field of winter sports but also due to the boost in tourism in numerous mountain regions around the globe. This continuous growth is of course followed by several improvements in the skiing equipment. Thereby, numerical simulations offer very promising possibilities to predict the interaction between snow and skier or skiing equipment. A larger portion of the design and construction of alpine skis is already conducted by computer aided engineering. But also the models of snow - ski interaction are still employed along several assumptions and thus new approaches and methods are continuously developed.

The transmission of forces between a tire and a snow covered road is the source of driving safety for any passengers car. But the force transmission also of major interest for landing stripes of airplanes in cold regions as much as the vehicle mobility on snow covered surfaces off road is important to the forestry, mining, construction industries and military.

However, in the field of winter tire development large series of outdoor tests are performed

all around the world. Under outdoor conditions the actual performance of tires is tested on snow and ice to compare new design concepts, as depicted in fig. 1.1. In the same time, results of outdoor tests are very sensitive on changing external conditions, like daily temperature evolution or precipitation.

*Figure 1.1: Outdoor test by Testworld.*

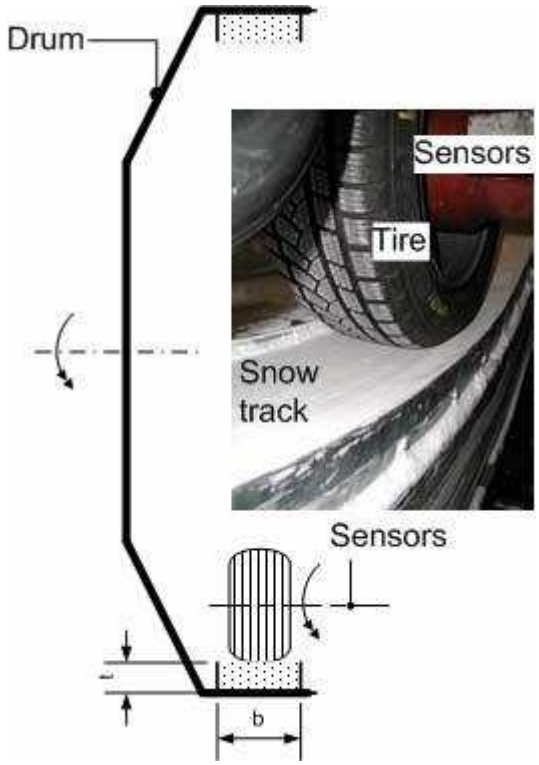


*Figure 1.2: Concave indoor drum test by Gießler et al. (2007).*

Therefore, winter tires are also tested in a controllable indoor environment under artificial winter conditions. This is for instance performed by using an indoor drum test as conducted by Gießler et al. (2007) in fig. 1.2.
As the effort and economical costs are high for experiments, increasing portions of the tire development is based on numerical methods. But the kinematics involved in the interactions between a tire tread and snow are complex and current modeling still lacks the understanding of several mechanisms.
All the above mentioned engineering applications are governed by the mechanical behaviour of snow. This behaviour however has proven to be difficult to model due to the heterogeneity of snow as a geo-material. The complex deformation mechanisms of snow are inherited from its micro-scale ($\approx 10^{-3}m$).
The micro-structure consists of ice grains connected by bonds which results in an open-foam like structure. The macroscopic response of a snow pack to loading is therefore determined by the deformation and failure of these ice bonds and the inter-granular collision and friction forces during rearrangement of the ice grains.

To forecast an avalanche from the stress developments in a snow cover, the behaviour of snow deforming at low strain rates is the governing mechanisms. On the other hand, in the industrial applications concerning transportation safety, the high strain rate behaviour of snow controls the force transmission.
Snow behaves very different depending on the rate of the deformation process. At low rates snow exhibits a ductile deformation behaviour while at high rates it deforms as brittle material. As snow is ice on micro-scale, these characteristics are inherited from the material behaviour of ice.
One can easily observe the brittle behaviour of ice when stepping too quickly on a frozen pond or when crushing ice for a soft drink. Ice fails entirely brittle, i.e. crushes into pieces, if subjected to rapid loading of seconds or minutes depending on the amount of load and the spacial dimensions. On the other hand, ice flows plasticly and changes its shape continuously when loaded slowly and over a long time, i.e. days or even months, as illustrated by the glacial flow in fig. 1.3.

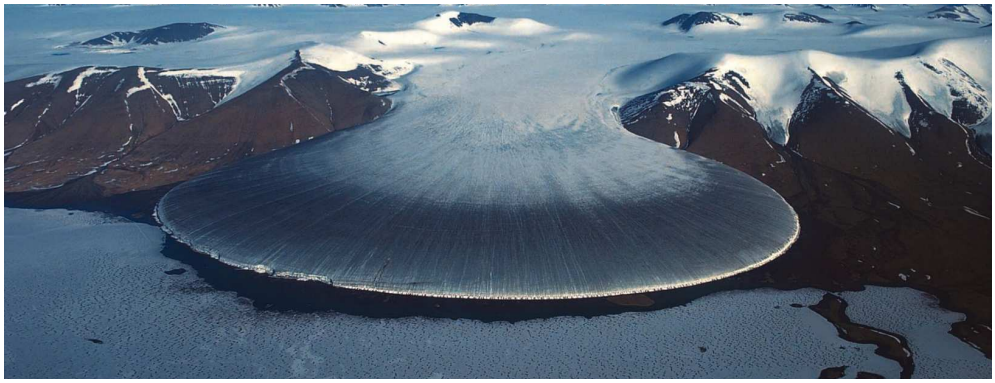

*Figure 1.3: Plastic flow of glacier ice under gravity by Ershkov (2000).*

If loaded rapidly, snow fractures in a brittle manner as seen in fig.1.1. One is experiencing every time as the collapse beneath footsteps when walking through fresh snow. But snow also flows plasticly if forces act constantly over a long range of time as seen by the deformed snow cover in fig. 1.4.
There is another mutual phenomena inherited from the ice micro-structure which increases the difficulties to model the mechanical behaviour of snow. Ice does not only melt due to temperature, it also relatively rapid melts under pressure. This is demonstrated in fig. 1.5 where a wire is pulled through an ice block under constant load.
The aim of this study is to develop a simulation technique enable to describe the interactions between snow and a moving surface. The developments of this study are focused on the application of the interactions between a tire tread and a snow-covered road. But the proposed models and numerical method are also applicable to all mentioned fields of snow mechanics.
This work proposes inter-granular snow models which are deployed using an extended discrete element technique. The micro-structure of a snow pack is thereby represented by generating an ensemble of explicit geometrical shapes describing the individual snow grains and bonds. In order to predict the deformation of the tire surface the Finite Element

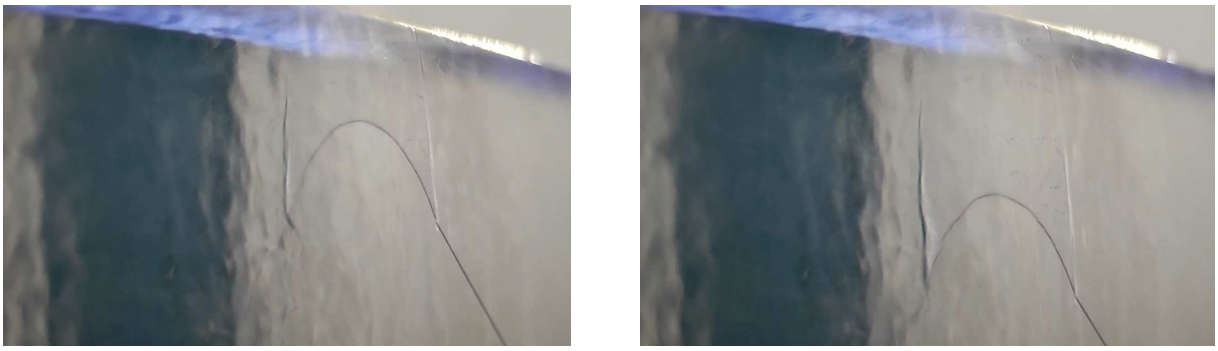

*Figure 1.5: Pressure melting of Ice due to constant long term loading by Veritasium (2011)*

Method is employed. A coupling method is developed between the discrete and the finite element approach for the tire tread.

*Figure 1.4: Plastic behaviour under long-term loading by Nicot (2003).*

This study focuses mainly on the high rate loading of snow. This enables to determine the ranges of interest for important physical quantities involved. This delimitation does not necessarily exclude comparisons with investigations outside these ranges, but it sets the focus within the predictions. Resulting from the described outdoor tests, the interesting temperatures range between 0 and $-30\,^{\circ}\mathrm{C}$ degree. From the tests in winter tire development, the important snow densities range from 200 to 600 $\mathrm{kg/m^3}$. A tire is slipping on snow at velocities between the lower limit of 1 mm/s and the higher limit of 2 m/s. Thereby, loads are developing from of 0.05 MPa up to 0.35 MPa. The characteristic length of a single tread block is about $25 \times 25$ $\mathrm{mm^2}$ in cross section as an initial approximation.

This thesis continues with a review chapter of the necessary background knowledge. Thereby, the current state in mechanical snow behaviour is described along common measurements followed by a review of numerical modeling in snow mechanics. Chapter 2. also contains the basics of the tire traction mechanics as well as a review of measurements and current models in tire-snow interactions. The background chapter is concluded by an insight into the coupling of discrete and continuum methods.

# Chapter 2

# Background

## 2.1 Snow as Geo-Material

### 2.1.1 Structure and Sintering of Snow

Snow can be seen as an open-foam like material whereby its micro-structure is composed of the solid, liquid and vapour phase of $H_2O$, i.e. water. The micro-structure strongly depends on the amount of solid, liquid and vapour present at the ambient temperature. Fig. 2.1 was published in the review of Blackford (2007) and gives a detailed overview of the broad spectrum of micro-structures which are formed by $H_2O$.
Beneath the melting point of solid water, i.e. ice, snow can be assumed as a two-phase-system. Under this assumption snow consists of an ice matrix and pore space filled with air and water vapour. As the mass of the pore space is negligible compared to the mass of ice in a snow sample the density of the sample $\rho_{snow}$ can be calculated as follows:

$$\rho_{snow} = \rho_{ice} \cdot \frac{V_{ice}}{V_{snow}} = \frac{m_{snow}}{V_{snow}}$$

where $\rho_{ice}$ describes the density of ice, $m_{snow}$ the sample mass, $V_{snow}$ the sample volume and $V_{ice}$ the volume of the ice matrix. At the pressures and temperatures of interest in this study the solid water phase consists of the crystal structure of a hexagonal lattice of ice, i.e. ice Ih, as depicted in fig. 2.2.
The volumetric portion of the gas phase, i.e. the porosity of the snow $\Lambda_{gas}$, can be calculated as follows:

$$\Lambda_{gas} = 1 - \Lambda_{ice} = 1 - \frac{\rho_{snow}}{\rho_{ice}}$$

where $\Lambda_{ice}$ describes the volumetric portion of the ice matrix $\rho_{ice}$ in relation to the total snow volume $\rho_{snow}$.

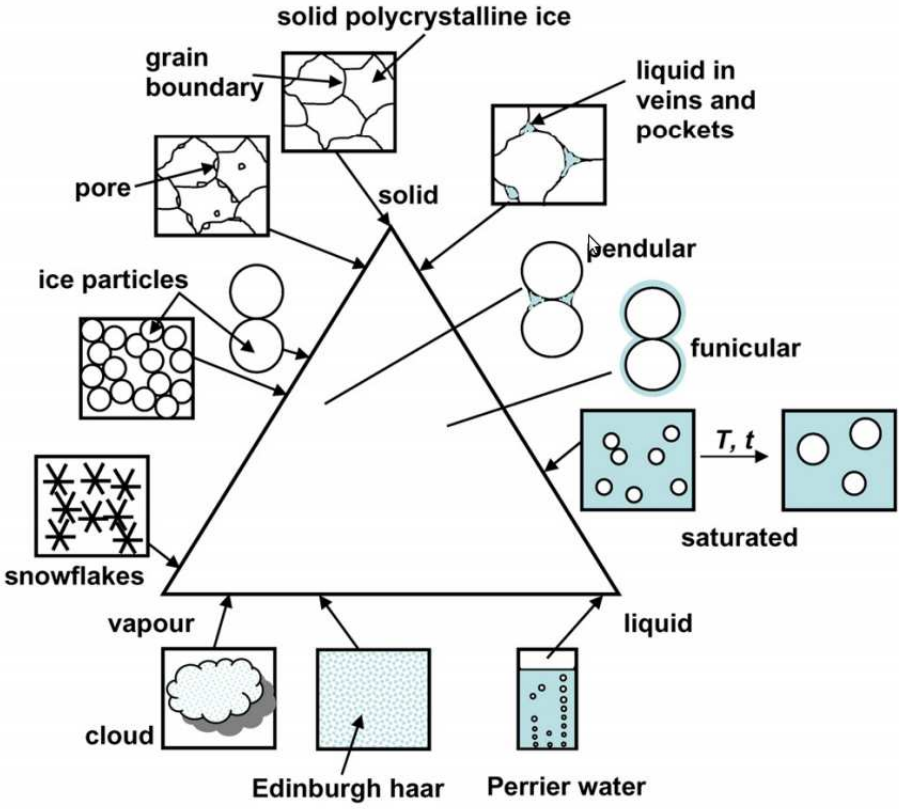


*Figure 2.1: Spectrum of micro-structures formed by $H_2O$ at a temperature of $0°C$, composed by Blackford (2007).*

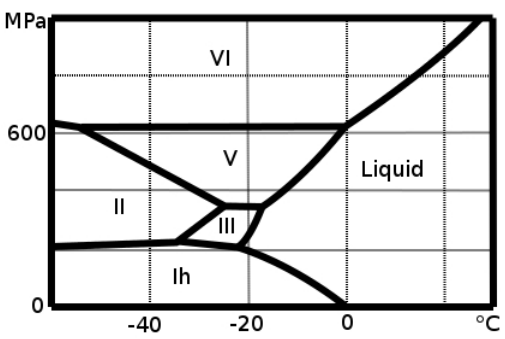


*Figure 2.2: Phases of $H_2O$.*

The density of snow has a large spectrum compared to other materials. Freshly fallen snow usually has a density of about 100 kg/m$^3$, which means that almost 90% of the volume is filled by the gas phase. After a season of undisturbed settling and sintering, a snow cover has densities around 300 to 400 kg/m$^3$. This might seem to be quite dense snow already, but it still consists of more than 50% of air and water vapour. If a snow cover survives a summer period it develops into the so called firn. Firn is snow densified up to 500 and 600 kg/m$^3$. Even this dense snow consists by most of 65% of ice. Snow can even consolidate further from 600 up to 700 and 800 kg/m$^3$ where it will become eventually porous ice or glacial ice. Tire-snow tests, which are the main focus of this study, are performed on specially prepared test track surfaces. The base of these tracks has a density around 400 to 600 kg/m$^3$, with a layer of relatively low density, loose snow covering their surface.

The high porosity shows the importance of the micro-structure of snow as only the ice-matrix can carry any applied load. This relationship between the low volumetric portion of the ice matrix and its entire responsibility as the supporting structure is one of the principal factors of the unique mechanical behaviour of snow. Just like other granular materials, snow consists of single grains. These ice grains, i.e. snow grains, can have very different sizes and even shapes depending on the metamorphism the snow experienced. But the ice grains are not just loosely packed together as in other granular materials like sand. Snow develops a unique deformational behaviour because the ice grains sinter immediately after contact and form bonds between each other. This composition of ice grains and bonds thus creates the ice-matrix, responsible for the strength of snow.

## Metamorphism of Snow

Freshly fallen snow crystals start to transform in shape and size immediately after their deposition. The newly formed micro-structure strongly depends on the temperature distribution inside the snow cover. The ground below the snow cover is usually warmer than the surface and can even heat up the snow to its melting point. On the other hand, the surface of the snow cover is cooled by winds and the surrounding air temperature. But the surface temperature is subjected to high fluctuation due to the rapidly changing conditions.
A Temperature gradient develops in the snow cover between surface and bottom temperature. Due to this gradient neighbouring grains have different temperatures and thus different vapour pressures of the ice develop. This plays a major role in the metamorphism of snow. Depending on the different temperature gradients, different kinds of metamorphism can be observed: equi-temperature metamorphism, temperature gradient metamorphism and melting transformation.

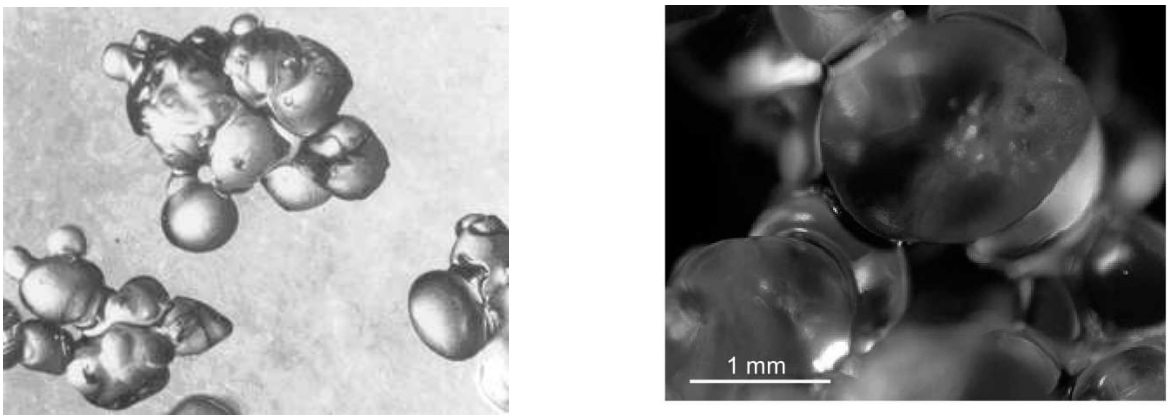


*Figure 2.3: Snow grain shape developed under equi-temperature metamorphism by Colbeck (1997) and Meyssonnier et al. (2009).*

The equi-temperature metamorphism is present at very low temperature gradients between $0 - 5$ °C/m. Fresh snow grains are very fine branched ice crystals and thus own a high surface area in relation to mass. These complex ice shapes seek to reduce their surface area

and to transform into sphere like grains as shown in fig. 2.3. This is forced by different vapour concentrations due to the different shapes and sizes of the grains in a snow cover. The temperature gradient metamorphism takes place under high temperature gradients in the snow cover. High temperature gradients cause an intensive vapour transport through the pore space of the snow pack and form very faceted and sharp-edged grains. Under this condition the number of bonds formed between adjoining grains decreases and the snow weakens.

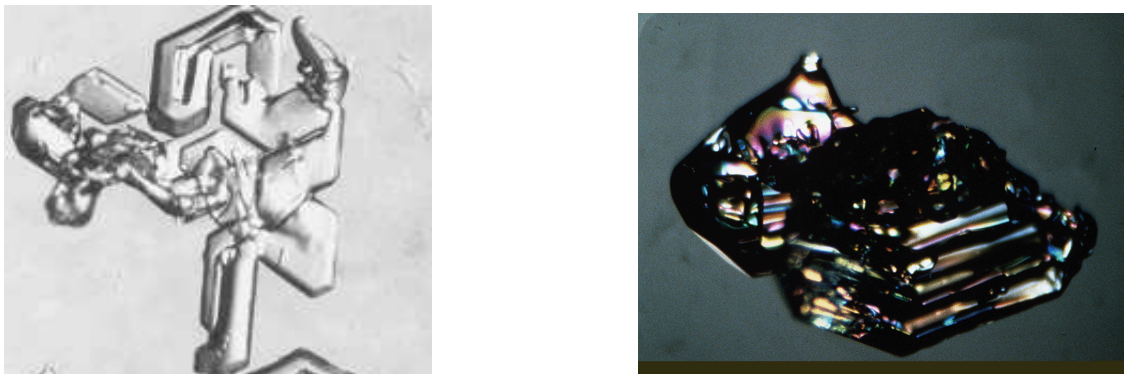

*Figure 2.4: Snow grain shape developed under temperature gradient metamorphism by Colbeck (1997) .*

The melting transformation is caused by the generation of water inside a snow pack when the temperatures raise above the melting point at the surface. Due to melt water, any kind of grain shape rounds and bigger grains grow on the cost of smaller ones.
All the observations for the different kinds of snow metamorphism show that the micro-structure, i.e. grain-scale properties, is strongly affecting the strength and deformational behaviour of snow. Therefore, the micro-structure of snow has to be taken into account when modeling its mechanical behaviour.

### Grain-Scale Properties of Snow

In the field of snow mechanics, the density of a sample is still commonly used to identify the strength of snow. However, the density is only one property and not necessarily the most relevant one to classify snow. Fukue (1977) showed that snow samples of the same density vary in strength by an order of magnitude with changes in their grain size and sintering age, i.e. strength and size of the ice matrix.
Therefore within this study, the developments of the models of snow behaviour are based on the grain-scale properties. Those grain scale properties are the size and shape of snow grains, the material properties of the grains as well as the thickness and growth behaviour of bonds between grains itself.
The most straightforward and simplest way to measure the size of grains of a granular material is sieving. Thereby, sieves of different slot size are used to sieve the material. By using different sieve slot sizes the distribution of the grain diameter as percentage of the total sample mass can be predicted.

Von Moos et al. (2003) sieved the grains of several snow samples between 180 to 440 kg/m$^3$. The sieve curve of the different snow samples are shown in fig. 2.5. The grain size measurements of Fukue (1977) described similar distributions as shown in fig 2.6.


*Figure 2.5: Cumulative distribution function of mass percentage versus grain size of snow, i.e. slot size, by Von Moos et al. (2003).*

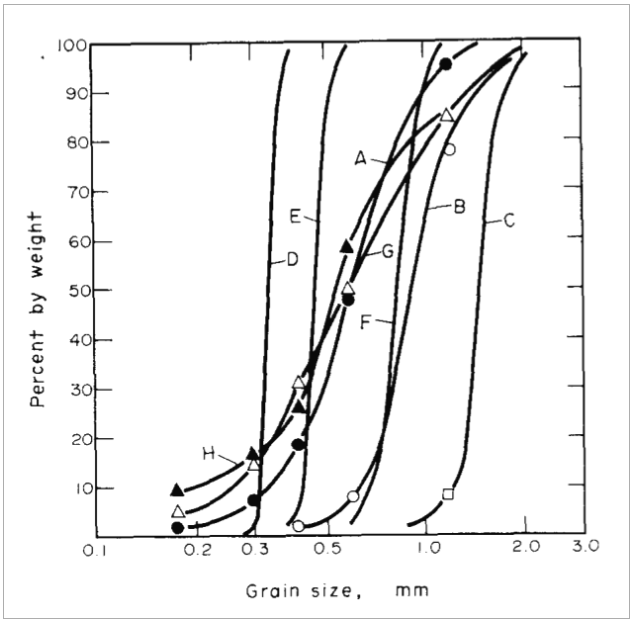


*Figure 2.6: Mass percentage versus grain size of different snow types measured in several series A to H by Fukue (1977).*

This methodology and the resulting sieve curves of fig. 2.5 can be mathematically expressed as follows:

$$Z(r_g) = \frac{\text{weight of grains} \leq r_g}{\text{weight of all grains}} \tag{2.1}$$

where $r_g$ describes the grain radius, i.e. the slot diameter of the sieve. By this method Von Moos et al. (2003) found a maximum grain diameter of 8 mm and a minimum diameter of 0.125 mm. The bandwidth of the distribution in fig. 2.5 is quite small compared to other common granular materials. Fig. 2.7 compares the size distribution of snow grains to moraine and cement grains. The average grain distribution of snow is however similar

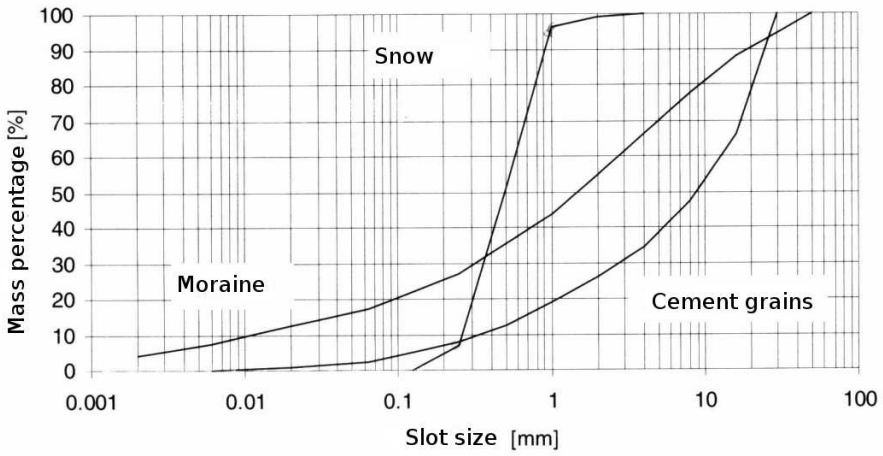


*Figure 2.7: Cumulative distribution function of mass percentage versus grain size of snow, i.e. slot size , by Von Moos et al. (2003) The snow curve is compared to sieve curves of moraine and cement grains.*

to the grain size distribution of sand. A major similarity is that also for the snow grains $80 - 90\%$ of the total grain mass is between 0.25 mm to 1 mm in diameter.
On the grain-scale, snow is an ensemble of ice grains connected by frozen bridges, i.e. the ice matrix. To describe the micro-scale processes during the deformation of snow, the grain-scale models have to be based on the mechanical properties and deformational behaviour of ice. The detailed behaviour of ice will be investigated in the following section.
Ice Ih, as shown in fig. 2.2, is a crystalline material. Therefore, before describing the mechanical behaviour of ice, the question has to be answered if snow on the grain-scale is single or poly-crystalline ice. For single crystalline ice, the mechanical properties and deformational behaviour show a strong dependence on the orientation of the crystal axes. The mechanical properties and deformational behaviour of polycrystalline ice can be assumed as spatial homogeneous.
Results of Colbeck (1997) showed that ice grains in dry snow generally consist of single crystals. Other authors, e.g. Hagenmuller (2011), Schneebeli (2004), assume the ice matrix of snow to be isotropic, i.e. poly-crystalline. But then again others, e.g. Theile et al. (2011), try to describe the ice at the grain-scale of snow as an anisotropic material, i.e. single crystal.
The question can be answered by micro-tomographic scans of the ice matrix of a snow structure. Meyssonnier et al. (2009) conducted such measurements. The technique identifies the orientation of crystalline c-axis and the geometrical shape of each crystal. A look at the cross section of scans of snow grains in fig. 2.8a reveals that a snow grain is composed

of a few ice crystals. Hence, the ice grains in a snow pack are neither fully single nor poly-crystalline ice. Snow grains can be seen as multi-crystals. In general, multi-crystalline ice

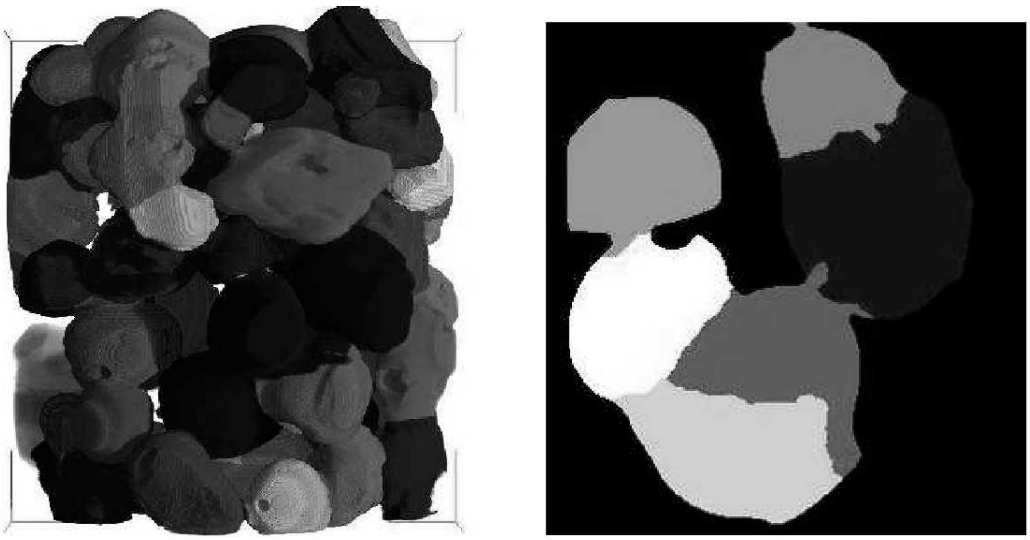

*(a) 3D image of a coarse-grained snow coloured by crystal orientation.*

*(b) Horizontal cross section of adjoined snow grains composed of a few ice crystals.*

*Figure 2.8: Micro-scale tomography scans of snow by Meyssonnier et al. (2009).*

does not show the pure anisotropic behaviour of a single-crystal. Further, a large number of multi-crystalline grains exist within a snow pack. Therefore within this study, a single snow grain is assumed to exhibit isotropic mechanical properties.
The ice matrix, i.e. bond structure, of a snow sample strengthens and weakens depending on the temperature conditions due to metamorphism in natural conditions. But snow samples can also strengthen under laboratory conditions of constant temperatures while sealed inside a container. This transformation is comparable to equi-temperature metamorphism but due to sealed condition the sample does not experience any changes in mass. For long-term deformations of snow this phenomena has to be taken into account. The time spent sintering also gives insight into the initial conditions of a snow sample before it is subjected to deformation. The ice making up the bond structure of a snow sample does also creep under applied pressure, i.e. load. Under sudden loading bonds in a snow sample fracture and grains are rearranged. If grains are pressed against each other, they immediately form new bonds which grow with time, temperature and pressure.
In the experiments of Kaempfer and Schneebeli (2007), fresh snow was aged and observed under isothermal and sealed conditions. The time spent ageing is called the sintering age. Kaempfer and Schneebeli (2007) kept the samples under the constant temperatures of $-2, -8, -19$, and $-54$ °C for an entire year. The samples were monthly captured by micro-tomography scans. A selection of the results is depicted in fig. 2.9.
In fig. 2.9, the ice matrices at $-2$ °C obviously thicken with increasing time and thus strengthen the snow sample. The ice matrices at week 45 also thicken with increasing temperature and strengthen the snow sample either. It has to be noticed that the change

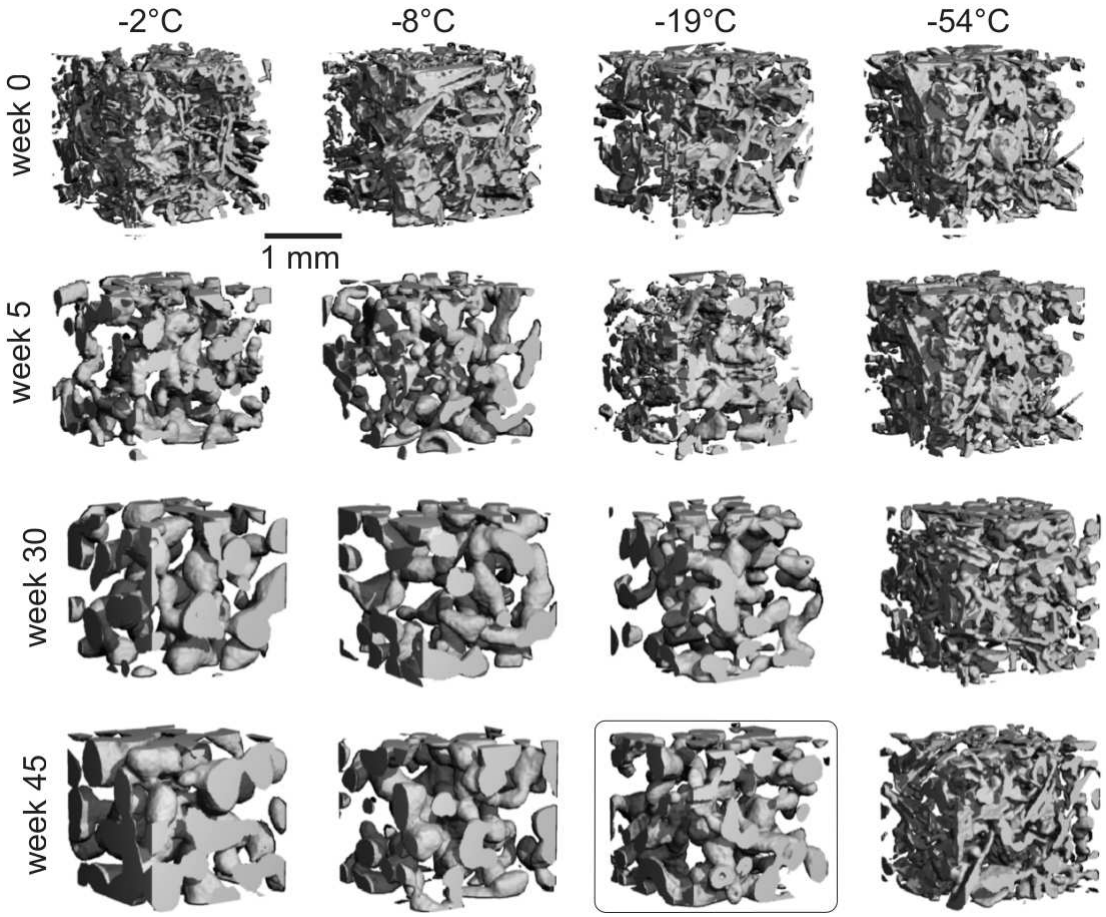


*Figure 2.9: Ice-structure scans of isothermal sintering experiments at four different temperatures conducted by Kaempfer and Schneebeli (2007).*

of the ice matrix at temperatures beneath −50 °C is significantly lower compared to higher temperatures. At temperatures close to the melting point of ice strong changes can be observed.
The ice matrix scans were used to gain several valuable micro-structural properties. One property monitored was the specific surface area of the ice matrix, calculated from triangulations of surfaces captured by the 3D image.
Further, the thickness histograms of the ice matrices have been derived. The mean thickness of the ice matrix is obtained by filling spheres into the triangulated surface structure. The thickness distribution of the different ice matrices is illustrated in fig. 2.10. A voxel can be seen as pixel of a photograph where by a voxel is a volume and pixel an area. The information contained in a voxel is if the capture is of the material ice or pore space. In fig. 2.10, sample 4 at the temperature of −54 °C shows almost no changes in thickness distribution over time. At temperatures above −50 °C, the thickness distribution broadens and flattens increasingly with increasing time. The tendency of the ice matrices visualises this behaviour by equalisation of the distribution of mass. The ice-structure thickening

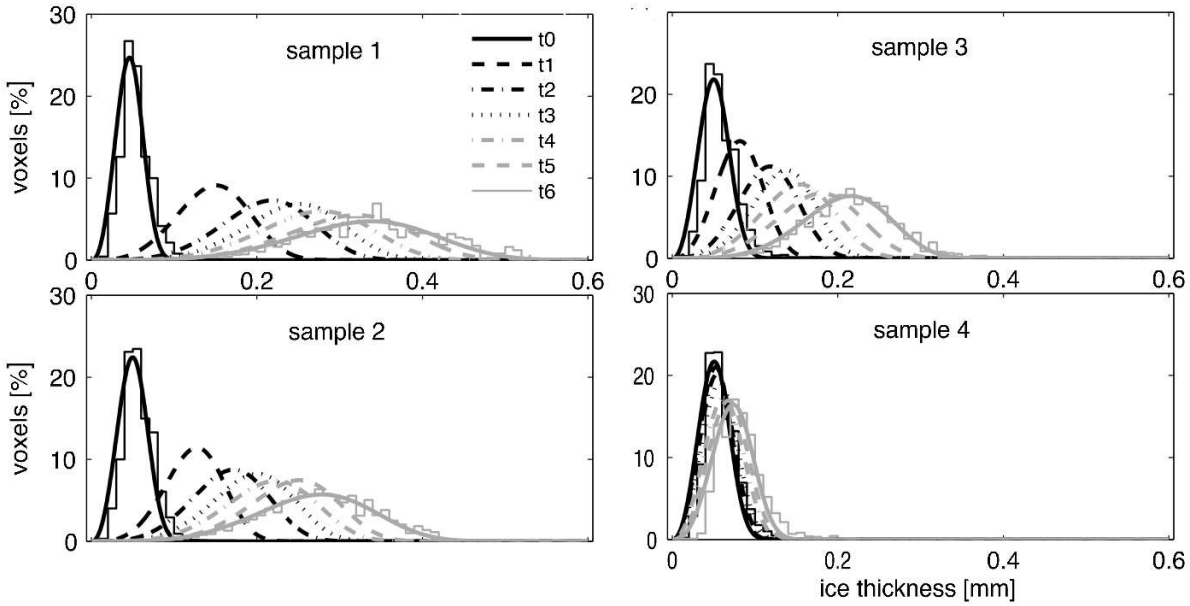


*Figure 2.10: Evolution of thickness distribution of ice matrix of snow samples at four different temperatures derived from isothermal sintering experiments conducted by Kaempfer and Schneebeli (2007), where sample 1 was at −2 °C, 2 at −8 °C, 3 at −19 °C and 4 at −54 °C. The seven measurement times $t = (0, 1, 2, 3, 4, 5, 6)$ correspond to $t = (0, 5, 11, 17, 23, 30, 45)$weeks, respectively.*

over time shown in fig. 2.10. A thicker ice-structure is able to carry more load and thus results in a strengthening of the snow. The effect of strengthening with age on the deformational behaviour of snow has been studied by Yong and Metaxas (1985) and is described in section 2.1.2.
Szabo and Schneebeli (2007) conducted measurements of the sintering force between two adjoining ice grains. Within the experiments ice cones with spherical tips of 3 mm radii have been used. The spherical tips were pushed together by different loads and at different temperatures. The contact load was kept constant over different time periods to allow an ice bond to sinter between the grains. After different contact times between 0 and 1000 $ms$ the ice grains were separated and the force to separate the grains was measured. The measured force is called the sintering force and is shown for the temperatures −1, −5, −12 and −23 °C in dependence of the contact time and load. The sintering force is a measure of the bonding strength between ice grains. Fig. 2.11 shows that the bond strength between ice grains grows with increasing contact time and contact load. The growth rate increases with ascending temperature. This temperature dependence is already seen in fig. 2.10. Szabo and Schneebeli (2007) related the growth in sintering force to the growth in bond size. They derived the following growth law of the bond radius:

$$a = \sqrt{R^2 - \left(\sqrt{R^2 - {a_0}^2} - \dot{\varepsilon}_{ice} \cdot l \cdot t\right)^2} \tag{2.2}$$

where $a$ describes the bond radius, $R$ the grain radius, $\dot{\varepsilon}_{ice}$ the creep rate of ice, $l$ the length

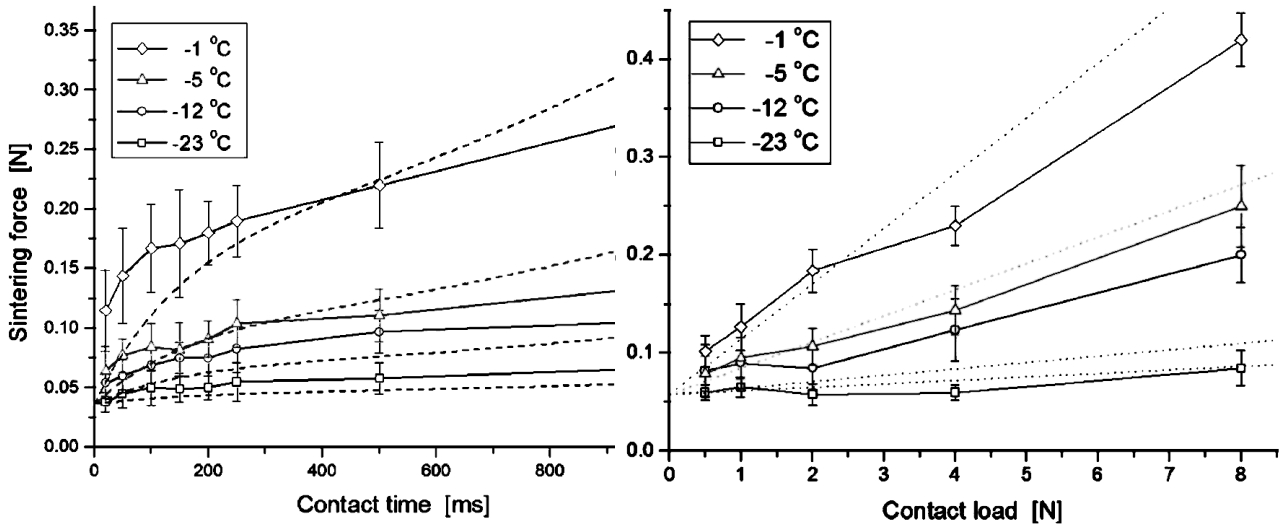


*Figure 2.11: Measurements of bond growth between adjoining ice grains by means of sintering in dependence of contact time and load by Szabo and Schneebeli (2007)*

of the bond and $t$ the contact time. The creep rate $\dot{\varepsilon}_{ice}$ of ice is thereby a function of the contact time and contact load. The creep rate of ice will be described in the following section.

### 2.1.2 Deformational Behaviour of Ice and Snow

As snow consists of ice on the micro-scale, several principal features of the deformational behaviour of ice can also be observed in the deformational behaviour of snow. Snow as of interest in the applications of this study exists close to its melting point. Under these thermal conditions, the mechanical behaviour of ice shows a strong dependence of deformation processes to changes in temperature, load and velocity. In other words, the velocity of the loading process is as important for the resulting strength as the load and temperature experienced by the ice structure. These dependencies are observed for the deformational behaviour of snow and ice similarly.
Hence, in this section the deformational behaviour of ice is presented first, followed by a discussion of the deformational behaviour of snow. The similar behaviour is demonstrated by relevant measurements of both materials.
Under the various dependencies the loading rate of ice and snow is commonly chosen to distinguish between the principal deformation behaviours. This loading rate or rate of deformation $\dot{\varepsilon}$ is defined as follows:

$$\dot{\varepsilon} = \frac{v_L}{L}$$

where $v_L$ describes the magnitude of the loading velocity and $L$ the characteristic length in direction of loading.

## Deformational Behaviour of Polycrystalline Ice Ih

As discussed along with fig. 2.8, this study considers polycrystalline ice Ih, also called terrestrial or normal ice, under engineering condition.

### Ductile to Brittle Behaviour

Depending on the rate of loading two principal inelastic behaviours are exhibited by ice. At low rates, i.e. below $10^{-4} - 10^{-3}$ s$^{-1} > \dot{\varepsilon}$, ice shows a ductile behaviour. Contrary, at high rates above $10^{-4} - 10^{-3}$ s$^{-1} < \dot{\varepsilon}$ ice fractures brittle during straining.

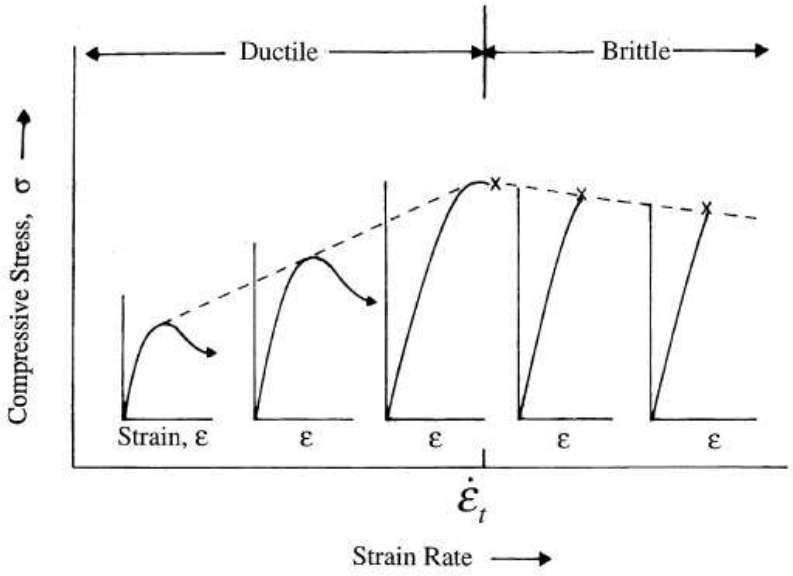


*Figure 2.12: Schematic illustration of the strain - stress relationship of ice in dependence of the strain rate by Schulson (1990).*

The transition between ductile and brittle behaviour of ice under tension and compression was investigated in detail by Schulson (1990). Fig. 2.12 illustrates the strain-stress relationship of ice under compressive loading in dependence of the strain rate.
At lower strain rates, the strain-stress curves are composed of an ascending and descending part. With increasing strain the stress increases until it reaches the peak stress, i.e. yield strength, of ice. Thereafter, ice softens with increasing strain. Over the entire loading time ice deforms plastic. The deformed ice can show cracks but does not collapse, i.e. does not show macroscopic failure. Wakahama (1967) conducted load tests on ice under ductile rates. The straining was stopped during the initial phase of stress increase. The ice started to relax the developed stress during the constant strain state. This shows that ice creeps under loading even in the initial phase and does not show pure elastic features. Schulson (2001) pointed out that the strain hardening is caused by basal gliding and dislocation climbs of the ice crystals while the strain softening is a result of internal cracking and re-crystallisation.

At higher strain rates in fig. 2.12, the strain-stress curves are only composed of a rapid ascending part. The stress ascends almost linear with increasing strain until it reaches the brittle strength at which the material ice collapses suddenly. Under the rapid loading the material ice has not enough time to relax the increasing stress via creep. This explains the almost linear elastic increase and lack of stress relaxation as it takes place under ductile deformation. Thus the remaining way to release the stress is sudden failure when the deformational energy reaches the failure limit.
The investigations of Schulson (1990) also reveal the dependence of the compressive and tensile strength in terms of the strain rate. Fig. 2.13 shows an increase in the compressive yield strength with increasing strain rate in the ductile regimes, i.e. $\dot{\varepsilon} < 10^{-3}$ s$^{-1}$. This increase in compressive strength is also schematically drawn in fig. 2.12. Further, the compressive strength shows a decrease with increasing temperature and increasing salinity and porosity. Hobbs (1974) is giving a detailed composition of the variety of dependencies of the mechanical behaviour of ice.

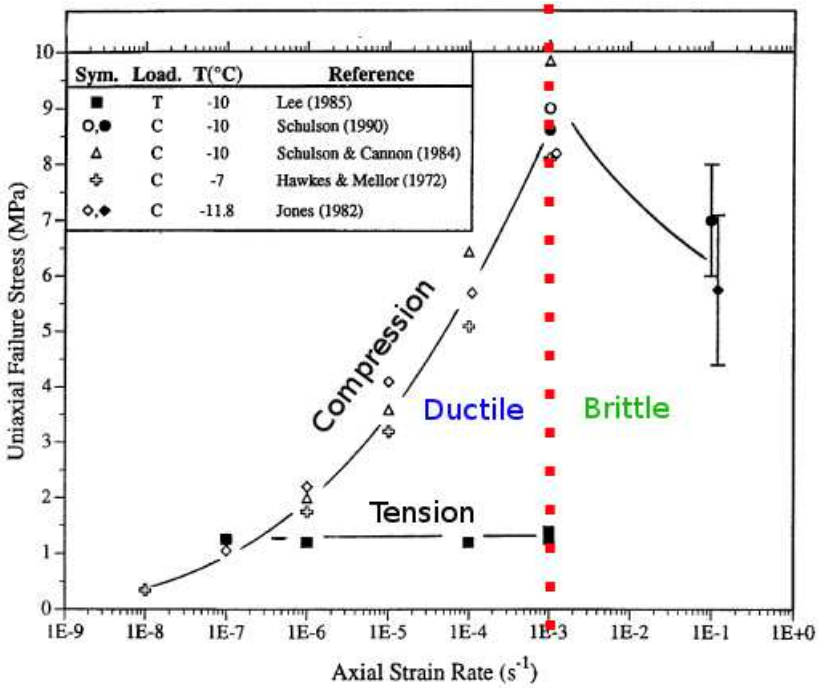


*Figure 2.13: Failure strength of ice in dependence of the strain rate by Schulson (1990)*

Fig. 2.13 and fig. 2.12 also illustrate the brittle failure strength under compressive straining for strain rates above $\dot{\varepsilon} > 10^{-3}$ s$^{-1}$. The brittle strength reduces with increasing strain rate. Contrary, the tensile strength does not show to be influenced by any change in strain rate.
Next to the brittle strength dependencies, Schulson (2001) also investigated in details into the grain size dependence of ice. The investigations allowed to derive empirical approximations for the strength of ice. The observations pronounce an increase of the brittle compression strength of ice by a factor 2.5 with a decrease in temperature from $-10$ °C to $-50$ °C. From the grain size and strain rate dependencies one can assume a brittle

compression strength of 10 MPa at 0 °C, the transition rate of $10^{-3}$ $s^{-1}$ and for a grain size of 1 mm. The resulting linear approximation for the brittle compression strength of ice can be formulated as follows:

$$\sigma_{bcs}\,[\text{MPa}] = [(-3/8)(T/\,^{\circ}\text{C}) + 10]\ \ \text{MPa} \tag{2.3}$$

where $T$ is the ambient temperature in °C. The strength of ice decreases with increasing temperature. Also for the temperature dependence of the strength, the creep of ice is the underlying mechanics. Close to its melting point ice shows to be more viscous and thus sustains the load with decreasing strength.

### Creep Behaviour of Ice

As mentioned, the creep behaviour governs the mechanical behaviour of ice and its principal dependencies.
Barnes et al. (1971) conducted an intensive study on the creep and friction of polycrystalline ice Ih. The creep experiments included uniaxial deformation tests under constant load and indentation test to measure the hardness of ice for specimens with a grain size of 1 mm.
During the uniaxial compression tests the ice specimen was compressed between two rigid plates under various constant loads and temperatures. Barnes et al. (1971) recorded the strain - time characteristic of the ice specimen. The resulting stress - strain rate relationship, i.e. creep curve of ice Ih, is depicted in fig. 2.14. The uniaxial compression experiments were conducted for strain rates of $10^{-9}$ to $10^{-2}$ $s^{-1}$ and temperatures of 0 to −48 °C. The creep curves of ice show an increase of the creep rate $\dot{\varepsilon}_{ice}$ with increasing stress and temperature. Barnes et al. (1971) approximated the creep measurements by using a power law equation and *sinh* functions. The model derived from the creep measurements of ice under constant load can be written as follows:

$$\dot{\varepsilon}_{ice} \;=\; A \cdot (sinh(\alpha \cdot \sigma))^n \cdot e^{\frac{-Q}{RT}} \tag{2.4}$$

where $\sigma$ describes the applied load, $Q$ the activation energy, $R$ the gas constant, $T$ the temperature and $A$, $n$ and $\alpha$ are constants. Barnes et al. (1971) give a detailed description which values to choose for the constants depending on the temperature regime.
However, for the development of interaction models between snow/ice grains within this study, the indentation hardness measurements conducted by Barnes et al. (1971) are of higher interest. Within the hardness measurements, a rigid spherical or pyramidal indenter is pushed into the surface of an ice specimen for a certain time $t$ and by a known load $f$. After removal the projected area $a$ of the indentation is measured which results in the hardness $H$ as follows:

$$H \;=\; \frac{f}{a}$$

The predicted hardness $H$ is depicted over different temperatures in fig. 2.15. The following equation of ice hardness $H_{ice}$ has been derived by Barnes et al. (1971) from the indentation measurements:

$$H_{ice} \;=\; B \cdot \left(\frac{1}{t}\right)^{\frac{1}{m}} \cdot e^{\frac{Q}{mRT}} \tag{2.5}$$

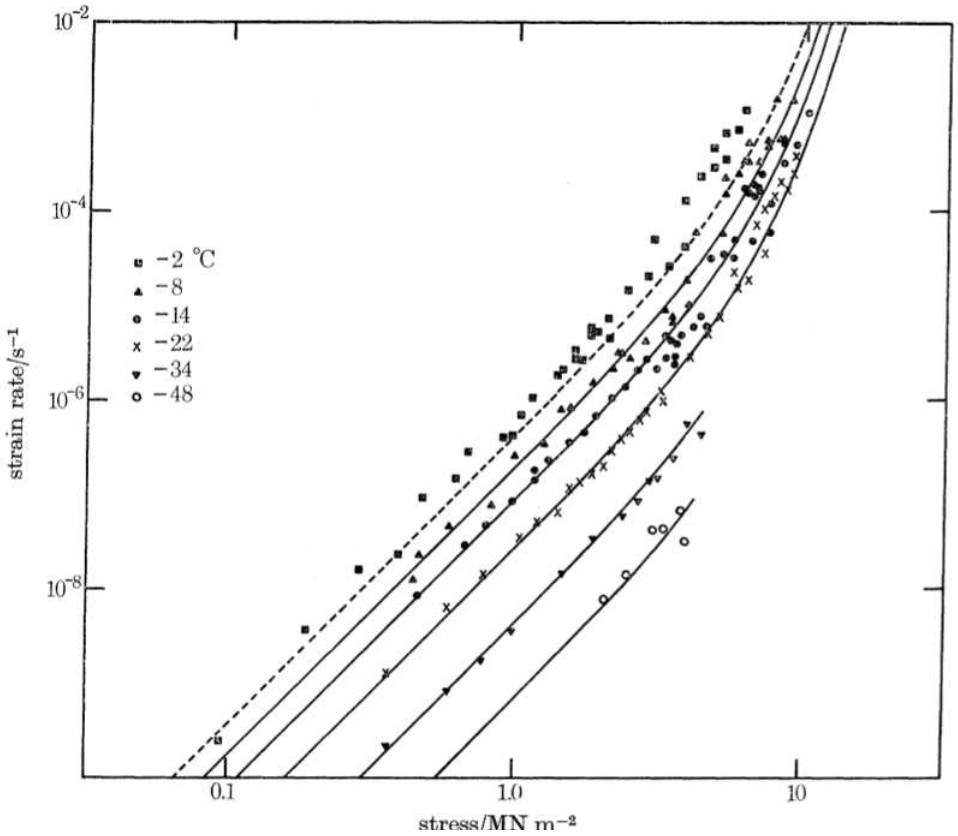


*Figure 2.14: Creep curve of polycrystalline ice obtained in uniaxial compression tests conducted by Barnes et al. (1971) at different temperatures. The lines are predicted by eq. 2.4.*

where $B$ and $m$ are constants depending on the temperature. Further, the indentation hardness measurements show that the strength value can not grow above a certain limit. As ice starts to melt under pressure this limit is set by the curve of pressure melting or melting point depression in fig. 2.15. The melting point is depressed under increasing indentation pressure and causes the ice surface to melt. This is an important phenomenon when deriving collision models for ice grains in a snow pack.
The creep equation derived from these indention hardness measurements of ice can be formulated as follows:

$$\dot{\varepsilon}_{ice} = \frac{1}{A} \cdot \sigma^n \cdot e^{\frac{-Q}{nRT}} \tag{2.6}$$

The creep rate behaviour described by the model and shown in fig. 2.15 describes similar curves but lacks the asymptotic behaviour of the creep measurements shown in fig. 2.14. Indentation tests are conducted by pressing a point-like indenter with its peak end into the surface of the sample. Hence, the creep rate $\dot{\varepsilon}$ derived from those measurements is closer to the micro- or meso-scale behaviour. Thus the scale of this relation of ice is naturally closer to the grain-scale of snow.

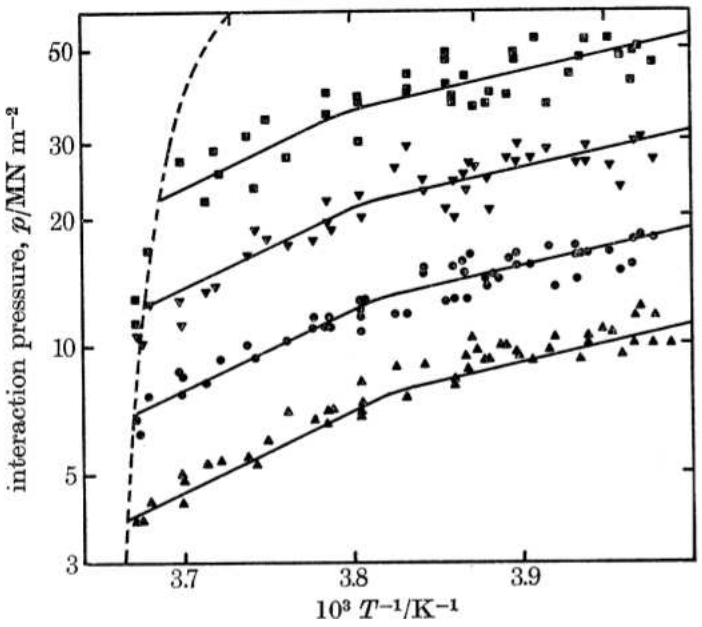


*Figure 2.15: Hardness of ice Ih measured by Barnes et al. (1971) by pressing a rigid indenter into the surface of an ice specimen under different temperatures. The dashed line describes the pressure melting curve.*

### Coefficient of Restitution of Ice

During the deformation of snow, the ice grains and ice bonds on the grains scale rearrange, deform and fracture. Hence, the microscopic deformation processes of ice determine the macroscopic strength and behaviour of snow. Therefore, next to the deformation and fracture of ice bonds, the collision behaviour of ice grains during rearrangement is of importance. This behaviour is also governed by the previously described dependencies of the mechanical behaviour of ice.
Higa et al. (1998) conducted measurements of the coefficient of restitution of ice by dropping spherical ice grains on an ice plate. The coefficient of restitution is thereby predicted as the ratio between impact $v_i$ and rebound velocity $v_r$:

$$e_{ice} = \frac{v_r}{v_i} \tag{2.7}$$

The investigations focused on the impact velocity, size and temperature dependencies of the coefficient of restitution $e_{ice}$. The results revealed a critical velocity $v_c$ which distinguishes the impact behaviour into a quasi-elastic and plastic/brittle regime. The critical velocity depends on the grain size and temperature. In the case of fig. 2.16 the critical velocity $v_c$ equals 40 cm/s for a grain radius of 1.5 *cm* and a temperature 261°$K$. In the quasi-elastic regime for $v_i < 40$ cm/s, the restitution coefficient does not change with velocity. The potential energy is almost entirely recaptured after impact during the quasi-elastic regime. Higa et al. (1998) reported no visual deformations or change on the impacted ice grains. During the plastic/brittle regime in fig. 2.16 for $v_i > 40$ cm/s, the ice grains showed plastic

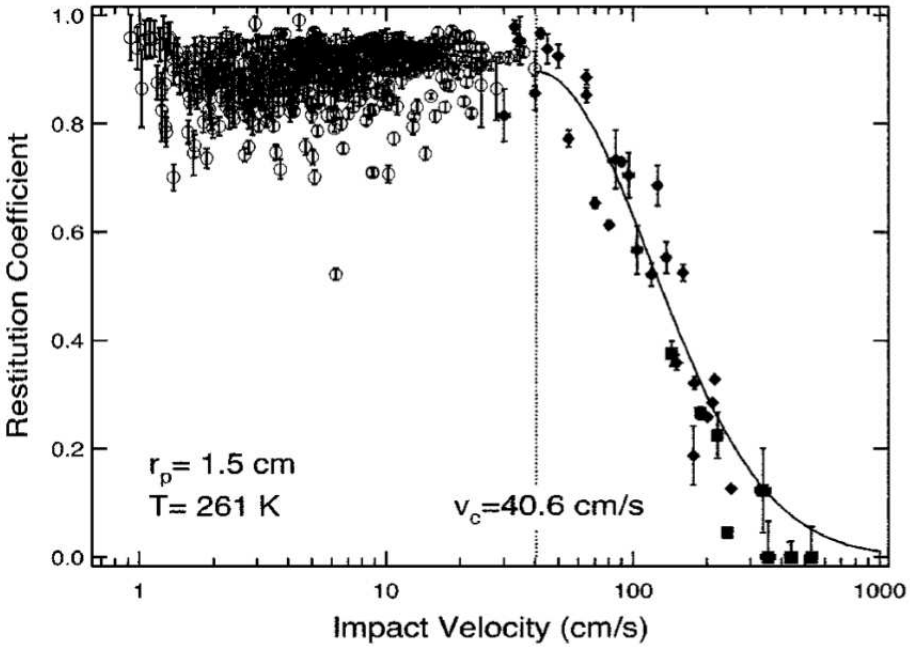


*Figure 2.16: Coefficient of restitution $e_{ice}$ versus impact velocity measured by Higa et al. (1998).*

deformation after impact. At even higher impact velocities, the ice grains fractured into pieces. For the coefficient of restitution $e_{ice}$ in fig. 2.16 this results in a decrease with increasing impact velocity.
From their measurements Higa et al. (1998) derived the following ideal relation:

$$e_{ice} = \left\{ \begin{array}{ll} \cong 1 & v_i < v_c \\ \left(\frac{v_i}{v_c}\right)^{-\log \frac{v_i}{v_c}} & v_i \geqslant v_c \end{array} \right\} \tag{2.8}$$

The relation assumes no energy loss within the quasi-elastic regime and thus full recovering of the rebound velocity. This however can not be the case according to the observations of Szabo and Schneebeli (2007) and Fan et al. (2003) who stated an instantaneous bonding between ice grains when contacting. Hence, the rebounding energy has to be less than the impact energy due to the necessary bond fracture. This loss in energy is found in the measurements in fig. 2.16. Szabo and Schneebeli (2007) calculated the initial bond size by using the contact theory of Hertz (1881). Together with the tensile fracture strength of ice, mentioned previously, the calculation predicted the energy loss very precisely.
However, in the case of snow the velocity regime of the plastic-brittle impact found in the investigations of Higa et al. (1998) correlates with the regime of the second kind of brittleness of snow reported by Kinosita (1967) and depicted in fig. 2.23. Even more so, the studies of Yong and Metaxas (1985) reveal the same velocity regime. In this regime, the age of snow loses its influence on the snow strength which is discussed along with fig. 2.34.

### Coefficient of Ice-Ice Friction

During rearrangement in a snow pack, ice grains are of course able to slide as well. This situation is governed by the friction behaviour of ice. The ice-ice friction behaviour can be divided into three regimes which again depend on the rate, i.e. sliding velocity $v_s$. Detailed measurements of the ice-ice friction coefficient $\mu_{ice}$ by Kennedy et al. (2000) and Akkok et al. (1987) captured the regimes in fig. 2.17. The first two regimes are thereby governed

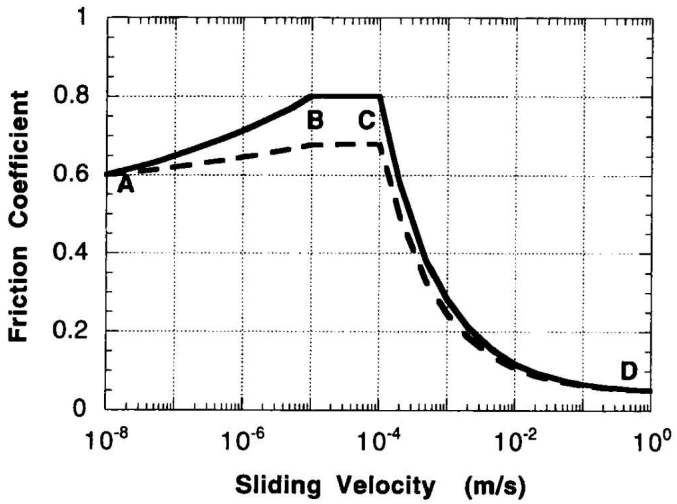


*Figure 2.17: The ice-ice friction coefficient versus sliding velocity $v_s$ as measured by Kennedy et al. (2000).*

by the deformational behaviour of ice as described previously.
In particular, the first regime $\overline{AB}$ of $v_s < 10^{-5}$ m/s is again controlled by the creep of ice. As ice sinters immediately, i.e. bonds, friction in this regime develops due to surface creep. The friction coefficient increases with increasing sliding velocity.
The second regime $\overline{BC}$ of $10^{-5}$ m/s $< v_s < 10^{-5}$ m/s, depicted in fig. 2.17, shows surface fracture behaviour. Similar to the described ductile to brittle transition of ice deformation, the friction in this velocity regime develops due to the fracture of the bonded and re-bonding ice surfaces of the contacting bodies. The friction coefficient shows no change with changing sliding velocity.
For sliding velocities $v_s > 10^{-4}$ m/s in the third regime $\overline{CD}$, the sintering effect of ice loses its influence. Due to the high velocity, the frictional heat melts the sliding surface which disables the bonding behaviour. The friction coefficient declines with decreasing sliding velocity due to increasing surface melting. The decrease of the coefficient is additionally supported by the pressure melting at the surface.
The measurements of Akkok et al. (1987) and Kennedy et al. (2000) focused on the surface melting regime and were used to derive the following relation:

$$\mu_{ice}(T, P, v_s, H) \;=\; C_1 \cdot (T_m - T)^a \cdot P^{-b} \cdot \left(\frac{k\rho c}{v_s \cdot L}\right)^c \cdot H^{-d} \tag{2.9}$$

Hence, the relation describes the sliding regime governed by surface melting of contact asperities where $T_m$, $T$ and $p$ are the pressure depressed temperature, the ambient temperature and the load applied, respectively. $L$ describes the characteristic length of the sliding body and $H$ is the hardness of ice. The constants $a, b, c$ and $d$ depend on the materials contacting with ice. Akkok et al. (1987) included a detailed description for several material pairs. The prediction of the friction coefficient thereby includes the melting point depression of ice.

## Deformational Behaviour of Snow

The study of the mechanical behaviour of snow points back until the first half of the 20th century, Bader (1962), to help forecast natural snow avalanches. For the natural densification of a snow cover deformations at low strain rates are of interest. Contrary, a large amount of engineering applications concerned with trafficability and transportation safety are interested in understanding the physics of snow as well. Engineering applications are thereby interested in the high strain rate behaviour of snow. Hence both applications benefit from the study of the mechanical behaviour of snow. A snow pack is composed of snow grains consisting of multi-crystalline ice as shown by Meyssonnier et al. (2009). Hence, on the grain-scale snow follows the mechanical behaviour of ice. Further, the snow grains are connected by bonds which results in an open-foam like structure. Thus, the macroscopic behaviour of snow under load is governed by the deformation and failure of micro-scale bonds, inter-granular collision and friction forces during rearrangement of the ice grains. This approach has already been successfully applied to snow in the micro- to macroscopic approach of Nicot (2004b).
Due to its micro-structure snow inherits the principal mechanical features of ice plus additional properties specific to its granular nature. These principal and additional features of the deformational behaviour of snow are presented in this section along with relevant measurements.
As for the mechanical behaviour of ice, the mechanical behaviour of snow can also be divided into two major regimes depending on the deformation rate or velocity. But contrary to ice, the transition behaviour between both regimes is distinctively developed for snow. As a rough approximation the transition behaviour can be defined at strain rates close to $5 \cdot 10^{-4}$ s$^{-1}$.
Hence, at low strain rates of $\dot{\varepsilon} < 5 \cdot 10^{-4}$ s$^{-1}$ snow deforms as a ductile material which is depicted in fig. 2.18a. On the other hand, at high strain rates of $\dot{\varepsilon} > 5 \cdot 10^{-4}$ s$^{-1}$ snow behaves like a brittle material as illustrated in fig. 2.18c.

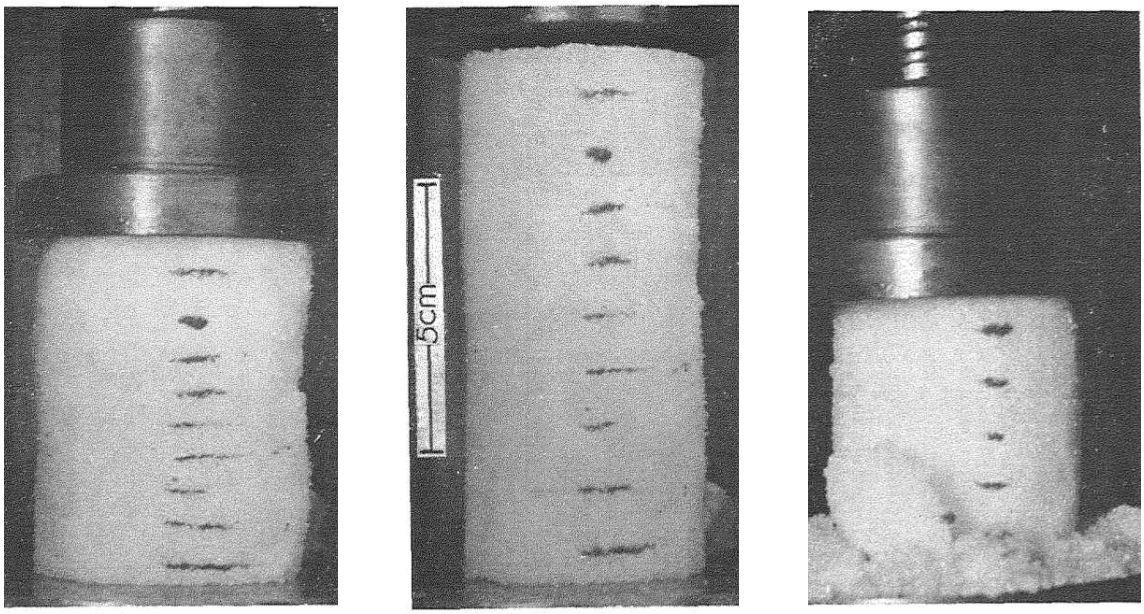


*(a) Ductile deformation (35%).* *(b) Initial configuration.* *(c) Brittle deformation (55%).*

*Figure 2.18: Cylindrical snow sample under unconfined compression conducted by Kinosita (1967).*

The unconfined compression tests on cylindrical snow samples shown in fig. 2.18 are conducted by Kinosita (1967) over a broad velocity and temperature range. The study covered ductile and brittle behaviour of snow under no confinement pressure. The tests were performed on natural snow of $150 - 400$ kg/m$^3$ deposited in Hokkaido. Looking at the microscopic pictures within the study it is obvious that the snow sintered to strong bonded and rounded grains.
Kinosita (1967) composed the results into fig. 2.19, which serves here as an overview of snow deformation before going into further details. For brittle deformations the measurements of Kinosita (1967) in fig. 2.19a show a linear growth of the stress with increasing strain until the stress reaches the strength limit. Thereafter, the stress suddenly drops. This is the very same behaviour as observed for ice. After the abrupt decline the stress builds up with the same inclination onto the almost same level before dropping again suddenly. This behaviour keeps repeating and thereby forms the typical saw-tooth shape of a deformation curve of brittle materials. Kinosita (1967) defined the brittle strength of snow as the maximum stress measured throughout the entire deformation. At the points of sudden decrease in stress the snow sample shows subsequent fractures, i.e. collapses, as depicted in fig. 2.18a. On the grain-scale this behaviour can be regarded as the progressing fracture of bonds and major rearrangement of the ice grains.
In fig. 2.19a, Kinosita (1967) depicted the ductile deformation curve of snow. The strain-stress curves demonstrate an initial stress increase with a high gradient with increasing strain until the ductile yield stress. Thereafter, the curves show a change in slope but the stress keeps increasing with strain which describes a work-hardening behaviour of snow after the yield point. Over the entire deformation time the snow sample shows an uniform

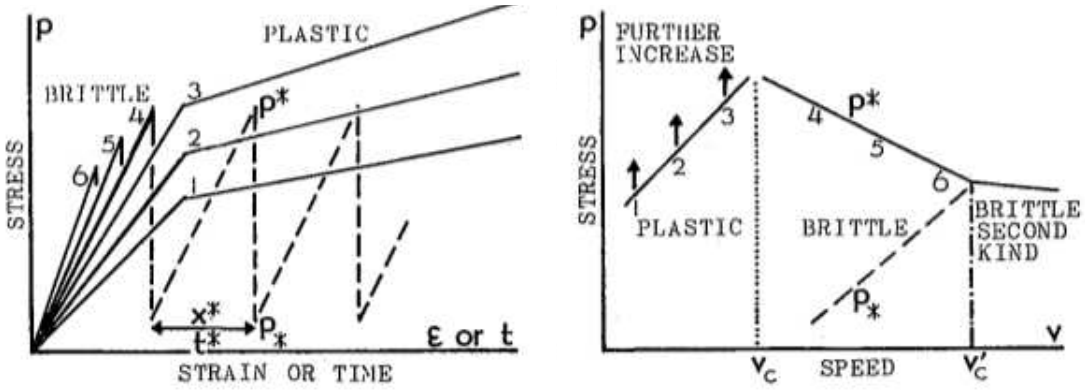


*(a) Strain-stress relationship.* *(b) Speed-strength relationship.*

*Figure 2.19: Schematic illustration of the confined compression tests on snow by Kinosita (1967).*

compaction with no change in shape. Looking at the grain-scale of a snow sample during ductile compression, the bonds deform plastically and relax the developing stress due to the creep of ice. Fig. 2.20 illustrates schematically the difference between the ductile and brittle failure types of snow.
Fig. 2.19b demonstrates a similar strength - strain rate relationship of snow as measured in compression tests of ice. Strength and deformational behaviour of snow are again a function of the strain rate, i.e. velocity. The unconfined ductile strength of snow ascends with increasing velocity applied. At the maximum value of the ductile strength the defor-

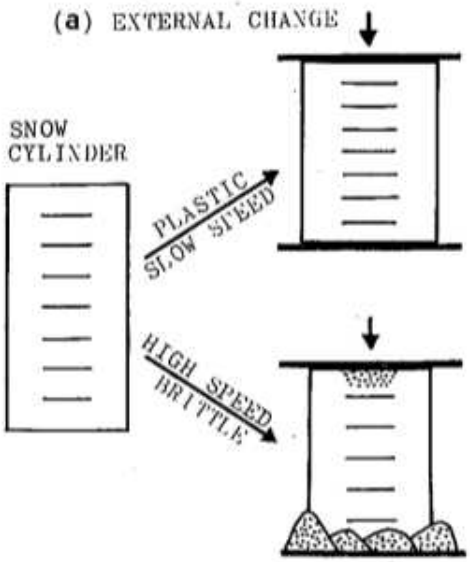


*Figure 2.20: Schematic representation of the difference between ductile and brittle deformation behaviour of unconfined snow samples by Kinosita (1967).*

mational behaviour undergoes a transition from ductile to brittle behaviour. With further increase in velocity the unconfined brittle strength reduces and the snow sample is deforming purely brittle as described previously.
Kinosita (1967) reported if one increases the velocity, i.e. strain rate, even further the deformation behaviour eventually reaches a second kind of brittle progression with increasing strain. In the stress - rate relationship of fig. 2.19b this regimes is identified by an almost constant strength value of snow which barely changes with changing strain rate. Previous to the regime of second brittleness the maximum and minimum value of the saw-tooth shape approaching each other with increasing velocity.
In his thesis, Fukue (1977) investigated in detail the performance of snow under load. The investigations also included unconfined compression tests of snow. The tests thereby focused on the micro-scale dependencies of the behaviour. Thus Fukue (1977) allowed snow samples to sinter in sealed isothermal conditions before the unconfined compression tests were conducted. Due to the sealed container he managed to avoid any changes in density. This procedure enabled to study the strength of the snow sample in dependence of the sintering age, i.e. increase in bonding strength. Fukue (1977) performed the unconfined compression tests with loading rates of the ductile, brittle and transition regime. Fig. 2.21 illustrates the ductile and brittle deformation behaviour with the dependence on the bonding strength.

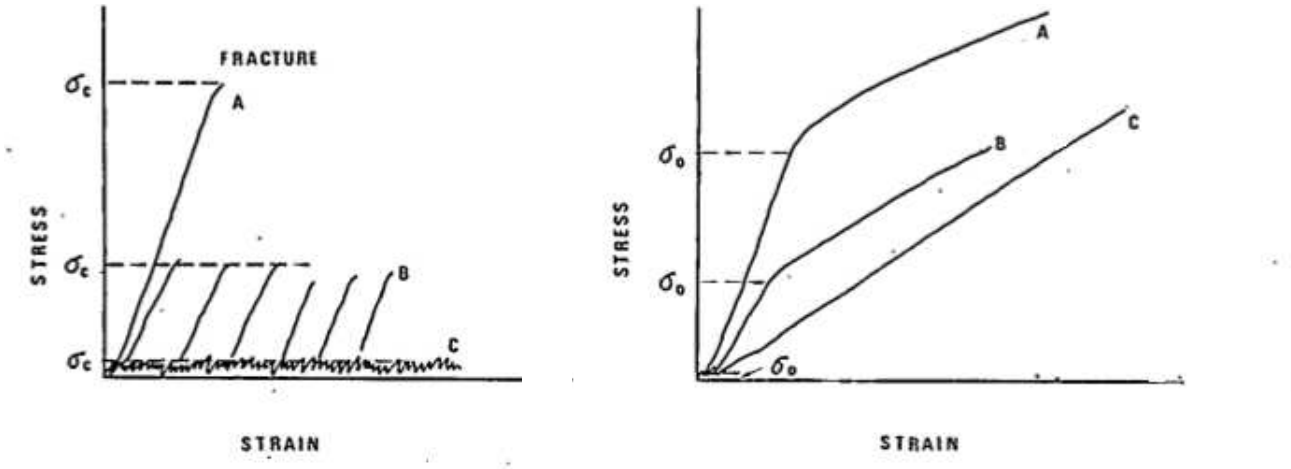


*(a) Strain-stress relationship.* *(b) Speed-stress relationship.*

*Figure 2.21: Strain-stress relationship of different snow types with constant density measured by Fukue (1977). The snow type (A) describes strongly bonded snow, (B) moderately bonded while (C) stands for poorly bonded snow.*

The brittle deformation behaviour in fig. 2.21a shows the same stress build up and sudden release with increasing strain as measured by Kinosita (1967). Also, the ductile curve in fig. 2.21b shows the same feature as described previously. With increasing strain the stress grows initially with a high gradient and experiences a decrease in the slope at the ductile yield strength.
However, fig. 2.21 shows a general increase in strength with increasing sintering time.

Further, the ductile strain-stress curves in fig. 2.21b demonstrate a distinct change in slope with increasing sintering age.
Von Moos et al. (2003) and Scapozza and Bartelt (2003) also conducted unconfined compression tests of snow under ductile rates which are depicted in fig. 2.22. The ductile stress-strain curves demonstrate that the initial stress build up follows a viscous-elastic path with increasing strain rather than linear progression as suggested in the previous schematic depictions. Scapozza and Bartelt (2003) defined the ductile strength of snow as the first stress value at the onset of the second slope.

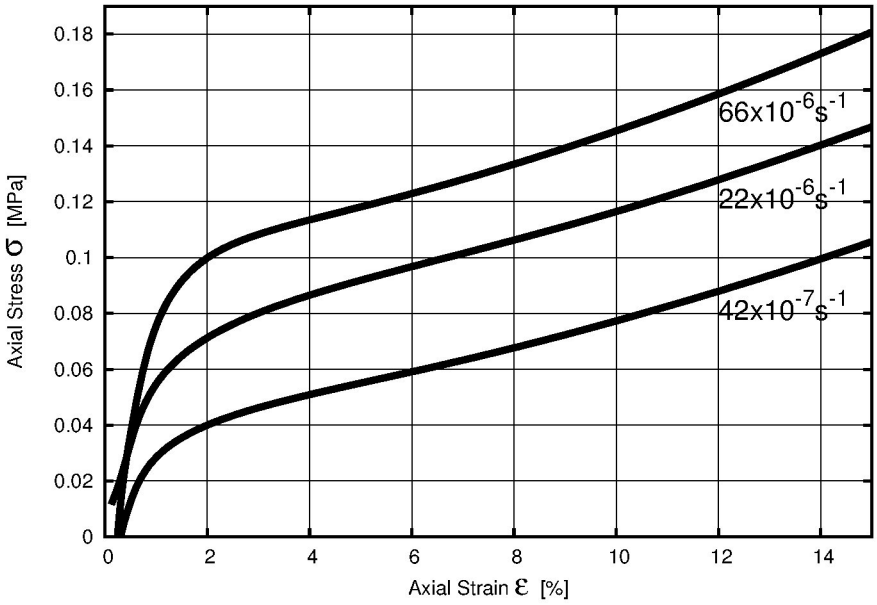


*Figure 2.22: Strain-stress relationship of unconfined compressions tests of snow by Scapozza and Bartelt (2003) conducted with ductile strain rates.*

Von Moos et al. (2003) developed an apparatus to conduct deformation controlled triaxial tests on snow and enabled the device to apply constant lateral pressure. The apparatus was used to apply ductile strain rates and different lateral pressures to cylindrical snow samples at a constant temperature of $-12$ °C. The compression was also conducted without lateral pressure, i.e. unconfined compression. Their tests mainly focused on ductile strain rates of $10^{-7}$ s$^{-1}$ up to $10^{-5}$ s$^{-1}$ . Scapozza and Bartelt (2003) analysed the results in order to reveal underlying relationship of stress and strain in snow.
Kinosita (1967) measured the ductile and brittle strength for snow of densities from 370 to 400 kg/m$^3$. His results are shown in fig. 2.23. The experimental strength is presented as iso-lines of constant stress values in dependence of the temperature $T$ and loading velocity $v_l$ , i.e. loading rate $\dot{\varepsilon}_l = v_l \cdot l_{cyl}^{-1}$ where $l_{cyl}$ describes the length of the cylindrical snow samples. In fig. 2.23 if one follows an isothermal path, the measured unconfined strength of ductile snow deformation increases with increasing velocity until the transition velocity $v_c$ is reached. Thereafter, with further increase of the loading velocity through the brittle deformation regime, the strength decreases until the second critical velocity $v_c'$ is reached.

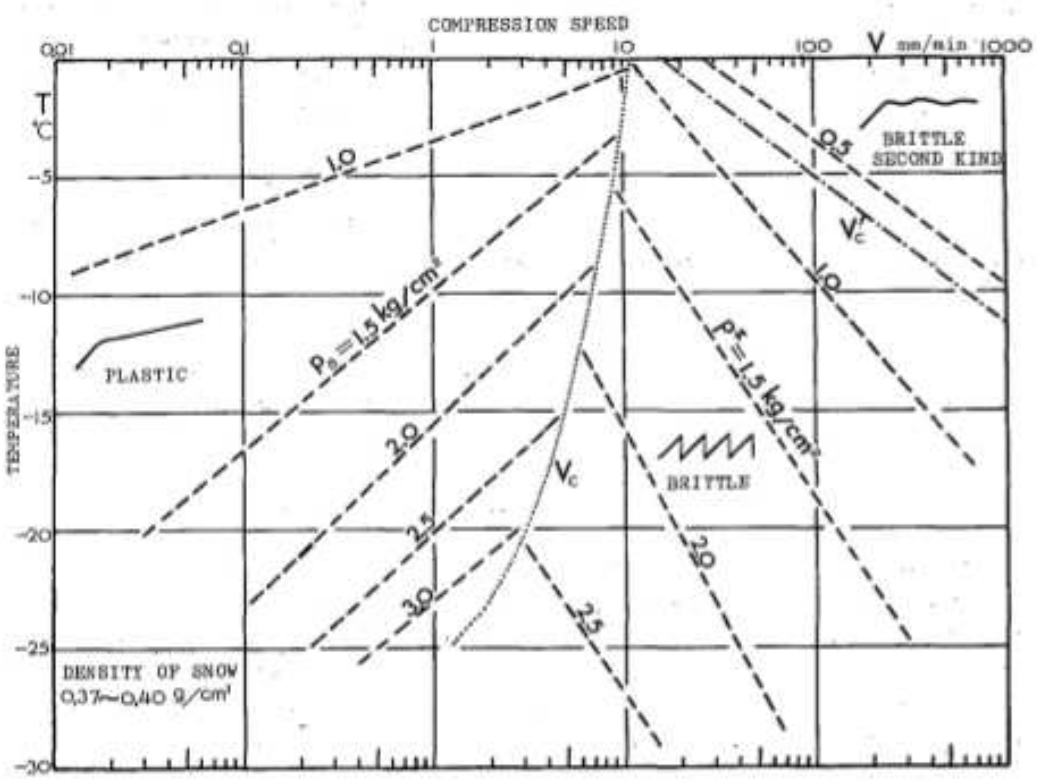


*Figure 2.23: The dependence of snow strength on temperature and loading rate from unconfined compression tests by Kinosita (1967).*

In the regime of second kind of brittle deformation the change in velocity and temperature has almost no influence on the strength of the snow sample.
Despite the second brittle regime, the strength in fig. 2.23 grows with decreasing temperature.
The measurements of Kinosita (1967) reveal that the transition velocity $v_c$, i.e. the transition rate $\dot{\varepsilon}_c$, of ductile to brittle behaviour of snow is not constant. According to the measurements in fig. 2.23 it depends on the temperature. The transition velocity aligns between $1 - 10$ mm/min which relates to a strain rate of $10^{-4} - 10^{-3}$ s$^{-1}$ when using the average of $l_{cyl}$ from the measurements of Kinosita (1967). The curve of $v_c$ in fig. 2.23 is provided in the study as follows:

$$T = (v_l - 20 \cdot \rho_{snow} - 3) \cdot 2.5 = (\dot{\varepsilon}_l \cdot l_{cyl} - 20 \cdot \rho_{snow} - 3) \cdot 2.5 \tag{2.10}$$

Hence, the approximation of the transition curve states that snow at temperatures closer to the melting point of ice inherits less brittleness. Similar snow samples loaded under similar transition rates can develop an increasing strength with increasing temperature. The transition behaviour stands thereby in contrast to the general behaviour of a decrease in snow strength with increasing temperature.
Eq. 2.10 also states a dependence of the transition rate on the density of snow. The rate generally declines with decreasing snow density.

It has to be noticed that the velocity regime of second kind of brittleness predicted by Kinosita (1967) correlates with the plastic/brittle velocity regimes found by Higa et al. (1998). This indicates that at such high rates or velocities the deformation of the ice matrix of snow experiences fracture only.
Scapozza and Bartelt (2003) also composed their ductile strength measurements which are shown in fig. 2.24. The figure illustrates the yield stress $\dot{\sigma}_y$ of ductile deformed snow in relation to the applied strain rate $\dot{\varepsilon}$ for different initial snow densities $\rho_0$. Scapozza and

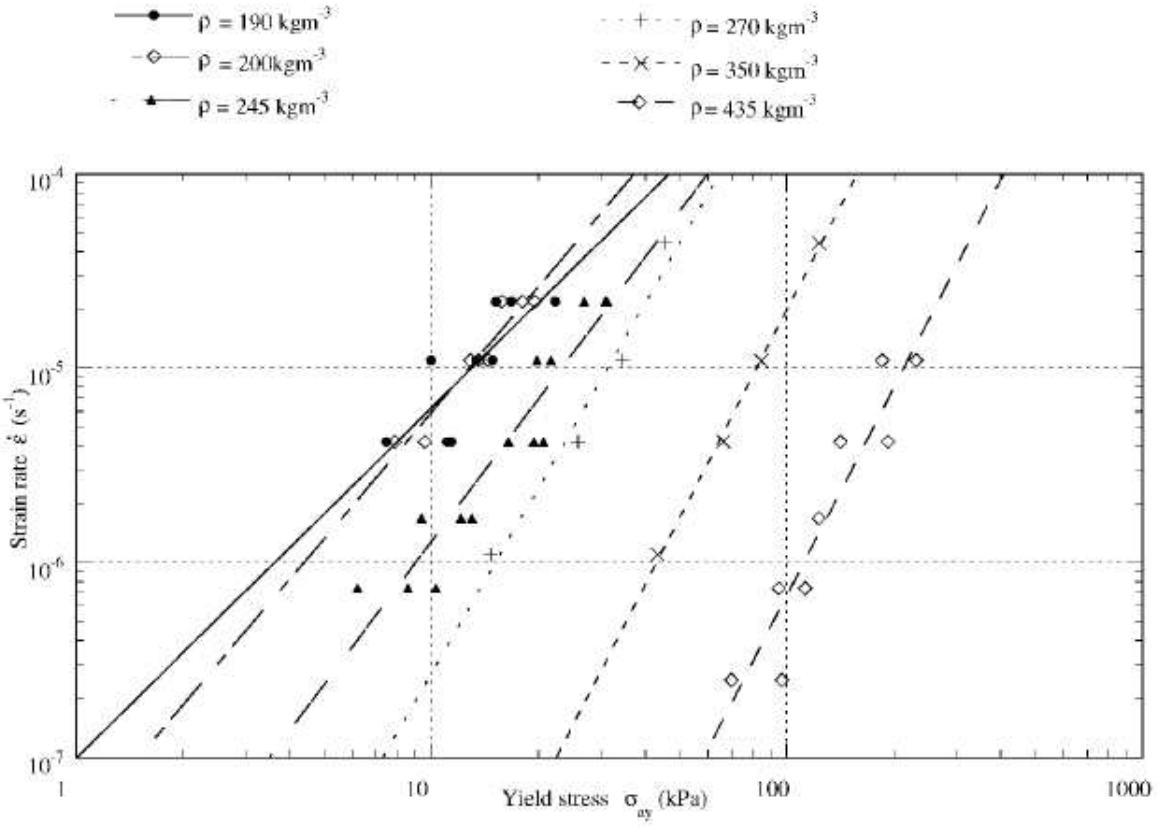


*Figure 2.24: The dependence of snow strength on strain rate predicted in unconfined compression tests on samples of* 320 kg/m$^3$ *and at* −12 °C *by Scapozza and Bartelt (2003)*

Bartelt (2003) capture the same trend in the ductile strength of snow as Kinosita (1967). The strength increases with increasing strain rate. Further, fig. 2.24 shows an increase in ductile strength with rising initial density of the snow samples.
Several authors use density as a measure for the strength of snow as the density is simple to measure compared to the state of sintering. But the strength only increases along with the density if the snow sintered under similar equi-temperature condition, i.e. as bonds build-up and grains are rounded. Hence, the density is a very weak and under certain circumstances even a misleading measure for the strength of snow.
Fukue (1977) demonstrated the weakness of snow density as a strength measure. He produced snow samples of the same density but at different sintering ages. Those were

used in unconfined compression tests of snow. Fukue (1977) analysed thin sections cut out of the ice matrix of the snow samples in accordance to predict the coordination number and the size of the bonds between the grains. The coordination number $N_b$ is defined as the average number of bonds per grain. The thin section analysis revealed a growth in coordination number and size with increasing sinter age. Fig. 2.25 shows the unconfined compression strength of snow samples at transition and brittle strain rates. The strength of snow of about 450 kg/m$^3$ is depicted at different sintering ages, i.e. 0.5, 1 and 2 hours and at 3 and 6 days. The brittle strength in fig. 2.25 declines with increasing strain rate.

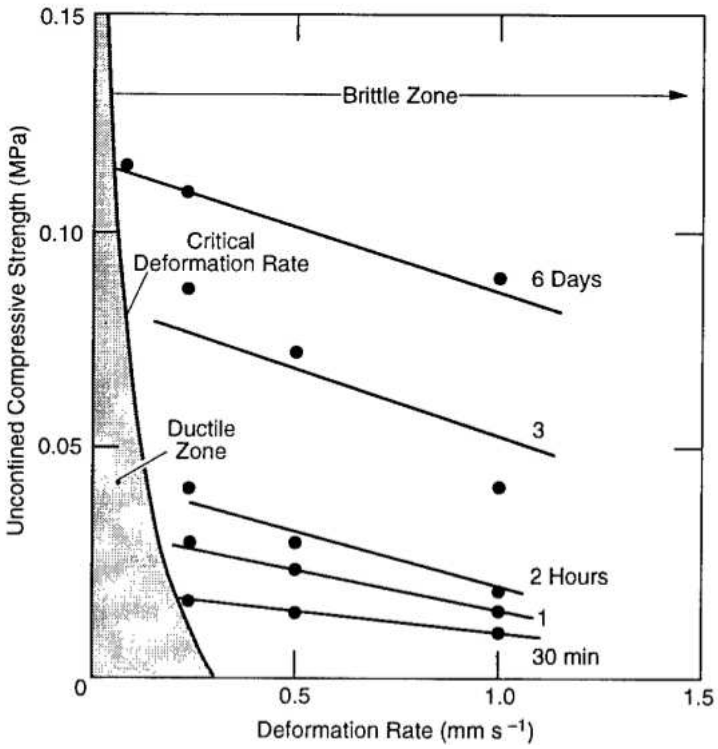


*Figure 2.25: Brittle compression strength of unconfined snow samples with constant density and temperature versus sintering age by Fukue (1977).*

But it grows with increasing sintering time of the snow samples. On the one hand, this demonstrates the major influence of the size and number of bonds in a snow sample on its strength. On the other hand, due to the strong increase in strength for a single snow density it reveals the weak reliability of the density as a strength measure. In other words, snow samples of the same density, in fig. 2.24, could take on almost any strength represented in the graph by a change in sintering age. But, the relation of the density to strength in fig. 2.24 is valid, because the measurements allow to assume a similar sintering histories of the samples.

One strain rate regime of the deformation behaviour of snow has to be highlighted individually, which is the transition between ductile and brittle deformation. Chandel et al. (2014) conducted unconfined compression tests at transitional rates to derive a finite element based description of the regime. The tests were performed on samples of $270 - 290$ kg/m$^3$

in density and at −20 °C. Fig. 2.26 shows the experimental results for two transitional rates which are $7.2 \cdot 10^{-3}$ s$^{-1}$ and $4.8 \cdot 10^{-4}$ s$^{-1}$.

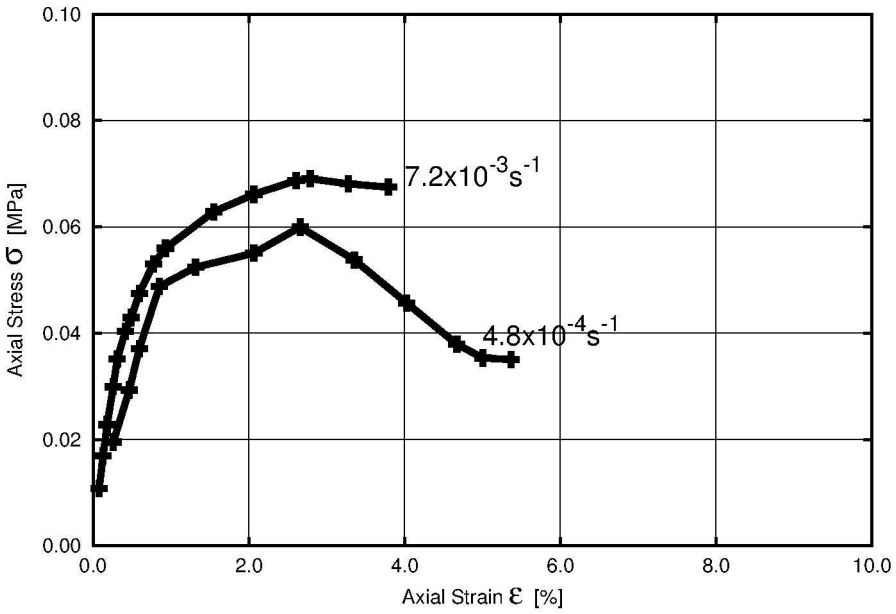


*Figure 2.26: Unconfined compression tests of snow by Chandel et al. (2014) with transition strain rate, initial density of* 270 − 290 kg/m$^3$ *and at* −20 °C.

The strain - stress curves measured by Chandel et al. (2014) at the transition regime do not show any sudden decrease in stress as observed for brittle deformation. The stress ascends on a similar viscous-elastic path with increasing strain as the ductile curves until the yield stress is reached. After the yield strength the curves demonstrate a strain-softening behaviour with increasing strain.
Also Fukue (1977) and Kinosita (1967) measured and described the deformational behaviour at the transition regime. Fig. 2.27 represents the measurements of Fukue (1977) schematically. Fukue (1977) reported a combined behaviour of brittle and ductile deformation in the transition regime. The transition curve initially shows the feature of a brittle deformation by a few build ups and sudden stress drops. The build ups increase with increasing strain until a certain densification is reached at which point the curve follows the ductile path.
Nevertheless, there is no clear explanation for the different observations of Chandel et al. (2014) and Fukue (1977) in the transition regime. Although, it has to be mentioned that the behaviour described by Fukue (1977) is actually common to confined compression tests of snow which will be discussed below.

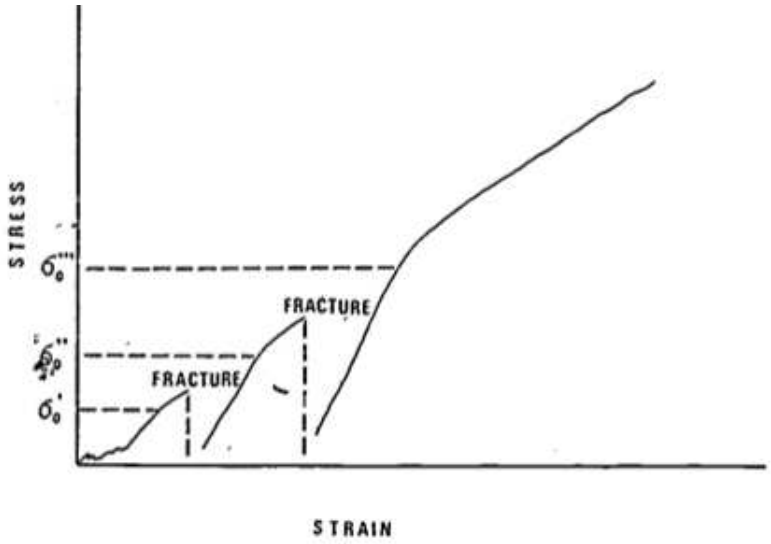


*Figure 2.27: Deformational behaviour at the transition regime by Fukue (1977).*

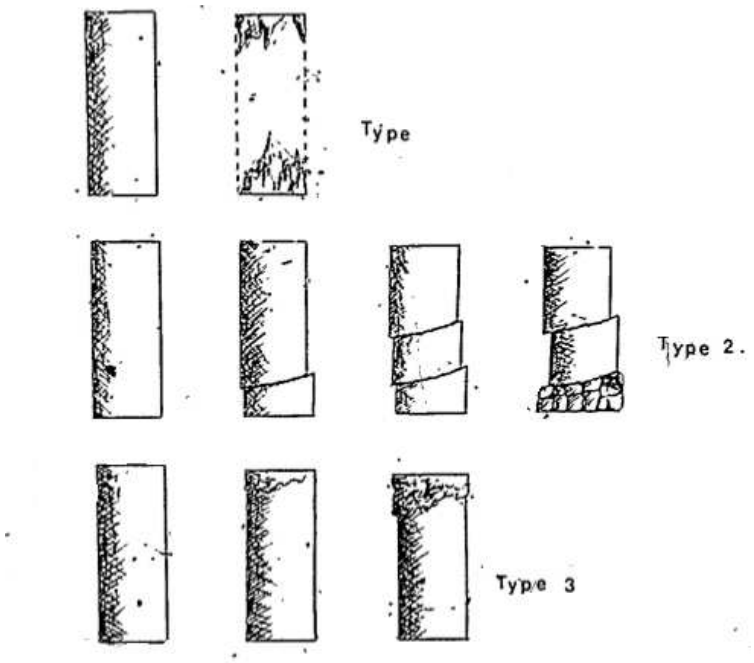


*Figure 2.28: Three different brittle failure types observed by Fukue (1977).*

Fukue (1977) distinguished three different types of brittle failure, which are shown in fig. 2.28. Type 1 is identified as a complete collapse with observable failure surfaces at the end plates of the unconfined loading device. This type is also common to other brittle materials.
The brittle failure type 2 is described as a multiple plane or surface fracture. This kind of failure is also observable in confined compression tests of snow.
Type 3 is a local crushing and rearrangement of snow grains at the end plates of the loading

device.
In contrast to the failure under unconfined compression, Narita (1984) investigated in detail the failure under unconfined tension of cylindrical snow samples. He conducted uniaxial tensile experiments in a cold laboratory at various temperatures and snow densities ranging from $240 - 470$ kg/m$^3$. The cylindrical snow specimens were subjected to tensile strain rates of $5.5 \cdot 10^{-7}$ to $-2.5 \cdot 10^{-3}$ s$^{-1}$ . The measurements allowed to distinguish four different types of deformation, which are labelled a, b, c and d in fig. 2.29.

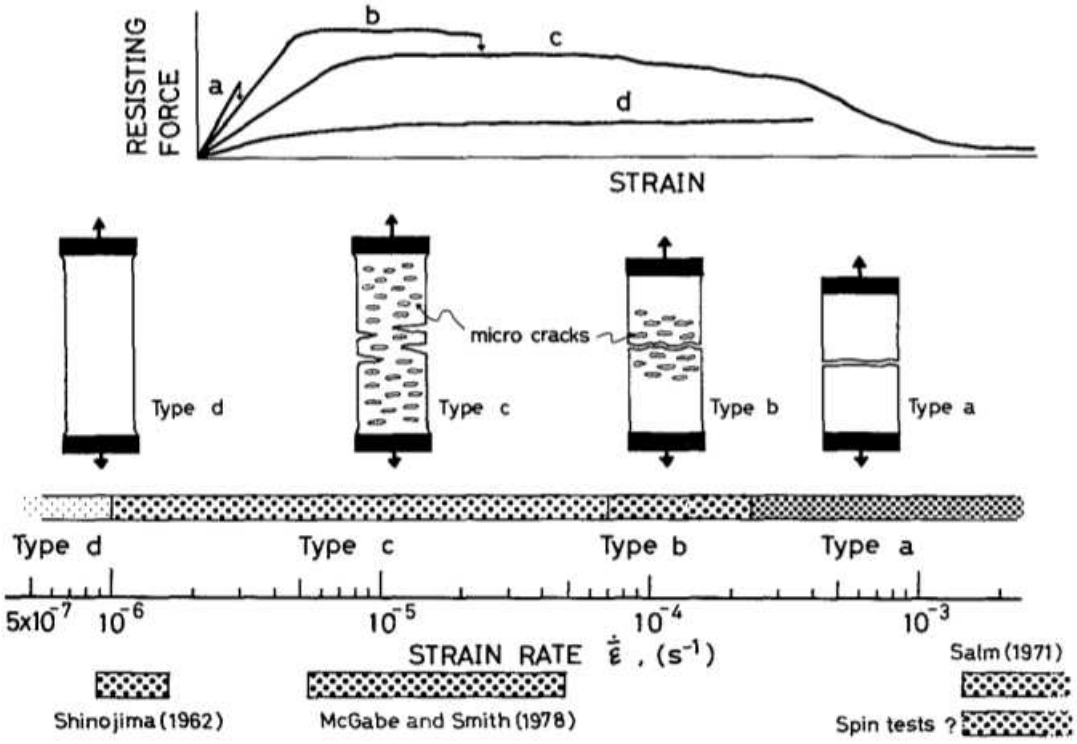


*Figure 2.29: Ductile, transition and brittle failure of snow under tension in dependence of the strain rate measured by Narita (1984).*

Type a and d are thereby similar to the pure brittle and pure ductile failure of snow, respectively, as described previously for the unconfined compression tests. Type b and c can be identified as two different types of transition behaviour between the ductile and brittle ranges of the strain rate.
Type a demonstrates the same sharp inclination and abrupt break up in stress with increasing strain as observed for the brittle unconfined compression. But logically under tensional deformation there is no subsequent build-up of the stress as the sample pieces are pulled apart after the first collapse.
Type d presents the ductile deformation with an viscous increase in stress along the increasing strain. There are no cracks or fracture features visual as the ice matrix of the sample creeps uniformly under expansion.
The transition types b, c show a similar behaviour to the one reported previously by

Chandel et al. (2014) in the unconfined compression measurements. The stress - strain curve, i.e. force-strain, curve in fig. 2.29 consist of an ascending branch in stress with increasing strain and a descending branch which describes the mentioned strain softening behaviour. The strain softening is thereby caused by an increasing number of micro cracks developing and expanding over the sample volume with ascending strain.
Fig. 2.30 shows the strength values versus the applied strain rate measured by Narita (1984).

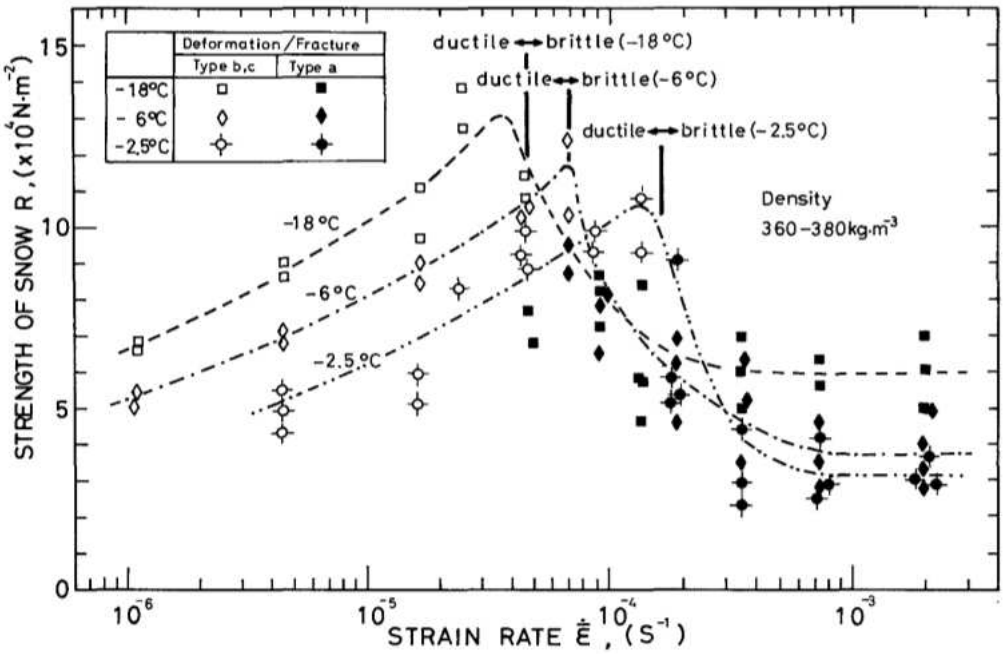


*Figure 2.30: Relationship between tensional strength and strain rate of snow in dependence of the temperature experimentally predicted by Narita (1984).*

The strength of the snow samples is depicted at different temperatures. The strength - strain rate dependence of the tensile tests demonstrates the same behaviour as already described for the unconfined compression tests by Kinosita (1967). Also here, the transition rate shows a similar temperature dependence as already discussed along with fig. 2.23. Snow shows less brittleness at temperatures closer to the melting point of ice.

Under confined conditions, the snow grains cannot escape the increasing load. Therefore the influence of the density of a snow sample increases with growing strain. The resulting deformation features are presented and discussed below.
Von Moos et al. (2003) compressed snow samples under confining lateral pressure of constant values between 0 and 40 $kPa$. The samples were strained by ductile rates from $7.4 \cdot 10^{-7}$ $s^{-1}$ to $6.6 \cdot 10^{-5}$ $s^{-1}$. Strain-stress curves for the lateral pressure of 0 are already shown in fig. 2.22. The shape of the curves stayed generally the same with increasing confinement pressure but the strength response increased.
Abele and Gow (1975) conducted a series of 52 compression tests on snow in a cylindrical

container, i.e. under wall confined conditions. The collected fresh snow was sintered at the temperatures −1, −4, −10 and −32 °C for time periods of 0.1, 3, 7 and 16 days. The container had a cylindrical shape with Teflon walls to eliminate friction. The compressions were performed by moving the top plate with 40 cm $s^{-1}$ which corresponds to brittle strain rates of about 4 to 16 $s^{-1}$. One can find a detailed description of the sample preparation, storage and test procedure in the publication of Abele and Gow (1975), which also holds an analysis of the microstructure of the samples. Their study shows a detailed analysis of the response of the loaded snow samples in dependence of the initial density , the sintering age and temperature. As the cross section in this kind of confined compression

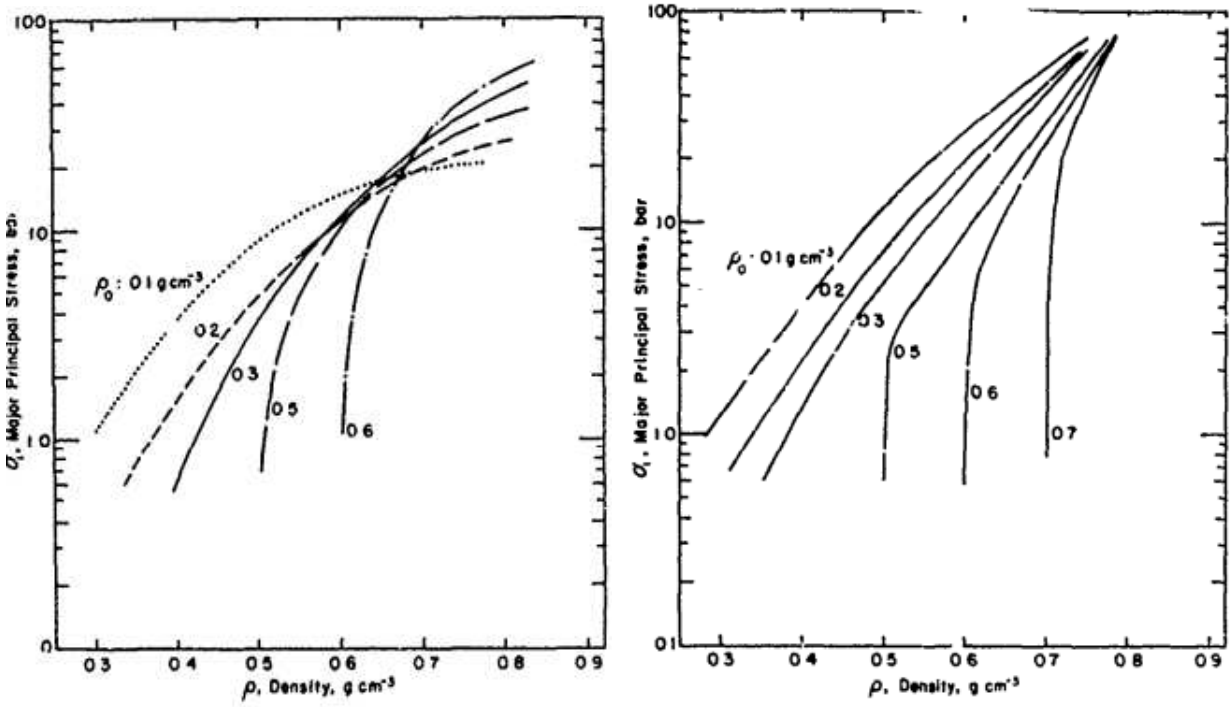


*(a) Stress-density relationships at −1°C.* *(b) Stress-density relationships at −34°C.*

*Figure 2.31: Summary of the stress - density relationships for various initial densities of confined compression measurements by Abele and Gow (1975) .*

test stays constant the state of densification and strain are directly related. In general the stress - density relationships in fig. 2.31 demonstrate an increase in stress with growing densification. However, the curves revealed a high dependence of the stress in relation to the initial density of the sample. When comparing the stress state of confined snow samples at the same state of straining, the stress response increases with increasing initial density.

The results in fig. 2.31 revealed a difference in the final strength of snow depending on the temperature. Samples compressed at temperatures below −10 °C converged towards a common stress value with growing compaction independent of the initial densities. This is exemplified in fig. 2.31b. For temperature above −10 °C, i.e. closer to the melting point, the dependence is presented in fig. 2.31a. Close to the melting point, the final stress value

grows with growing initial density of the sample. This inherits a turning point between the different curves of the different initial densities.
Yong and Fukue (1977) and Yong and Metaxas (1985) conducted wall-confined compression tests on snow of different sintering ages in a cylindrical Lucite tube. The samples are deformed under transition to brittle strain rates of $8,8 \cdot 10^{-3}$ s$^{-1}$ and $0,75$ s$^{-1}$ at a constant temperature of $-13$ °C. The results showed a difference in the strain - stress, i.e. density - stress, curves depending on the initial sample density.

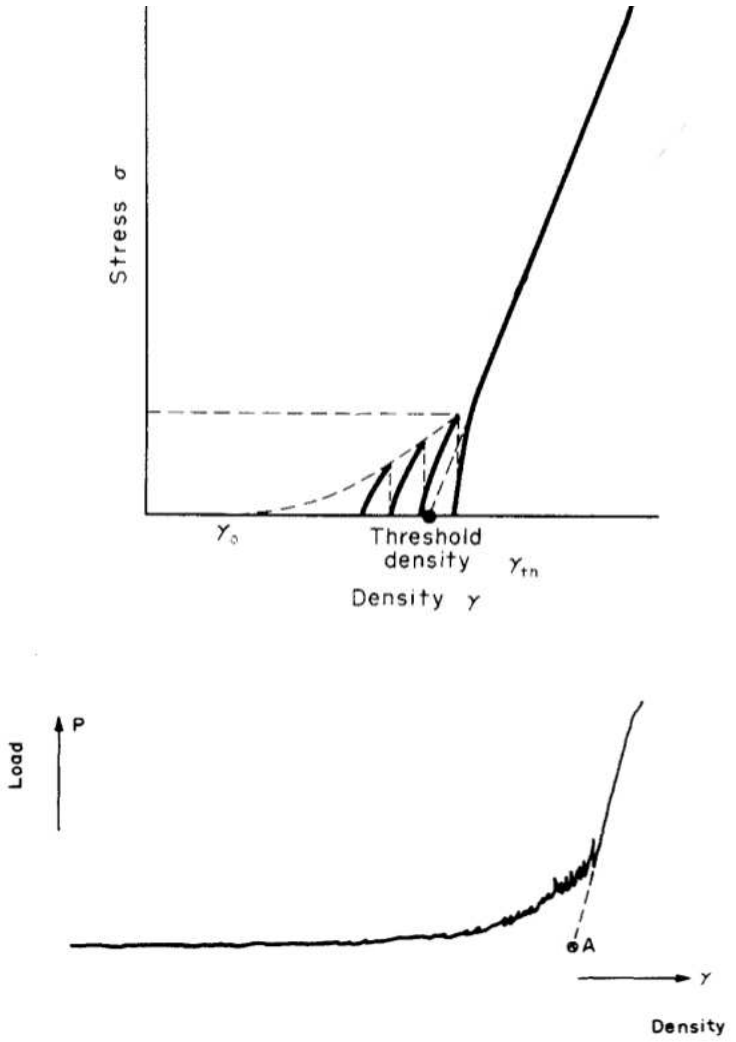


*Figure 2.32: Threshold density $\gamma_{th}$ of wall-confined compression tests of snow by Yong and Metaxas (1985).*

The measurements revealed that samples of a initial density below a certain threshold show the brittle features in their density-stress curves. Yong and Metaxas (1985) called this particular initial density the threshold density $\gamma_{th}$. Fig. 2.32 shows compression curves of samples below that threshold density. Initially the stress in these curves increases with densification showing the mentioned saw-tooth feature of unconfined brittle compression.

With each subsequent collapse of the confined sample the following stress builds up onto a higher value. This repeats until the threshold density is reached. Thereafter, the stress ascends uniformly with densification. The threshold density is thereby the backward projection of the uniform curve portion onto the density axis as shown in fig. 2.32. Any sample of an initial density above the threshold density grows uniformly in stress from the onset of densification, i.e. lacks the saw tooth feature, although brittle strain rates are applied. Yong and Metaxas (1985) discovered that the threshold density depends mainly on the strain rate and partially on the grain size of the snow. Fig. 2.33 depicts the threshold density in dependence of the strain rate for different grain sizes.

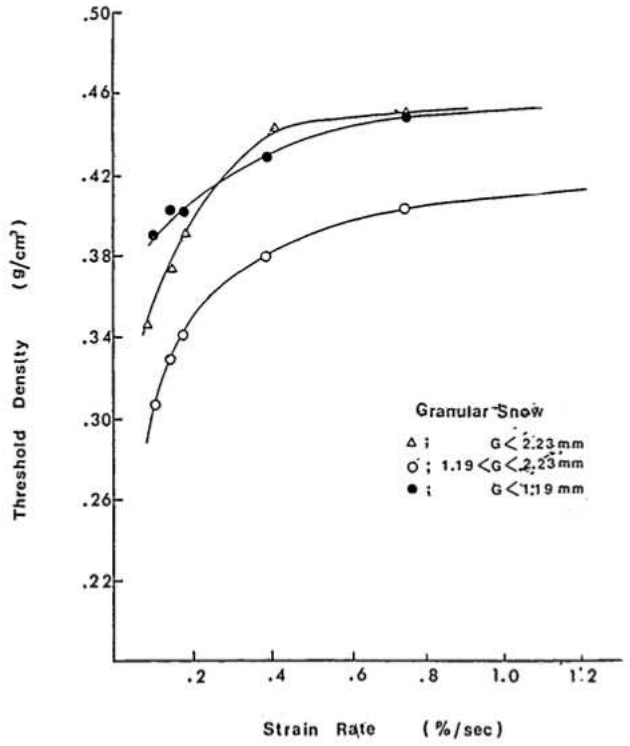


*Figure 2.33: Threshold density versus strain rate for different grain sizes by Yong and Fukue (1977).*

For lower strain rates close to the transition regime the brittle feature vanishes and thus the threshold density approaches zero with decreasing strain rate. With increasing brittle strain rates the threshold density converges onto 400 kg/m$^3$ to 460 kg/m$^3$ depending on the grain size.
However, Yong and Metaxas (1985) also analysed the confined compression tests in relation to the sintering age of the samples, similar to Fukue (1977) in fig. 2.25. The samples sintered under isothermal conditions as well. Fig. 2.34 composes the brittle strength for different sintering ages in dependence of the loading velocity. The general decrease in strength with increasing brittle velocity confirms the previous observations. Similar to the observations in fig. 2.25 the strength of snow in fig. 2.34 grows with ascending sintering

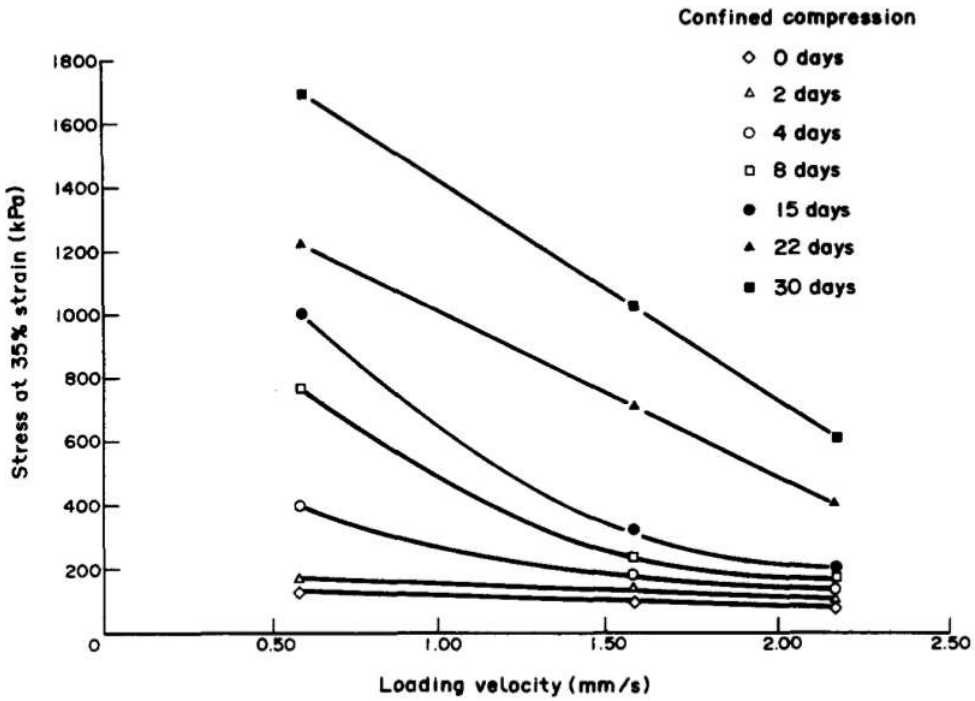


*Figure 2.34: The dependence of the snow strength on isothermal sintering age and velocity for confined compression tests by Yong and Metaxas (1985)*

age. But the growth gradient between the different ages increases with decreasing velocity, i.e. with decreasing strain rate. This means the sintering age has a higher influence on the strength of snow at lower strain rates. With increasing strain rate, i.e. loading velocity, the strength curves converge to a constant value. Fig. 2.34 also shows that above a certain loading velocity, i.e. strain rate, the strength barely changes with sinter age. This loading velocity aligns well with the second kind of brittle velocity reported by Kinosita (1967) in fig. 2.23. At a temperature of $-10$ °C the brittle velocity of second kind is about 10 mm/$s$. Kinosita (1967) also reported that the strength takes an almost constant value at higher velocities.

Next to the compression tests in his thesis, Fukue (1977) also conducted penetration tests in sintered snow with a thin metal blade, as shown in fig. 2.35. The width of the blade used was 12 mm and the thickness was 0.6 mm. The penetrated snow had a density of 350 kg/m$^3$ to 480 kg/m$^3$. Blade penetration measurements in snow are easy to conduct outside and indoors. The thin blade penetration is thereby a measure of the rupture of bonds and grain structures and minimises the influence of the compaction of snow during penetration. The blade hardness index or BPF is defined as the maximum force of penetration and is a highly repeatable measure.

However, this investigation of Fukue (1977) also reveals the previously described rate dependent behaviour of ductile to brittle failure of snow under load. Fig. 2.36 shows the ductile, brittle and completely brittle regimes of the blade penetration tests. In the ductile regime the penetration force increases with increasing penetration velocity as already seen

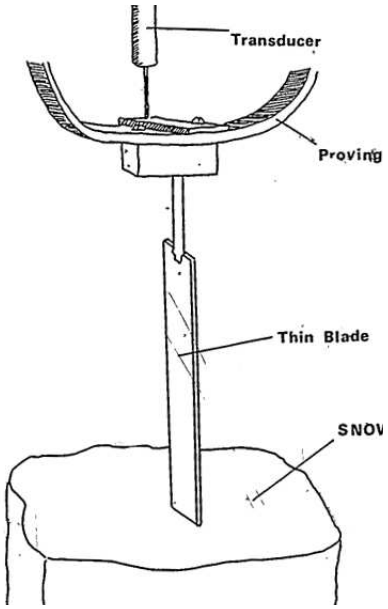


(a) Schematic presentation by Fukue (1977)

(b) Field measurements by Borstad and McClung (2011)

*Figure 2.35: Blade penetrations in snow*

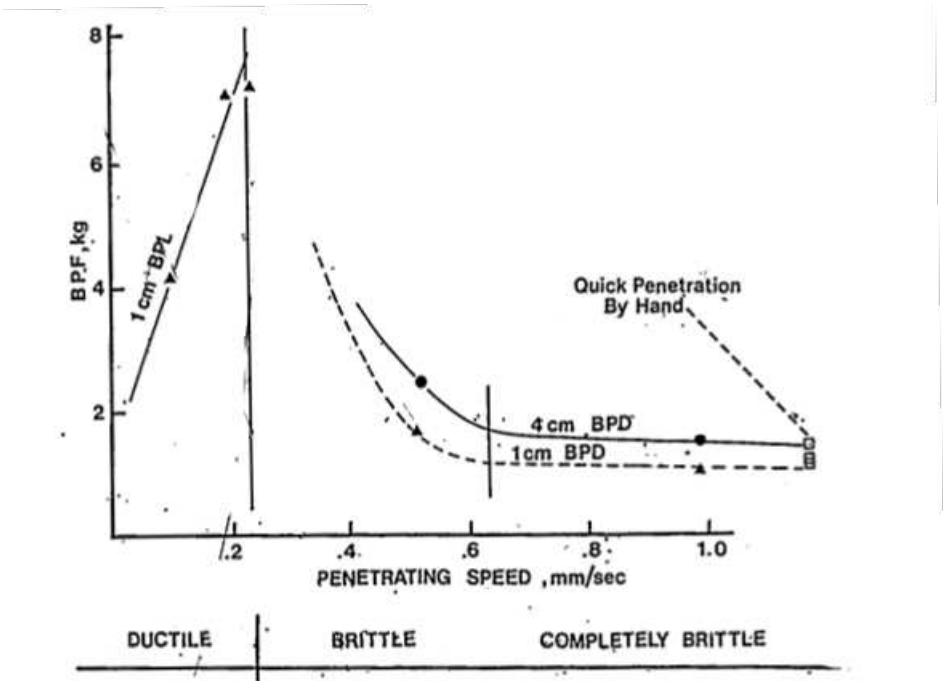


*Figure 2.36: The dependence of the penetration force on the penetration speed by Fukue (1977)*

for the strength of snow in fig. 2.30 and 2.23. The brittle regime is again identified by the decrease in penetration force with descending velocity. Interestingly, the regime of complete brittleness correlates again well with the second kind of brittleness presented by

Kinosita (1967) in fig. 2.23. In this regime the penetration force is independent of the velocity as the strength is independent of the rate.
Borstad and McClung (2011) also conducted blade penetration tests in the field and laboratory. The blade used was a 100 mm wide and 0.6 mm thick stainless-steel blade attached to a digital push–pull gauge. The penetration speed was high to ensure the penetration force would align within the rate-independent brittle regime identified by Fukue (1977). The measurements also investigated the density dependence of the penetration force as shown in fig. 2.37. The naturally sintered snow was penetrated with a speed of about

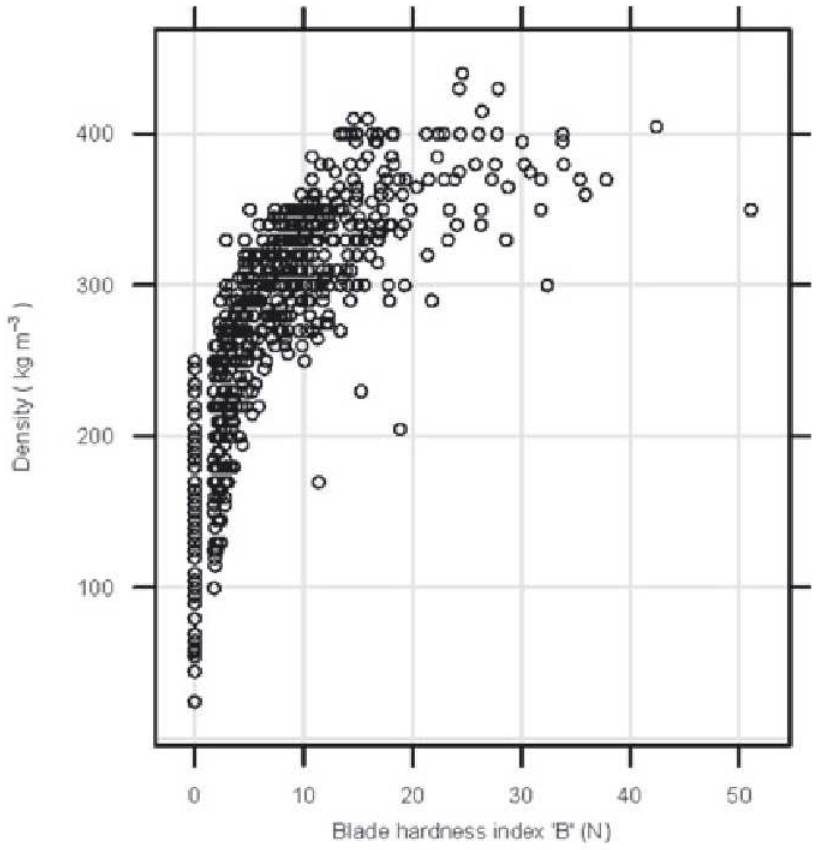


*Figure 2.37: The dependence of the penetration force on the natural snow density by Borstad and McClung (2011)*

100 mm/s. The measured force is comparable to the force measured by Fukue (1977) but it shows an increase in spread with increasing density. An increase in density in naturally sintered snow can also be linked to an increase in bonding strength. Therefore, the spread in the force values at higher densities can be explained by different bonding strengths.
There are far more very valuable experimental predictions in snow mechanics than the mentioned ones but not all can be discussed here in order to keep the focus onto related measurements.

However to name a few, Johnson et al. (1993), for instance, measured the shock response of snow at an impact velocity of 150.7 $m\ s^{-1}$. Lawrence and Lang (1981) conducted uniaxial compression and tension tests at stain rates around $10^{-6}$. They derived a constitutive description based on their tests. Haehnel and Shoop (2004) modeled uniaxial compression and plate sinkage tests for vehicle induced strain rates and loads. Their derived models were validated by the conducted experiments. Yong and Metaxas (1985) also carried out shear tests in parallel with the above described compression tests. Kirchner et al. (2001) investigated into the brittle-ductile transition regime of snow. They found values for the activation energy of snow creep behaviour and analysed the deformation mechanisms from the point of view that snow is a foam of ice.

For the purpose of developing snow models for the discrete element technique the following points have to be kept in mind:

- Mechanical behaviour of snow is based on the microstructure
- The microstructure of snow is composed of grains connected by bonds
- Snow grains are composed of multi-crystalline ice
- Mechanical properties of grains are assumed to behave like polycrystalline ice
- The mechanical behaviour of ice and snow can be separated into ductile and brittle behaviour depending on the strain rate
- Ice creeps under stress which increases with temperature
- The ductile strength of ice and snow increases with strain rate
- The brittle strength of ice and snow decreases with strain rate
- The strength of snow increases with bonding strength, i.e. sintering age

### 2.1.3 Modeling of the Mechanical Behaviour of Snow

A large number of engineering applications and physical problems in snow mechanics have been solved by mathematical models and numerical methods from the field of solid mechanics.
The problems in snow mechanics are thereby almost exclusively considered by continuum approaches. Just a few authors have chosen a discrete approach to predict the mechanical response of snow. Even less problems have been solved based on a hybrid approach.
When modeling the mechanical behaviour of snow by continuum description, the finite element method is chosen almost solely as the solving tool.
The major physical problems in snow mechanics accounted by numerical methods are stress development, creep and failure properties of snow as well as snow avalanche release and weak layer dependencies. But the major engineering applications studied by numerical

approaches are tire - snow and ski - snow interaction as well as loading of structures of snow defence.
As mentioned, the finite element method is also in snow mechanics, despite all anisotropies and heterogeneities of snow, the most used method of all. For the mechanical problems in snow mechanics described by this method the general goal is to solve for the developing stress state. The majority of application, as avalanche studies, skier-induced stress and snow defence structures, are including an angle between the principal problem directions. Therefore, these problems are solved for the stress state developing in inclined layers or slopes of snow.
But also the stress developing under simple laboratory condition is widely described by numerical methods to study the underlying mechanisms and material properties responsible for the mechanical behaviour of snow.
Very early in the history of the finite element method, Smith (1972) used a two-dimensional finite element model to compute the stress state in inclined snow layers. His studies also included the influence of weak layers which is common in the study of avalanches. The employed models increased in complexity from linear elastic to finally viscous-elastic with ascending research years.
Very recently Cresseri et al. (2010) developed a highly advanced constitutive model based on an elastic-viscous-plastic law and included constitutive equations to account for the sintering effect of snow. By means of FEM simulations the model was very successfully validated in relation to the rate dependence of snow in the ductile regime by comparing with the mentioned measurements of Von Moos et al. (2003) and Scapozza and Bartelt (2003).
In his thesis von Moos (2001) already used his compression measurements to derive a constitutive model describing the ductile behaviour of snow. The developments of the model included different steps by starting with a Kelvin-Voigt and Maxwell model and later combining the elastic and viscous material laws into more complex Burgers-Model. The derivations also accounted for the actual load carrying ice matrix.
The series of a Maxwell and Kelvin-Voigt material, the so called Burgers material, has been used before several times to describe the behaviour of snow. Shapiro et al. (1997) are presenting a detailed description about the Burgers model. It showed to be very suitable but contains a large number of parameters compared to simpler constitutive laws.
However, viscous-elastic laws have been used since and are still widely used to describe snow with sufficient success.
Lang and Sommerfeld (1977) model the deformation of sloping snow packs by means of a viscous - elastic description.
To model creep of snow and loading on snow defence structures, Stoffel and Bartelt (2003) used a viscous-elastic law in a 2D finite element code.
Schweizer (1993) investigated into skier induced load carried by snow layers. The snow was thereby described as a linear viscous material.
Along with the viscous - elastic description of snow behaviour an increasing number of problems were solved by means of constitutive laws with elastic - plastic material descriptions. The snow was described by the Drucker-Prager model, i.e. a modified version of this elastic-plastic material model.

Haehnel and Shoop (2004) re-computed confined loading and plate sinkage tests. The investigation aimed on wheel - snow interactions. They developed a capped Drucker - Prager model for low density snow. They also compared their finite element simulations to Abele and Gow (1975).
Gaume et al. (2011) studied the influence of the heterogeneity of snow on weak layers and on the avalanche release angle. The derived elastic -plastic material described the snow deformations and accounted for strain-softening due to shear.
In more recent studies, the development of material laws in snow mechanics showed an increasing awareness that the micro-structure can not be neglected. Hence, very sophisticated constitutive material laws have been developed taking not only the macro but also the micro-scale behaviour into account.
Nicot (2004a) developed a constitutive material for snow based on a viscous-elastic law whereby the macroscopic response is founded on the statistical micro-scale properties, i.e. bonding and bond direction. By means of a directional probability approach the constitutive model takes the existence and fracture of bonds into account. In a follow up publication by Nicot (2004b), this model was used to study the interaction of inclined snow covers on avalanche protection structures.
Also Bartelt et al. (2000) studied the forces exerted onto snow avalanche protection structures. The viscous elastic snow model used does not only base its prediction on macroscopic but also on provided microscopic parameters.
However, the finite element method can also be used to fully resolve the micro-scale of snow, i.e. discretising the real ice matrix. This is usually done together with volumetric X-ray scans of the underlying ice matrix of a snow sample. Unfortunately, decreases the describable sample size tremendously with increasing resolution. Therefore, full resolution simulations are generally used to study the influence of micro-scale properties on the macroscopic material properties only. Those simulations are also employed to predict the representative volume of snow. The representative volume element (RVE) thereby represents the critical size of a simulated volume relevant for a comparison with experiments or to develop constitutive models of snow deformation.
The first author who fully represented the micro-structure of snow in a finite element model was Schneebeli (2004). The development of the X-ray microtomography on snow was used to reconstruct the three dimensional microstructure of a snow sample with a high resolution. The micro-structure scans were taken as input for the finite element method to reproduce the elastic behaviour of snow. Hence, Schneebeli (2004) considered the ice matrix to consist of a pure linear elastic material which of course excluded any strain rate dependence.
By the same approach, Hagenmuller (2011) obtained finite element meshes from X-ray microtomography scans of snow fabrics. This ice matrix discretization of snow samples was used together with a linear elastic material law including a maximal stress fracture criterion to investigate into the strength of snow. Hagenmuller (2011) also investigated in the RVE for different snow types in dependence of the failure strength. The investigations showed that the failure strength converges to a certain value with increasing sample size as shown in fig. 2.39.

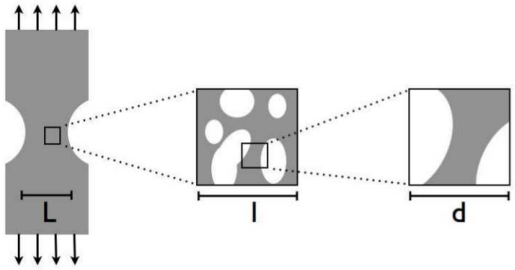


*Figure 2.38: Representative volume element of snow (schematically by Hagenmuller (2011))*

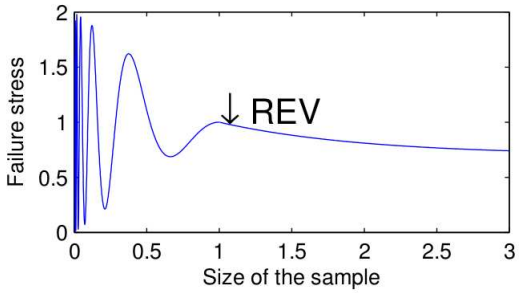


*Figure 2.39: Failure strength in dependence of sample volume (schematically by Hagenmuller (2011))*

Hagenmuller (2011) concluded that the RVE of snow is a parameter of the type of snow and no material constant. Fig. 2.38 shows the three scales which can be distinguished when determining the RVE in dependence of the failure strength of snow. The microscopic scale $d$ is the scale at which a crack in the ice structure was measured. The mesoscopic scale $l$ is the scale at which the snow strength reaches local homogeneity. The third scale is the macroscopic scale of the material snow which is the scale of experimentally measured values.
Also Theile et al. (2011) used 3D tomography scans to compute the full microstructure as a beam network. They simulated the creep by the finite element methods and investigated into the failure properties of snow. Whereby the material law used was linear elastic but involved Glen's law for secondary creep of ice and accounts for the anisotropic creep behaviour of single crystals.
The full representation of the ice matrix of snow showed to be too computational expensive to attack full scale engineering applications. Constitutive laws are able to model the snow behaviour on the macroscopic scale, i.e. engineering scale. But the majority of models demonstrated either to account too less for the micro-scale dependence or are too limited to a certain strain rate regime of snow behaviour, i.e. brittle or ductile.
As snow can be considered as an ensemble of ice grains and bonds, the idea of modeling this construct by a discrete description comes naturally. Modeling each grain and bond as discrete interacting shape allows to account for the micro-mechanical and sintering processes acting at the grain-scale. Those processes are bond formation, grain and bond deformation, rupture and grain rearrangement.
As the first investigators Johnson and Hopkins (2005) developed a micro-structural snow model, the $\mu$ Snow Model, based on the discrete element method. They used cylindrical shapes with spherical ends to represent the snow grains. The model thereby computes the forces and moments developed during collision of grains. Grains were also able to freeze through bonds. These bonds were represented by bond models accounting for the forces developing due to tension, compression, twisting and bending of the inter-granular cementations. For the fracture of the bonds a temperature dependent criterion reflecting the strength of ice was employed. The sintering of new ice bonds between contacting grains was based on an empirical description. Johnson and Hopkins (2005) did the first

simulation attempt with this novel method by computing compression and shear tests of snow.
Next to this study there are currently new attempts to describe the mechanical behaviour of snow by means of the discrete element method. But the current developments seemingly base there inter-granular contacts solely on a cohesive force description which again lacks the strain rate and ice fracture processes taking place on the grain-scale of snow. Hence, Johnson and Hopkins (2005) published so far the most sophisticated discrete description of snow.
Nevertheless, the cohesive force models are very successful when it comes to model wet or sticky granular materials. Richefeu et al. (2009) applied a model of capillary cohesion to study force transmission in wet granular matter. The model was implemented as a force law expressing the capillary force as a function of the water content and the distance between particles.
However, there are other materials that show similar sintering and fracture behaviour as snow and some of these materials have already been successfully approximated by discrete models. The sintering materials have been modeled discretely by means of cylindrical bond descriptions.
Brendel et al. (2006) used a similar DEM approach to describe the caking behaviour of the bulk materials polyethylene and urea. The investigation successfully modeled the macroscopic material and yield properties.
Kim and Sasaki (2010) investigated the fracture limits of porous coke material by a similar discrete element approach. They also modeled cylindrical bonds between spherical coke particles. The bonds were able to bare forces and moments and to fracture under increasing deformation. The simulated compression and cleavage tests captured the straining and brittle behaviour of a coke specimen very satisfactory.
Parallel to this study, Kuzkin and Asonov (2012) developed a vector based bonding model to describe the elastic behaviour of sintering material by employing the model in discrete element method. The so called V-Model accounts for longitudinal stretch, shear, torsion and bending of a bond between adjoining grains by means of two body fixed reference systems attached to each grain. The model was implemented successfully into the DEM package LIGGGHTS.
The most recent development in the numerical description of snow behaviour are hybrid methods. Hybrid methods implicitly describe one portion of the material as a continuum and the other portion as discrete grains.
So far there is only one investigation known from the field of computer graphics. Thus the method does not focus on the scientific results, but it is solely based on physical quantities. Stomakhin et al. (2013) modeled the dynamics of snow with the material point method as an alternative method with the purpose of visual simulations. Their model uses an empirical description to recapture the phenomenological behaviour of snow and ice. This is to keep the model efficient in describing the geometrical details in almost real time. Basically the MPM relies on the continuum approximation and thus avoids to model each single snow grain individually as done in DEM. But the MPM method uses a cartesian grid to make topology changes and conserves mass through the tracking of Lagrangian particles similar to DEM. To simulate different types of snow, they introduced a stretch

and compression coefficient to produce chunky or powdery kind of snow. With a hardening coefficient and the Young's modulus they acquired ductile or brittle behaviour of snow, i.e. muddy or dry snow.

## 2.2 Tire - Snow Interaction

The force transmission between a tire and a snow-covered road can be very low compared to the force transmission on dry roads. Thereby the strength of the snow influences the friction coefficient $\mu$ even stronger than the tread properties. For tire and snow interactions without melting effects the measurements of Gießler et al. (2007) showed a significant increase of $\mu$ when the tire was rolling through highly compacted snow with almost no slip. But contrary in the case of less densified snow higher friction coefficients where measurable for higher slip values.
The slip is thereby predicted as follows:

$$s = \frac{(\omega \cdot R - V)}{\omega \cdot R}$$

where $\omega$ is the angular tire velocity, $R$ the outer radius of the tread and $V$ is tire velocity in travel direction.
The main mechanisms contributing to the friction of the tire on a snow-covered road are the compression and shear resistance of the snow, the rubber - snow grain friction and cornering effects of the tread blocks.
Before looking into the theory and measurements of force transmission between a tire tread and snow, the terminology and basic rolling mechanism of a tire are presented. Thereafter, the numerical predictions in the field of snow - tire interactions are discussed.

### 2.2.1 Tire Terminology and Basics

In this section, the common conventions and rolling mechanics of a modern radial tire are presented. The travelling direction of a tire is defined as the longitudinal direction. The so called lateral or transverse direction aligns with the axis of rotation perpendicular to the longitudinal direction. A modern radial passenger tire is constructed of more than 15 compounds and more than 20 elements of which the principal ones are presented in fig. 2.40. Each tread element influences the structural performance of a tire under loading. When analysing the deformations of a tire during contact the three principal parts to keep in mind are the tread area, the sidewall and the bead area.
A tire tread rolling onto a snow surface transmits a large portion of the traction force due to stressing the tread enclosed snow blocks. The tread pattern design consists of blocks generated by grooves cut across the tread ribs as depicted in fig. 2.41. Gießler et al. (2007) measured that the enclosed area of a tread, i.e. the void space of the ribs created by sipes, kerfs and slots, correlates with the friction coefficient in snow. When the snow compacts between the blocks and sipes a higher shear resistance is created which increases the force transmission.

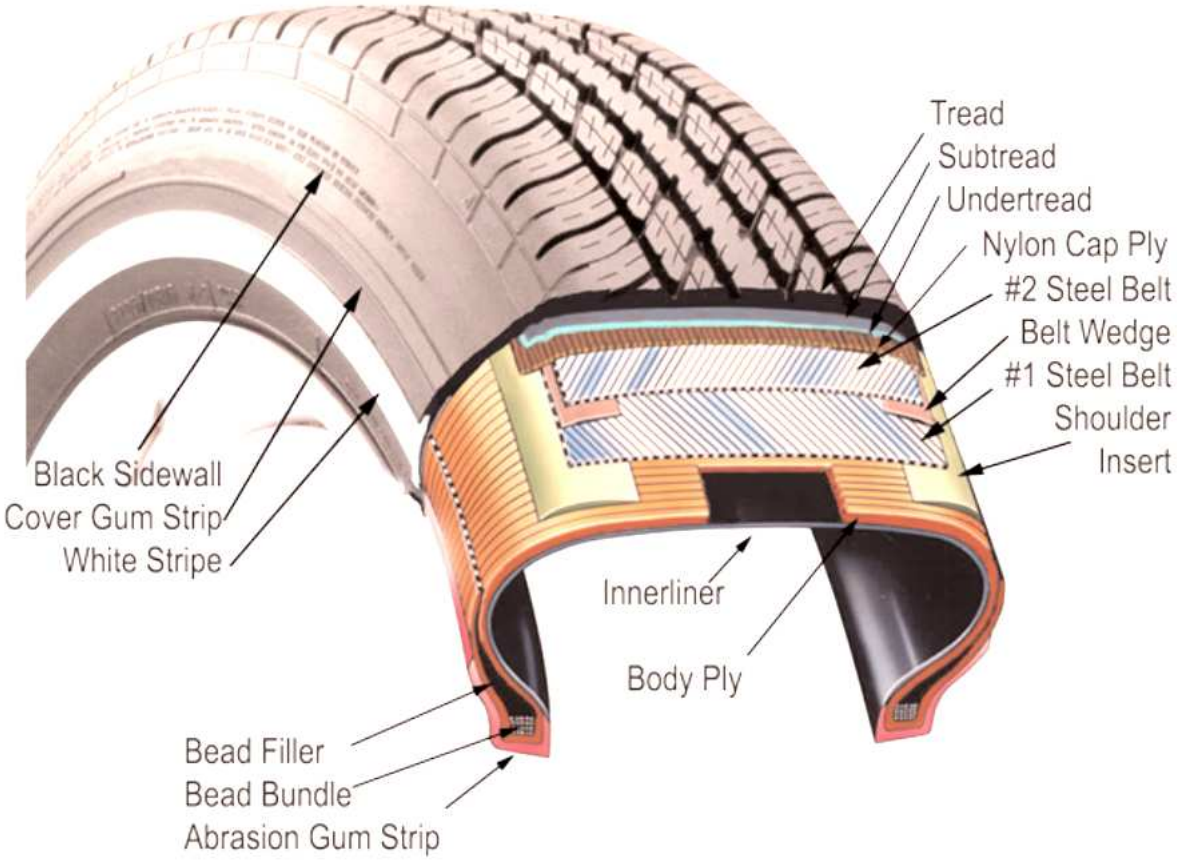


*Figure 2.40: Radial tire components as presented by Lindenmuth (2005).*

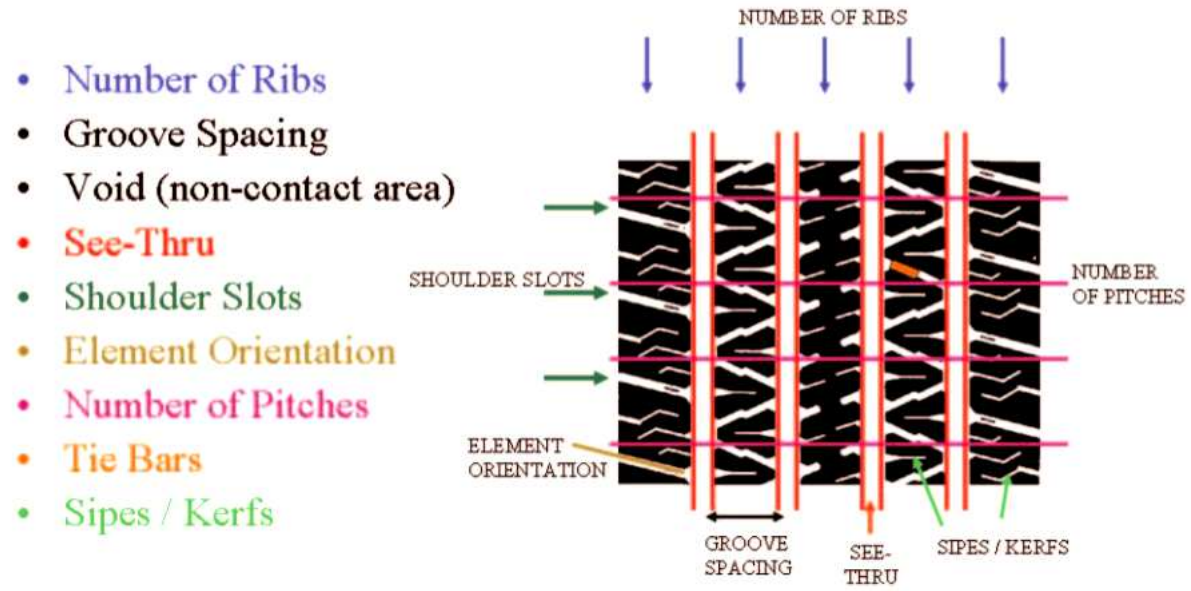


*Figure 2.41: Design of tread patterns by Lindenmuth (2005).*

However, a tread design as illustrated in fig. 2.41 is constructed of a number of ribs and grooves which control the hydroplaning performance. The void space, shoulder slots size and orientation are influencing the traction, handling and the exits for water in the contact area. The traction, noise and wear off of the tread are controlled by the sequence and number of pitches.
The contact area between road surface and tire tread reflects the print left by those components and is named the tire footprint. Fig. 2.42 exemplifies a footprint whereby the tire is rolling in X-direction.

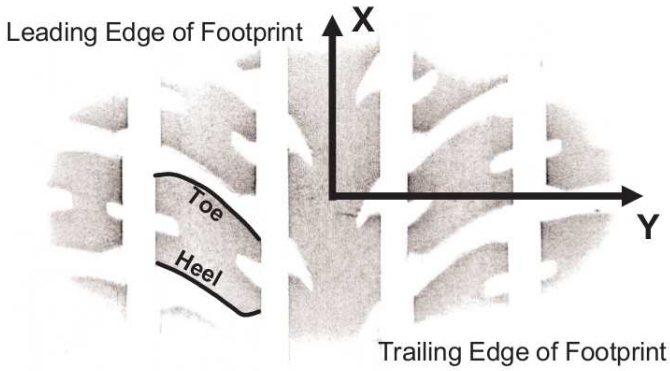


*Figure 2.42: Footprint geometry by Pottinger (2005).*

Looking at a single block during the rolling motion of the tire, the first edge entering the contact area is commonly referred to as the heel. The edge leaving the contact last is called the toe.
Under the rolling motion and loading, a tire undergoes various deformations which also affects the force transmission and deformation of a single tread block in the contact patch between tread and road surface. The tire deformation is thereby the difference between the unloaded and the loaded configurations as shown in fig. 2.43.
The tire undergoes a deformation cycle during rolling. The deformations repeat due to subsequent adaption of the tire to the road surface. This adaption to the road, as depicted in fig. 2.43, causes a flattening in the contact patch and results in three principal deformations. The so called tire crown, sidewalls and the bead area are bended. Secondly, shearing occurs in the tread and sidewalls. Finally, the tread itself compresses onto the surface.
An additional source of stress is shear generated due to acceleration and braking.
Within the contact patch the crown is flattened which results in an infinite radius of curvature. As the rest of the tire holds its shape approximately, the minimum and the maximum curvature of the crown develop at the borders of the contact patch.
Hence, the described tire deformations affect the interaction between the tread blocks in the contact patch and the contacting surface, i.e. also tread and snow covered road. Additionally, the tire belt beneath the rubber tread is relatively inextensible and thus forces the tread blocks to follow its progression. A tread block entering the contact patch in longitudinal direction touches the surface in an angle while leaning backwards which is illustrated in fig. 2.44. Assuming no slip, the angle of the block can be measured by the

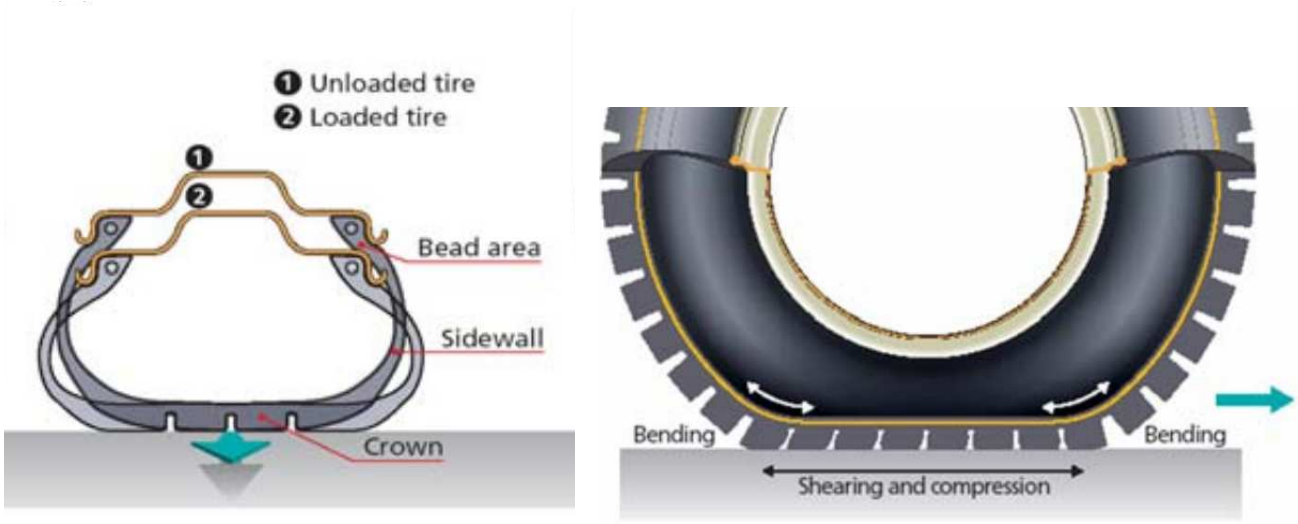


*(a)* *(b)*

*Figure 2.43: Longitudinal and transversal bending of a tire in road contact by LaClair (2005).*

position between the green point attached to the belt and the red point in contact with the surface. The belt progresses which straightens the tread block gradually into the center of the contact patch. Just before leaving the contact patch the block is sheared which makes it lean forward in the final location. The bending of the crown in transversal direction also exerts shear stress into the contact patch. When designing the crown profile of a tire its generally desired to minimise the stress and thereby reducing the rolling resistance.

### 2.2.2 Tread - Snow Traction Mechanism

For the force transmission between a tread block and snow several mechanisms have been reported by Gießler et al. (2010), Fukuoka (1994) and Gießler et al. (2007) which depend on the specific conditions of the contact situation. The mechanism can be separated into 3 principal types. The first mechanism can be described as rubber - snow friction which depends on speed and temperature, i.e. frictional heat converted into snow melting. This portion is marked by (K) in fig. 2.45.
The second type of force is exerted due to cornering of the snow with the tread blocks. Gießler et al. (2010) named this type form closure which is marked by (F) in fig. 2.45.
The third type of forces develops due to snow - snow friction or shear resistance of snow compacted into the sipes or between blocks. Fig. 2.46 depicts snow trapped in tread sipes of a footprint after driving by Goodyear Advertisement.
Fig. 2.45 illustrates two rubber blocks progressing through the contact patch of a tire rolling on snow as described in fig. 2.44. The rubber blocks deform due to the acting compression and shear. If there is no cornering of the blocks, the only force exerted would be due to friction or adhesion (K) between the rubber and snow surface.
However, usually the tread blocks incline when moving along the longitudinal direction

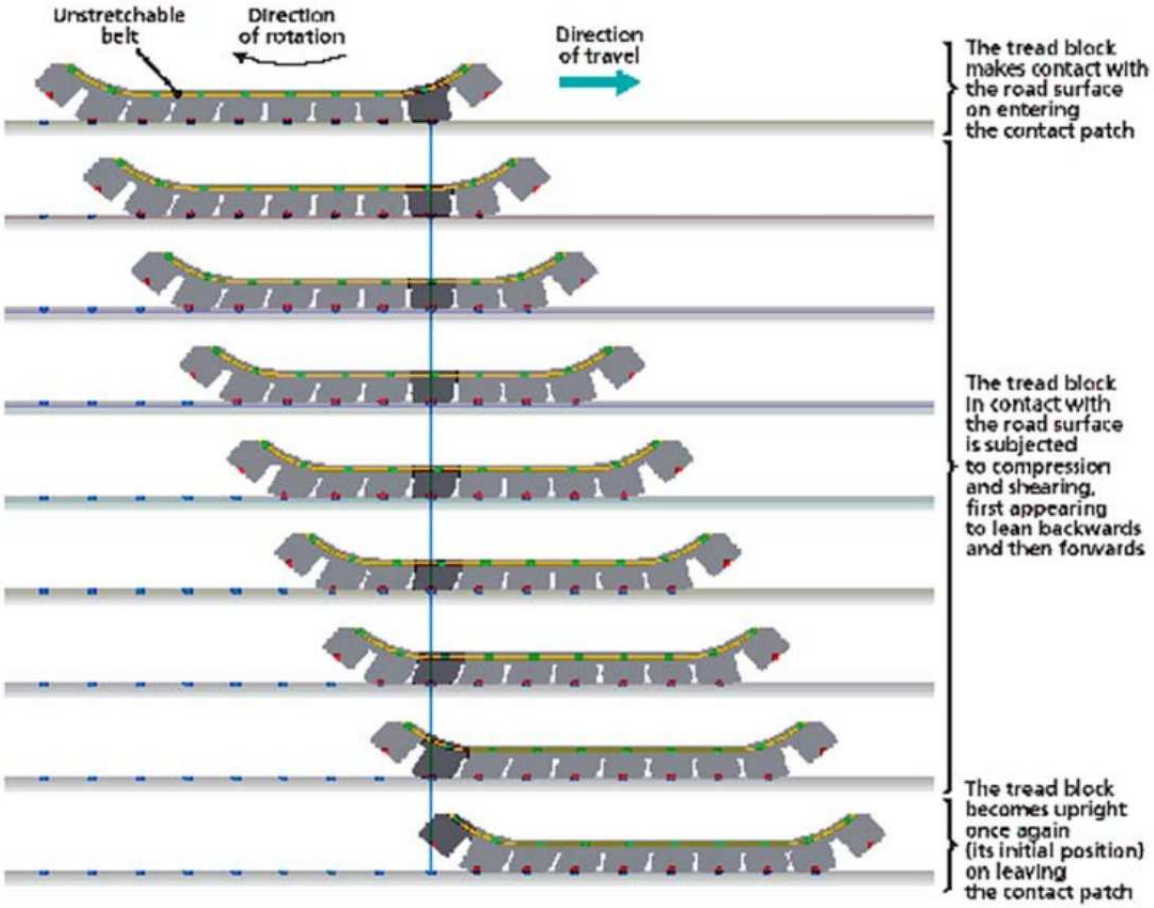


*Figure 2.44: Movement of a tread block motion through the contact patch for no-slip rolling tire by LaClair (2005).*

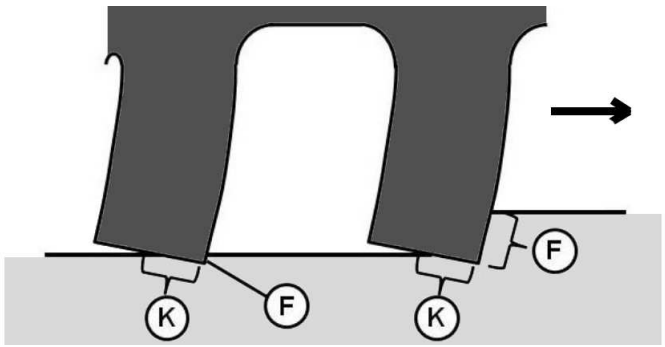


*Figure 2.45: Form closure (F) and rubber-snow friction (K) portion of force transmission by Gießler et al. (2010).*

due to shear. This results in a cornering between the sipe edges and the snow in front of the block. The developing portion of the force (F) due to form closure increases with the number of sipes as stated by Gießler et al. (2007).
On one hand, the form closure is dependent on the rubber deformation and thus on the

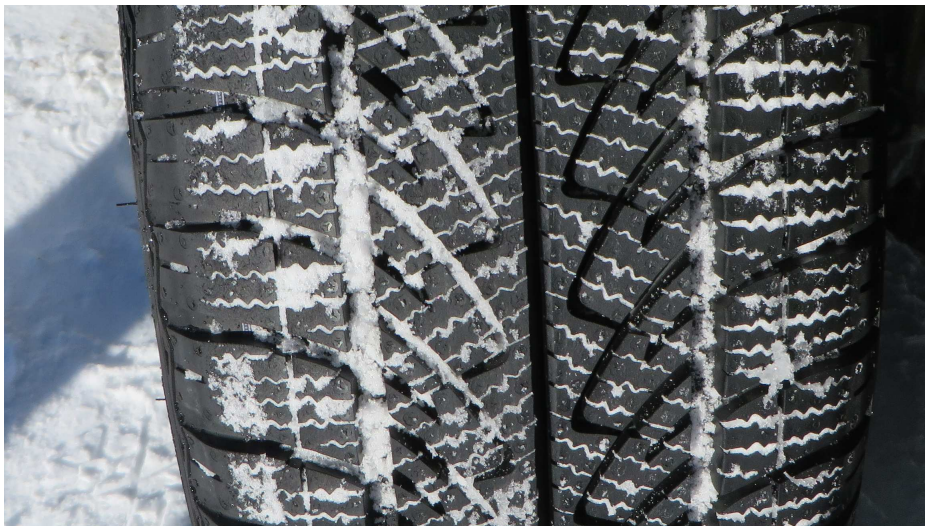

*Figure 2.46: Snow trapped in tread sipes by Goodyear Advertisement.*

material properties. On the other hand, the force transmission due to form closure is even more dependent on the mechanical properties of the snow.
When a portion of the total force in the contact patch is transmitted through the enclosed snow in the sipes, as shown in fig. 2.46, this mechanism is commonly called interlocking. In that case snow is compacted into the sipes, shear stress develops in the enclosed snow block and transmits forces. If the shear caused fracture between the enclosed snow and surface snow the forces are transmitted by snow - snow friction.
Gießler et al. (2010) observed that at high slip values when the shear resistance of the interlocking snow is reached the tread blocks slide with high speed. The high velocity sliding generates frictional heat. In that case the friction coefficient drops due to melting and generation of a liquid layer at the contact surface. This of course depends also strongly on the temperature of the snow and is further influenced by the heat loss over the snow pack and the tread.
The described mechanisms show a strong dependence of the force transmission on the properties of the snow surface, i.e. temperature, strength and densification.

### 2.2.3 Modeling of Tire - Snow Interaction

The modeling approaches of tire - snow interaction which can be found in the literature so far are all continuum based description.
Haehnel and Shoop (2004) simulated the tire - snow interaction by means of the finite element method. They composed an extensive study with own field measurements to compare with their FEM simulations. The constitutive model used was elastic-plastic, i.e. a modified version of the Drucker-Prager model for low-density snow. The model was successfully validated with own conducted compression and plate-sinkage tests. The simulations of wheel rolling through deep and shallow snow were also compared to measurements conducted in the same study.

Lee (2009) conducted finite element simulations of plate indentation tests and the sinkage of pneumatic tires into snow. Both studies revealed the relation between common indentation tests and the sinkage of pneumatic tires. In these simulations the elastic-plastic Drucker-Prager model was used but additionally included a snow hardening law. The simulations and comparison with measurements revealed different deformation zones of the snow under the vehicle wheel. Within the study, models have been derived to describe the deformation zones.
Seta et al. (2011) also conducted finite element predictions of the tire - snow interaction. They used a crushable foam model to describe the snow deformation. The numerical models were parametrised by laboratory experiments in order to reflect the properties of a snow-covered road. The simulations estimated the force factors in good agreement with tire traction tests on compacted snow.
The continuum nature of the finite element method disables to account for the discrete micro-scale properties of snow, i.e. distribution and size of grains and bonds. However, the discrete element method enables to take these measurable properties into account when modelling the mechanical behaviour of snow. One objective of this study is to relate the results to the micro-scale structure of snow. Therefore, in this study the mechanical behaviour of snow is described by the discrete element method.
So far there is no attempt known which approaches the problem of tire - snow interaction by coupling continuum and discrete methods.

## 2.3 Coupling of Discrete and Continuum Approaches

A broad range of engineering applications are facing multi-scale problems. A large number of these problems involve heterogeneous materials such as granular media. Applications in fracture mechanics, soil-structure interaction, fluidised particle beds and tire-terrain interaction are major fields to name when it comes to dealing with different length scales. The ever increasing computation power allows to account for these problems by different numerical simulation techniques.
The combination of discrete and continuum approaches (CCDM - Combined Continuum and Discrete Model) is a powerful tool to account for different scales within problems. Hereafter, different methods of combined discrete and continuum models are reviewed and discussed. Traditional numerical methods, such as the Finite Element Method (FEM), describe materials as continuous entities. This assumption allows an increasing number of engineering problems to be solved conveniently at the macroscopic scale by means of numerical simulations. But this approach inherits one fundamental drawback: the homogenisation of individual characteristics of the micro-scale. However, high performance computer technique now enables the employment of methods, such as the Discrete Element Method (DEM), able to account for the individual behaviour of each grain within a granular assembly. This allows to derive the macroscopic characteristics from the behaviour observed at each single grain. But since the discrete approach requires contact detection, calculation of all contact reactions and a high temporal resolution, the method inherits large computation times as a significant disadvantage. Hence, the idea seems quite natural

to utilise the advantages of both the continuum and the discrete approach and thereby compensating the shortages of each method.
Numerical methods of coupling continuum and discrete approaches are under constant development with the purpose to resolve different scales within engineering applications. The field of coupling between continuum and discrete methods can be separated into two parts: methods with overlapping and methods with separated physical domains.
One typical field of application connected to overlapping domains is computations of fracture and fragmentation of materials and structures.
For instance, Morris et al. (2006) simulated crack propagation within rock structures of tunnels. A combined DEM - FEM method was use by employing discrete approaches in necessary regions. If the yield stress is reached within the FEM domain, the crack region and new generated fracture surface are handled by DEM related description.
To solve multiscale problems, Nitka et al. (2009) derived a two scale approach to predict the behaviour of heterogeneous materials. The different scales were resolved by computing the micro-scale behaviour by DEM and the macro-scale with the FEM method. The different length scales were linked by a homogenisation method of the micro-response. The resultant stress was then fed into the macroscopic quantities of the FEM description. Thus, the macro-scale models depended on the discrete micro variables.
The approach of coupling between discrete particles and FEM with overlapping domains finds its application also in the field of hypervelocity impacts on structures. Beissel et al. (2006) predicted the burst of materials due to hypervelocity impacts. Thereby, the developed method relies on the conversion of finite elements into particles. After the conversion the particle-like pieces propagate further based on a meshfree Lagrangian description.
Further effort comes from research of fluid flows in interaction with solid structures or with floating solid parts. Generally in the field of fluid flows, when it comes to continuum-discrete coupling, algorithms with an interface for transport phenomena are employed instead of overlapping domains. But PFEM is a Lagrangian formulation to calculate Fluid-Solid Interaction and an exception in this research field. The method discretizes any domain by means of FEM, but the mesh nodes are tracked like individual particles, Idelsohn et al. (2006). The Lagrangian formulation allows to handle the nodes like solid particles. This enables to compute the separation of fluid particles from the main domain.
As mentioned before, in the field of coupling methods with non-overlapping domains major contributions evolved from the research of fluid flows with solid parts and flows through porous media. The purpose of these methods is to share or transport quantities, like drag forces and heat flux, see Tsuji et al. (1993) and Xu and Yu (1998), between the different domains through the particle-fluid interface. Coupling methods with separated physical domains logically involve an interface, which provides the flexibility to apply different models for the exchange of information. This encompasses a natural link to coupling models for contact problems. This field of research is also addressed within this current study. To analyse different length scales in structural mechanics the coupling between the discrete element method presenting solid particles and the finite element method reflecting a deformable structure is most suitable.
Valuable effort comes from the field of soil mechanics and terramechanics where soil structures have to be reinforced or solid bodies are build into the underground. Villard et al.

(2009) presented a coupling approach between a finite element model used to describe a geosynthetic sheet and the discrete element method used to describe the behaviour of granular soil. They paid special attention to friction laws between the finite and discrete elements in contact. In this approach both methods are governed by the Newtonian laws of motion. The numerical model has been validated by means of an analytical solution and experimental results. Their FE mesh consists of triangular elements describing the geosynthetic sheet as a membrane like geometry. In an iterative approach the static equations of large deformations are solved within the coupling method. To describe the granular material they employed a discrete element method based on spherical particles. The particle contact force was described using a elastic-perfectly-plastic law. The normal contact force between a finite and discrete element is based on the overlap of both. The tangential force is kept under a certain limit of the normal force and is predicted independently. The interface model of the tangential force depends on the incremental relative displacement, a micro-mechanical stiffness modulus of the interface and the influence area of a contact computed by means of the particle radius.
Applications of DEM - FEM coupling with a more dynamical interaction come from vehicle - soil or tire - terrain interaction. Nakashima and Oida (2004) and Nakashima et al. (2009) employed a two dimensional FE-DE method to describe tire-soil interaction and the traction dependency of a tread. For this purpose, they derived their model in a similar manner as described above. Both domains were governed by the fully time dependent discretization of Newton's second law. The contact force developed at the interface between particle and surface element was also based on the overlap. The counter part of the contact force is interpolated to the nodal points of the surface element based on a virtual work equivalent. Horner et al. (2001) used the same virtual work approach to map forces between discrete and finite elements. Both employed linear triangular elements to approximate the surface. Horner et al. (2001) discussed his approach in the view of large parallel computations of applications for vehicle - soil interaction. Despite the advantages of these coupling approaches, in many fields it is still more common to approximate the behaviour of granular materials with continuum models.

## 2.4 Review Conclusions and Manuscript Outline

The objective of this project is to develop a simulation technique able to describe the interactions between a tire tread and a snow-covered road. Therefore, after reviewing the current state of art, three principal developments of the simulation technique can be addressed:

1. Inter-granular snow models need to be developed which have to account for the properties of ice and snow summarised at the end of subsection 2.1.2. Deploying an extended discrete element technique, the micro-structure of a snow pack has to be represented by generating an ensemble of explicit geometrical shapes describing the individual snow grains and bonds.

2. For the purpose of predicting the deformation of the tire surface, the Finite Element

Method needs to be employed. A fully time dependent model of elastic deformation would be most suitable in relation to the fully time dependent description of snow.

3. An efficient coupling procedure between the FEM and DEM domain has to be derived. On one hand, this includes an efficient algorithm for a fast prediction of potential contact pairs between snow grain and tread element. On the other hand, the contact force and displacement have to be shared properly at the interface of the domains.

This chapter reviewed the necessary background knowledge.
The third chapter contains the developed inter-granular snow models and derived material laws of the grain-scale. It further describes the principal equations beyond the extended discrete element method as well as the developed algorithms to enable sufficient simulations. In addition, the method to generate virtual snow samples is also presented in chapter three.
The fourth chapter explains the finite element method and the differential equations used to describe the elastic deformations of the tire tread.
Chapter five contains the coupling procedure of the discrete and finite element method. It also describes a homogenisation method enabling to compare discrete and continuous simulation results.
Finally, several micro- and macro-scale simulations are conducted in chapter six to validate the derived simulation technique. The simulations are conducted along and compared to related measurements.

# Chapter 3

# Extended Discrete Element Method (XDEM)

Engineering applications governed by snow behaviour have been proven difficult to solve due to the spatial heterogeneity of the geo-material. The complex deformation mechanisms of snow are inherited from the inhomogeneities on the micro-scale ($10^{-3}m$). In general, continuum models are employed to predict the material behaviour at the local scale of snow. Those models are developed from the concept of a representative volume element (RVE), which has been shown already in fig. 2.38. But this concept logically requires the ability to accurately represent the micro- to RVE scale of a material. This results in an homogenisation of the micro-mechanical processes. In the case of snow deformation, the micro-mechanical processes are complex due to inter-granular bonding, rate dependent creep and fracture of grains and bonds involved. Consequently, the development of an accurate RVE description accounting for such a high amount of complexity is difficult and limited.
However, a discrete element approach allows to describe explicitly each grain of an entire ensemble and micro-mechanical processes between neighbouring grains directly. To overcome the continuum limitation, an extension of the discrete element model is developed to represent the motion of each snow grain individually and explicitly model the micro-mechanical interaction at each contact point. Hence, the Extended Discrete Element Method (XDEM) introduced in this chapter considers the geo-material snow as a granular material.
This chapter proposes inter-granular snow models developed and deployed using an extended discrete element technique. The developed approach predicts the displacement of the individual grains due to inter-granular contact and bonding forces. The micro-structure of a snow pack is represented by generating an ensemble of explicit geometrical shapes describing the individual snow grains and bonds. The developed inter-granular bond models assume a cylindrical neck between adjoining snow grains. Material properties and constitutive models of polycrystalline ice (Ih) are used to describe the material behaviour of

each individual bond and snow grain during loading. The developments aim to study the dependencies of the macroscopic snow behaviour from its micro-structural and mechanical properties on grain-scale, particularly for the mentioned high strain applications. Despite any temperature distribution over a snow pack, this dissertation focuses on the isothermal behaviour.
The assumptions of the developed models in this chapter are:

- Snow on grain-scale is consisting of polycrystalline ice (Ih)
- A snow pack is loaded under isothermal conditions

With increasing computational power over the last decades, see Moore (1965), computer simulations have become a powerful tool in the everlasting ambition of engineers and scientists to describe physical phenomena. In the field of granular matter, the Discrete Element Method is the leading approach to describe numerically the kinematics of a granular ensemble, see Poeschel and Schwager (2005). Cundall and Strack (1979) presented the method first and stated that the DEM is a numerical approach where statistical measures of the global behaviour of a phenomenon are computed from the individual motion and mutual interactions of a large population of elements. A very detailed description by Radjai and Dubois (2011), highlighting all aspects of computations in granular matter by means of discrete element modeling, was recently published.

## 3.1 Time-Driven Approach

In discrete element modeling, either an event- or time-driven method is employed to simulate the behaviour of granular materials. Event-driven methods have successfully been applied to applications where the interaction time between particles is small compared to the time of free inter-particle motion. This is the case in granular gas motion where gravity can be neglected, as shown by Goldhirsch and Zanetti (1993). The event-driven approach is also known as the hard particle approach. This is due to the fact that the method could also be used in cases where the particles are very hard, i.e. their deformation during contact is small compared to the time the particles move freely. When particle interactions are enduring in comparison to free motion, a time driven or soft particle approach has shown to be most suitable, as described Campbell (1982).
Within the context of XDEM, a time driven method is employed as the main use are granular matter applications with closely packed particle beds. Thus, the Lagrangian Time-Driven Method is applied to each discrete particle of a moving ensemble. The ensemble is thereby defined as a system of a finite number of particles with a distinctive shape and material properties.
The state of the particles is computed through integration in time of the equations of rigid body motion. Thereby, the timescale is subdivided by the discrete timestep length $\Delta t$. The state of each particle in the granular ensemble, such as position, velocity, orientation and angular velocity, is calculated at every discrete timestep $t_i$. Alternatively to the equations of motion, the displacement of each particle could also be gained by calculations based on the equations of equilibrium, as successfully done by van Baars (1996). But in the current

study, Newton's second law for translation and rotation of each particle in the ensemble is integrated over time. Therefore, all forces and torques acting on each particle need to be determined at each timestep.

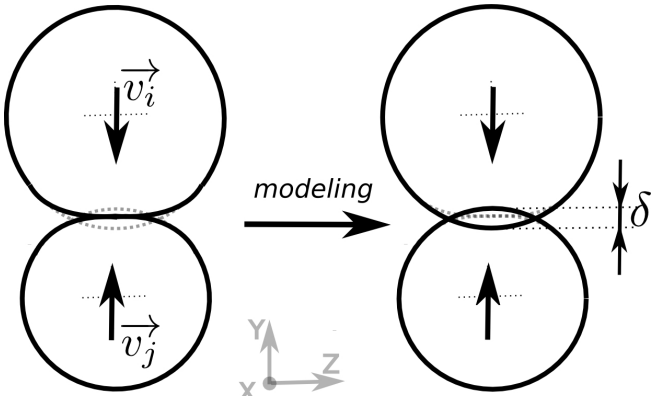


*Figure 3.1: Particle deformations modeled by shape overlap*

The described method models every single particle as a deformable body. Two colliding bodies experience small deformations which cause stress to develop at the contacting surfaces. In the case of an elastic collision, repulsive forces develop to resolve the stress state. The deformations between two colliding particles, also named gains in the following context, are modeled by means of an overlap $\delta$ between the two geometrical shapes as shown in fig. 3.1. Hence, the developing collision forces are derived from the overlapping geometry, material properties and kinematic quantities of the adjoining particles. Within

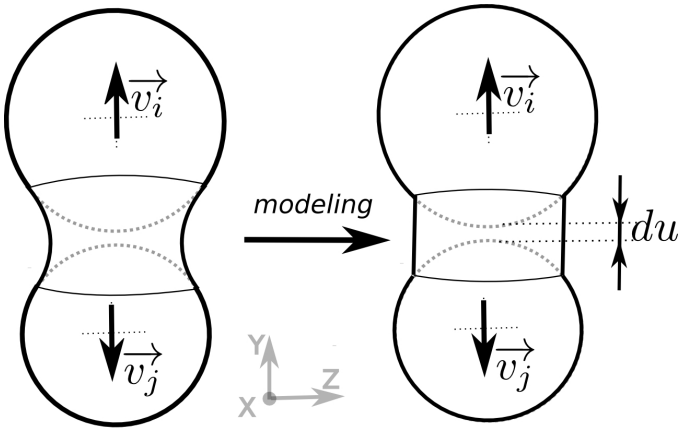


*Figure 3.2: Bond shape modeled as cylindrical neck*

this study the classic DEM description was extended by additionally modeling the bonding behaviour between contacting gains. Following the objectives, two particles in contact are allowed to sinter a neck at the contact point. Natural bond geometries can be quite complex due to their dependence on the material inherited sintering process. This is also

the case for the sintering between snow grains as investigated in detail by Colbeck (1997). Therefore, in this study the material neck is described as a finite cylindrical bond aligning between the adjoining grains, as depicted in fig. 3.2. When deformed, due to displacement of the adjoining grains, the bond develops an internal stress state which recursively results in forces and torques acting back on the adjoining grains. The deformations of a bond are modeled by means of the relative translational and rotational displacement, $d\vec{u}$ and $d\vec{\phi}$, of the adjoining grains. The resulting bond forces and torques are depending on the bond deformation state, the rate and material properties of the bond. Additionally, bonds between adjoining grains rupture if their stress state exceeds certain limits. Contrary to the classic collision modeling, this means that resulting bond forces cannot only be repulsive but also be attractive and vanish in the case of stress relaxation or bond fracture.
Similar bonding approximations have already been proposed and successfully employed in related discrete and constitutive models in the field of snow deformation by Johnson and Hopkins (2005) and Nicot (2004a), respectively. But snow is not the only sintering material which has been modeled discretely by means of cylindrical bond descriptions. Brendel et al. (2006) used a similar DEM approach to describe the caking behaviour of the bulk materials polyethylene and urea. Kim and Sasaki (2010) investigated the fracture limits of porous coke material with the same method.

## 3.2 Material Properties

This section lists all derived material laws and selected parameters which are used within the snow models presented in this chapter. In this study, a snow grain is assumed to consist of ice Ih as shown in fig. 2.2. A snow grain can be seen as multi-crystalline ice, as shown by Meyssonnier et al. (2009). Thus material properties of poly-crystalline ice are assumed. Therefore, the following section describes the elastic parameters, creep rate, hardness, restitution and friction of poly-crystalline ice. Further, resulting from this assumption, the density of a snow grain is assumed to be constant at the density of ice Ih, i.e. $\rho_{ice} \simeq 920\ \mathrm{kg/m^3}$.

### Elasticity of Ice

Ice cannot be considered as a linear elastic material solely as described in section 2.1.2. Although it shows a linear behaviour until a certain state of deformation, the initial state is not retrieved entirely when releasing the load.
However, table 3.1 lists the elastic properties of polycrystalline ice found in literature. Gammon et al. (1983) showed that the temperature dependency of any of the elastic parameter can be approximated linearly by $X(T) = X(T_0)[1 + 1.42 \cdot 10^{-3}\mathrm{K}^{-1} \cdot (T - T_0)]$. This temperature approximation is valid for the commonly used higher part of the temperature range of snow, 0 °C to −30 °C, as shown by Gammon et al. (1983).

*Table 3.1: Average values of elastic properties of ice*

| **Parameter** | **At** $-5$ °C composed from Hobbs (1974) | **At** $-16$ °C by Gammon et al. (1983) |
|---|---|---|
| Young's Modulus $E$ | 9.3 GPa | 9.33 GPa |
| Shear Modulus $G$ | 3.562 GPa | 3.52 GPa |
| Poisson's Ratio $\nu$ | 0.33 | 0.352 |

### Creep Rate of Ice

The viscous-plastic creep behaviour of ice affects the snow grain collision and bonding significantly. In this study two different power laws are used which are derived by Barnes et al. (1971).
The first relation 3.1 is based on measurements of the creep rate $\dot{\varepsilon}$ of ice samples under constant load and can be written:

$$\dot{\varepsilon}_{vol} = A \cdot (sinh(\alpha \cdot \sigma))^n \cdot e^{\frac{-Q}{RT}} \tag{3.1}$$

where $\sigma$ is the applied load, $Q$ is the activation energy, $R$ is the gas constant, $T$ is the temperature and $A$, $n$ and $\alpha$ are constants. Barnes et al. (1971) gives a detailed description which values to apply for the constants depending on the temperature regime. This creep relation is a macroscopic relation because it describes the creep behaviour of a representative volume of polycrystalline ice. The dependence of the creep rate on load and temperature is depicted by the grey curves in fig. 3.3 along with the measured data of respective tests by Barnes et al. (1971). The curves show an increase in the creep rate with increasing temperature and stress whereby the later dependence shows an asymptotic behaviour.
The second creep relation of eq. 3.2 is derived from measurements of the indentation hardness of polycrystalline ice.

$$\dot{\varepsilon}_{ind} = \frac{1}{A} \cdot \sigma^n \cdot e^{\frac{-Q}{nRT}} \tag{3.2}$$

As indentation tests are conducted by pressing a conical indenter with its peak end into the surface of an ice sample. The creep rate $\dot{\varepsilon}$ derived from indentation measurements is closer to the micro- or meso-scale behaviour. Thus the scale of this relation of ice is naturally closer to the grain-scale of snow. The quantities are the same as described in eq. 3.1. The dependence of the creep rate on load and temperature is depicted by the black curves in fig. 3.3. The curves resulting from the indentation relation show the same dependencies on increasing temperature and stress. But this relation lacks the asymptotic behaviour of eq. 3.1. Further, details on the experiments and derivation are described in chapter 2.1.2 or by Barnes et al. (1971).

### Hardness of Ice

Eq. 3.3 predicts the hardness $H^*$ of ice Ih and has been derived by Barnes et al. (1971) from the previously mentioned indentation measurements.

$$H^* = B \cdot \left(\frac{1}{t}\right)^{\frac{1}{m}} \cdot e^{\frac{Q}{mRT}} \tag{3.3}$$

In the equation above, $\sigma$ describes the applied load, $Q$ is the activation energy, $R$ is the gas constant, $T$ is the temperature and $B$ and $m$ are constants. In this case, $t$ describes the time that the indenter has been acting on the ice surface. Fig. 3.4 shows a comparison between eq. 3.3 and measurements. The hardness decreases with increasing indentation time, but increases with decreasing temperature. However, if the load applied on ice Ih reaches a certain value, depending on the ice temperature, the loaded surface starts to melt due to pressure. This of course prevents any further increase of the measured force. Therefore, relation 3.3 is limited by the melting pressure curve of ice. This correlates well with the measurements, shown as symbols in fig. 3.4. Pressure melting change is the upper limit for ice loading. Here, the Clausius - Clapeyron equation 3.4 is used to predict the

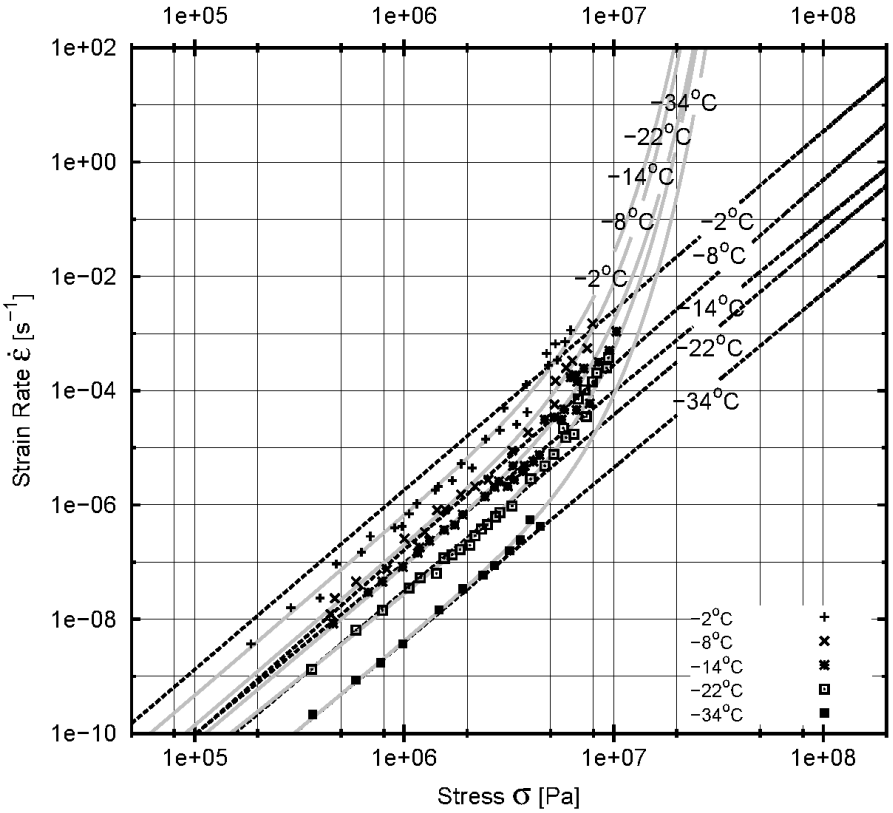


*Figure 3.3: Creep rate of ice versus stress at different temperatures. The black and grey lines are predicted according to eq. 3.2 and eq. 3.1, respectively. Symbols denote measurements of the creep tests of ice conducted by Barnes et al. (1971)*

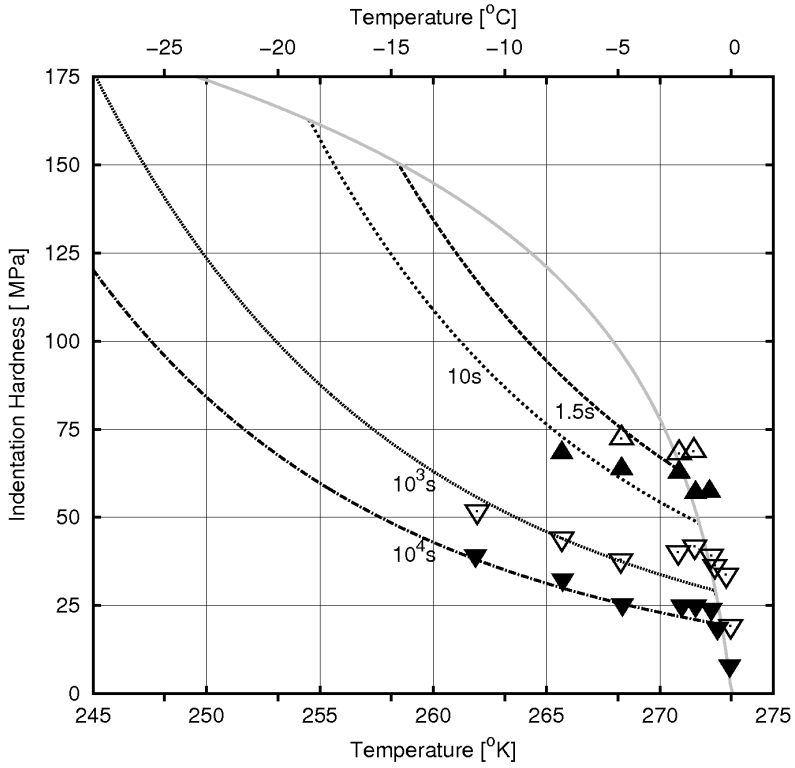


*Figure 3.4: Hardness of ice versus temperature at four indentation periods of* $1.5s$, $10s$, $10^3s$ *and* $10^4s$. *The lines are predicted according to eq. 3.3 and the symbols represent measured data by Barnes et al. (1971). The melting point depression is shown by the grey curve.*

melting pressure $p^*$ as follows:

$$p^* = \frac{dL}{T_0 \cdot dV} \cdot (T - T_0) + p_0 \tag{3.4}$$

where $dL$ is the latent heat, $dV$ is the change in volume and $T$ is the temperature at the point of transition, $T_0$ and $p_0$ are the ambient temperature and pressure, respectively. Eq. 3.4 accounts for the phase transition between the solid and liquid phase of water during the loading of ice. Eq. 3.5 composes the relations used to predict the hardness $H$ of ice.

$$H = \begin{cases} B \cdot (t)^{\frac{-1}{m}} \cdot e^{\frac{Q}{mRT}} & : H^* < p^* \\ \dfrac{dL}{T_0 \cdot dV} \cdot (T - T_0) + p_0 & : H^* \geqq p^* \end{cases} \tag{3.5}$$

The relation above is plotted in fig. 3.4 and is used frequently in this study.

### Coefficient of Ice-Ice Friction

The friction coefficient $\mu_{ice}$ for ice-ice contacts employed in this study is derived from measurements and observations by Akkok et al. (1987), which are depicted as symbols in fig. 3.5. The lines in fig. 3.5 are predicted by the following equation:

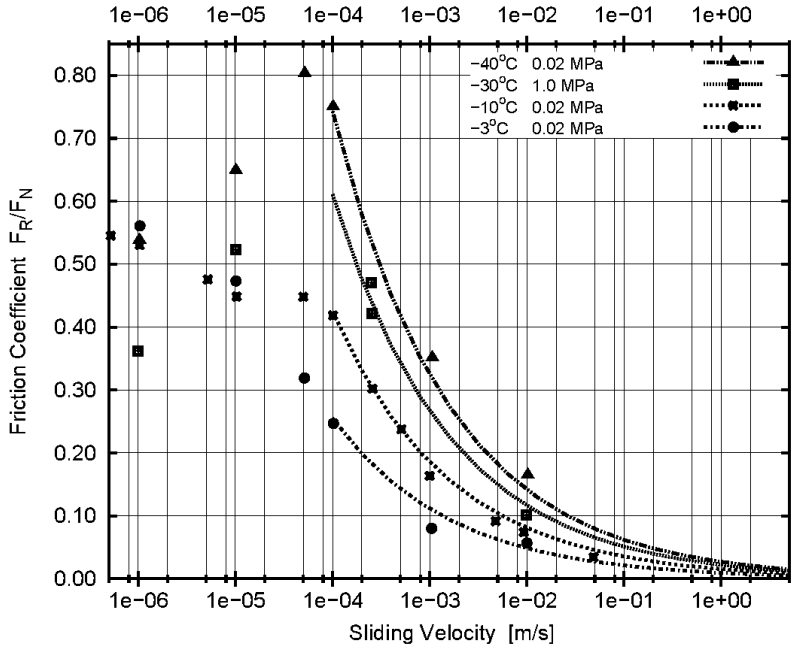


*Figure 3.5: Friction coefficient of ice-ice contact versus sliding velocity at different temperatures and contact pressures. The lines represent eq. 3.6 and the symbols are measurements by Akkok et al. (1987) and Kennedy et al. (2000)*

$$\mu_{ice}(T,p,v,H) \;=\; (T_m - T)^a \cdot p^{-b} \cdot \left(\frac{k\rho c}{vL}\right)^c \cdot H^{-d} \tag{3.6}$$

where $T_m$, $T$, $v$ and $p$ are the pressure depressed temperature, the ambient temperature, the sliding velocity and the load applied, respectively. $L$ describes the characteristic length of the sliding body and $H$ is the hardness of ice. Eq. 3.6 is valid for the higher velocity behaviour of the friction coefficient, i.e. for $v \geqq 10^{-4}$ m/s. Akkok et al. (1987) included a detailed description of the constants $a, b, c$ and $d$ for several material pairs. The relation describes the sliding regime governed by surface melting of contact asperities. However, the regime of the lower sliding velocities, i.e. for $v < 10^{-4}$ m/s, is governed by creep and fracture of the contacting surface. This behaviour is accounted by the bond deformation and fracture, i.e. frozen contacts. The models of bond deformation and fracture will be derived in section 3.4.3

## 3.3 Equations of Rigid Body Motion

In this study, the translation of a rigid body, i.e. discrete particle, is described by the explicit integration of Newton's second law. Further, Euler's equation of rotational motion is used to determine the evolution of the orientation of a particle over time, see Radjai and Dubois (2011).

### 3.3.1 Particle Translation

#### Notation

The position of a rigid body in space is defined uniquely by the three component vector $x_\alpha$ referring to the three spacial dimensions. The change in position occurs due to the force $\vec{F}_i$ acting on a particle. As shown in fig. 3.6, a change in position causes a new state of the three components $x_1$, $x_2$ and $x_3$ on the three orthogonal axes of the space-fixed reference system $\vec{X}_S$.

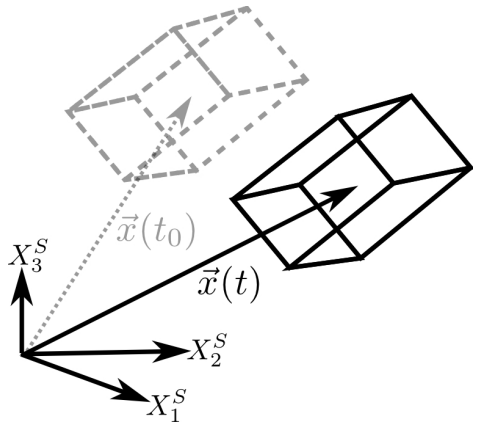


*Figure 3.6: Change of position*

#### Particle Forces

The force vector $\vec{F}_i$ acting on a particle $i$ is the sum of all collision $\vec{F}_i^c$, bonding $\vec{F}_i^b$, gravitational $\vec{F}_i^g$ and external forces $\vec{F}_i^e$ in eq. 3.7.[1]

$$\vec{F}_i = \vec{F}_i^c + \vec{F}_i^b + \vec{F}_i^g + \vec{F}_i^e \tag{3.7}$$

For example, the sources of external forces are interactions between electromagnetic charged particles, drag of surrounding fluids or attraction forces. Due to the objective of this thesis to describe snow behaviour, the focus herein lies on the collision and bonding forces and the corresponding developments for XDEM and its software architecture. The collision force $\vec{F}_i^c$ of a particle $i$ is the sum of all collision forces $\vec{F}_{ij}^c$ generated while colliding with the neighbouring bodies $j$. This is mathematically described by eq. 3.8 where $n$ is the number of neighbouring particles in contact and boundary shapes interacting with the particle $i$.

$$\vec{F}_i^c = \sum_{j=1, j\neq i}^{n} \vec{F}_{ij}^c \tag{3.8}$$

[1] The roman indices $i,\ j,\ k$ identify the $i^{th}$ particle out of $n$, i.e. $i = (1, 2, ..., n)$

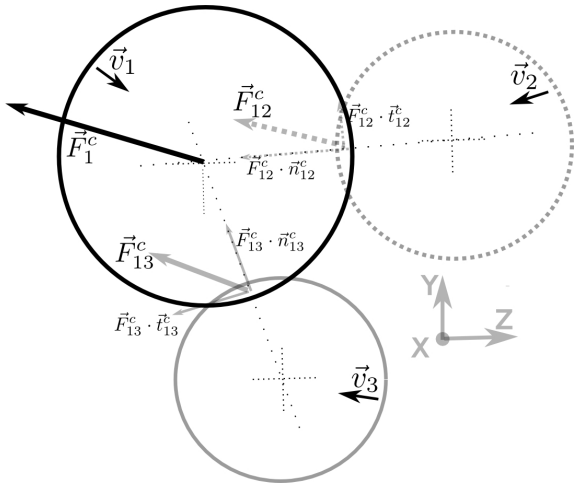


*Figure 3.7: Particle force due to colliding with particle* 2 *and* 3

Fig. 3.7 shows the collision forces acting on a particle while colliding with two neighbours. At the point of collision, each collision force is composed of a tangential and normal component. The normal unit vector $\vec{n}^c_{ij}$ points from the center of the particle $j$ to the center of $i$ with the tangential direction $\vec{t}^c_{ij}$ orthogonal to $\vec{n}^c_{ij}$.
The bonding force $\vec{F}^b_i$ experienced by the particle $i$ is the sum of all bonding forces plus forces caused by moments generated due to bond deformation. Hence, the vector $\vec{F}^b_i$ can be separated into a sum of forces $\vec{F}^b_{ij}$ and a sum of forces due to bond moments $\vec{F}^{bm}_{ij}$ as follows:

$$\vec{F}^b_i = \vec{F}^{bf}_i + \vec{F}^{bm}_i = \sum_{j=1, j\neq i}^{n} \vec{F}^b_{ij} + \vec{F}^{bm}_{ij} = \sum_{j=1, j\neq i}^{n} \vec{F}^b_{ij} + \vec{M}^b_{ij} \times \vec{d^b_{ij}}^{-1} \tag{3.9}$$

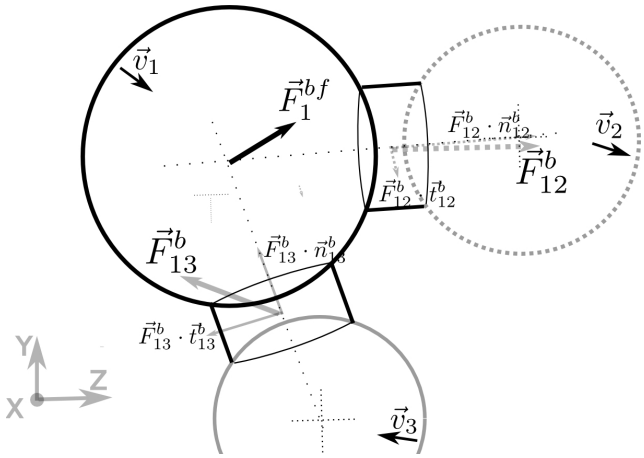


*Figure 3.8: Particle force generated by bonding forces of the joints* 2 *and* 3

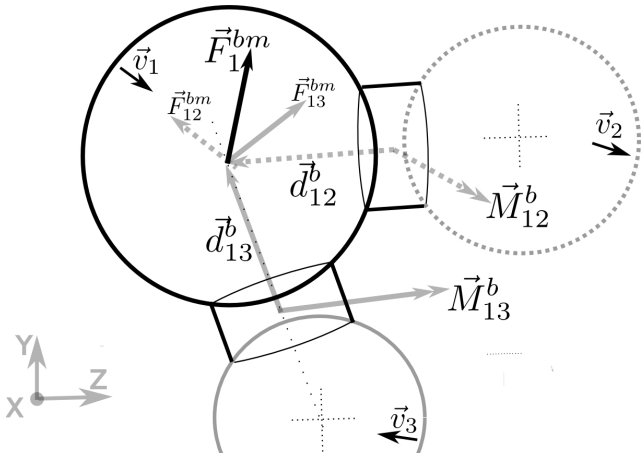


*Figure 3.9: Particle force generated by torques of the bonds 2 and 3*

The bonding forces and moments in eq. 3.9 are depict in fig. 3.8 and 3.9, respectively. In fig. 3.8, the forces $\vec{F}_{ij}^{b}$ generated in each bond center due to deformation are acting in the normal $\vec{n}_{ij}^{b}$ and orthogonal tangential $\vec{t}_{ij}^{b}$ direction of the joint. Additionally, as shown in fig. 3.9, the moments $\vec{M}_{ij}^{b}$ develop inside a deformed bond and contribute to bond forces experienced by a particle $i$. Thus, together with the according lever $\vec{d}_{ij}^{b}$, between the bond center and the center of particle $i$, each moment $\vec{M}_{ij}^{b}$ results in a force $\vec{F}_{ij}^{bm}$ acting at the particle center.

### Time Integration of the Particle Position

The translation of a rigid body, i.e. discrete particle, is described by Newton's second law. Newton's well-known equation 3.10 relates to the kinematic quantities at the center of gravity of a particle $i$ as follows:

$$\frac{d\vec{x}_i^{\,2}}{dt^2} = \frac{d\vec{v}_i}{dt} = \vec{a}_i = \frac{\vec{F}_i}{m_i} \tag{3.10}$$

where $m_i$ denotes the particle mass, $\vec{v}_i$ is the velocity, $\vec{a}_i$ is the acceleration, $\vec{x}_i$ is the center of gravity and $\vec{F}_i$ describes the force acting on the particle.
Consequently with the summation of all forces acting on a particle, Newton's second law 3.10 is used to obtain the particle acceleration. To further follow the evolution of a granular ensemble, the new position $\vec{x}_i^{\,t+\Delta t}$ and new velocity $\vec{v}_i^{\,t+\Delta t}$ of every particle are computed by numerical integration over every discrete time $\Delta t$ between $t$ and $t+\Delta t$. The procedure of obtaining the new state from the particle acceleration, i.e. forces, is commonly expressed by:

$$\ddot{x} \longrightarrow \dot{x} \longrightarrow x$$

For the software environment of XDEM, different algorithms have been derived to perform the integration in time. All available integration schemes are listed in table 3.2. In the

study of Samiei (2012) a very detailed discussion of all schemes is presented. He points out that the performance of any integration scheme is only challenged in a contact situation between particles and does not differ considerably in free motion of particles. The study compares the accuracy of the integration schemes in relation to the chosen contact resolution $CR$, which is defined as follows:

$$CR = \frac{t_{contact}}{\Delta t} \tag{3.11}$$

The contact resolution is a coefficient identifying how many discrete timesteps $\Delta t$ resolve the duration of a collision. From the investigations of Samiei (2012), this study draws the conclusion to employ the Velocity Verlet method. The Velocity Verlet method showed the best balance between accuracy and computational effort in relation to the snow simulations ahead. Thus here only the Velocity Verlet method is used and introduced.

*Table 3.2: Time Integration Schemes*

| **Integration method** | **Velocity,** $\vec{v}_{t+\Delta t}$ | **Position,** $\vec{x}_{t+\Delta t}$ |
|---|---|---|
| Symplectic Euler | $\vec{v}_t + \Delta t \vec{a}_t$ | $\vec{x}_t + \Delta t \vec{v}_{t+\Delta t}$ |
| Taylor | $\vec{v}_t + \Delta t \vec{a}_t$ | $\vec{x}_t + \Delta t \vec{v}_t + \frac{\Delta t^2}{2}\vec{a}_t$ |
| Position Verlet | $\frac{1}{2}(\vec{x}_{t+\Delta t} - \vec{x}_{t-\Delta t}) \cdot \Delta t^{-1}$ | $2\vec{x}_t - \vec{x}_{t-\Delta t} + \Delta t^2 \vec{a}_t$ |
| Velocity Verlet | $\vec{v}_t + \frac{\Delta t}{2}(\vec{a}_t + \vec{a}_{t+\Delta t})$ | $\vec{x}_t + \Delta t \vec{v}_t + \frac{\Delta t^2}{2}\vec{a}_t$ |
| Gear 4th order | $\vec{v}_t + \frac{7\Delta t}{12}\vec{a}_t + \frac{5\Delta t}{12}\vec{a}_{t+\Delta t} + \frac{11\Delta t^2}{12}\frac{\partial^3 \vec{x}_t}{\partial t^3}$ | $\vec{x}_t + \vec{v}_t \Delta t + \frac{5\Delta t^2}{12}\vec{a}_t + \frac{\Delta t^2}{12}\vec{a}_{t+\Delta t} + \frac{\Delta t^3}{12}\frac{\partial^3 \vec{x}_t}{\partial t^3}$ |

*Derivation of the Velocity Verlet Scheme*
All schemes presented in table 3.2 can be derived by an approximation of a Taylor series of eq. 3.12.

$$f(t + \Delta t) = f(t) + \frac{f'(t)}{1!}\Delta t + \frac{f''(t)}{2!}\Delta t^2 + \frac{f^{(3)}(t)}{3!}\Delta t^3 + ... \tag{3.12}$$

Thus, the method proposed by the French physicist Loup Verlet, Verlet (1967), can also be derived by means of a Taylor series. The basic Verlet method makes use of a central difference approximation. Employing the Taylor polynomial, the first derivative of a function $f$ can be gained by deriving the polynomial to the second degree for the backward and forward time direction. The two directions are shown in the following equations, respectively.

$$f(t+\Delta t) = f(t) + \Delta t \cdot f'(t) + \frac{1}{2} \cdot \Delta t^2 f''(t) \tag{3.13}$$

$$f(t-\Delta t) = f(t) - \Delta t \cdot f'(t) + \frac{1}{2} \cdot \Delta t^2 f''(t) \tag{3.14}$$

Thereafter, the two derivations are subtracted from one and another. This results in a central difference approximation for the first derivative of the function $f$ as written in eq. 3.15.

$$f'(t) = \frac{f(t+\Delta t) - f(t-\Delta t)}{2\Delta t} \tag{3.15}$$

Further, the Taylor polynomial needs to be formed again for both time direction, but this time truncated after the third degree. By summing these derivations, the second derivative of a function $f$ takes the form of eq. 3.16.

$$f''(t) = \frac{f(t+\Delta t) - 2f(t) + f(t-\Delta t)}{\Delta t^2} \tag{3.16}$$

Using eq. 3.16 on the acceleration of a particle, where the second derivative $f''(t)$ equals $\vec{a}_i(t) = \ddot{\vec{x}}_i(t)$, the eq. 3.17 yields a relation for the new position $\vec{x}_i(t+\Delta t)$ of a particle $i$.

$$\vec{x}_i^{\,t+\Delta t} = 2\vec{x}_i^{\,t} - \vec{x}_i^{\,t-\Delta t} + \vec{a}_i^{\,t} \cdot \Delta t^2 \tag{3.17}$$

The current acceleration $\vec{a}_i^{\,t}$ is obtain from the sum of all forces according eq. 3.10. Further, using the first derivative $f'(t)$, a relation for the velocity $\vec{v}_i(t) = \dot{\vec{x}}_i(t)$ can be derived as follows:

$$\vec{v}_i^{\,t} = \frac{\vec{x}_i^{\,t+\Delta t} - \vec{x}_i^{\,t-\Delta t}}{2\Delta t} \tag{3.18}$$

Looking at Eq. 3.18 one notices that the velocity is still one step behind the position. To retrieve the position and the velocity at the new time $t+\Delta t$ simultaneously further derivations are undertaken in this scheme. Hence, eq. 3.18 is resolved to the position term $\vec{x}_i^{\,t-\Delta t}$ and placed into eq. 3.17. In this scheme, the new particle position $\vec{x}_i^{\,t+\Delta t}$ is now predicted by eq. 3.19.

$$\vec{x}_i^{\,t+\Delta t} = \vec{x}_i^{\,t} + \vec{v}_i^{\,t}\Delta t + \frac{1}{2}\vec{a}_i^{\,t} \cdot \Delta t^2 \tag{3.19}$$

By choosing this approach the new particle velocity $\vec{v_i}^{t+\Delta t}$ is determined as follows:

$$\vec{v_i}^{t+\Delta t} = \vec{v_i}^{t} + \frac{1}{2}(\vec{a_i}^{t} + \vec{a_i}^{t+\Delta t})\Delta t \tag{3.20}$$

where $\vec{a_i}^{t}$ is the sum of all current and $\vec{a_i}^{t+\Delta t}$ is the sum of all new forces. Concerning the implementation, this approach does not allocate additional memory as the prediction of the new velocity is split into a predictor and a corrector phase of the procedure. In details this means that the current acceleration $\vec{a_i}^{t-\Delta t}$ is determined and added on the new velocity ahead of the prediction of the new forces. After the prediction of the new forces the new velocity object is corrected by adding the new acceleration.

### 3.3.2 Particle Rotation

#### Notation

The orientation of a rigid body in space can be defined by the three Euler angles $\phi_\alpha$. The change of orientation occurs with a torque $\vec{M}_i$ acting on a particle. A change in orientation causes a new state of the Euler angles. Hence, the angles present a sequence of three rotations about the axes of the reference system. The sequence of rotation is depicted in fig. 3.10. By definition in XDEM, the first rotation is about $X_3^S$ by the angle

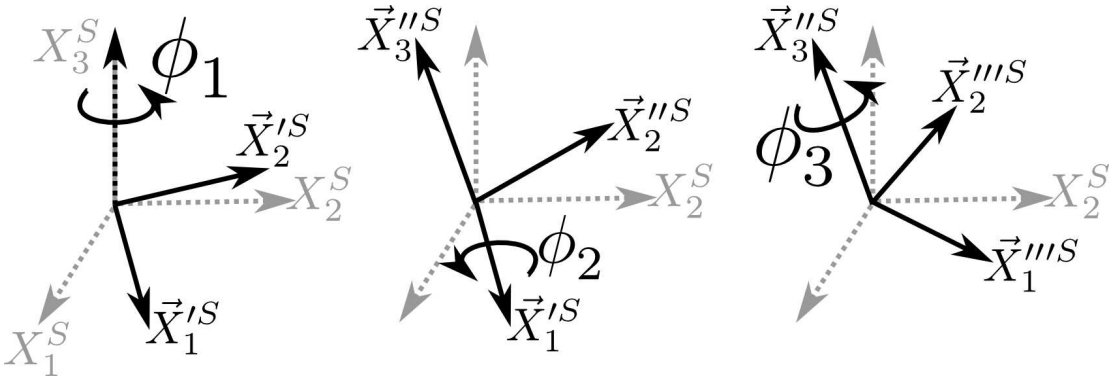


*Figure 3.10: Sequence of rotation*

$\phi_1$, the second about $X_1'^S$ by the angle $\phi_2$ and the final rotation is again around $X_3''^S$ but by the angle $\phi_3$.
However, the new orientation, i.e. the new Euler angles, can be derived in all three spacial dimensions from the total torque $\vec{M}_i$ acting on a particle. But this inherits somehow more complexity compared to translational motion. Therefore, different co-coordinate systems have to be defined for the derivation of the new orientation. The following description will distinguish between the space-fixed, the co-moving and the body-fixed coordinate system. All three are simultaneously exemplified in fig. 3.11. First, the space-fixed coordinate system $\vec{X}_S$ is self-explanatory fixed in space and time, which consequently means it does not dependent on the motion of the body in a system. Therefore, the space-fixed system is

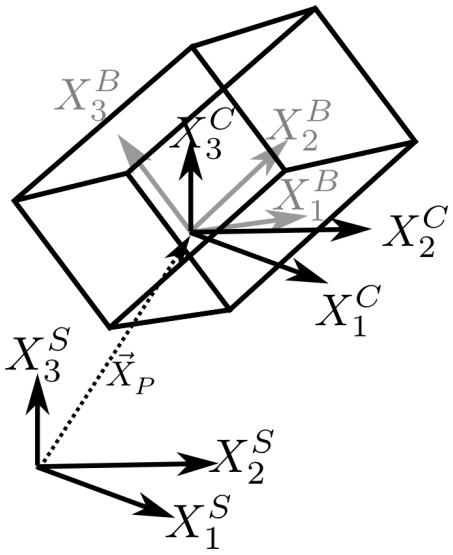


*Figure 3.11: Different coordinate systems: Space-fixed$^S$, Co-moving$^C$ and Body-fixed$^B$*

the reference system for all derived equations of motion and for the simulation environment of XDEM. Secondly, for a clean handling and understanding, the rotational motion can be treated separately from the translation by introducing the co-moving coordinate system $\vec{X}_C$, as seen in fig. 3.11. The origin of the co-moving system is aligned with the body center and the axes direction are aligning with the space-fixed coordinate system. Thus it relates to the space-fixed system by pure translation and the position vector of the co-moving system equals the position vector of the particle $\vec{X}_P$. The origin of the body-fixed coordinates $\vec{X}_B$ is similar to the co-moving but its axes directions orient with the principal axes of the moving body at the particular time $t$. Hence, contrary to the space-fixed system, this coordinate system translates and rotates through time according to the body motion. But the state of the body-fixed system can be described by pure rotation of the co-moving coordinate system.

### Particle Torques

The total torque $\vec{M}_i$ on a particle $i$ is composed of collision $\vec{M}_i^c$ and bonding moments $\vec{M}_i^b$ acting on adjoining particles. Eq. 3.21 includes the described sources of torques and additionally accounts for external moments $\vec{M}_i^e$, for instance moments experienced by a particle due to friction with a surrounding fluid.

$$\vec{M}_i = \vec{M}_i^c + \vec{M}_i^b + \vec{M}_i^e \tag{3.21}$$

The torque $\vec{M}_i^c$ on a particle $i$ developed during a collision is the sum of all the forces $\vec{F}_{ij}^c$ acting at the collision point times the relative distance $\vec{d}_{ij}^c$ to the center of mass of the

particle:

$$\vec{M}_i^c = \sum_{j=1,j\neq i}^{n} \vec{M}_{ij}^c = \sum_{j=1,j\neq i}^{n} \vec{d}_{ij}^c \times \vec{F}_{ij}^c \tag{3.22}$$

The mathematical formulation of eq. 3.22 is illustrated accordingly in fig. 3.12. Additionally,

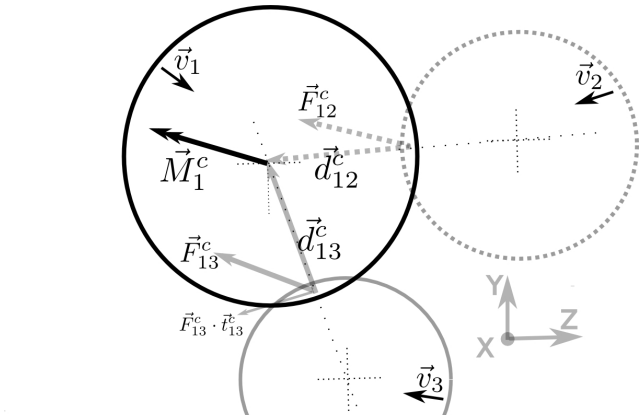


*Figure 3.12: Particle torque during collision with two neighbours*

the torque experienced by a particle $i$ further includes all moments developing due to bond deformations. Thus, the vector $\vec{M}_i^b$ contains the sum of all torques $\vec{M}_{ij}^b$ and $\vec{M}_{ij}^{bf}$ as follows:

$$\vec{M}_i^b = \sum_{j=1,j\neq i}^{n} \vec{M}_{ij}^b + \vec{M}_{ij}^{bf} = \sum_{j=1,j\neq i}^{n} \vec{M}_{ij}^b + \vec{d}_{ij}^b \times \vec{F}_{ij}^b \tag{3.23}$$

Fig. 3.13 illustrates the torques $\vec{M}_{ij}^b$ generated in each bond center due to deformation. The sum of these torques, $\vec{M}_i^{bm}$, results in the center of gravity of the particle $i$. The moments $\vec{M}_{ij}^{bf}$ develop as a product of the according bond force $\vec{F}_{ij}^b$ times the according lever $\vec{d}_{ij}^b$. These moments result in the particle center and are depict in fig. 3.14.

### Time Integration of the Particle Orientation

In XDEM, the Euler equation of rotational motion is applied to predict a change of the particle orientation. Details about the derivation of the Euler equations from Newton's equations or the Lagrange equation of motion can be found in the publications of Radjai and Dubois (2011), Poeschel and Schwager (2005), Dziugys and Peters (2001) and Tatum (2010). Euler's equation in the body fixed coordinate system can be written as follows:

$$\begin{bmatrix} M_1^B \\ M_2^B \\ M_3^B \end{bmatrix} = \begin{bmatrix} I_{11}\dot{\omega}_1^B - \omega_2^B\omega_3^B(I_{22} - I_{33}) \\ I_{22}\dot{\omega}_2^B - \omega_3^B\omega_1^B(I_{33} - I_{11}) \\ I_{33}\dot{\omega}_3^B - \omega_1^B\omega_2^B(I_{11} - I_{22}) \end{bmatrix} \tag{3.24}$$

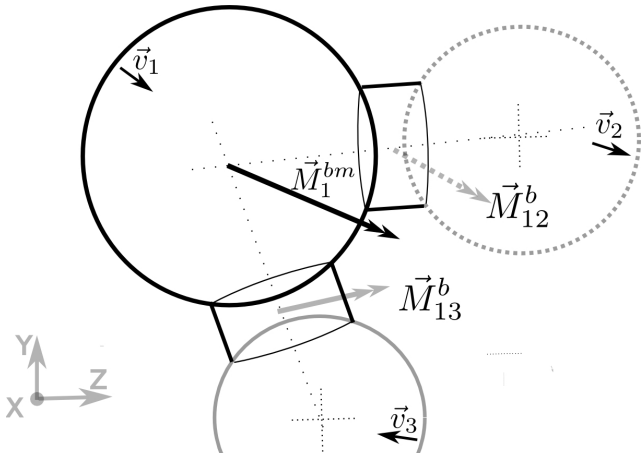


*Figure 3.13: Particle torque induced by bond moments with adjoining particles*

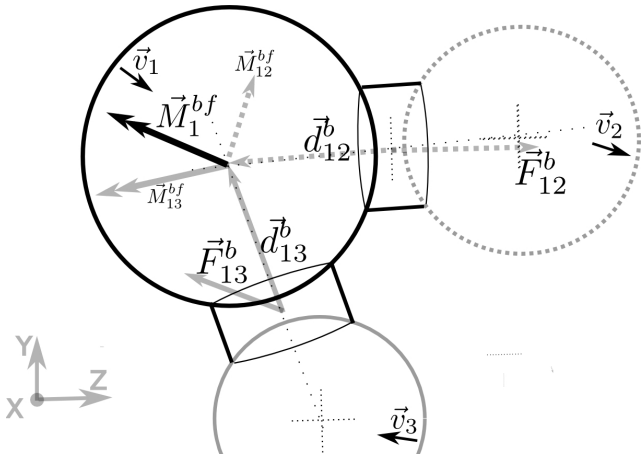


*Figure 3.14: Particle torque due to bond forces of two bonds*

where $\vec{M}^B$ and $\vec{\omega}^B$ describe the torque and the angular velocity of the bodies in the body-fixed coordinate system, respectively. To make use of the moment of inertia $I_{\alpha\beta}$ in the principal directions, i.e. $I_{11}$, $I_{22}$ and $I_{33}$, of a shape, the torque in eq. 3.24 has to be transformed into body-fixed coordinates. In case the moments would be given in space-fixed coordinates, the moment of inertia results in a time-dependent tensor dyad $I_{\alpha\beta}$ which in all probability contains off-trace elements.[1] However, the three equations in 3.24 are solved for the three unknown angular velocities $\omega_\alpha^B$ of a particle. Thereafter, the change

[1]The Greek indices $_\alpha$, $_\beta$, $_\gamma$ identify the three spatial components of a quantity.

in Euler angles $\dot{\phi}_\alpha$ is predicted by making use of the relations in eq. 3.25.

$$\begin{bmatrix} \dot{\phi}_1 \\ \dot{\phi}_2 \\ \dot{\phi}_3 \end{bmatrix} = \begin{bmatrix} \dfrac{\omega_x^B \sin\phi_3 + \omega_y^B \cos\phi_3}{\sin\phi_2} \\ \omega_x^B \cos\phi_3 - \omega_y^B \sin\phi_3 \\ \omega_z^B - (\omega_x^B \sin\phi_3 + \omega_y^B \cos\phi_3)\dfrac{\cos\phi_2}{\sin\phi_2} \end{bmatrix} \tag{3.25}$$

However, it needs to be mentioned that the eq. 3.25 inherits singularities when the Euler angles take the values 0, $\pi$, $2\pi$, .. etc. To avoid complications, XDEM makes use of quaternions internally to describe rotations. This is simply a different method to express the orientation of a body in space. A quaternion is a vector with four components $q_i = (q_0, q_1, q_2, q_3)$ which have to satisfy the following constraint:

$$q_0^2 + q_1^2 + q_2^2 + q_3^2 = 1 \tag{3.26}$$

The relation between quaternions and Euler angles used can be expressed as follows:

$$\begin{bmatrix} q_0 \\ q_1 \\ q_2 \\ q_3 \end{bmatrix} = \begin{bmatrix} \cos\dfrac{\phi_2}{2}\cos\dfrac{\phi_1+\phi_3}{2} \\ \sin\dfrac{\phi_2}{2}\cos\dfrac{\phi_1-\phi_3}{2} \\ \sin\dfrac{\phi_2}{2}\sin\dfrac{\phi_1-\phi_3}{2} \\ \cos\dfrac{\phi_2}{2}\sin\dfrac{\phi_1+\phi_3}{2} \end{bmatrix} \tag{3.27}$$

With the particle orientation expressed by a quaternion, the eq. 3.28 computes directly the change in orientation from the angular velocities of the eq. 3.24.

$$\begin{bmatrix} \dot{q}_0 \\ \dot{q}_1 \\ \dot{q}_2 \\ \dot{q}_3 \end{bmatrix} = \frac{1}{2}\begin{bmatrix} -q_1 & -q_2 & -q_3 \\ q_0 & -q_3 & q_2 \\ q_3 & q_0 & -q_1 \\ -q_2 & q_1 & q_0 \end{bmatrix} \cdot \begin{bmatrix} \omega_x^B \\ \omega_y^B \\ \omega_z^B \end{bmatrix} \tag{3.28}$$

Simultaneously, the eq. 3.28 accounts for the final backwards transformation from body-fixed to space-fixed coordinates of the angular velocities, which are the reference coordinates for all spacial quantities.

## 3.4 Interaction Models of Snow and Ice Grains

The grain-scale properties and processes affect the behaviour of snow under load on different time scales.
One time scale is the long-term evolution of the micro-structural properties of a snow sample due to metamorphism. The micro-structural properties depending on this evolution of the snow sample are the grain geometry, bond size, coordination number and the ice matrix, i.e. foam structure, of the whole sample. The isothermal observations conducted by

Kaempfer and Schneebeli (2007) at different temperatures describe the evolution of these particular snow properties in a very detailed analysis. Yong and Metaxas (1985) aged samples in similar isothermal conditions and showed that the strength of a snow sample increases with increasing age, i.e. increasing bond size and number. These properties constitute initial conditions for models derived in this chapter. Chapter 3.5 describes the preparation and pre-processing of a snow specimen as well as the setup of the above mentioned initial bulk and micro-structural properties.
The second time scale governing snow behaviour is the characteristic rate applied to a snow sample during loading. As described in chapter 2.1, the transition between ductile and brittle material behaviour of snow is inherited from ice on the micro-scale. This transition behaviour depends on the strain rate acting during the deformation process. Kinosita (1967) and Schulson (1990) described this macroscopic transition phenomena in detail. Consequently, the derivations of the inter-granular models are focused on the reproduction of these phenomena of snow on the macroscopic scale. Therefore, the creep behaviour of ice is employed on the grain scale by the power law of Barnes et al. (1971).
The rate dependence is the major characteristic of snow behaviour. But snow behaviour also shows strong dependencies on the ice temperature $T$ and the loading pressure $p$. Thus, the collision and bonding models between snow grains also account for temperature and contact pressure, i.e. stress, dependent behaviour. Thereby, the description of the elastic viscous-plastic deformation and the growth of a bond between two adjoining grains is based on the material properties and the creep behaviour of ice. Furthermore, the bond fracture, impact fracture and pressure-melting of colliding grains is represented by the models in this study.
All the above-mentioned micro-scale characteristics of snow are accounted for to approximate the macroscopic behaviour. How much each characteristic participates to the macroscopic behaviour of snow will be discussed along with the simulation results in chapter 6.

### 3.4.1 Contact Properties

The forces and torques developing between colliding or bonding grains are estimated from the contact properties at the point of contact. The properties are described within the local contact frame which is defined by the normal $\vec{n}_{ij}$ and tangential $\vec{t}_{ij}$ unit vector at the contact point, as shown in fig. 3.15. Along with the specific collision and bonding properties, which are described in the following sections 3.4.2 and 3.4.3, the relative velocity $\vec{v}_{ij}$ at the point of contact is applied for interaction. In this section, the mathematical relationships describing the dynamics of a contact are derived. The normal direction $\vec{n}_{ij}$ of a contact is given by eq. 3.29 and points always from grain $j$ to grain $i$.

$$\vec{n}_{ij} = \frac{\vec{x}_i - \vec{x}_j}{|\vec{x}_i - \vec{x}_j|} \tag{3.29}$$

Having the normal direction estimated the location of the point of contact $\vec{x^c}_{ij}$ itself is given by eq. 3.30.

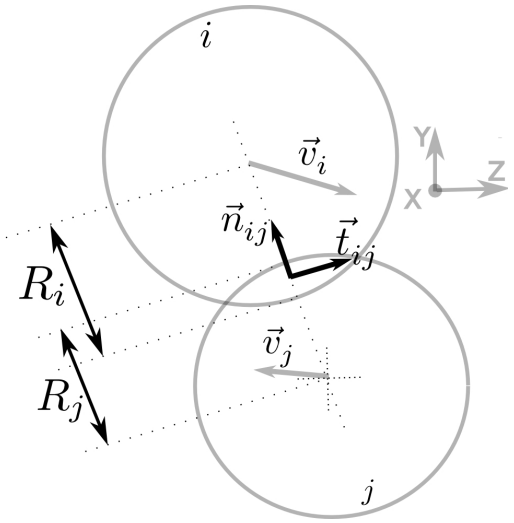


*Figure 3.15: Contact configuration and normal overlap of grain i and j*

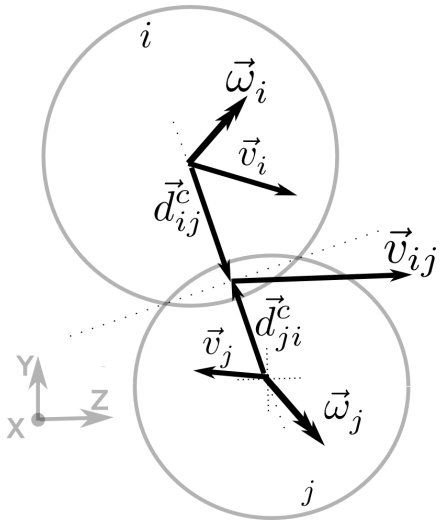


*Figure 3.16: Velocity at the point of contact*

$$\vec{x^c}_{ij} = \vec{x}_i + \vec{n}_{ij} \cdot (r_j - |\vec{x}_i - \vec{x}_j|) \tag{3.30}$$

The velocity $\vec{v}_{ij}$ at the contact point is predicted by eq. 3.31 taking into account the angular and translational velocities of the contacting particles, as shown in fig. 3.16.

$$\vec{v}_{ij} = (\vec{\omega}_i \times \vec{d}^c_{ij} + \vec{v}_i) - (\vec{\omega}_j \times \vec{d}^c_{ji} + \vec{v}_j) \tag{3.31}$$

The normal and tangential velocity, $\vec{v^n}_{ij}$ and $\vec{v^t}_{ij}$ respectively, at the point of contact are defined as:

$$\vec{v^n}_{ij} = (\vec{v}_{ij} \cdot \vec{n}_{ij}) \cdot \vec{n}_{ij} \tag{3.32}$$

$$\vec{v^t}_{ij} = \vec{v}_{ij} - \vec{v^n}_{ij} \tag{3.33}$$

The tangential direction $\vec{t}_{ij}$ of the contact configuration is defined as the direction of the tangential velocity at the contact point by eq. 3.34.

$$\vec{t}_{ij} = \frac{\vec{v^t}_{ij}}{\left|\vec{v^t}_{ij}\right|} \tag{3.34}$$

The effective radius $R_{ij}$ and reduced mass $m_{ij}$ of two grains in contact are determined by eq. 3.35 and eq. 3.36, respectively.

$$\frac{1}{R_{ij}} = \frac{1}{r_i} + \frac{1}{r_j} \tag{3.35}$$

$$\frac{1}{m_{ij}} = \frac{1}{m_i} + \frac{1}{m_j} \tag{3.36}$$

### 3.4.2 Grain Collision

#### Collision Properties

The forces developing between colliding grains are estimated from the collision properties at the point of contact. The characteristics of a collision are the duration of a contact $t_c$, the normal $\delta^n_{ij}$ and tangential overlap $\delta^t_{ij}$ and the relative velocity $\vec{v}_{ij}$ at the point of contact. Here, the normal overlap $\delta^n_{ij}$ represents the deformation of the grains in normal direction. As deformation causes stress, the normal overlap is finally used to estimated the resulting normal force $\vec{F}^{c,n}_{ij}$. Hence, the tangential overlap represents the deformation of the asperities at the grain surface. Therefore, the tangential overlap is employed to predict the frictional force $\vec{F}^{c,n}_{ij}$ in tangential direction.
Equation 3.37 evaluates the normal overlap $\delta^n_{ij}$ with the radii $r_i$ and $r_j$ of the spherical particles and is presented in fig. 3.17.

$$\delta^n_{ij} = r_i + r_j - |\vec{x}_i - \vec{x}_j| \tag{3.37}$$

The duration of a collision $t_c$ is defined as the time in which normal overlap is existing continuously. The collision time is estimated as follows:

$$t_c = t - t^c_0 = i_c \cdot \Delta t \tag{3.38}$$

where $t$ denotes either the end time of the contact or the current time, $t^c_0$ denotes the start time of the contact and $i_c$ the total number of time steps in contact. The number of time steps of a contact is given by $i_c = t_c/\Delta t$.
As shown in fig. 3.18, the tangential overlap derives from the relative tangential path taken by the point of contact over the entire time spent in a collision. Therefore, the tangential overlap $\delta^t_{ij}$ is calculated as follows:

$$\delta^t_{ij}(t) = \left|\vec{\delta}^t_{ij}(t)\right| \qquad \vec{\delta}^t_{ij}(t) = \sum_{i=1}^{i_c} \vec{v^t}_{ij}(t^c_0 + i \cdot \Delta t) \cdot \Delta t \tag{3.39}$$

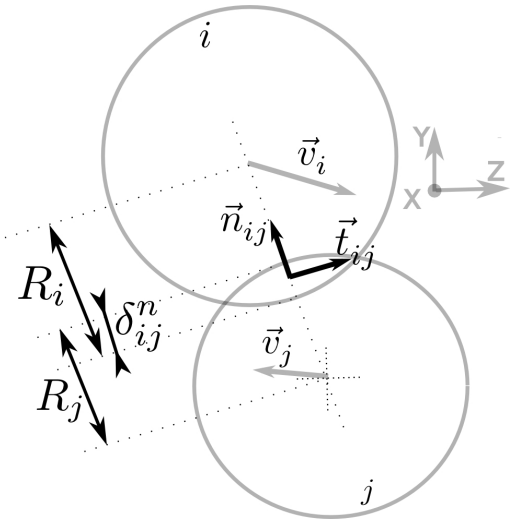


*Figure 3.17: Normal overlap of grain i and j*

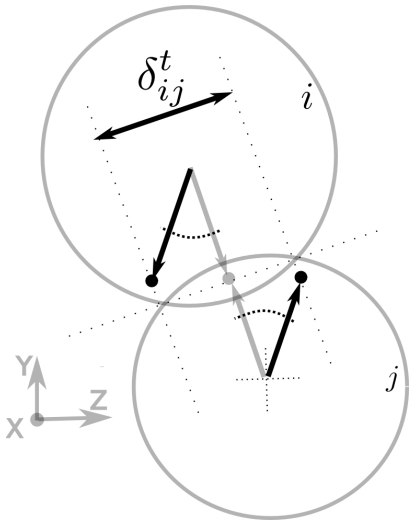


*Figure 3.18: Tangential overlap of grain i and j*

where $t$ equals the current time step, $t_0^c$ is the start time of the contact and $i_c$ is the total number of time steps during a contact. Thus eq. 3.39 predicts $\delta_{ij}^t$ as the sum of all tangential velocities over the contact time.
According to Hertz (1881), the effective Young's modulus $E_{ij}$ at the interface of two colliding grains is given by:

$$\frac{1}{E_{ij}} = \frac{1-\nu_1^2}{E_i} + \frac{1-\nu_2^2}{E_j} \tag{3.40}$$

### Hardness - Creep Model

In this study, the collision model for snow grains is based on the linear hysteretic model developed by Walton and Braun (1986), which accounts for the effect of plasticity. This

collision model aims to describe the elastic and viscous-plastic response of colliding snow grains. The deformed grains do not fully recover their initial shape at the end of a collision. This is arranged by defining a plastified portion of the normal overlap $\delta_{ij}^{n}$ denoted $\delta_{ij}^{n,p}$. The rate of the overlap is identified as $\dot{\delta}_{ij}^{n}$. During collision, the model distinguishes between loading $\dot{\delta}_{ij}^{n} \geqslant 0$ and unloading phase $\dot{\delta}_{ij}^{n} < 0 \wedge \delta_{ij}^{n} \geqslant \delta_{ij}^{n,p}$ of the collision. The responding normal force $\vec{F}_{ij}^{c,n}$ is predicted as follows:

$$\vec{F}_{ij}^{c,n} = \vec{n}_{ij} \cdot \begin{cases} -k_{l}^{n} \cdot \delta_{ij}^{n} & : \dot{\delta}_{ij}^{n} \geqslant 0 \\ -k_{unl}^{n} \cdot (\delta_{ij}^{n} - \delta_{ij}^{n,p}) & : \dot{\delta}_{ij}^{n} < 0 \wedge \delta_{ij}^{n} \geqslant \delta_{ij}^{n,p} \end{cases} \tag{3.41}$$

where $k_{l}^{n}$ and $k_{unl}^{n}$ denote the loading and the unloading stiffness, respectively. In hysteretic models, different rheological models are used in loading and unloading phases as demonstrated in fig. 3.19. The unloading part can be described as a elastic perfectly

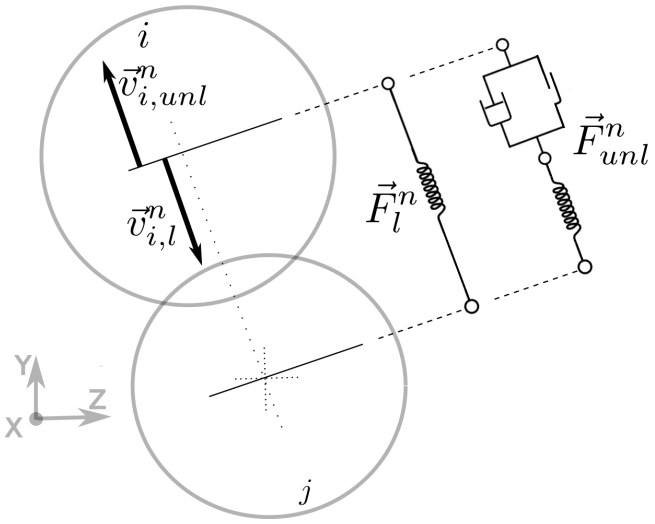


*Figure 3.19: Schematic demonstration of hardness-creep impact model*

viscous-plastic model, which is also known as a Bingham-Maxwell model or the Bingham-Norton model. For such rheological models the sliding friction element and the damper are arranged in parallel and additionally mounted in series to the elastic spring element. Thereby, the elastic part employs the described hardness of ice and the viscous-plastic part is based on the indentation creep behaviour of ice. Therefore, loading and unloading stiffness are determined from the hardness of ice by eq. 3.5. The hardness of ice is employed for two reasons. First, the hardness reflects the response force of an indenter colliding punctual with an ice surface. This is a natural link to the response experienced by two colliding ice grains. Second, the hardness law of eq. 3.5 accounts for the pressure melting effect of ice. This prevents implicitly the development of any unnatural collision energy. Hence, the loading stiffness $k_{l}^{n}$ is predicted as follows:

$$k_{l}^{n} = H(t_c, T) \cdot \sqrt{R_{ij} \cdot (\delta_{ij,max}^{n} - \delta_{ij}^{n,p})} \tag{3.42}$$

where $H(t_c, T)$ stands for the hardness of ice, $R_{ij}$ the effective radius, $\delta_{ij}^{n,p}$ the plastified portion and $\delta_{ij,max}^{n}$ is the maximum normal overlap of the collision. To reflect the plastification while unloading, the unloading stiffness $k_{unl}^{n}$ is predicted as follows:

$$k_{unl}^{n} = \frac{\delta_{ij,max}^{n}}{(\delta_{ij,max}^{n} - \delta_{ij}^{n,p})} \cdot k_{l}^{n} \tag{3.43}$$

Thereby, the unloading stiffness is derived in relation to the loading stiffness.
The plastic overlap is predicted incrementally by summing up all viscous-plastic deformations $\dot{\varepsilon}_{ind}(t_c)$ occurring at each time step $t_c$ of the collision. This is done by eq. 3.44, where $\dot{\varepsilon}_{ind}(t_c)$ is the creep rate by eq. 3.2.

$$\delta_{ij}^{n,p}(t) = \sum_{t_c}^{t} \dot{\varepsilon}_{ind}(t_c) \cdot \Delta t \cdot (\delta_{ij,max}^{n} - \delta_{ij}^{n,p}) \tag{3.44}$$

Plastic deformations during a collision are only caused while compressing the contact area. Thus, the plastic overlap only grows during the loading phase. The creep rate $\dot{\varepsilon}_{ind}(t) = f(\sigma_{ij}^{c}, T)$ is a function of the current contact pressure $\sigma_{ij}^{c}$ and the ambient temperature $T$. As only the elastic part of the deformation can undergo further plastification, the Hertzian contact eq. 3.45 is used to predict the current stress $\sigma_{ij}^{c}$ acting at the collision area of two grains.

$$\sigma_{ij}^{c} = \left( \frac{6 \cdot \left| \vec{F}_{ij}^{c,n} \right| \cdot E_{ij}}{\pi^3 \cdot R_{ij}^2} \right)^{1/3} \tag{3.45}$$

In eq. 3.45, $\vec{F}_{ij}^{c,n}$ is the predicted normal force, $E_{ij}$ the effective Young's modulus by eq. 3.40 and $R_{ij}$ the effective radius.

### Friction

For all collision models derived in this study and commonly used in the literature, the tangential collision force $\vec{F}_{ij}^{c,t}$ is predicted from the static friction between the particles and is limited by a dynamic friction force. This can be written as follows:

$$F_t = min\,(\text{static friction, dynamic friction})$$

Hence in this study, the tangential collision force $F_{ij}^{c,t}$ between two grains is determined as follows:

$$\vec{F}_{ij}^{c,t} = \vec{t} \cdot min\left( \left| \vec{F}_{ij}^{b,t} \right| \;,\; \mu_{ice} \cdot \left| \vec{F}_{ij}^{c,n} \right| \right) \tag{3.46}$$

where $\vec{t}$ is the tangential direction, $\vec{F}_{ij}^{b,t}$ denotes the tangential bonding force, $\mu_{ice}$ the ice-ice friction coefficient and $\vec{F}_{ij}^{c,n}$ the normal collision force. In eq. A.8, the dynamic part of friction is based on the Coulomb's law of friction. The friction coefficient $\mu_{ice}$ employed is given by eq. 3.6 derived by Akkok et al. (1987). The static friction can be estimated as a

viscous damping force using a viscous constant and the tangential overlap, e.g. $c_t\dot{\delta}_t$. This is for instance the case in the common discrete element models described in Appendix A.1. However, in this study the grains are able to bond for the simulation of snow behaviour. The bonds develop tangential forces under deformation. Therefore, the static friction force is predicted by the bonding models of section 3.4.3. Thus the static friction force $\vec{F}_{ij}^{c,t}$ equals the tangential bond force $\vec{F}_{ij}^{b,t}$ in eq. A.8.

#### Dissipation

During a collision between two grains a part of the deformational energy dissipates. Hence, every collision force $\vec{F}_c$ predicted at the point of collision experiences damping. For this purpose, a counter directional force $\vec{F}_{c,d}$, which reflects the dissipated energy, is added to $\vec{F}_c$. The energy dissipation is based on the theory proposed by Hertz (1881). The formula for the dissipation force $\vec{F}_{c,n,d}$ in normal direction can be written as follows:

$$\vec{F}_{ij}^{c,n,d} \;=\; c_d \cdot \sqrt{\left(\frac{5}{6} \cdot k_l \cdot m_{ij}\right)} \cdot |v_{ij}^n| \cdot \vec{n}_{ij} \tag{3.47}$$

where $k_l$ stands for the loading stiffness, $m_{ij}$ is the reduce mass, $c_d$ is the dissipation coefficient and $v_{ij}^n$ is the normal velocity at the point of contact. The dissipation coefficient is derived by Tsuji et al. (1993) and is determined as follows:

$$c_d \;=\; \frac{2 \cdot \ln e_d}{\sqrt{\pi^2 + (\ln e_d)^2}} \tag{3.48}$$

where $e_d$ is a coefficient of restitution. It has to be noted that the coefficient of restitution $e_d$ in eq. 3.48 is not related to the restitution of ice mentioned earlier. The restitution coefficient $e_d$ is defined as the ratio between the impact and the rebound velocity, i.e. $e_d = \frac{v_i}{v_0}$. Thereby, the coefficient $e_d$ controls the amount of energy that dissipates generally during any collision. In this study, a coefficient of restitution $e_d$ of 0.95 is used. This results in a lost of approximately 10% of the kinetic energy during a collision. The dissipation during a collision can have several sources which are not entirely clarified at this point. A dissipation of $\approx 10\%$ showed to be a reasonable size to assume within the DEM predictions of this study.

### 3.4.3 Bond Deformation

#### Bonding Properties

The forces and torques developed due to the deformation of a bond between adjoining grains are estimated based on the bonding properties of the current bonding configuration. Those properties are the temporal and geometrical properties of a bond and its state of deformation.
The life time of a bond $t_b$ can be estimated using the number of time step $i_b$, at which the bond is intact, as follows:

$$t_b \;=\; i_b \cdot \Delta t \;=\; t_f^b - t_0^b \tag{3.49}$$

where $t_f^b$ describes the time of fracture of a bond, which can be calculated together with the time of creation $t_0^b$ as follows: $t_f^b = i_b \cdot \Delta t + t_0^b$
A bond can be either defined as an initial condition of a simulation or is generated at first contact between two grains. A bond is represented by a cylindrical geometry of the length $L_b$ and the radius $r_b$, as shown in fig. 3.20. The cylindrical bond geometry is an

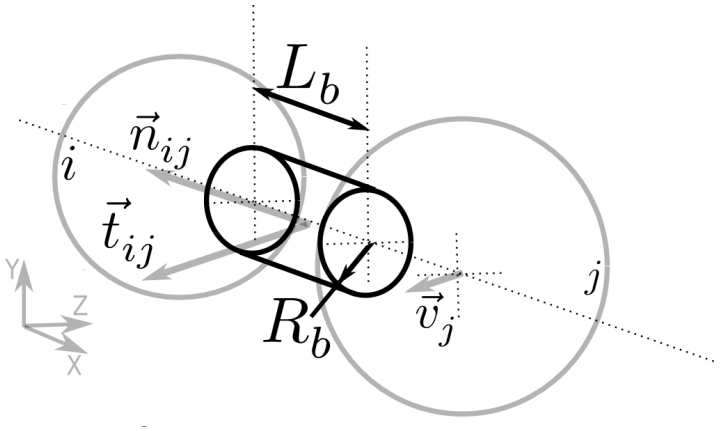


*Figure 3.20: Bonding geometry and configuration*

approximation of a natural bond between snow grains which can have a very complex shape.
The bond properties are described in the local contact frame. The local contact frame is defined by the normal $\vec{n}_{ij}$ and tangential $\vec{t}_{ij}$ unit vector at the contact point $\vec{x^c}_{ij}$. Further, the center of a bond is always positioned at the center between the adjoining grains. Therefore, the bond center $\vec{x}_b$ equals the point of contact $\vec{x}_{ij}^c$ which is estimated by eq. 3.30. As depicted in fig. 3.20, the length of a bond $L_b$ is aligned with the normal direction. Hence, the cross section perpendicular to the normal direction of a bond is denoted as the area of a bond $A_b = \pi \cdot r_b$.
In this study, the following four displacements define the state of deformation of a bond:

1. Deformation along the normal direction by the normal displacement $du_n$
2. Shearing along the tangential direction by the tangential displacement $du_t$
3. Torsion about the normal direction by the relative angular displacement $d\phi_n$
4. Bending by the relative angular displacement $d\phi_b$ around the bending axis $\vec{b}_{ij}$ perpendicular to the bond normal

The normal and tangential displacement of a bond are depicted in fig. 3.21a and 3.21b, respectively. Further, the bending and torsional displacement of a bond are depicted in fig. 3.22a and 3.22b, respectively. The relative angular velocity of two adjoining particles can be predicted as follows:

$$\vec{\omega}_{ij} = (\vec{\omega}_i - \vec{\omega}_j) \tag{3.50}$$

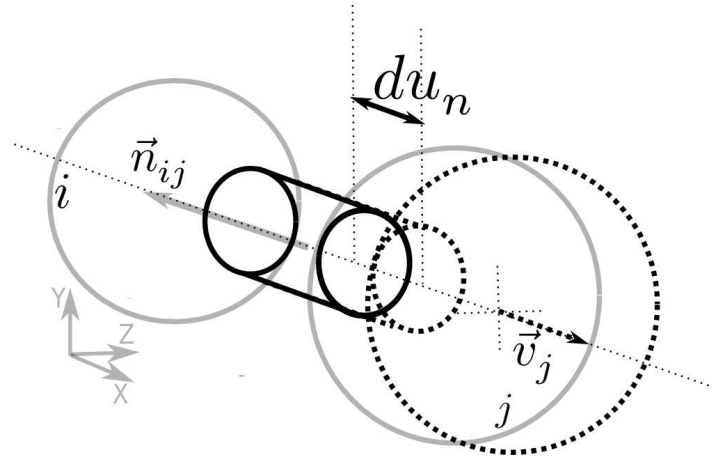


*(a) Tension deformation of a bond in normal direction.*

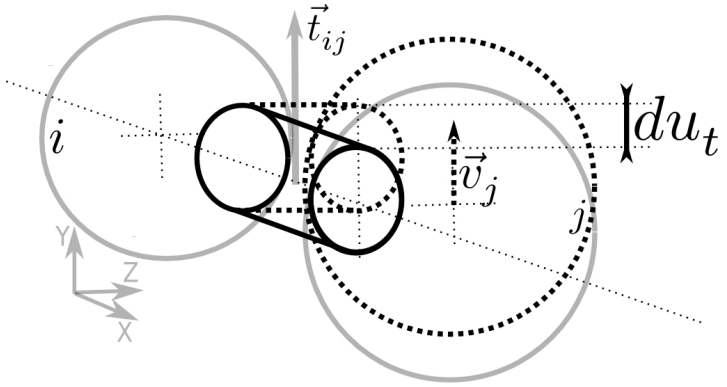


*(b) Shear deformation in tangential direction.*

*Figure 3.21: Bond stretch and shearing.*

where $\vec{\omega}_i$ and $\vec{\omega}_j$ are the angular velocity of the adjoining particles in space-fixed coordinates. Using the relative angular velocity, the bending axis can be estimated as follows:

$$\vec{b}_{ij} = \frac{\vec{\omega}_{ij}}{|\vec{\omega}_{ij}|} - \vec{n}_{ij} \tag{3.51}$$

While the torsional displacement is acting about the normal axis, the bending displacement takes place about the bending axis. The bending axis is the difference between the resultant angular direction and the normal direction. The two angular displacements of a bond are depicted in fig. 3.22. Hence in this study, the relative displacement vector $\vec{du}_{ij}$ of a bond contains the following four components:

$$\vec{du}_{ij} = \begin{pmatrix} du^n_{ij} \\ du^t_{ij} \\ d\phi^n_{ij} \\ d\phi^b_{ij} \end{pmatrix} = \Delta t \cdot \begin{pmatrix} \vec{v}_{ij} \cdot \vec{n}_{ij} \\ \vec{v}_{ij} \cdot \vec{t}_{ij} \\ \vec{\omega}_{ij} \cdot \vec{n}_{ij} \\ \vec{\omega}_{ij} \cdot \vec{b}_{ij} \end{pmatrix} \tag{3.52}$$

where $\vec{v}_{ij}$ is the relative velocity and $\vec{\omega}_{ij}$ is the relative angular velocity which are predicted

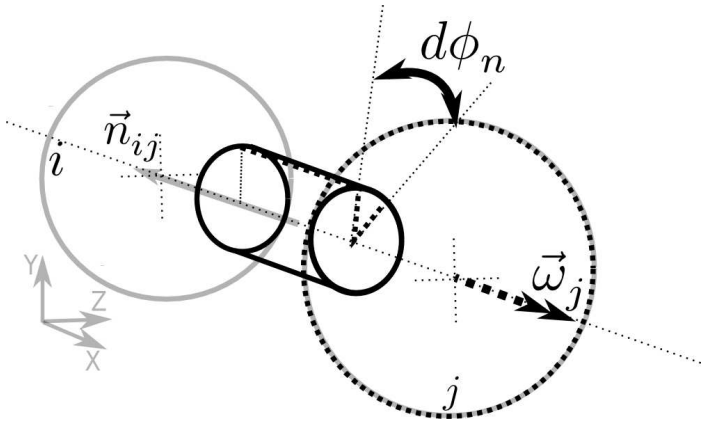


*(a) Torsion of a bond around normal direction.*

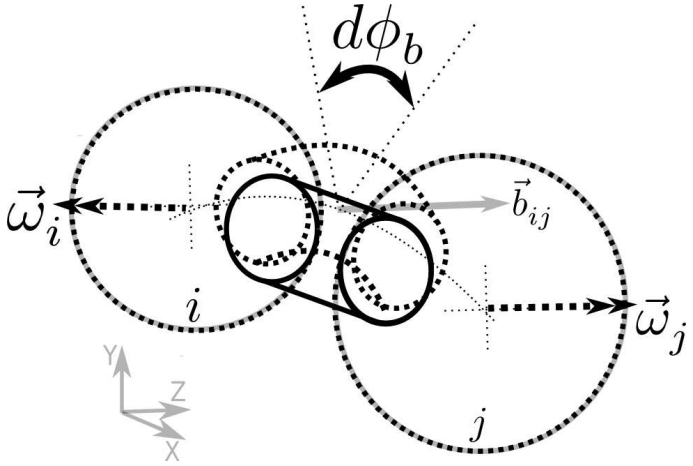


*(b) Bending deformation perpendicular to bond normal.*

*Figure 3.22: Torsion and bending of bond.*

by eq. 3.16 and eq. 3.50, respectively. Within eq. 3.52 each displacement describes the incremental displacement at the current time step. A homogeneous stress and strain state is assumed to develop over the length of the cylindrical bond. The displacement vector $\vec{du}_{ij}$ and the characteristic length $L_b$ are used to estimate the four strain components, i.e. $\varepsilon^n_{ij}$, $\varepsilon^t_{ij}$, $\gamma^n_{ij}$ and $\gamma^b_{ij}$, as follows:

$$\vec{\varepsilon}_{ij} = \begin{pmatrix} \varepsilon^n_{ij} \\ \varepsilon^t_{ij} \\ \gamma^n_{ij} \\ \gamma^b_{ij} \end{pmatrix} = \frac{1}{L_b} \cdot \begin{pmatrix} du^n_{ij} \\ du^t_{ij} \\ d\phi^n_{ij} \\ d\phi^b_{ij} \end{pmatrix} \tag{3.53}$$

The displacements are estimated between the previous and the current step. Thus, the strain components are the incremental strain components of the current time step.
The stress inside a bond is assumed to develop homogeneously. Each of the four resultant

stress components is a function of the according strain component which can be written:

$$\vec{\sigma}_{ij} = \begin{pmatrix} \sigma_{ij}^{n}\left(\varepsilon_{ij}^{n}\right) \\ \sigma_{ij}^{t}\left(\varepsilon_{ij}^{t}\right) \\ \tau_{ij}^{n}\left(\gamma_{ij}^{n}\right) \\ \tau_{ij}^{b}\left(\gamma_{ij}^{b}\right) \end{pmatrix} \tag{3.54}$$

Each stress component is thereby predicted individually. The finally multiplication of the stress components and the bond area results in two bond forces and two torques. The bond forces are a force $\vec{F}_{ij}^{b,n}$ in normal direction and a second forces $\vec{F}_{ij}^{b,t}$ in tangential direction. The resultant bond torques are a torque $\vec{M}_{ij}^{b,n}$ due to torsion about the normal direction and a second torque $\vec{M}_{ij}^{b,b}$ resulting from bending of the bond.

### Elastic Viscous-Plastic Model

This bond model describes the deformations of a bond between two adjoining snow grains based on an elastic viscous-plastic material law. The elastic part is arranged in series to the parallel arranged viscous-plastic element which is depicted in fig. 3.23. The elastic

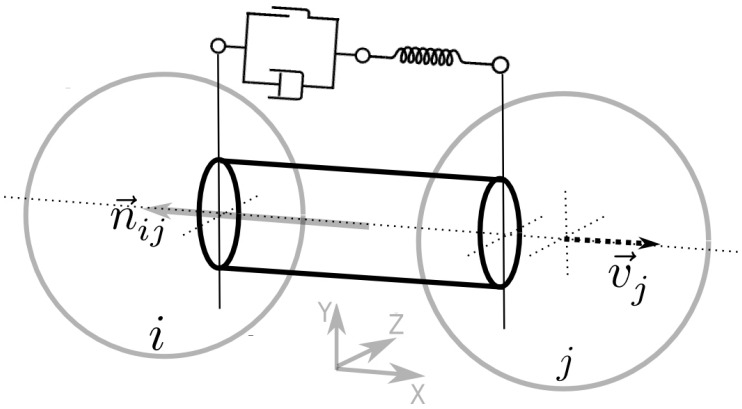


*Figure 3.23: Schematic representation of the elastic viscous-plastic material behaviour of a bond*

properties, provided in table 3.1 by Gammon et al. (1983), are used to relate the strain to the stress state of the bond. The viscous-plastic part of the deformation is accounted for by the creep relation of ice. In this model the creep rate is estimated by eq. 3.2. Furthermore, the model includes a law for the bond growth derived from the observations of Szabo and Schneebeli (2007) which are also employed for validation. The bond growth relation allows to predict the creep expansion of a bond under compression. In addition, the model also includes a temperature-dependent relation for the rupture of a bond derived by Schulson (1990).

In the described configuration of the elastic viscous-plastic model, under any applied axial stress, the total stress $\sigma_t$ and the total strain $\varepsilon_t$ can be defined as follows:

$$\sigma_t \;=\; \sigma_e \;=\; \sigma_{vp} \qquad \text{and} \qquad \varepsilon_t \;=\; \varepsilon_e + \varepsilon_{vp} \tag{3.55}$$

where the subscript $vp$ indicates the viscous-plastic element which is assembled by a damper and a friction slider element in fig. 3.23. The subscript $e$ indicates the elastic spring element. As previously mentioned, such a material law is also known as a Bingham-Maxwell or the Bingham-Norton model. For such a material law the elastic and viscous-plastic stress are equal. Thus, the prediction of the resultant elastic stress part is enough to estimate the resultant forces and torques generated during deformation of the bond. Therefore, the strain relation in eq. 3.55 can be re-writing as follows:

$$\varepsilon_e \;=\; \varepsilon_t - \varepsilon_{vp} \;=\; \varepsilon_t - \dot{\varepsilon}_{ind} \cdot \Delta t \tag{3.56}$$

to predict the elastic strain $\varepsilon_e$. The viscous-plastic part of the bond strain $\varepsilon_{vp} \;=\; \dot{\varepsilon}_{ind} \cdot \Delta t$ is estimated by the creep law of eq. 3.2. Applying eq. 3.56 to the strain vector in eq. 3.53, the elastic strain components are estimated as follows:

$$\vec{\varepsilon^e}_{ij} \;=\; \begin{pmatrix} \varepsilon^{n,e}_{ij}(t) \\ \varepsilon^{t,e}_{ij}(t) \\ \gamma^{n,e}_{ij}(t) \\ \gamma^{b,e}_{ij}(t) \end{pmatrix} \;=\; \sum_{i=1}^{i_b} \begin{pmatrix} \varepsilon^{n}_{ij}(t) - \dot{\varepsilon}_{ind}\left(\sigma^{n}_{ij}(t-\Delta t), T\right) \cdot \Delta t \\ \varepsilon^{t}_{ij}(t) - \dot{\varepsilon}_{ind}\left(\sigma^{t}_{ij}(t-\Delta t), T\right) \cdot \Delta t \\ \gamma^{n}_{ij}(t) - \dot{\varepsilon}_{ind}\left(\tau^{n}_{ij}(t-\Delta t), T\right) \cdot \Delta t \\ \gamma^{b}_{ij}(t) - \dot{\varepsilon}_{ind}\left(\tau^{b}_{ij}(t-\Delta t), T\right) \cdot \Delta t \end{pmatrix} \tag{3.57}$$

$$\text{with} \quad t \;=\; t^b_0 + i \cdot \Delta t$$

where the elastic strain $\vec{\varepsilon^e}_{ij}$ is the sum of total strain $\vec{\varepsilon}_{ij}$ minus the viscous-plastic strain $\vec{\varepsilon^{vp}}_{ij}$ over the bonding time. In eq. 3.57, the viscous-plastic strain $\vec{\varepsilon^{vp}}_{ij}$ is a function of the previous stress state $\vec{\sigma}_{ij}(t-\Delta t)$ and the ambient temperature $T$. As the total stress $\sigma_{ij}$ equals the elastic stress part $\sigma^e_{ij}$, the elastic parameters are used to predict the total stress acting in a bond as follows:

$$\vec{\sigma}_{ij} \;=\; \begin{pmatrix} \sigma^n_{ij} \\ \sigma^t_{ij} \\ \tau^n_{ij} \\ \tau^b_{ij} \end{pmatrix} \;=\; \frac{E}{(1+\nu)(1-2\nu)} \cdot \begin{pmatrix} (1-\nu) & \cdot & \varepsilon^n_{ij} \\ 2\cdot(1-2\nu) & \cdot & \varepsilon^t_{ij} \\ (1-2\nu) & \cdot & \gamma^n_{ij} \\ (1+\nu)(1-2\nu) & \cdot & \gamma^b_{ij} \end{pmatrix} \tag{3.58}$$

where $\sigma^n_{ij}$ describes the stress developing due to tension or compression. $\sigma^t_{ij}$ is the stress component due to shear, $\tau^n_{ij}$ denotes the stress component due torsion and $\tau^b_{ij}$ describes the bending stress of the ice bond between the adjoining grains $i$ and $j$. The Young's modulus $E \;=\; f(T)$ and the Poisson's ratio $\nu \;=\; f(T)$ are the elastic parameters by Gammon et al. (1983) shown in table 3.1. The temperature dependence of the elastic parameters is accounted by the linear approximation by Gammon et al. (1983). The resultant bond force $\vec{F}^b_{ij}$ and moment $\vec{M}^b_{ij}$ are estimated from the stress state at the current time step. Multiplying the bond area $A_b$ and the normal stress component $\sigma^n_{ij}$, the bond forces $\vec{F}^{b,n}_{ij}$ results as follows:

$$\vec{F}^{b,n}_{ij} \;=\; \sigma^n_{ij} \cdot \vec{n}_{ij} \cdot A^b_{ij}(t) \tag{3.59}$$

The force $\vec{F}_{ij}^{b,n}$ is acting in normal direction on the adjoining grains $i$ and $j$ due to tension and compression experienced by the bond. The bond force $\vec{F}_{ij}^{b,t}$ resulting from the shear stress $\sigma_{ij}^{t}$ times the bond area can be written as:

$$\vec{F}_{ij}^{b,t} = \sigma_{ij}^{t} \cdot \vec{t}_{ij} \cdot A_{ij}^{b}(t) \tag{3.60}$$

The shear force $\vec{F}_{ij}^{b,t}$ acts in tangential direction on $i$ and $j$ due to the shearing of the bond. The torsion of a bond generates the torque $\vec{M}_{ij}^{b,n}$ about the normal direction $\vec{n}_{ij}$ which can be written as follows:

$$\vec{M}_{ij}^{b,n} = \tau_{ij}^{n} \cdot \vec{n}_{ij} \cdot A_{ij}^{b}(t) \tag{3.61}$$

where $\tau_{ij}^{n}$ describes the shear stress due to torsion and $A_{ij}^{b}$ is the current bond area. The bending stress $\tau_{ij}^{b}$ multiplied by the bond area results in the second torque $\vec{M}_{ij}^{b,b}$ as follows:

$$\vec{M}_{ij}^{b,b} = \tau_{ij}^{b} \cdot \vec{b}_{ij} \cdot A_{ij}^{b}(t) \tag{3.62}$$

where $\vec{b}_{ij}$ is the bending axis predicted by eq. 3.51.
Along with the predictions of the bond forces and torques the bond area is predicted at each time step. The current bond area $A_{ij}^{b}(t) = f\left(\sigma_{ij}^{n}(t_m - \Delta t), T\right)$ is a function of the previous normal stress $\sigma_{ij}^{n}(t-\Delta t)$ and the ambient temperature $T$ and is predicted by the following equation:

$$A_{ij}^{b}(t) = \pi \cdot \left( {R_{ij}}^2 - \left( \sqrt{{R_{ij}}^2 - r_{ij}^{b}(t-\Delta t)^2} - \dot{\varepsilon}_{ind}\left(\sigma_{ij}^{n}(t-\Delta t), T\right) \cdot L_b \cdot \Delta t \right)^2 \right) \tag{3.63}$$

where $R_{ij}$ is the effective radius, $r_{ij}^{b}(t-\Delta t)$ is the previous bond radius, $\dot{\varepsilon}_{ind}$ is the creep rate and $L_b$ is the length of the bond. Eq. 3.63 is based on the sintering model of ice grains by Szabo and Schneebeli (2007). The relation is used to predict the current bond area before the force and torque prediction. The bond growth model of eq. 3.63 predicts the expansion or shrinking of the bond area due to compression or tension stress acting inside the bond. In fig. 3.24 the growth of the bond area is depicted in dependence to contact time and contact load. The predictions and measurements in fig. 3.24 describe the growth of a bond between two spherical ice grains of 3 mm radius. The grains are pressed together in normal direction at different temperatures, for different periods of time and by different forces. The measurements in fig. 3.24 indicate an immediate bond creation at the point of contact. This is apparent as the bond area size does not decrease beneath a certain value. This initial size of the bond area correlates with the contact area produced by the elastic deformation of the ice grains at initial collision. Hence, the initial bond area can be predicted according to the Hertzian contact theory. Hertz (1881) analysed the stress in the contact area of two elastic bodies. According to Hertzian theory, if two elastic bodies collide on their central line by a force $F_{ij}^{c,n}$, the radius of the contact area can be estimated as follows:

$$r_{ij}^{b} = \left( \frac{3 \cdot \left| \vec{F}_{ij}^{c,n} \right| \cdot R_{ij}}{4 \cdot E_{ij}} \right)^{1/3} \tag{3.64}$$

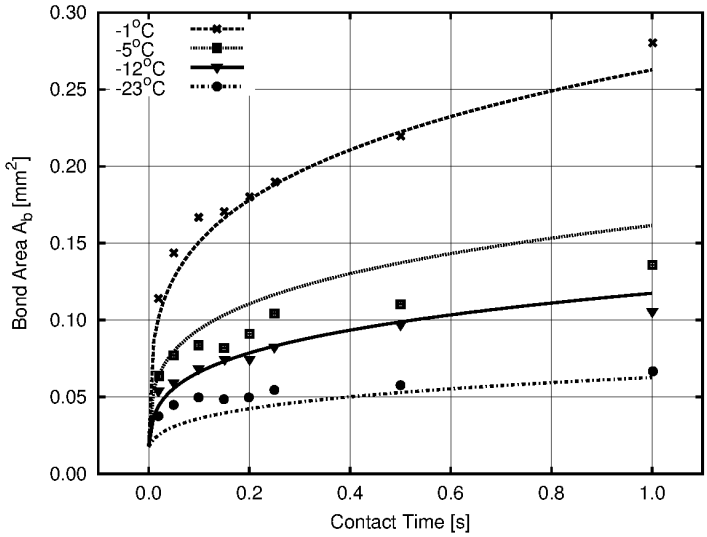


*(a) Bond growth over contact time under the constant loading of* 2 N.

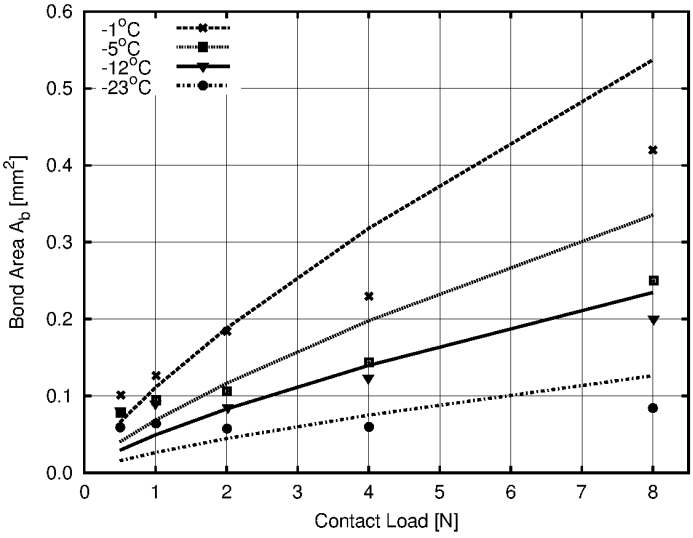


*(b) Load dependence of the growth of the bond area after* 0.25 s *compression.*

*Figure 3.24: Growth of a bond between two spherical ice grains of* 3 mm *radius due to compressive load at four different temperature* $(-1, -5, -12, -23\ ^\circ\mathrm{C})$*. The lines are the values predicted by eq. 3.63 and the symbols are measurements by Szabo and Schneebeli (2007).*

where $E_{ij}$ is the effective Young's modulus and $R_{ij}$ describes the effective radius of curvature. For the evolution of an ensemble of snow grains, every new collision instantaneously establishes a new bond between the colliding grains. Hence, the initial bond area $A^b_{ij}(t^b_0) = \pi \cdot r^b_{ij}(t^b_0)$ is estimated by eq. 3.64.
Further, this model accounts for the fracture of a bond. A bond ruptures as soon as one of the stress components reaches the strength limit of ice. These employed strength limits are derived from the observations by Schulson (1990). His investigations provide

detailed insights into the compressive and tensile strength of ice. His observations reveal the dependencies on the temperature, strain rate and grain size of a loaded ice sample for ductile and brittle behaviour.
The measurements of Schulson (1990) show the constancy of the tensile strength against all the mentioned dependencies. Thus, the tensile strength of ice can be assumed constant for brittle and ductile loading rates. The tensile strength $\sigma_{ts}$ of an ice bond is $1.1 \cdot 10^6$ Pa as shown in fig. 2.13.
During ductile loading the compression strength $\sigma_{dcs}$ of a bond is accounted by the creep law 3.57 intrinsically. This approximation is validated in section 6.1.2.
However, the brittle failure of a bond under rapid loading, i.e. above the rate of $10^{-3}$ $s^{-1}$, is accounted for by the brittle compression strength $\sigma_{bcs}$. The brittle compression strength is approximated as follows:

$$-\sigma_{bcs} = 10 \text{ MPa} - \frac{3}{8}\left(\frac{T}{^\circ\text{C}}\right) \tag{3.65}$$

Eq. 3.65 is an empirical formulation of the brittle compression strength derived from the observation of Schulson (1990). Schulson (1990) and Petrenko and Whitworth (1999) showed an increase of the brittle compression strength of ice by a factor of 2.5 with decreasing temperature from −10 °C to −50 °C. From the grain size and strain rate dependency published by Schulson (2001) a brittle compression strength of 10 MPa can be assumed for 0 °C and a grain size of 1 mm at the transition rate $10^{-3}$/ s. Eq. 3.65 provides the brittle failure limit in MPa in dependence of the temperature $T$ in degree Celsius °C.
By means of the derived strength limits, the failure or survival of a bond during loading of a snow sample is estimated at each time step as follows:

$$\left.\begin{aligned} -\sigma_{bcs} \;&\geq\; \sigma^n_{ij} \;\geq\; \sigma_{ts} \\ \left|\sigma^t_{ij}\right| \;&\geq\; \tfrac{1}{3}\cdot\sigma_{bcs} \\ \left|\tau^n_{ij}\right| \;&\geq\; \tfrac{1}{3}\cdot\sigma_{bcs} \\ \left|\tau^b_{ij}\right| \;&\geq\; \tfrac{1}{3}\cdot\sigma_{bcs} \end{aligned}\right\} = \textit{Bond Failure} \tag{3.66}$$

The tensile stress is thereby defined to be positive and compression negative. Hence, a bond fails when the normal stress $\sigma^n_{ij}$ reaches the tensile strength $-\sigma_{ts}$ or below the brittle compression strength $\sigma_{bcs}$. A bond also fails if the magnitude of any of the three shear components $\sigma^t_{ij}$, $\tau^n_{ij}$ or $\tau^b_{ij}$ equals or exceeds one third of the brittle compression strength $\sigma_{bcs}$. Thus, a new bond between the according grains $i$ and $j$ can only be formed by a new contact.

### Dissipation

Along with the forces and torques generated during bond deformation dissipative forces $\vec{F}_{b,d}$ and torques $\vec{M}_{b,d}$ are employed. During a bond deformation between two adjoining

grains, portions of the deformational energy dissipates. In this study, every bond force $\vec{F}_b$ and torque $\vec{M}_b$ generated by a deformed bond experiences dissipation.
Therefore, the counter directional forces $\vec{F}_{b,n,d}$ and $\vec{F}_{b,t,d}$ which reflect the dissipated energy are added to the resultant bond forces $\vec{F}_{b,n}$ and $\vec{F}_{b,t}$, respectively, as follows:

$$\begin{aligned} \vec{F}_{ij}^{b,n,d} &= \sqrt{m_{ij} \cdot k_{ij}^{b,n}} \cdot |du_{ij}^{n}| \cdot \Delta t^{-1} \cdot \vec{n}_{ij} \\ \vec{F}_{ij}^{b,t,d} &= \sqrt{m_{ij} \cdot k_{ij}^{b,t}} \cdot |du_{ij}^{t}| \cdot \Delta t^{-1} \cdot \vec{t}_{ij} \end{aligned} \tag{3.67}$$

where $m_{ij}$ is the reduced mass, $k_{ij}$ describes the stiffness, $\vec{F}_{ij}^{b,n,d}$ is the dissipation in normal direction, $\vec{F}_{ij}^{b,n,d}$ is the shear force and $d\vec{u}_{ij}/dt$ are the according displacement rates of the bond. The normal and shear stiffness of the bond is thereby predicted as follows:

$$\begin{pmatrix} k_{ij}^{b,n} \\ k_{ij}^{b,t} \end{pmatrix} = \begin{pmatrix} \frac{E}{(1-\nu^2)} \sqrt{R_{ij} \cdot |\varepsilon_{ij}^{n}| \cdot r_{ij}^{b}} \\ \cdot \frac{4E}{2(1+\nu)\cdot(2-\nu)} \cdot \sqrt{R_{ij} \cdot |\varepsilon_{ij}^{t}| \cdot r_{ij}^{b}} \end{pmatrix} \tag{3.68}$$

Further, the counter rotational torques $\vec{M}_{b,n,d}$ and $\vec{M}_{b,b,d}$ are added to the torques due to torsion and bending, respectively, and can be written as follows:

$$\begin{aligned} \vec{M}_{ij}^{b,n,d} &= \tfrac{1}{4} \left(r_{ij}^{b}\right)^2 \cdot \sqrt{m_{ij} \cdot \theta_{ij}^{b,n}} \cdot |d\phi_{ij}^{n}| \cdot \Delta t^{-1} \cdot \vec{n}_{ij} \\ \vec{M}_{ij}^{b,b,d} &= \tfrac{1}{4} \left(r_{ij}^{b}\right)^2 \cdot \sqrt{m_{ij} \cdot \theta_{ij}^{b,b}} \cdot |d\phi_{ij}^{b}| \cdot \Delta t^{-1} \cdot \vec{b}_{ij} \end{aligned} \tag{3.69}$$

where $r_{ij}^{b}$ denotes the bond radius, $\theta_{ij}$ is the rotational stiffness, $\vec{M}_{ij}^{b,n,d}$ is the dissipation of the torsional deformation, $\vec{M}_{ij}^{b,b,d}$ dissipates during bending and $d\vec{\phi}_{ij}/dt$ are the according displacement rates of the bond. The rotational stiffness es used for torsion and bending dissipation are predicted as follows:

$$\begin{pmatrix} \theta_{ij}^{b,n} \\ \theta_{ij}^{b,b} \end{pmatrix} = \begin{pmatrix} \frac{4E}{2(1+\nu)\cdot(2-\nu)} \cdot \sqrt{R_{ij} \cdot |\gamma_{ij}^{n}| \cdot r_{ij}^{b}} \\ \frac{E}{(1-\nu^2)} \cdot \sqrt{R_{ij} \cdot |\gamma_{ij}^{b}| \cdot r_{ij}^{b}} \end{pmatrix} \tag{3.70}$$

A similar approach for the bond dissipation has been used by Brendel et al. (2006). In eq. 3.67 and 3.69, $\sqrt{m_{ij} \cdot k_{ij}}$ describes the critical damping. The critical damping can be used because deformations are slow which makes details of the dissipation irrelevant. Slow deformations have to fulfil the following condition:

$$v = \frac{{r_b}^2 \cdot \sigma_s}{\sqrt{m \cdot k}} \tag{3.71}$$

where $v$ is the deformation induced velocity and $\sigma_s$ is the strength limit.

## 3.5 Creation of Snow Samples

Snow can be described as an open foam structure assembled by ice grains and bonds. The snow forming processes take place over hours and up to months as described in detail in

chapter 2.1.1. The sintering processes inside the ice matrix and pore space of snow define the grain and bond size of a specimen. Those metamorphic processes can change the grain-scale properties dramatically. But it is not in the interest of this study to investigate the history of a snow sample. The current conditions of a snow sample will be prepared before the deformational process is simulated. This section describes the initiation of size and distribution of the snow grains and the adjoining bonds. As the size of a snow grain ranges from 0.125 mm to 8 mm it is clear that the RVE of snow is not a material constant. Hagenmuller (2011) predicted the RVE for different snow types in dependence of the strength as presented in fig. 2.39.
The tests run within this study showed that a number of thousand grains and above are more than sufficient to reproduce identical simulation results.

### 3.5.1 Preparation of Snow Samples

This section describes the generation of the initial positioning of snow grains, i.e. particles, within a prepared sample.

#### Gravitational Deposition Method

The most natural way to obtain an virtual snow sample is to rain snow grains into a fixed form. Then, the snow grains are allowed to settle until the disappearance of all kinetic energy, i.e. transformation into potential energy. This method is generally called the gravitational deposition method. A predefined container volume is filled from above with particles. Layer after layer is produced and deposited into the containing volume under gravity as depict in fig. 3.25. The particles are generated randomly on an predefined inlet plane with the size distribution described in section 3.5.2.
With this method, snow samples of density about 500 kg/m$^3$ to 600 kg/m$^3$ can be reached by disabling the bonding between colliding grains. If bonding is enabled very low density samples of almost 200 kg/m$^3$ can be generated. Another way to generate samples of lower densities is by ending the settled grain structure. Thereby, particles inside a prepared specimen with a low coordination number are erased. However, to gain specimens of higher densities the grain structure can be compacted, i.e. loaded, by confining walls until the aimed density is reached.

### 3.5.2 Grain Size Distribution

As discussed in section 2.1.1, the bandwidth of the grain size distribution of snow is quite narrow compared to other common granular materials. Fig. 3.26 compares the size distribution of snow grains to the one of moraine and cement grains. In this study, the size generation of a snow grains is based on a linear distribution function $D(r_g)$ which can be written as follows:

$$D(r_g) = \frac{1}{r_{max} - r_{min}} \cdot (r_g - r_{min}) \qquad \text{for} \quad r_{min} \leq r_g \leq r_{max} \tag{3.72}$$

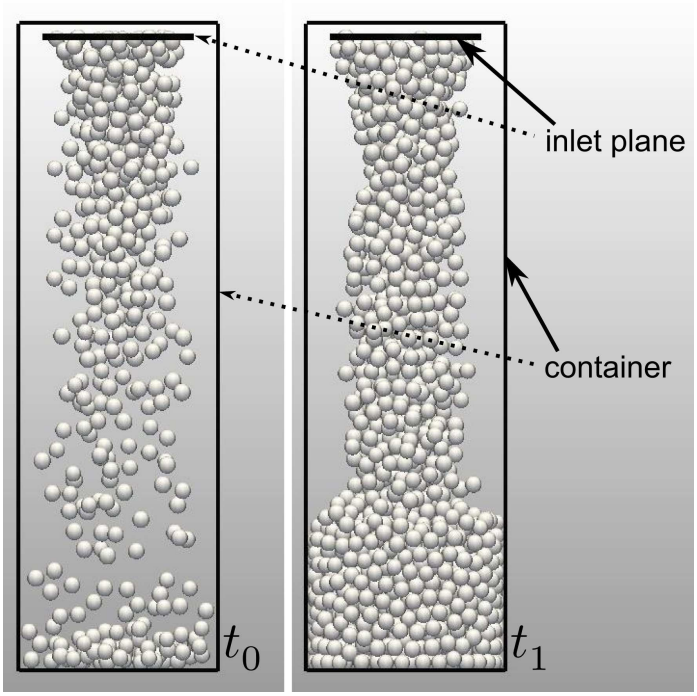


*Figure 3.25: Example of filling by gravitational deposition method.*

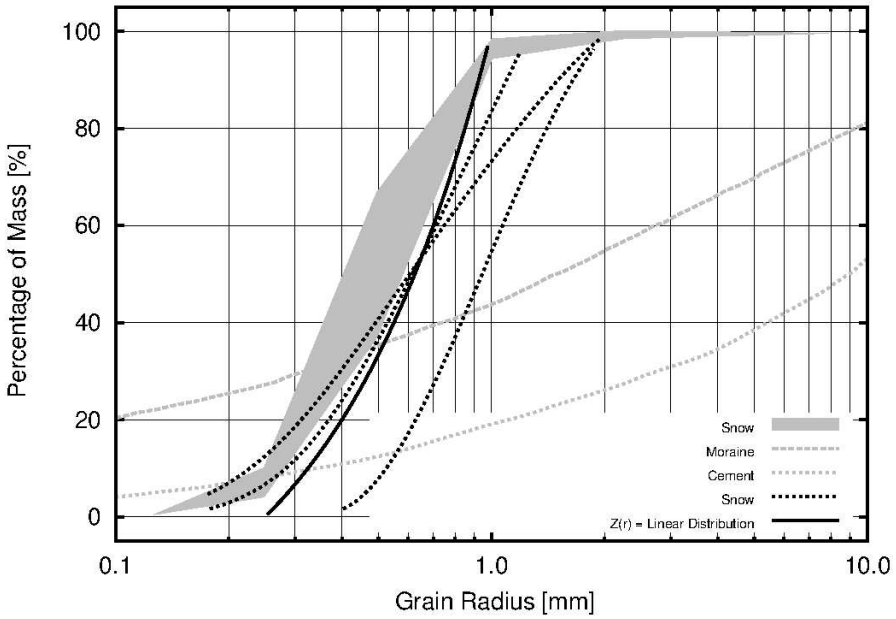


*Figure 3.26: Sieve curves of snow, moraine and cement grains. The grey band corresponds to sieve curves measured by Von Moos et al. (2003), the dotted black lines by Fukue (1977) and the solid black line equals eq. 3.75.*

where $r_g$ describes the grain radius and $r_{min}$ and $r_{max}$ are the minimum and maximum grain radii, respectively. The probability density function $P(r_g)$ is defined as the derivative of the distribution function $D(r_g)$ and thus can be written as follows:

$$P(r_g) = \frac{1}{r_{max} - r_{min}} \qquad \text{for} \quad r_{min} \leq r_g \leq r_{max} \tag{3.73}$$

Both functions are depicted in fig. 3.27 and are defined by the two parameters $r_{min}$ and $r_{max}$. The probability density is thereby described by a rectangular functions. Hence, for

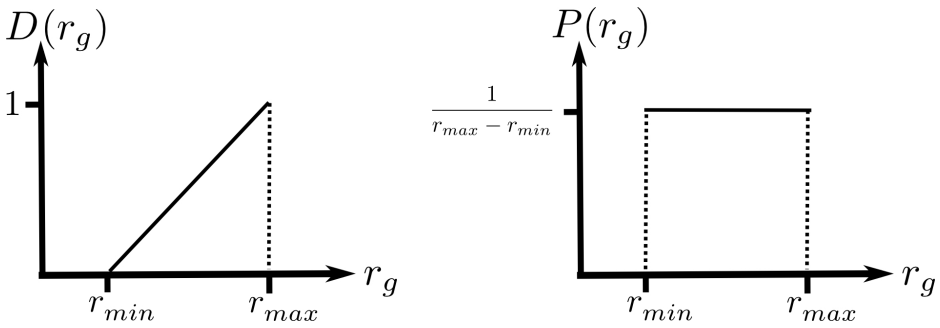


*Figure 3.27: Cumulative distribution $D(r_g)$ and probability density function $P(r_g)$ .*

this probability density the actual distribution of the grain radius $r_g$ is predicted as follows:

$$r_g = r_{min} + (r_{max} - r_{min}) \cdot \widetilde{x} \qquad \text{with} \quad \widetilde{x} = random(0...1) \tag{3.74}$$

where $\widetilde{x}$ is computed by a random generator. The black line in fig. 3.26 is the corresponding sieve curve of the grain size distribution for $r_{min} = 0.25$ mm and $r_{max} = 1$ mm. The sieve curve can be predicted by integration of the distribution function $D(r_g)$ in the following way:

$$Z(r_g) = \frac{\text{weight of grains} \leq r_g}{\text{weight of all grains}} = \frac{W_g(r_g)}{W_g(r_{max})} \quad \text{with} \quad W_g(x) = \int_{r_{min}}^{x} D(r_g)\, dr_g \tag{3.75}$$

### 3.5.3 Initiation of Bond Structure

As mentioned, if snow grains collide newly the bond radius $r_b$ is predicted by eq. 3.64. But the bond radius $r_b$ and the entire bond structure, defined by the coordination number $N_b$, are also established before the time integration.
The coordination number $N_b$ of a snow sample is predicted as follows:

$$N_b = \frac{1}{N_g} \cdot \sum_{i=1}^{N_g} N_i^b \tag{3.76}$$

where $N_i^b$ is the number of bonds of the grain $i$.
The initial generation of the bond structure is established in accordance to the pre-defined coordination number $N_b$. The desired coordination number $N_b$, i.e. bond structure, is

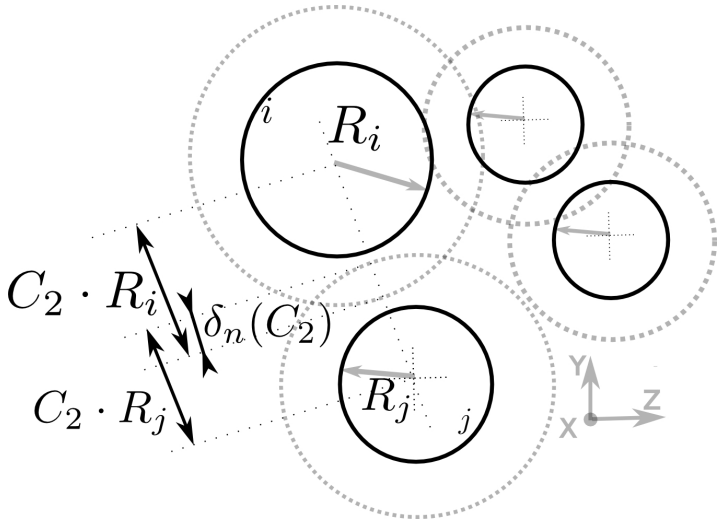


*Figure 3.28: Generation of bonds by the pre-defined factor $C_2$.*

established by means of the scale factor $C_2$ as shown fig. 3.28. If two scaled grain radii overlap by the normal overlap $\delta_n(C_2)$ a bond is generated between the adjoining grains as follows:

$$if \quad \delta_n(C_2) \geq 0 \Rightarrow \textit{Bond Generation with} \Rightarrow r_{ij}^b = C_1 \cdot r_{ij} \tag{3.77}$$

where $C_1$ is the predefined size ratio of $\frac{r_b}{r_g}$.
While pre-processing, the scale factor $C_2$ is iteratively modified and the initial bond structure re-computing until the desired coordination number $N_b$ is reached.

## 3.6 Complex Boundary Shapes

To account for complex geometries, e.g. a tire tread during the interaction with snow grains, the geometry of any surface is represented as a polygonal mesh. The polygonal mesh is thereby an ensemble of vertices, edges and faces that approximate the shape of a polyhedral object. The faces are described by linear triangles as depicted for a double sinus surface in fig. 3.29. The triangulated surface provides a high flexibility in describing any complex geometry.
These face - vertex meshes are implemented as a list of faces and a list of vertices. This is the most common mesh representation and is used as typical input in modern computer graphics. This storing method of meshes allows an explicit look-up of the vertices of a face and the faces surrounding a vertex.
Each triangle of such a surface is handled individually during contact with particles or during translation and rotation of the surface.
Hence, in difference to single triangle the compound is now moving in relation to the center point of the surface. The surface owns an absolute vector pointing to its center of mass and relative vectors pointing to each center of a surface triangle.

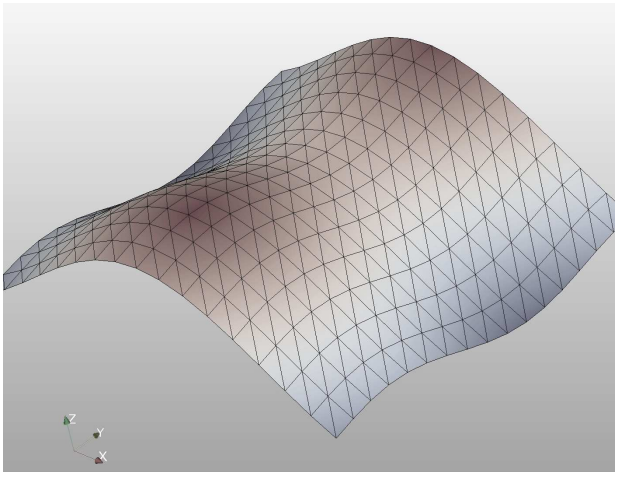

*Figure 3.29: Polygonal mesh of sinus surface by triangular elements.*

In case of contact with particles, the contact between a spherical sub-shape of a particle and a surface triangle is predicted individually. In this contact situation, the deformations between two colliding objects are modeled by means of a representative overlap $\delta$ between the particle and the surface triangle. Hence, the developing collision forces are deriving from the overlap geometry, material properties and kinematic quantities of the colliding objects.
The exact prediction of the overlap $\delta_{ij}$ and point of contact $\vec{x^c}_{ij}$ is described in section 5.3 as this approach was developed in the context of the coupling between discrete and finite elements.

# Chapter 4

# Finite Element Method (FEM)

The Finite Element method is a highly practical and common tool used in engineering and research. The amount of problems attacked with this method became as numerous as articles and books in this field. Felippa (2004), Betten (2003) and Bathe (1982) are just a few of a number of respectable works.

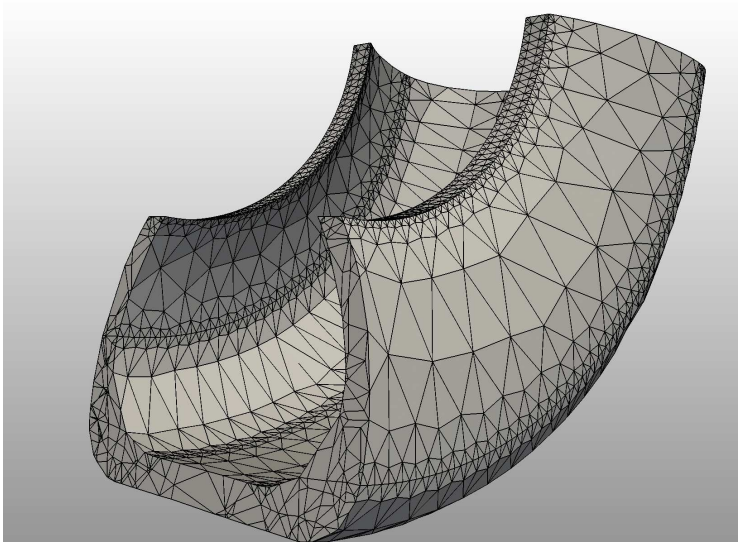

*Figure 4.1: Finite element mesh of a portion of a tire tread.*

The tire treads and tread parts investigated in this study are described as continuous bodies. The displacement or change of the configuration of a continuous body is the sum of motion, i.e. translation and rotation, and the deformation of its shape. Thereby, the deformational part reflects the stress act inside the body. A configuration of a continuum body describes a continuous number of material points occupying a certain amount of space at a particular time. Deformation, i.e. the change of shape or size of the body, equals the change between the initial and the current configuration. The deformation can

thereby be described as the change in distance of two neighbouring material points in the initial and current configuration. To analyse the evolution of deformation of a continuous body it is necessary to describe the change of configurations throughout time.
For this purpose, the finite element method is used to describe the deformation of the continuous bodies, i.e. tire treads and tread parts. Therefore, the method discretized the volume of a body by means of a mesh, as exemplified in fig. 4.1. This mesh is represented by a finite number of nodes spanning a finite number of elements over the body volume. The displacements of the body shape are predicted at the mesh nodes and thus the deformations and stresses are derived over the finite elements.
However, in this study the finite element method is employed for linear elastic deformations. Hence, the investigated tire treads and tread parts are described as linear elastic materials.

## 4.1 Elastic Body Deformation

This section covers the description of a fully time dependent model of elastic deformation with thermal expansion effects. The mathematical model of elastic deformation of solid bodies is also based on Newton's second law, which has already served as the foundation of the discrete element method. Additionally, for the description of deformation a constitutive relation between stress and strain has to be incorporated. Thereafter, the finite element formulation is introduced as a general numerical approach to discretize the derived mathematical models and to solve the established PDE's. The continuum description of elastic deformation by means of finite element method played a key role and was a the biggest success while establishing mathematical modeling and scientific computing into the engineering world.
The deformation of an elastic continua is described by the differential form of Newton's second law of eq. 4.1. [1] Contrary to the discrete approach this equation is valid in every volume point of the continuum.

$$\rho \frac{\partial u_\alpha^2}{\partial t^2} = \frac{\partial \sigma_{\alpha\beta}}{\partial x_\beta} + \rho\, b_\alpha \tag{4.1}$$

Notice within this context $u_\alpha$ describes the displacement where in the discrete form the position $\vec{x}_i$ is placed. The usage of the indicial notation is widespread in solid mechanics. Thus, $\alpha$, $\beta$ and $\gamma$ are indices of the spatial dimensions. In eq. 4.1 $\rho$ is the density, $\sigma_{\alpha\beta}$ reflects the internal forces due to stresses and the final term represents body forces $\vec{b}$. The main interest is usually to study the stress. If the stresses exceed certain limits, the material might rupture or the validity limits of the elastic model are reached and need to be replaced. As the density and body forces are prescribed, six unknowns remain within the symmetric stress tensor by three equations. To yield closure of the system the stresses and deformations are linked by Hooke's generalized thermo-elastic law which can be written as follows:

[1] The Greek indices $\alpha$, $\beta$, $\gamma$ identify the three spatial components of a physical quantity, i.e. $\alpha = (1, 2, 3)$

$$\sigma_{\alpha\beta} = \lambda \frac{\partial u_\gamma}{\partial x_\gamma} \delta_{\alpha\beta} + \mu \left( \frac{\partial u_\alpha}{\partial x_\beta} + \frac{\partial u_\beta}{\partial x_\alpha} \right) - \alpha \, (3\lambda + 2\mu)(T - T_0) \, \delta_{\alpha\beta} \tag{4.2}$$

where $\sigma_{\alpha\beta}$ describes the stresses, $\lambda$ and $\mu$ are the Lame's linear elastic parameter, $\alpha$ the thermal expansion coefficient and $T$ and $T_0$ are current and reference temperature, respectively. In this section $\delta_{\alpha\beta}$ describes the Kronecker symbol. The law describes the isotropic linear elasticity as well as isotropic expansion and contraction in case of heating and cooling respectively.

## 4.2 The Finite Element Formulation

The problem and the governing eq. 4.1 are fully time dependent. Hence, the discretization of the equation has to be temporal and spatial.
The discretization in time is described by a three-point central difference scheme. The scheme is employed by introducing the superscript $t$ reflecting the time level. Therefore, the time discrete equations can be written as follows:

$$\rho \, \frac{u_\alpha^{t-\Delta t} - 2u_\alpha^t + u_\alpha^{t+\Delta t}}{\Delta t^2} = \frac{\partial \sigma_{\alpha\beta}^t}{\partial x_\beta} + \rho \, b_\alpha^t \tag{4.3}$$

where all quantities super-scripted with $t$ are time dependent and $\Delta t$ sets the time step length.
For the spatial approximation the straightforward Galerkin method is applied to the governing equation. Thereby, the displacement field is approximated at $n$ discrete nodal points of finite element mesh as follows:

$$\hat{u}_\alpha = \sum_{j=1}^{n} u_j^\alpha \cdot N_j(x_\alpha) \tag{4.4}$$

where $N_j$ are trial functions of the finite element and $u_j^\alpha$ contains $n \cdot 3$ unknowns.
As the Galerkin method inserts the approximation $\hat{u}_\alpha$ for $u_\alpha$, a residual results. By multiplication with the trial function the resulting residual is required to vanish.
The final discretized form of the governing eq. 4.1 to compute isotropic elastic deformation shows eq. 4.5.

$$\mathbf{u}^{t+\Delta t} = 2\mathbf{u}^t - \mathbf{u}^{t-\Delta t} + \mathbf{M}^{-1} \Delta t^2 \cdot \left( -\mathbf{K}\mathbf{u}^t + \mathbf{b}^t \right) \tag{4.5}$$

where $\mathbf{M} = M_{ij}^{\alpha\beta}$ being the mass matrix of the system. $M_{ij}^{\alpha\beta}$ thereby holds the following entries:

$$M_{ij}^{\alpha\beta} = \int_\Omega \cdot N_i \cdot N_j d\Omega \tag{4.6}$$

where $\Omega$ describes the whole domain of the body and is replaced by the domain $\Omega_e$ of the element $e$, restricting $i$ and $j$ to be nodes of the finite element. Further, $-\mathbf{K}\mathbf{u}^t + \mathbf{b}^t$ is the discretized form of $\sigma^t_{\alpha\beta,\beta} + \rho b^t_\alpha$. $\mathbf{K}$ thereby equals the stiffness matrix of the system with the entries $K^{\alpha\beta}_{ij}$. The stiffness matrix holds thereby the following entries:

$$K^{\alpha\beta}_{ij} = \int_\Omega [\ \mu\,(N_{i,\gamma} \cdot N_{i,\gamma}) \cdot \delta_{\alpha\beta} \ + \ \mu \cdot N_{i,\alpha} \cdot N_{j,\beta} \ + \ \lambda \cdot N_{i,\beta} \cdot N_{j,\alpha}\ ]\ d\Omega \tag{4.7}$$

where $i$ and $j$ run over all nodal points $n$ of the mesh while $\alpha$, $\beta$ and $\gamma$ are presenting the three spatial dimensions (= 1, 2, 3). The term $\mathbf{b}$ holds all nodal forces. In the discretized form the force term $\mathbf{b}$ also holds the forces due to thermal effects which have been introduced with the Hooke's model Equation (4.2).

## 4.3 The Computational Algorithm

Looking at the time-stepping scheme of eq. 4.5 one notices that it gains the new value $\mathbf{u}^{t+\Delta t}$ just by conducting vector addition, matrix-vector and scalar multiplication. Hence, the scheme is an explicit procedure where no linear equation system needs to be solved. Eq. 4.5 is assuming that $\mathbf{u}^t$ and $\mathbf{u}^{t-\Delta t}$ are already predicted. Therefore, the computational algorithm starts at $t = t_0$ by solving the stationary elasticity problem $\mathbf{K}\mathbf{u}^{t_0} = \mathbf{b}^{t_0}$ implicitly before it enters the time loop. Thus, the linear equation system $\mathbf{K}\mathbf{u}^t = \mathbf{b}^t$ needs to be solved ones for $t = t_0$ by an iterative method. The solution provides $\mathbf{u}^{t_0}$. Thereafter, $\mathbf{u}^{t_0}$ and $\mathbf{u}^t$ are equalised which implies the entire system is stationary unless $\mathbf{b}^t$ changes which is a reasonable assumption. While solving eq- 4.5 at every time step $t_0 + i \cdot \Delta t$ the initial gained stiffness matrix $\mathbf{K}$ of the stationary solution is reused.

## 4.4 Isoparametric Elements

The deformable body needs to be meshed by finite elements to assemble the matrices and vectors of eq. 4.5 to solve the problem. To do so in this study isoparametric elements are employed, in particular linear tetrahedral elements containing 4 nodes. This approach is chosen to allow the later presented coupling method, between DEM and FEM, handle the surface elements of a mesh as linear triangular elements. As the biggest portion of a coupled computation is spent on contact predictions, the contact between spherical grains and linear triangles are relatively simple to compute while triangles still allow to describe complex geometry.
The key idea of the isoparametric concept is to use the shape functions $N^e_j$ to represent both the geometrical description of an element and the unknowns of the problem. In this section, $e$ describes the element number whereby the roman index $j$ describes a node of $(1, 2, .., m)$ of the $m$ nodes of the element $e$.
Any quantity, e.g. the displacement $\overrightarrow{u} = u_\alpha$, velocity $v_\alpha$, force $f_\alpha$ or the temperature $T$, may be interpolated over an element by means of the shape functions as well as the

element geometry $x_\alpha$. This can be formulated as follows: [1].

$$1 = \sum_{j=1}^{m} N_j^e \quad x_\alpha = \sum_{j=1}^{m} x_\alpha^j N_j^e \quad u_\alpha = \sum_{j=1}^{m} u_\alpha^j N_j^e \quad T = \sum_{j=1}^{m} T^j N_j^e \tag{4.8}$$

$$\begin{pmatrix} 1 \\ x_\alpha \\ u_\alpha \\ T \end{pmatrix} = \begin{pmatrix} 1 & 1 & .. & 1 \\ x_\alpha^1 & x_\alpha^2 & .. & x_\alpha^m \\ u_\alpha^1 & u_\alpha^2 & .. & u_\alpha^m \\ T^1 & T^2 & .. & T^m \end{pmatrix} \cdot \begin{pmatrix} N_1^e \\ N_2^e \\ .. \\ N_m^e \end{pmatrix} \tag{4.9}$$

Therefore, isoparametric shape functions have to be derived from natural coordinates of a master element. A master element represents the basic shape of an element with an interpolated shape. For instance, the master of a curved triangular element is a triangle with straight sides. This concept enables to construct shape function for elements with curved boundaries which fulfil the consistency requirements. Further, even for high order elements, the integral expression of the stiffness matrix and nodal quantities can be described in simple closed forms.
In the following the linear tetrahedral and linear triangular elements and their shape functions are introduced. As linear tetrahedral elements are employed in this study then shape functions are necessary while deriving the stiffness and mass matrix in eq. 4.5 and interpolating the particle forces onto the FEM structure, as described in the following coupling chapter.

### Natural Coordinates of a Triangle

Any point $\overrightarrow{P}$ aligning in the plane of a triangle may be located in terms of natural coordinates $\zeta_i$, depict in fig. 4.2.

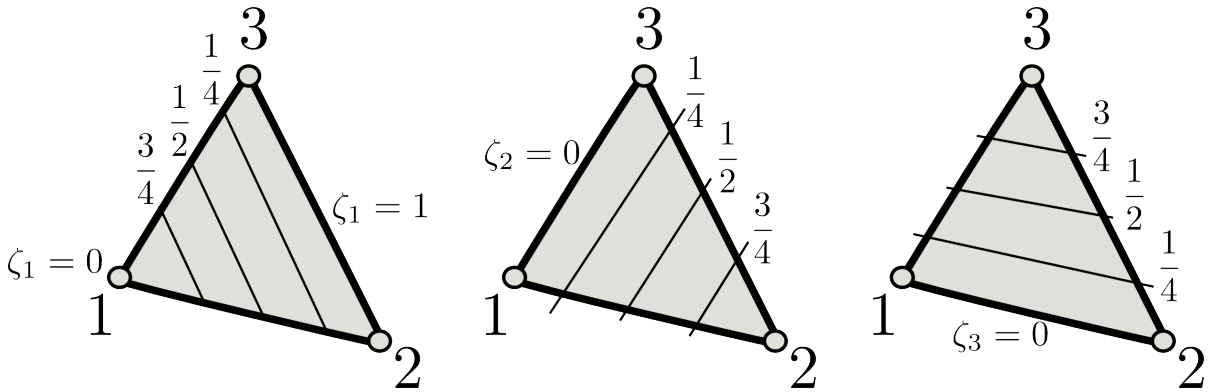


*Figure 4.2: Constant lines of natural coordinates of a triangle.*

The range of the natural coordinates of a triangle thereby writes:

$$0 <= \zeta_i <= 1 \tag{4.10}$$

[1] spatial index $\alpha\ \varepsilon(1, 2, 3)$

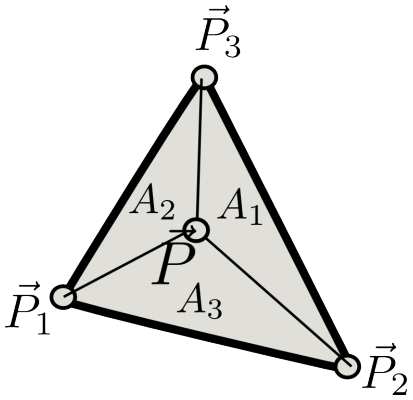


*Figure 4.3: Natural coordinates of a triangle.*

so that the sum of the coordinates has to fulfil the following constraint:

$$\zeta_1 + \zeta_2 + \zeta_3 = 1 \tag{4.11}$$

For triangles with non-curved sides these natural coordinates can be interpreted by means of area coordinates $A_i$ as formulated in eq. 4.12 and depict in fig. 4.3.

$$\zeta_1 = \frac{A_1}{A_\Delta} \quad \zeta_2 = \frac{A_2}{A_\Delta} \quad \zeta_3 = \frac{A_3}{A_\Delta} \tag{4.12}$$

However, the relation of eq. 4.12 is not carried over to general isoparametric triangles with curved sides. Thus the universal description is to consider $\zeta_i$ as curves of constant value within a triangle, rather than areas, which is depict in fig. 4.2 for a linear triangle.
Hence, in natural coordinates the three node points $\vec{P}_i(\zeta_1, \zeta_2, \zeta_3)$ are located at $(1, 0, 0)$, $(0, 1, 0)$ and $(0, 0, 1)$ while the centroid of a triangle is $(\frac{1}{3}, \frac{1}{3}, \frac{1}{3})$.
To transform a point $\vec{P}(x_1, x_2, x_3)$ from global coordinates into natural triangle coordinates $\vec{P}(\zeta_1, \zeta_2, \zeta_3)$, the point has to lie in the plane spanned by the three triangle vertices. This is secured when $\vec{P}$ fulfils:

$$\overrightarrow{n} \cdot (\vec{P} - \vec{P}_j) = n_\alpha \cdot (P_\alpha - P_\alpha^j) = 0 \tag{4.13}$$

where $\vec{n}$ is the plane normal and $\vec{P}_j$ can be any of the three vertices of the triangle.
When solving the linear equation system 4.14 the components $P_\alpha$ are transformed into the natural coordinates $\zeta_i$.

$$\begin{pmatrix} 1 & 1 & 1 \\ P_1^1 & P_1^2 & P_1^3 \\ P_2^1 & P_2^2 & P_2^3 \\ P_3^1 & P_3^2 & P_3^3 \end{pmatrix} \cdot \begin{pmatrix} \zeta_1 \\ \zeta_2 \\ \zeta_3 \end{pmatrix} = \begin{pmatrix} 1 \\ P_1 \\ P_2 \\ P_3 \end{pmatrix} \tag{4.14}$$

This can be written in a general way as follows:

$$\begin{pmatrix} 1 & 1 & 1 \\ x_1^1 & x_1^2 & x_1^3 \\ x_2^1 & x_2^2 & x_2^3 \\ x_3^1 & x_3^2 & x_3^3 \end{pmatrix} \cdot \begin{pmatrix} \zeta_1 \\ \zeta_2 \\ \zeta_3 \end{pmatrix} = \begin{pmatrix} 1 \\ x_1 \\ x_2 \\ x_3 \end{pmatrix} \tag{4.15}$$

### Linear Triangular Elements

In case of a linear triangular element, as seen in fig. 4.4, the natural coordinates equal the shape functions of eq. 4.16.

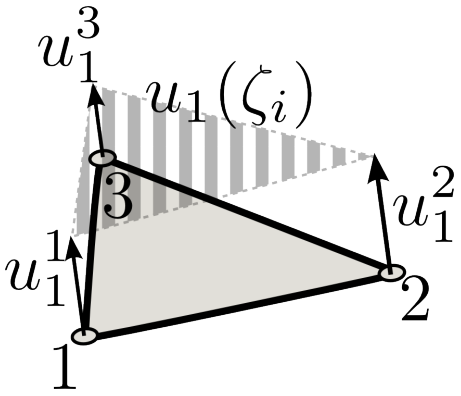


*Figure 4.4: Linear triangle plus linear interpolation of field $u_1(\zeta_i)$.*

$$\zeta_j = N_j \rightarrow \quad N_1 = \zeta_1 \quad N_2 = \zeta_2 \quad N_3 = \zeta_3 \tag{4.16}$$

Following eq. 4.8 any quantity to be described over the element may be interpolated by means of the natural coordinates of eq. 4.17.

$$\begin{pmatrix} 1 \\ x_i \\ u_i \end{pmatrix} = \begin{pmatrix} 1 & 1 & 1 \\ x_i^1 & x_i^2 & x_i^3 \\ u_i^1 & u_i^2 & u_i^3 \end{pmatrix} \cdot \begin{pmatrix} N_1^e \\ N_2^e \\ N_3^e \end{pmatrix} = \begin{pmatrix} 1 & 1 & 1 \\ x_i^1 & x_i^2 & x_i^3 \\ u_i^1 & u_i^2 & u_i^3 \end{pmatrix} \cdot \begin{pmatrix} \zeta_1 \\ \zeta_2 \\ \zeta_3 \end{pmatrix} \tag{4.17}$$

Fig. 4.4 exemplifies a linear distribution of the displacement component $u_1$. In case of the linear triangle the master element and linear triangle are similar shaped.

### Natural Coordinates of a Tetrahedron

For a linear tetrahedral element one can extend the approach of the linear triangular element by using volume instead of area coordinates. Hence, also any point $\overrightarrow{P}$ aligning in the volume of a tetrahedron can be described in terms of the natural coordinates $\zeta_i$ of a tetrahedron as depicted in fig. 4.5.

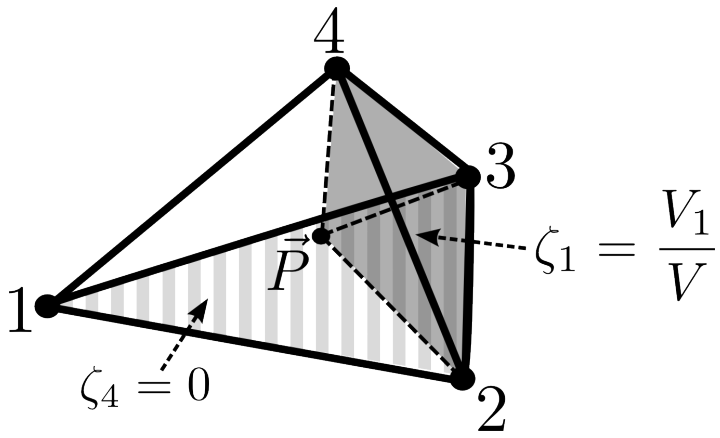


*Figure 4.5: Natural coordinates of a tetrahedron, i.e. linear tetrahedral element .*

The natural coordinates of a tetrahedron can be interpreted by means of volume coordinates $V_i$ in the following manner:

$$\zeta_1 = \frac{V_1}{V} \quad \zeta_2 = \frac{V_2}{V} \quad \zeta_4 = \frac{V_4}{V} \quad \zeta_4 = \frac{V_4}{V} \tag{4.18}$$

where $V_i$ describes the portion of the tetrahedral volume and $V$ the entire volume of the tetrahedron. Also here the sum of the natural coordinates has to fulfil:

$$\zeta_1 + \zeta_2 + \zeta_3 + \zeta_4 = 1 \tag{4.19}$$

To transform a point $(x_1, x_2, x_3)$ from global coordinates into natural tetrahedral coordinates $(\zeta_1, \zeta_2, \zeta_3, \zeta_4)$, the following linear equation system has to be solved:

$$\begin{pmatrix} 1 & 1 & 1 & 1 \\ x_1^1 & x_1^2 & x_1^3 & x_1^4 \\ x_2^1 & x_2^2 & x_2^3 & x_2^4 \\ x_3^1 & x_3^2 & x_3^3 & x_3^4 \end{pmatrix} \cdot \begin{pmatrix} \zeta_1 \\ \zeta_2 \\ \zeta_3 \\ \zeta_4 \end{pmatrix} = \begin{pmatrix} 1 \\ x_1 \\ x_2 \\ x_3 \end{pmatrix} \tag{4.20}$$

where $x_\alpha^j$ are the nodal points of the tetrahedron with $j$ holding the node number and $\alpha$ the spatial component.

### Tetrahedral Elements

In case of a tetrahedral element, the natural coordinates equal the shape functions as follows:

$$\zeta_j = N_j \rightarrow \quad N_1 = \zeta_1 \quad N_2 = \zeta_2 \quad N_3 = \zeta_3 \quad N_4 = \zeta_4 \tag{4.21}$$

Thus, following again the approach of eq. 4.8, any quantity to be described over the element can be interpolated by means of the natural coordinates as follows:

$$\begin{pmatrix} 1 \\ x_i \\ u_i \end{pmatrix} = \begin{pmatrix} 1 & 1 & 1 & 1 \\ x_i^1 & x_i^2 & x_i^3 & x_i^4 \\ u_i^1 & u_i^2 & u_i^3 & u_i^4 \end{pmatrix} \cdot \begin{pmatrix} N_1^e \\ N_2^e \\ N_3^e \\ N_3^e \end{pmatrix} = \begin{pmatrix} 1 & 1 & 1 & 1 \\ x_i^1 & x_i^2 & x_i^3 & x_i^4 \\ u_i^1 & u_i^2 & u_i^3 & u_i^4 \end{pmatrix} \cdot \begin{pmatrix} \zeta_1 \\ \zeta_2 \\ \zeta_3 \\ \zeta_4 \end{pmatrix} \tag{4.22}$$

Fig. 4.6 exemplifies a linear interpolation of the displacement $\vec{u}$ by the shape functions $\zeta_i$.

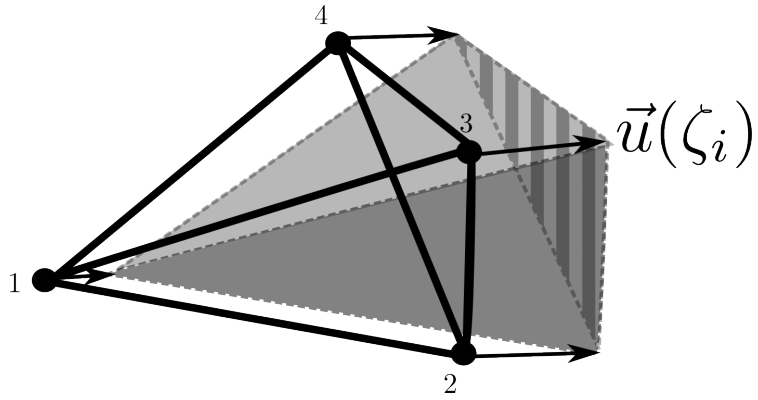


*Figure 4.6: Linear tetrahedral element with linear interpolation of field $\vec{u}(\zeta_i)$.*

Also in case of the linear tetrahedral element the master element and linear tetrahedron are similar shaped.

## 4.5 Linear Equation System

In most cases when discretising partial differential equations by the finite element method, a system of linear algebraic equations has to be solved. In this study the C++ libraries of the finite element toolbox DiffPack are utilised to assemble and solve such a system. For that purpose the libraries offer direct and iterative methods and provide flexible functionality to utilise the specific matrix and vector structure assemble.
As the main part of the finite element solution in this study, the time-stepping scheme of eq. 4.5 does not force any solving of a linear equation system. But the initial prediction of the stationary elasticity problem $\mathbf{K}\mathbf{u}^{t_0} = \mathbf{b}^{t_0}$ is a solution of a system of linear algebraic equations. Therefore, the linear equation system $\mathbf{K}\mathbf{u}^{t_0} = \mathbf{b}^{t_0}$ needs to be solved for $n \cdot 3$ unknowns which are contained in the vector $\mathbf{u}$.
In this study, the Conjugate Gradient Method as an successful iterative method to solve $\mathbf{A} \cdot \mathbf{x} = \mathbf{b}$ linear systems is chosen to do so.

# Chapter 5

# Efficient XDEM - FEM Coupling Method

The coupled computation conducted in this study are separated into two domains, namely the Finite Element and the Discrete Element simulations. These two domains stay separated through the entire time loop and integrate their quantities without interferring. Only at characteristic points within the time loop necessary data is shared to update each domain.
In the following the coupling procedure is described within the time loop. Thereafter, the key parts of the coupling are presented in detail. The first key part is the efficient algorithm for a fast prediction of potential contact pairs between particle and surface element. After the prediction of potential contact pairs, the actual intersection of particle and surface element of the FE mesh is explained. Finally, the interpolation of the contact force onto the element nodes is derived.
Additionally, a spatial homogenisation of discrete quantities is presented to allow later comparison to a continuum field.

## 5.1 Coupling Procedure

Within the context of explicit time integration the procedure of the DEM - FEM coupling algorithm is relatively straightforward. The procedure is schematically depicted in fig. 5.1. Before the procedure enters the time loop to predict the motion of particles and the deformation of the solid body an initiation phase is required to establish the foundation for later information exchange. While generating the mesh of the solid body one has to take care of meshing the surface of the body with linear triangular finite elements. The efficient contact detection is based on the intersection between spheres and triangles.
As depicted in fig. 5.1, the initiation starts with solving the stationary problem within the FEM domain. This step provides two information to the procedure.

Initiation

↦ solve $\rightarrow \mathbf{K}\mathbf{u}^0 = \mathbf{b}^0$

↦ mirror displaced surface elements

Time Loop $\rightarrow i \rightarrow t_i = t_0 + i \cdot \Delta t$

↦ integrate time step $t_i$ of particle motion, eq. 3.10 & 3.24

↦ transfer contact forces

↦ predict potential contact pairs

↦ compute contact forces

↦ interpolate forces to finite element

↦ integrate time step $t_i$ of body deformation, eq. 4.5

↦ update boundary shapes

*Figure 5.1: General Procedure of the Coupling Algorithm*

First, the matrices and initial displacement values for eq. 4.5 of the FEM domain are established. This predicts the first deformed structure for the DEM domain.
The second step of the initiation phase mirrors the deformed surface elements of the FEM mesh into DEM domain. Hence, at all time the surface geometry of the deformed body exists in a similar way inside the DEM domain. The DEM domain sees the deformed surface elements of the finite element mesh as geometrical boundary conditions. On this basis the coupling algorithm is linking the particular surface element with the according boundary shape between FEM and DEM domain.
The loop over time is separated into four major parts. The order of the computations follows the physical events logically.
First, the motion of the granular assembly is integrated. Following this step, the impacts between particles and the elastic body are predicted. Thereafter, the deformation of the elastic body due to the impacting forces can be solved by the FEM scheme. The last part of the procedure updates the position of the boundary shapes before the particle motion is re-predicted within the new time step.
Within a single time loop the motion of the granular material is predicted first. This step integrates the position and orientation of particles according to eq. 3.7 and 3.25. The change in the dynamic quantities can also be due to forces of previous interactions between particles and solid body.
Logically, between the integration of the motion of particles and the integration of the deformation of the elastic body contact forces need to be computed and transferred. Therefore, the step of transfer of contact forces aligns between them at the second position within the time loop. This step is partitioned into three sub steps.
First, the potential contact pairs are detected by means of an efficient contact detection

algorithm. The algorithm spares valuable computation time by a fast selection of the important particle - element pairs from all possible pairs in the system. The fundamentals of the algorithm are explained below.
The next sub-step computes contact forces for all pairs provided by the contact detection algorithm. The contact force between particle and triangular element is derived from a representative overlap as described for particle - particle contacts in section 3. The overlap prediction in this particular geometrical case is described in the following sections. The contact force is decomposed into normal and tangential components which depend on displacements and velocities normal and tangential to the point of contact between the particle and surface element. The contact force is added to the particle force and the counter force is transferred to the according surface element of the FE mesh.
Thus, the third sub-step executes the interpolation of counter force onto the nodal forces of the finite element. After the transfer of contact forces the computations of elastic deformation are executed. This step incorporates the insertion of interpolated contact forces into the force vector $b^l$ of the finite element formulation.
Thereafter, the new displacement value $\mathbf{u}^{l+1}$ will be gained by solving eq. 4.5.
Finally, before the new loop starts over, each boundary shape within the DEM domain is updated according to the appropriate surface element. Therefore, the position and displacement vector of every nodal point of the surface mesh are added and the appropriate vertex of the triangular boundary shape is undated with the result.

## 5.2 Contact Detection

For an efficient coupling of discrete and finite elements the contact situation has to be clarified as quick as possible. The coupling and quantity exchanging procedure is based on the information that pairs of particles and elements are in contact. To avoid testing the contact situation of each pair, an algorithm for quick contact detection has been developed. The algorithm is based on a binary tree structure storing cubic bounding volumes. Fig. 5.2 shows such a binary at the example of a tire tread. The binary tree holds bounding volumes at every tree level.
The root node encapsulates all surface elements of the meshed body. By accessing a lower level of the tree the bounding volume of the previous level split in half by spatial dimensions and number of elements encapsulated. The final branches of the binary tree only hold the reference to a single surface element.
For the prediction of contact pairs, the algorithm simply runs along the branches. It predicts if a particle is within the dimensions of a bounding volume. If this is the case the algorithm repeats the prediction on the next lower level. As the algorithm reaches a bottom node of the binary tree, the particle and the remaining surface element will be returned as a potential contact pair. In any other case the contact detection algorithm ends.

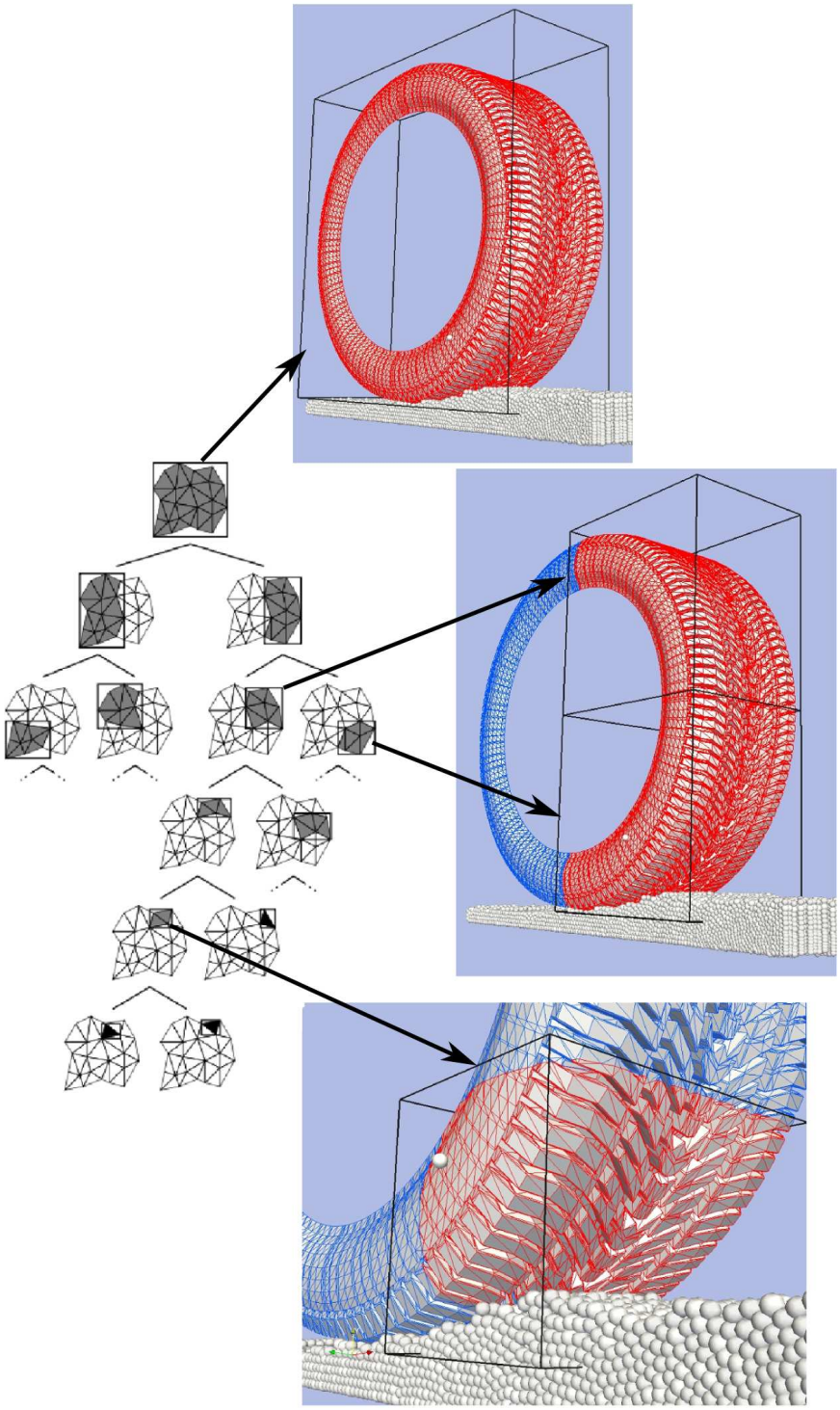

*Figure 5.2: Binary tree with stored bounding volumes exemplified by a tire tread. The root bounding volume encapsulates the entire surface elements while the bottom branch holds a single surface triangle.*

## 5.3 Contact Prediction

For each detected contact pair of particle and finite element, the particular overlap $\delta_{ij}$ and point of contact $\vec{x}_{ij}^{c}$ are predicted. These predictions are provided to the force computation described in chapter 3.
Each particle is composed of spherical shapes. Therefore the following procedure follows the contact prediction between sphere and triangle. The contact prediction between a sphere and triangle can be separated into three contact situations as depicted in fig. 5.3. The spherical particle can intersect with the interior, the edges or a vertex of the triangular shape.

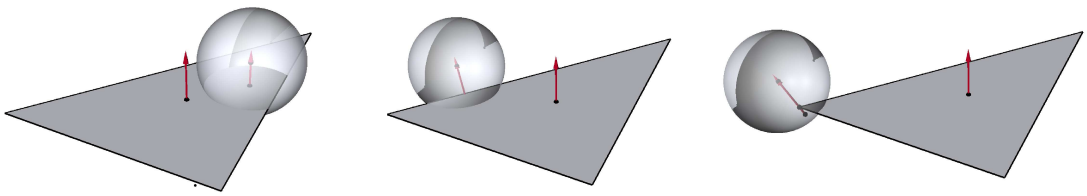

*Figure 5.3: Three contact situations of sphere - triangle intersection: contact point within triangle dimensions, triangle edge intersection and triangle vertex contact, respectively.*

By means of the natural coordinates of a linear triangle an efficient and quick prediction of the contact situation is enabled. The natural coordinates can be presented as the portion of the area $A_i$ of the entire triangle area $A_\Delta$ which is depicted in fig. 4.3 and already formulated in eq. 4.12.
In the following the exact contact prediction implemented will be described demonstratively.
The prediction is based on seven input values which are the three triangle vertices $\vec{P}_1$ $\vec{P}_2$ and$\vec{P}_3$, the triangle normal $n_i = \frac{n_i^p}{|\vec{n}_p|}$, the centroid $\vec{M}_T$, the sphere midpoint $\vec{M}$ and radius $r$. The normal can also be predicted by the vertices as follows:

$$n_i^p = \epsilon_{ijk} \left(P_j^1 - P_j^2\right) \cdot \left(P_k^3 - P_k^2\right)$$

where $\epsilon_{ijk}$ is the permutation tensor.
The values gained from the contact prediction for use in the subsequent force computations are the overlap $\delta$ of spherical sub shape, the contact position $\vec{x}_c$ and the contact direction $\vec{n}_c$.
First, the prediction of the intersection between sphere and triangle plane is conducted. The distance $D$ between midpoint and plane is thereby computed as follows:

$$D = n_i \cdot M_i - (n_i \cdot P_i^1)$$

If the distance $D \leq |r|$, an intersection with plane is predicted, as depict in fig. 5.5. In this case the predictions proceed other wise the contact loop progresses with the next triangle provided by the contact detection algorithm of section 5.2.

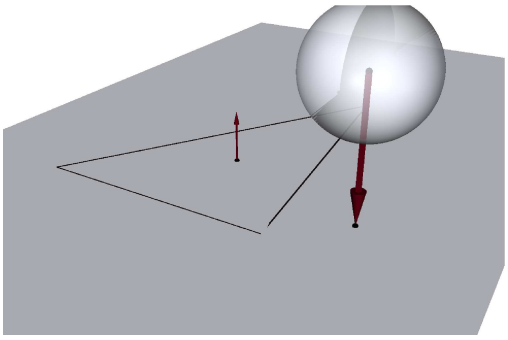

*Figure 5.4: Projection of $\vec{M}$ on triangle plane, if $D > |r| \rightarrow$ no intersection with plane.*

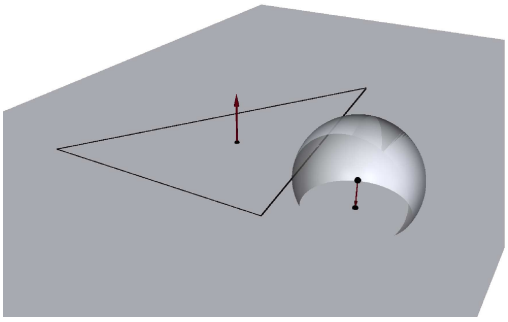

*Figure 5.5: Projection of $\vec{M}$ on triangle plane, if $D <= |r| \rightarrow$ intersection with plane.*

Further, the projection of the spherical midpoint on the plane $C_i^p = M_i - n_i \cdot D$ is calculated and transformed into triangular coordinates $\zeta_i$. This transformation is accomplished by solving the linear equations system $\zeta_i = P_{ji} \cdot C_j^p$.
If $\zeta_i \leq 1 \;||\; \zeta_i \geq 0$, the projection $C^p$ aligns within the triangle dimensions and an intersection occurs as shown in fig. 5.6.

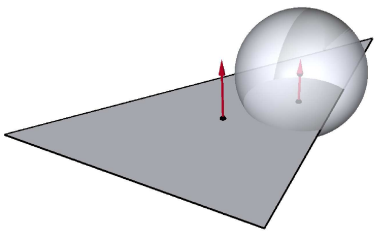

*Figure 5.6: Intersection within triangle dimensions.*

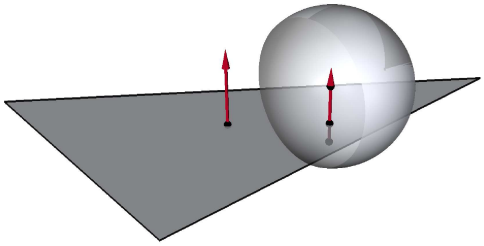

*Figure 5.7: Contact point $x_i^c$ and direction $n_i^c$ if intersection takes place within triangle dimensions.*

Hence, the overlap equals $\delta = |D| - |r|$, the contact normal gives $n_i^c = \frac{M_i - C_i^p}{|\vec{M} - \vec{C_p}|}$ and contact position is predicted as follows $x_i^c = C_i^p + \frac{1}{2} \cdot \delta \cdot n_i^c$.
In this case the prediction ends and the algorithm proceeds with the next surface triangle detected. If the intersection does not occur within the triangle dimensions, the prediction progresses to check for edge or vertex intersection. If $\zeta_i > 1 \;||\; \zeta_i < 0$, the sphere intersects with an edge or a vertex of the triangle as depicted in fig. 5.9 and fig. 5.8, respectively.

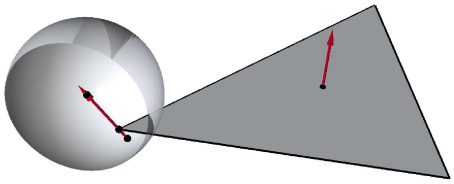

*Figure 5.8: Intersection with a vertex.*

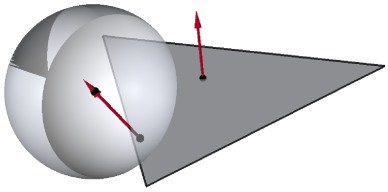

*Figure 5.9: Intersection with an edge.*

First, the check for closest vertex is conducted by means of:

$$D = min\left(|\vec{P}_i - \vec{M}|\right)$$

At this stage the closest point $\vec{C}_p$ between the triangle and the sphere is set equal with the closest vertex $\vec{P}_i$. Thereafter, the checking proceeds with the closest edge using the height between the three edges and the midpoint $\vec{M}$ as shown in fig. 5.10.

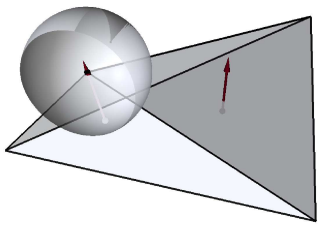

*Figure 5.10: Three triangles formed by edges and midpoint.*

Every obtuse triangle fulfilling $c^2 + b^2 < a^2$ or $c^2 + a^2 < b^2$ can be neglected. If the distance $D$ is larger than the height $h_i$ of any of the three triangles, an intersection with an edge will be predicted. This can be written as follows:

$$D > h_i = \frac{|A_i|}{|c_i|}$$

where $c_i$ describes the length of the edge $i$. For the case $D > h_1$ the closest point on the edges id predicted by:

$$\vec{C}_p = \vec{P}_1 + \left(\frac{\vec{c}_1 \cdot \left(\vec{M} - \vec{P}_1\right)}{\vec{c}_1 \cdot \vec{c}_1}\right) \cdot \vec{c}_1$$

If $0.0 \geq |\vec{M} - \vec{C}_p| - r$, the edge contact is confirmed and the contact properties are predicted as follows:

$$\vec{n}_c = \frac{\vec{M} - \vec{C}_p}{|\vec{M} - \vec{C}_p|}$$
$$\delta = \left(|\vec{M} - \vec{C}_p| - r\right) \cdot \frac{1}{2}$$
$$\vec{x}_c = \vec{C}_p + \frac{1}{2} \cdot \delta \cdot \vec{n}_c$$

## 5.4 Discrete to Continuum Conversion

The contact between a continuous and discrete approached media requires transformations between continuum and discrete quantities. This implies certain difficulties caused by the fundamental differences of the approaches. However, the purpose here is to transfer impact values from DEM to FEM.

### 5.4.1 Point Force to Nodal Force

The computation is virtually separated into two domains, the FEM and the DEM domain. The DEM domain sees the surface elements of the finite element mesh as geometrical boundary conditions. The nodal positions of this surface elements are updated at each time step as the finite mesh moves and deforms. This means within a single time step a particle contacting a finite element impacts a static wall. Thus the calculation of the impact forces at the contact point are in accordance to the description in chapter 3.
Within the FEM domain impacting particles are recognised as point forces acting on the surface of an element, see fig. 5.11. But the displacements are computed at the nodal points of an element. Hence, the point has to be interpolated consistently onto the nodes to account for them within the finite element formulation of eq. 4.5. The force interpolation is based on the virtual work equivalent to secure consistent nodal forces for FEM. This equivalent states that the work of the particle force paired with the interpolated displacement equals the work achieved by the nodal forces and nodal displacement. Nakashima and Oida (2004) and Horner et al. (2001) used the same approach of DEM - FEM coupling to analyse vehicle - soil and tire - soil interactions.
Looking at the contact situation in fig. 5.11, the finite element sees a point force acting on certain point of its surface. A point force can be written as the force multiplied by the Dirac functions. Eq. 5.1 represents the particle force $\vec{F}$ acting on the point $P(\zeta_1^P, \zeta_2^P, \zeta_3^P)$ of the triangle surface in natural coordinates.

$$F_j \cdot \delta(\zeta_1 - \zeta_1^P) \cdot \delta(\zeta_2 - \zeta_2^P) \cdot \delta(\zeta_3 - \zeta_3^P) \tag{5.1}$$

Let $\delta\vec{u}_n$ be the virtual node displacement and $\vec{f}_n$ the paired nodal force, the left side term of eq. 5.3 represents the virtual work at the nodes. The right side term is the virtual work

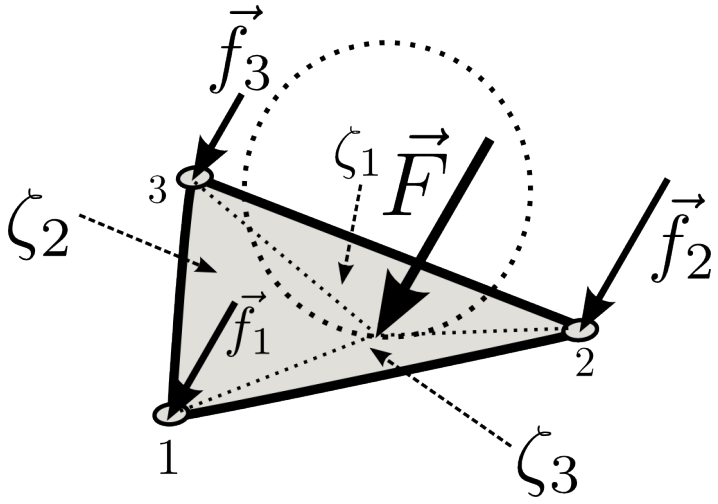


*Figure 5.11: Particle force interpolated onto a linear triangle element.*

achieved by external forces.

$$\sum_n \delta W_n = \delta W_S \tag{5.2}$$

$$\sum_n \vec{f}_n \cdot \delta\vec{u}_n = \int_S \vec{f}_s \cdot \delta\vec{u}\, dS \tag{5.3}$$

$$\sum_n \vec{f}_n \cdot \delta\vec{u}_n = \int_S \vec{f}_s \cdot \left( \sum_n N_n \cdot \delta\vec{u}_n \right) dS$$

In eq. 5.3, $\delta\vec{u}_n$ is the virtual nodal displacement and $N_n(\zeta_n) \cdot \delta\vec{u}_n$ its associated variation. The interpolated virtual displacement for a linear triangle is described as follows:

$$\delta\vec{u} = N_1(\zeta_1) \cdot \delta\vec{u}_1 + N_2(\zeta_2) \cdot \delta\vec{u}_2 + N_3(\zeta_3) \cdot \delta\vec{u}_3$$

Introducing this into eq. 5.3 and cancelling $\delta\vec{u}_n$ from both sides yields the following equation:

$$\vec{f}_n = \int_S \vec{f}_s \cdot N_n(\zeta_n)\, dS \tag{5.4}$$

Interpreting the surface integral by means of the natural coordinates and substitute the particle reaction force in eq. 5.4 by eq. 5.1 the following equation yields:

$$\vec{f}_n = \int_0^1 \vec{F} \cdot \delta(\zeta_n - \zeta_n^P) \cdot N_n(\zeta_n)\, d\zeta_n \tag{5.5}$$

$$\int_b^a Q(x) \cdot \delta(x - y)\, dx = Q(y) \quad \rightarrow \quad a \leq y \leq b \tag{5.6}$$

Using the integration law 5.6 of a Dirac function, the distribution of the point force $\vec{F}$ onto the nodal forces can be predicted by means of the shape functions, as formulated in eq. 5.7.

$$\left( \vec{f_n} = N_n(\zeta_n^P) \cdot \vec{F} \right)^e$$

$$\left( f_i^n = N_n(\zeta_n^P) \cdot F_i = \zeta_n^P \cdot F_i \right)^e \tag{5.7}$$

### 5.4.2 Homogenisation of Discrete Quantities

Analysis of the discrete results involves mostly comparison to macroscopic measurements. Measurements are necessarily presented as or in relation to continuum quantities, e.g. volume, density or pressure. Thus it is often convenient and sometimes even necessary to find a continuum representation of discrete results, e.g. position and force. In this study, three-dimensional Voronoi tessellation of Rycroft (2007) is used to connect the discrete representation of a particle ensemble to a bulk continuum description. The developed Voronoi library thereby carries out the computations of a Voronoi cell, i.e. volume, for each particle individually. Fig. 5.12 shows the example generation of Voronoi cells from the grain distribution of a cylindrical snow sample of macroscopic density of 408 kg/m$^3$. Having a cell volume associated with each particle allows to relate any discrete quantity of

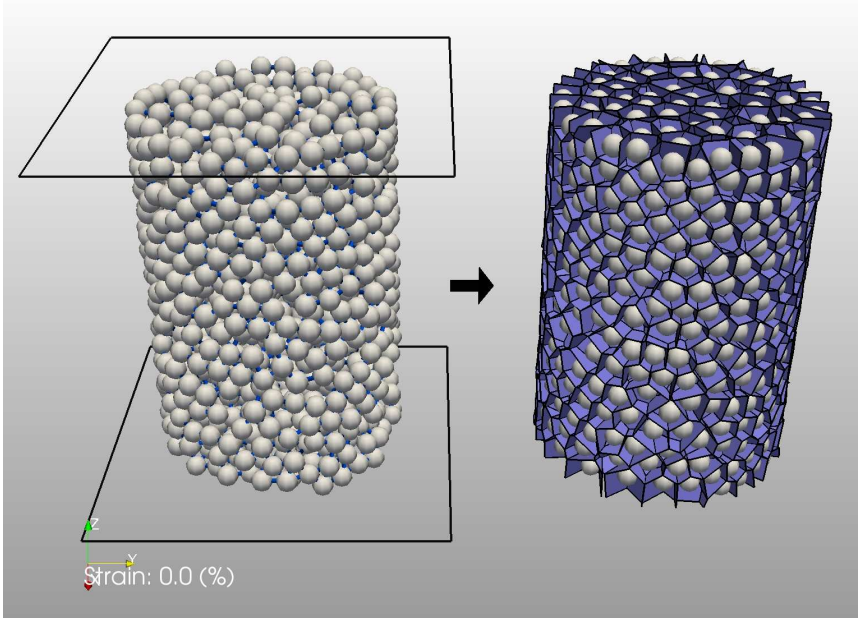


*Figure 5.12: Voronoi cells of a cylindrical snow sample of macroscopic density of* 408 kg/m$^3$.

the particle to the continuum cell. In the following the generation of a density and stress field is introduced from a discrete grain position and force distribution, respectively.

## Density Distribution

The density of a cell volume $\rho_c$ is predicted as follows:

$$\rho_c = \frac{V_p}{V_c} \cdot \rho_p \tag{5.8}$$

where $V_p$ denotes the particle volume, $V_c$ is the Voronoi cell volume and $\rho_p$ is the particle density. Fig. 5.13 exemplifies the density distribution of a cylindrical snow sample with a macroscopic density of 400 kg/m$^3$. The density of a snow grain $\rho_p \simeq \rho_{ice} \simeq 920$ kg/m$^3$ is assumed to be the density ice Ih.

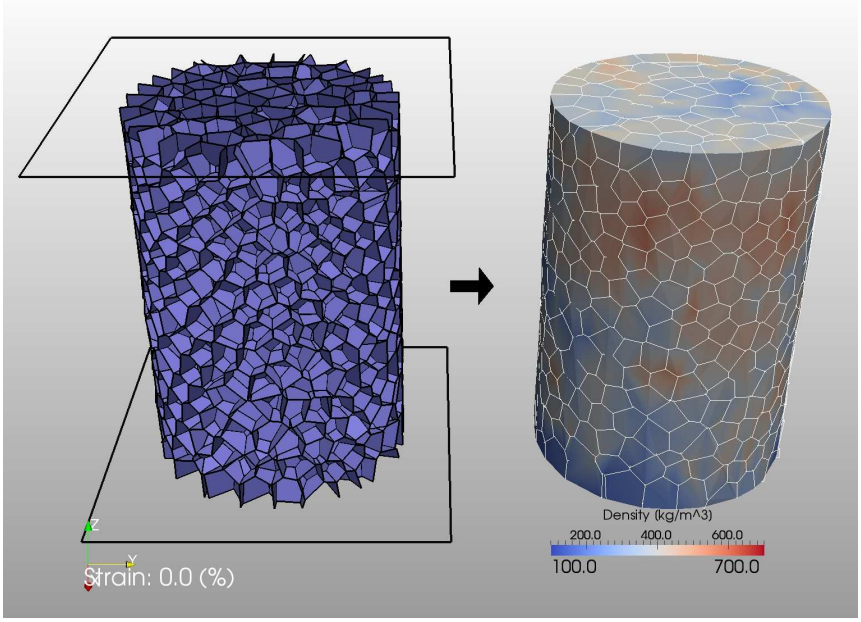


*Figure 5.13: Density distribution by Voronoi cells in a cylindrical snow sample of macroscopic density of* 408 kg/m$^3$.

## Continuum Stress Field

The stress tensor $\sigma_{\alpha\beta}$ of cell volume $V_i$ related to the particle $i$ and resulting from contact $j$ is predicted as follows:

$$\sigma^i_{\alpha\beta}(t) = \frac{1}{V_i} \cdot \sum_{j=1, j\neq i}^{n} F^{ij}_{\alpha}(t) \cdot d^{ij}_{\beta}(t) \tag{5.9}$$

where $\vec{F}_{ij}$ is the contact, $\vec{d}_{ij}$ distance vector between the two particle centers and $n$ the number of all interactions.

# Chapter 6

# Results and Discussions

## 6.1 Validation at the Grain-Scale

### 6.1.1 Bond Growth and Fracture

Szabo and Schneebeli (2007) conducted measurements of the sintering force between two adjoining ice grains. Within the experiments two conical ice cylinder with a spherical tip of 3 mm radius have been pushed together under a constant load of 2 N. The measurements were performed at the temperatures of $-1$ °C and $-12$ °C . The contact load was applied for different time lengths to sinter an ice bond between the grains.

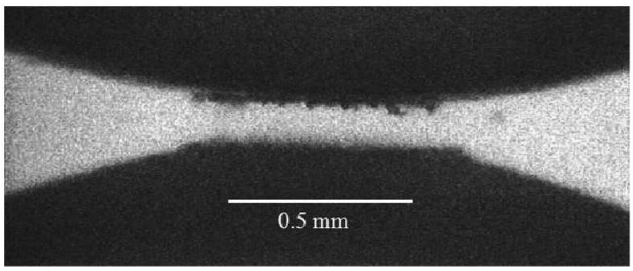


*Figure 6.1: Fracture of freshly sintered bond between two spherical ice grains by Szabo and Schneebeli (2007).*

The ice grains were separated after different contact times between 0 and 1000 ms. Fig. 6.1 shows the force measured during the separation of the grains. The measured force is called the sintering force and is shown by symbols in fig. 6.2.
The experiments were numerically repeated by pushing together two spherical ice grains of the same size and under the same load and temperatures. After the different contact times, i.e. sintering times, the ice grains were separated and the resulting force, i.e. sintering force, was recorded.

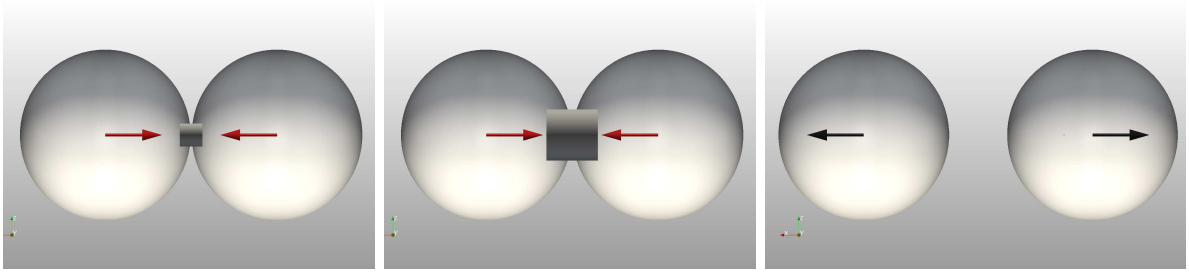

$t_1$ $t_2$ $t_3$

*Figure 6.2: Two ice grains pushed together under constant normal load 2 N at $t_1$ and $t_2$ and pulled apart by constant velocity at $t_3$. The bond grows under load between the two ice grains.*

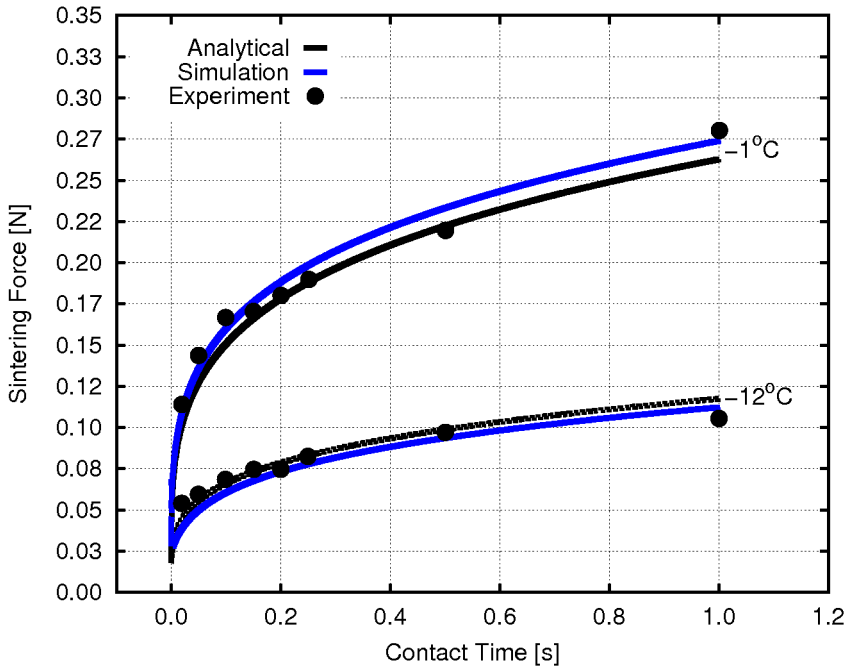


*Figure 6.3: Experimental, analytical and numerical predicted sintering force between two ice grains. The bond grew under a constant load of 2 N and at temperature of −1 and −12 °C. The blue lines illustrate the predicted results, the black lines are predicted by eq. 3.63 and the symbols are the measurements of Szabo and Schneebeli (2007)*

The sintering force is a measure of the bonding strength between ice grains. Fig. 6.3 shows that the sintering force between the ice grains grows with increasing contact time and ascending temperature. The developed bond growth model of eq. 3.63 is re-capturing the bond growth between two adjoining ice/snow grains very well. The model accounts for the pressure, the rate and the temperature dependence. It has to be noticed that the experimental and numerical results in fig. 6.3 never approach zero. The initial bond area

is resulting from the elastic deformation during the grain collision. According to Hertz (1881), the contact area is predicted by eq. 3.64.

### 6.1.2 Ductile and Brittle Bond Deformation

Each bond between a pair of snow grains is assumed to be a continuous cylindrical ice bridge. In this section, two ice grains with a predefined bond size are compressed. The predictions were carried out for six selected configurations, shown in table 6.1. These configurations describe the typical characteristics of snow grain deformation in dependence of different strain rates and temperatures.

*Table 6.1: Strain Rate and Temperature Configurations*

| $\dot{\varepsilon}\,[\mathrm{s}^{-1}]$ | $1 \cdot 10^{-6}$ | $2 \cdot 10^{-5}$ | $2 \cdot 10^{-5}$ | $5 \cdot 10^{-4}$ | $5 \cdot 10^{-4}$ | $1 \cdot 10^{-1}$ |
|---|---|---|---|---|---|---|
| $T\,[^\circ\mathrm{C}]$ | $-12$ | $-5$ | $-12$ | $-1$ | $-5$ | $-1$ |

Within the predictions are conducted with the brittle strain rate of $\dot{\varepsilon} = 10^{-1}$ s$^{-1}$, the transition rate of $5 \cdot 10^{-4}$ s$^{-1}$ and the two ductile rates of $2 \cdot 10^{-5}$ s$^{-1}$ and $10^{-6}$ s$^{-1}$. The stress response of the bonds to increasing strain is shown in fig. 6.4.

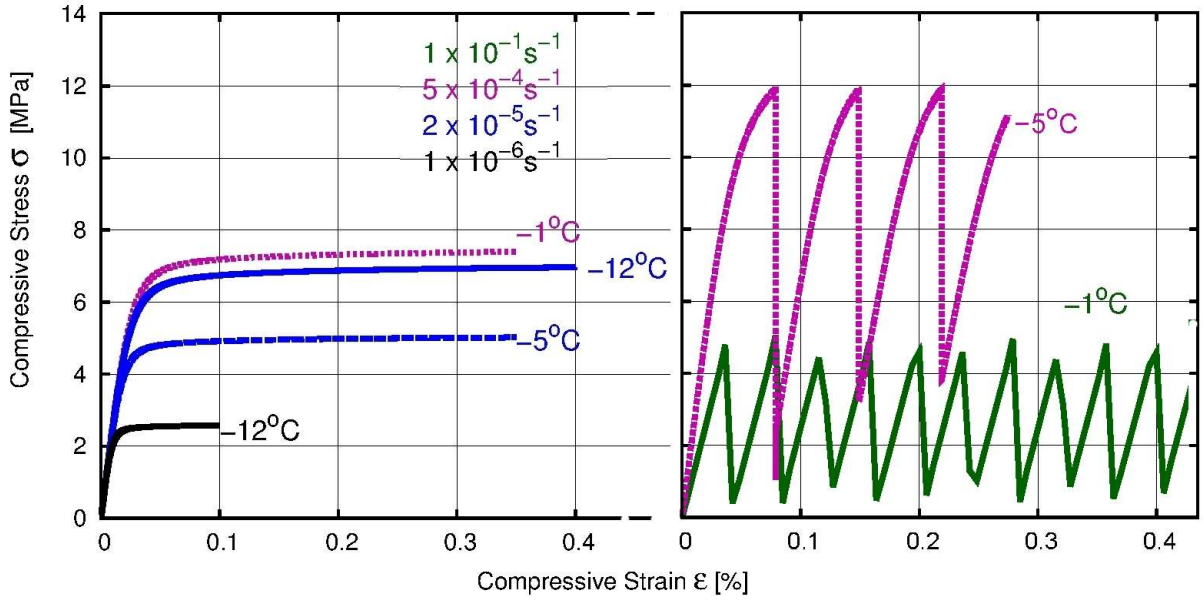


*Figure 6.4: Bond deformation of the six selected configurations of different strain rates and temperatures. The predicted results are coloured by strain rate and marked by the applied temperature.*

The overall strength of the ice bond increases with decreasing temperature which correlates with the observations by Schulson (1990) described in section 2.1.2.
The black and blue curves in fig. 6.4 show the predicted results of the low strain rates of $2 \cdot 10^{-5}$ $s^{-1}$ and $1 \cdot 10^{-6}$ $s^{-1}$. With increasing strain, the stress increases until it reaches the yield strength of ice. Thereafter, the straining proceeds, i.e. bond deforms, without any change in stress. The curves shows the typical ductile deformation behaviour at such low strain rates. This behaviour is predicted by the applied creep model of eq. 3.2.
In fig. 6.4, the green curve shows the bond deformation under the high strain rate of $1 \cdot 10^{-1}$ $s^{-1}$. The curve describes a saw-tooth shape due to subsequent stress build up and fracture of the bond. This is the typical shape of the strain-stress curve of brittle deformation behaviour.
The violet curves in fig. 6.4 illustrate the results of the transition rate of $5 \cdot 10^{-4}$ $s^{-1}$. The stress-strain curves show a mixture of ductile and brittle behaviour. For $-5$ °C, the stress increases viscous-elastic with ascending strain until the fracture strength is reached by eq. 3.65 of the bond model. For $-1$ °C, the creep law of eq. 3.2 relaxes the stress before the fracture strength can be reached under the straining. The decrease in brittleness closer to the melting point was also observed in measurements of snow deformation, e.g. fig. 2.23.
For transitional and brittle behaviour, the highest stress reached during straining is defined as the strength. The strength - strain rate relationship is shown in fig. 6.5.

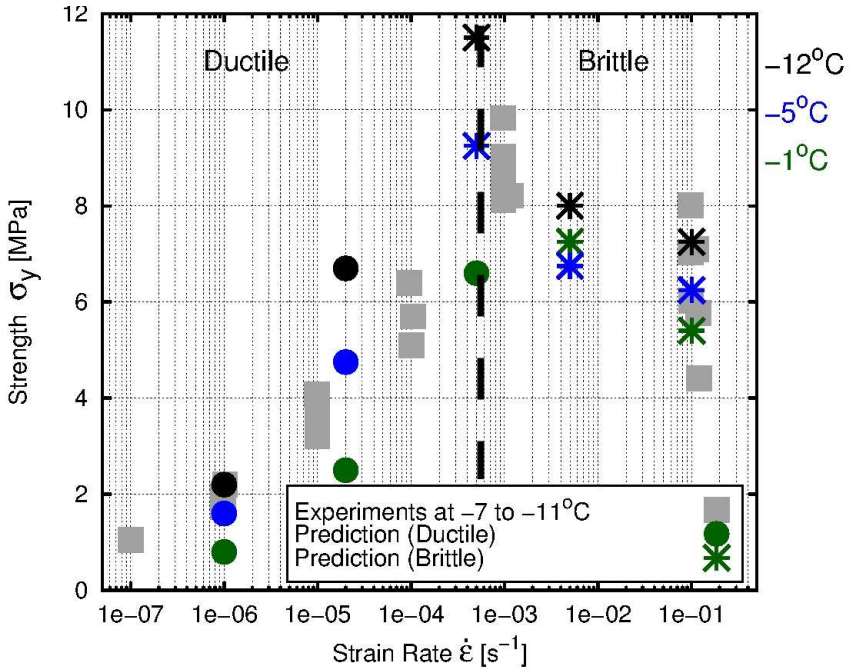


*Figure 6.5: Bond strength versus strain rate at different temperatures. The grey rectangular symbols are measurements of the compressive ice strength by Schulson (1990). The coloured symbols are the simulation results. A circle describes ductile and a star describes brittle behaviour of the ice bond.*

Fig. 6.5 shows the predicted results at the different strain rates together with the compres-

sive ice strength measured by Schulson (1990).
The results show an increase in the compressive yield strength with ascending strain rate in the ductile regimes. Furthermore, the compressive strength decreases with increasing temperature. The brittle failure strength under compressive strain reduces with increasing strain rate. The stress-strain and strength-rate relationships of the ice bond deformation correlate very well with the experimental results. Also the temperature dependence is captured by the developed bond model. It has to be noticed that there is no reason for the results to diverge from the physics as a phenomenological model used. The model includes all principal physics observed in the experiments.

## 6.2 Macroscopic Predictions of Snow under Load

The objectives of the predictions of this section are to validate the derived snow models at the macroscopic scale. Therefore different load tests are simulated with representative snow samples. The tests are related to common phenomenological and mechanical experiments from the field of snow mechanics. Further, the results are compared and discussed in relation to measurements and experimental data found in the literature. The validation will be done in order to increase the complexity of the tests with confirmation of valid snow behaviour. The comparison with the experimental data is analysed and discussed along the characteristic features measured during the tests. Snow shows a strong dependence on test temperature, load, velocity as well as on the sample density and sintering strength. Thus, all numerical setups are studied with a representative collection of those parameters.

### 6.2.1 Compression Tests

Compression tests of simple geometries are the most common characteristic tests to study the mechanical behaviour of granular materials. These tests are widely used in the field of soil mechanics and have also been adopted in the field of snow mechanics. Thus, measurements of compression tests on snow samples are relatively numerous in the literature. In this section, two different kinds of compression tests are simulated in relation to conducted experiments of different authors. The first test is an unconfined compression test with a deformation controlled load plate. The second test is an one-dimensional compression test with the same controlled deformation rates but confining walls. For later comparisons, both tests are conducted on the same variety of virtually prepared snow samples. The test parameters varied are the loading rate $\dot{\varepsilon}_l$ and the temperature $T$. Further, the sample parameters were varied during preparation to study there influence on the snow strength. The sample parameters studied are initial snow density $\rho_0$, grain size $r_g$ and distribution, coordination number $N_b$ of the bonds as well as initial bond strength $r_b$, i.e. size.
The predictions of the unconfined compression test follow the measurements of Kinosita (1967) as well as Von Moos et al. (2003) and Scapozza and Bartelt (2003).
The rigid-confined compression tests are compared to the measurements of Abele and Gow (1975), Yong and Fukue (1977), Fukue (1977) and Yong and Metaxas (1985).

#### 6.2.1.1 Experimental Setup

To avoid edge effects most compression tests are conducted on cylindrical snow samples, e.g. Kinosita (1967) or Von Moos et al. (2003). Hence, the predictions in this section are conducted on cylindrical snow samples of radius $r_c$ and height $h_c$. Fig. 6.6 shows a schematic representation of the wall confined compression test whereby fig. 6.7 shows the unconfined compression test.

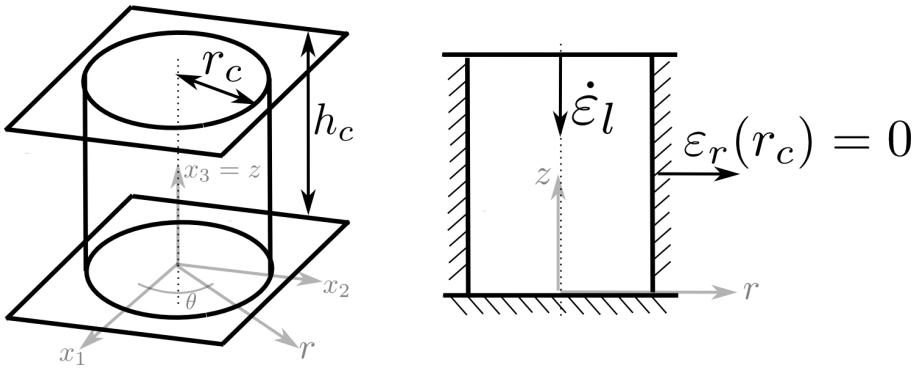


*Figure 6.6: Schematic presentation of confined one-dimensional compression test.*

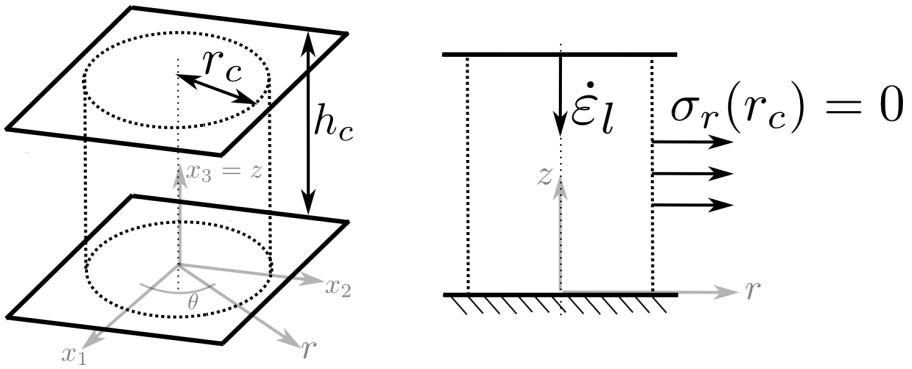


*Figure 6.7: Schematic presentation of unconfined compression test.*

In both configurations, the cylinder axis of the sample is aligned with the $z$ or $x_3$ direction of the coordinate system. The cylindrical snow samples are thereby assembled between a bottom plate and a top load plate. The plate normals point in $z$ direction. The origins of the cartesian coordinate system $(x_1, x_2, x_3)$ are aligned within the plane of the bottom plate. Fig. 6.6 and 6.7 also indicate the cylindrical coordinate system $(r, \theta, z)$ aligning with the Cartesian. Generally, the quantities in this study are described in Cartesian coordinates but for these predictions it is more convenient to apply cylindrical coordinates. Thus, spatially dependent quantities with the indices $r, \theta, z$ describing a component in cylindrical coordinates while of course the Cartesian components carry the indices $1, 2, 3$.
In both compression tests the top plate compacts the sample with a constant load rate $\dot{\varepsilon}_l$ which acts in $-z$, i.e. $-x_3$, direction. The bottom plate is fixed ($\varepsilon_3 = 0$) throughout the entire compression. The confining walls within the one-dimensional compression test

of fig. 6.6 prevent any deformation $\varepsilon_r = 0$ in radial direction at $r = r_c$. In the unconfined compression test the radial deformation of the snow sample is not prevented. Thus, the radial stress $\sigma_r = 0$ at $r = r_c$ is constant throughout the entire deformation. The response

*Table 6.2: Temperatures and Strain Rates of Compression Tests*

| $T$ [ °C] | $-1$ | $-4$ | $-10$ | $-16$ | $-32$ |
|---|---|---|---|---|---|
| $\dot{\varepsilon}_l$ [ $s^{-1}$] | 4.0 | 0.4 | $4 \cdot 10^{-2}$ | $4 \cdot 10^{-3}$ | $4 \cdot 10^{-4}$ | $4 \cdot 10^{-6}$ |

of a snow sample during compression is studied at different temperatures and with different strain rates which are listed in table 6.2. The investigations of Abele and Gow (1975) showed a change in the mechanical behaviour of snow above and below temperatures of $-10$ °C. Thus, the temperatures are chosen to study the ability of the newly developed snow models to capture the behaviour close to the melting point as well as at the low temperatures with very little creep of ice. Several authors showed the transition from ductile to brittle deformation behaviour of snow with an increase of the loading rates above transition rates of $4 \cdot 10^{-3}$ to $4 \cdot 10^{-4}$ $s^{-1}$. Therefore, the compression tests are conducted at the six different strain rates reported in table 6.2 to study the validity of the models at ductile, transitional and brittle deformations of snow.

#### 6.2.1.2 Snow Sample Preparation

Cylindrical snow sample of three different initial densities, ≈400 kg/m$^3$, ≈500 kg/m$^3$ and ≈600 kg/m$^3$ have been prepared by the gravitational deposition method of section 3.5.1. The snow samples are setup with three different grain size distributions of two different radii. The different grain size distributions are produced by the method described in section 3.5.2. The two average radii $\overline{r}_g$ are shown in table 6.3 together with the three distributions of $r_{max}$ and $r_{min}$. In table 6.3, $\pm s$ describes the maximum and minimum deviation with respect to the average radius $\overline{r}_g$. Hence, the average radii are distributed by the rectangular probability function with the deviations of 30%, 15% and 5%.
Table 6.4 shows the initial dimensions and properties of the prepared snow samples. In table 6.4 $\rho_0$ describes the initial density, $r_c$ the initial sample radius, $h_c$ the initial sample height and $N_g$ the number of grains inside a sample. The initial density is thereby predicted as follows:

$$\rho_0 = \frac{1}{V_c} \sum_{i=1}^{N_p} V_p \tag{6.1}$$

where $V_c$ denotes the cylinder volume and $V_p$ a single particle volume. The presented initial densities deviate negligibly with the grain size distributions ( max. ±0.8%). The

*Table 6.3: Grain Size Distribution of Snow Sample of Compression Tests*

| | $\overline{r}_g$ [ mm] | | | |
|---|---|---|---|---|
| | 2.480 | | 0.124 | |
| $\pm s$ [%] | $r_{max}$ | $r_{min}$ | $r_{max}$ | $r_{min}$ |
| ±5 | 2.604 | 2.356 | 0.1302 | 0.1178 |
| ±15 | 2.852 | 2.108 | 0.1426 | 0.1054 |
| ±30 | 3.224 | 1.736 | 0.1612 | 0.0868 |

*Table 6.4: Initial Dimensions and Densities of Snow Sample of Compression Tests*

| **Sample** | $\rho_0$ [kg/m$^3$] | $2 \cdot r_c$ [ mm] | $h_c$ [ mm] | $N_g$ |
|---|---|---|---|---|
| **1.** | 408 ±0.7% | 58.0 | 86.0 | ≈1700 |
| **2.** | 509 ±0.6% | 2.9 | 3.92 | ≈1700 |
| **3.** | 509 ±0.7% | 5.8 | 8.4 | ≈13950 |
| **4.** | 509 ±0.7% | 116.1 | 167.3 | ≈13950 |
| **5.** | 511 ±0.8% | 58.0 | 74.4 | ≈1700 |
| **6.** | 580 ±0.7% | 5.8 | 7.4 | ≈13950 |
| **7.** | 580 ±0.7% | 116.1 | 147.4 | ≈13950 |

compression tests are conducted on samples with about 1700 and 13950 grains per sample. This large difference was chosen to prove the independence of the results on the number of grains.
Fig. 6.8 shows the samples 1, 5 and 7 to visualise the properties of table 6.4. The figure shows the sample structure by grains and adjoining bonds in the left column. The initial densities increase from top to bottom together with the number of grains.
In the right column of fig. 6.8 the respective density distributions are shown. These initial density distributions are predicted by eq. 5.8 by means of the Voronoi tessellation. The Voronoi tessellation is described in chapter 5.4.2 and in detail by Rycroft (2007).
Fig. 6.9 depicts a slice through the density distribution of fig. 6.8. With increasing initial

sample density the slices depict the densification of the field.

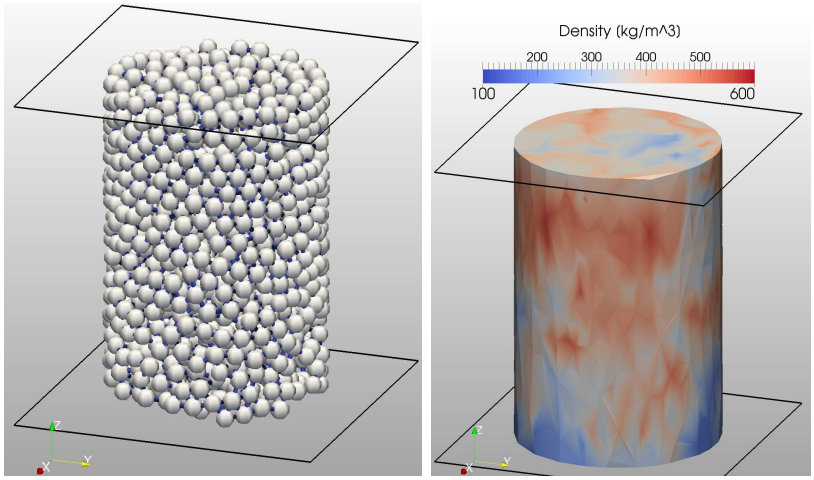


**S.1.** $\rho_0 \approx 408 \mathrm{kg/m^3}$ $N_g \approx 1700$

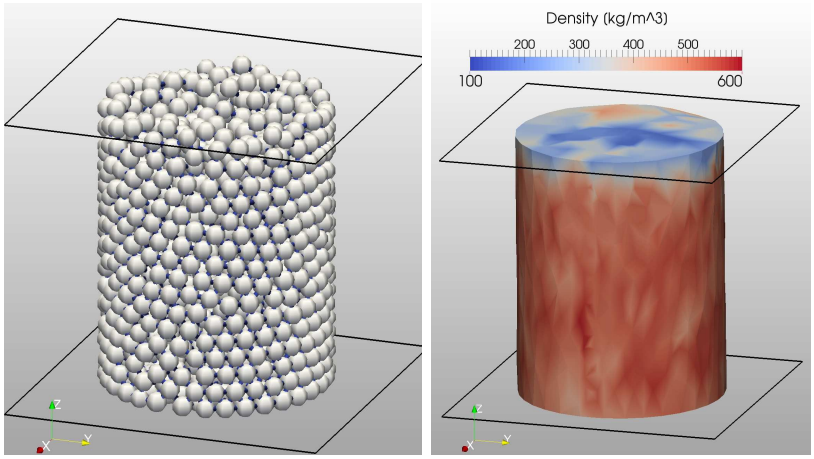


**S.5.** $\rho_0 \approx 511 \mathrm{kg/m^3}$ $N_g \approx 1700$

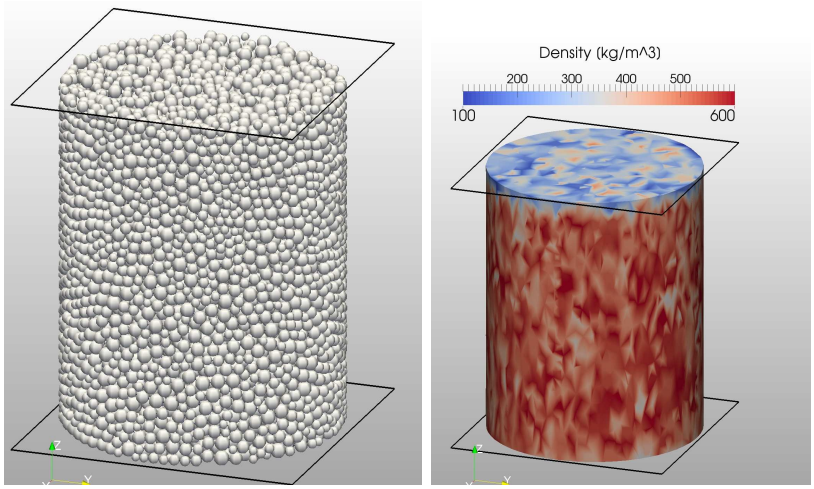


**S.7.** $\rho_0 \approx 580 \mathrm{kg/m^3}$ $N_g \approx 13950$

*Figure 6.8: Grain and Bond Structure of three cylindrical snow sample in left column. Density distribution in right column.*

Also the dependencies of the initial bond strength and coordination number are supposed

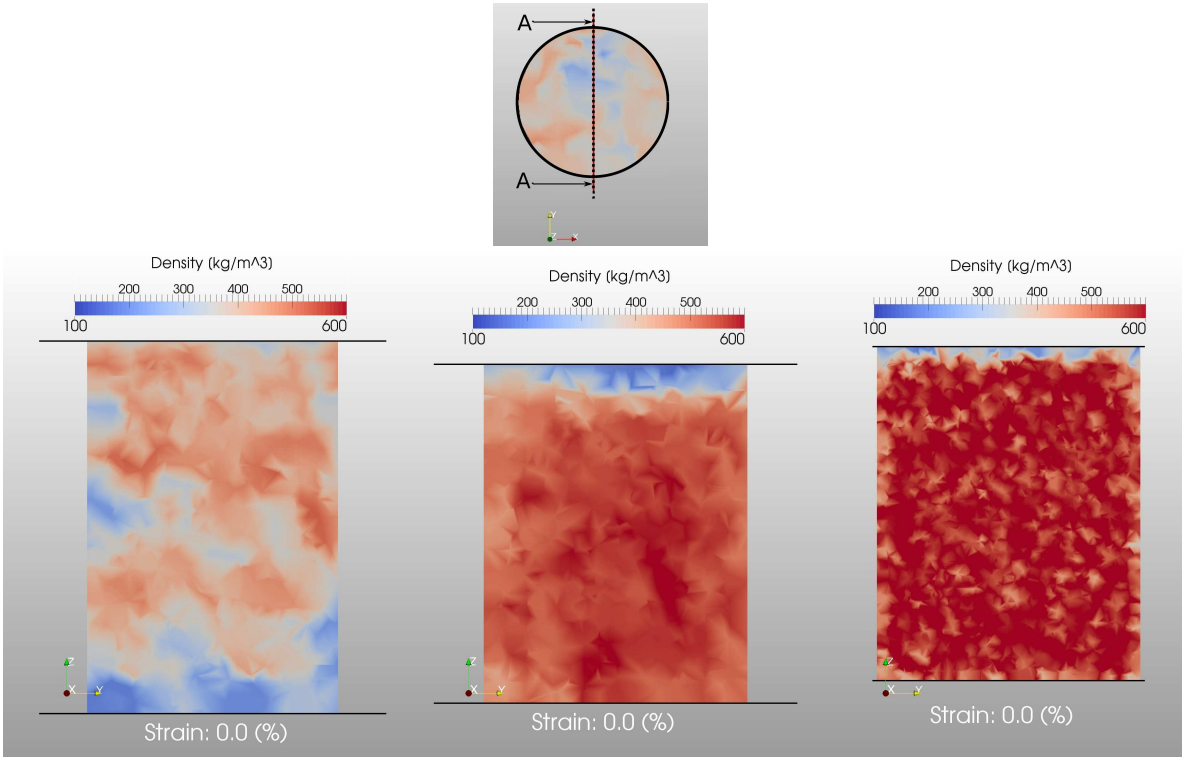


*(a) S.1. of* 408 kg/m$^3$ *(b) S.5. of* 511 kg/m$^3$ *(c) S.7. of* 580 kg/m$^3$

*Figure 6.9: Density distribution in slice through cylindrical snow samples.*

to be studied by the compression tests. Therefore, table 6.5 shows the variation of the initial properties of the preprocessed bond structure. The ratio $\frac{r_b}{\overline{r}_g}$ between bond and

*Table 6.5: Initial Bonding Properties of Snow Sample of Compression Tests*

| | | | | | | | | |
|---|---|---|---|---|---|---|---|---|
| $\frac{r_b}{\overline{r}_g}$ | 0.0 | 0.1 | 0.3 | 0.3 | 0.3 | 0.5 | 0.5 | 0.9 |
| $N_b$ | 0.0 | 1.0 | 2.5 | 3.0 | 3.5 | 3.0 | 3.5 | 4.0 |

grain radius is used to setup the initial bond size according to eq. 3.77. The average number of bonds per grain $N_b$ of a snow sample is predicted by eq. 3.76. In table 6.5, the bonding configuration of $\frac{r_b}{\overline{r}_g} = 0.0$ and $N_b = 0.0$ indicates that no initial bond structure is constructed. Fig. 6.10 shows three example bond structures of the three samples already used in the previous figures.

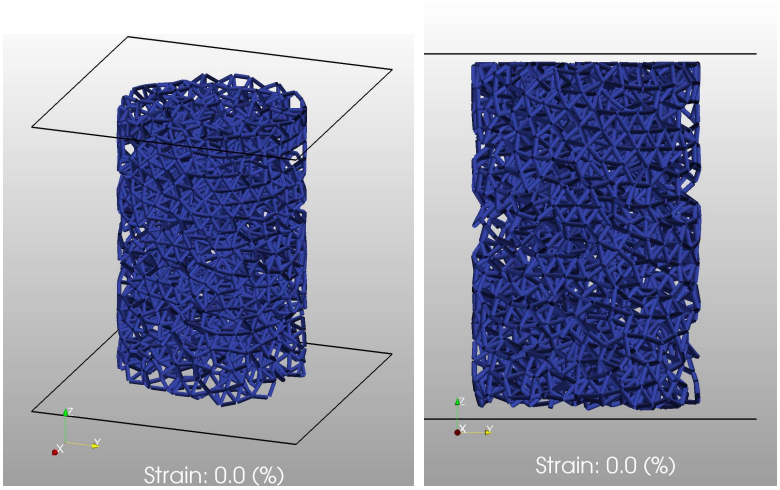


**S.1.** $\frac{r_b}{\overline{r}_g} = 0.5,\ N_b = 3$

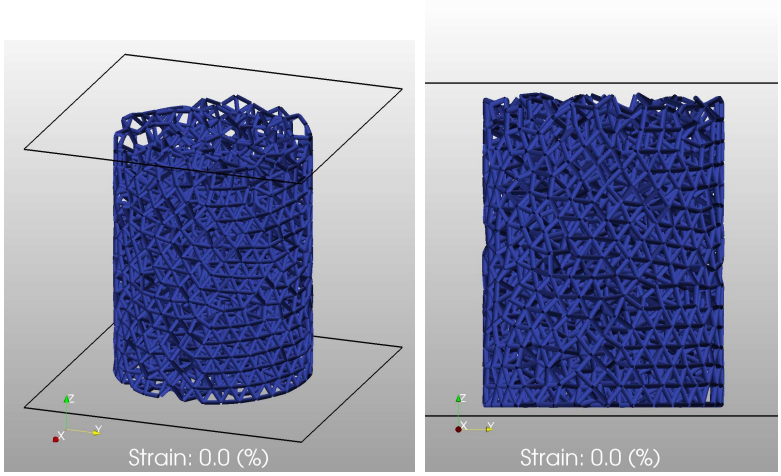


**S.5.** $\frac{r_b}{\overline{r}_g} = 0.5,\ N_b = 3.5$

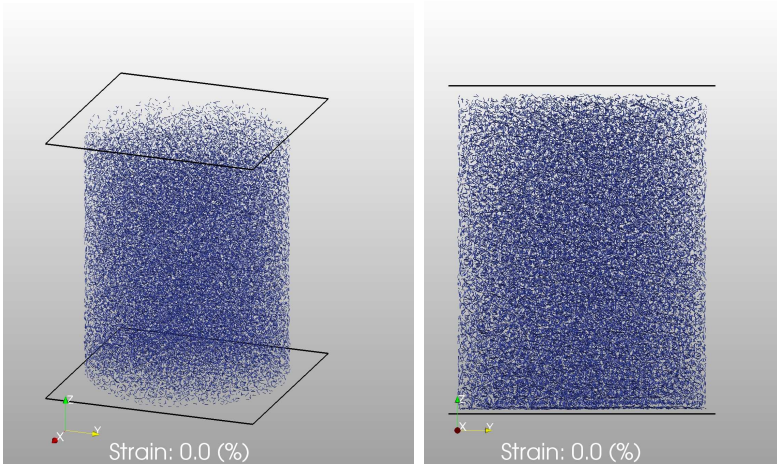


**S.7.** $\frac{r_b}{\overline{r}_g} = 0.1,\ N_b = 3$

*Figure 6.10: Bond Structure of three cylindrical snow sample.*

#### 6.2.1.3 Unconfined Strain - Stress Relationship of Snow

A large number of predictions of compression tests of cylindrical snow samples have been conducted under unconfined conditions and various parameter configurations. Under the various parameters studied the strain rate $\dot{\varepsilon}_l$ of the tests appeared to be most suitable to characterise the principal deformation behaviour of snow. By this measure the relationship between stress and strain can be divided into brittle and ductile behaviour of snow. Further, a third additional regime can be defined as a combined behaviour of brittle and ductile, hereafter called the transitional behaviour. This separation of the mechanical snow behaviour by the strain rate is well established in the field snow mechanics and thus has been found and stated previously in several experimental studies, for instance by Kinosita (1967), Narita (1984) and Fukue (1977). From the experimental results of Kinosita (1967) and Fukue (1977) the transitional behaviour can roughly be defined at strain rates close to $5 \cdot 10^{-4}$ s$^{-1}$. The brittle behaviour of snow is therefore apparent at strain rates above the transition rate while the snow deforms plastic at rates below $5 \cdot 10^{-4}$ s$^{-1}$. These strain rate dependent behaviour was also found within the predictions of snow under load in this study. This section starts with the description of the typical features of the three individual regimes observed in the predictions. Those descriptions are followed by an overview on the relationship between strain rate and behaviour as well as strength of snow. The two final sections analyse the micro-structural and temperature dependence of the unconfined snow performance. The results are compared to measurements found in the literature.

##### Brittle Deformation Behaviour

Fig. 6.11 depicts typical strain-stress curves observed in the predictions of brittle deformation of unconfined snow samples at strain rates equal to and larger then $4 \cdot 10^{-3}$ s$^{-1}$. The two curves were predicted at similar initial sample densities, i.e. 408 kg/m$^3$, but at two different compression rates, i.e. $4 \cdot 10^{-2}$ s$^{-1}$ and $4 \cdot 10^{-3}$ s$^{-1}$. Fig. 6.11 also depicts an experimental curve of the unconfined compression tests by Kinosita (1967) at a similar strain rate of $\dot{\varepsilon}_l = 10^{-3}$ s$^{-1}$.The predicted curves show the same saw-tooth shape as the experimental result. The difference in strength due to rate, temperature and bonding properties will be discussed in the following sections. The saw-tooth shapes of the curves is a typical characteristic of the brittle deformation behaviour and similar to other brittle material, as already shown in fig. 2.19 and 2.21 and discussed in section 2.1.2. The strain-stress curve of brittle deformation of snow has been described by several authors as a roughly linear increase of the stress with increasing strain. When a certain stress value is reached, an abrupt decrease in stress with no notable portion of plastic deformation can be observed. With further progressing strain the stress increases again with almost the same gradient as the previous increase. When the stress reaches approximately the same threshold the sudden rupture of the curve reoccurs. The maximum stress reached over the repeated ruptures is defined as the strength or yield stress $\sigma_y$ of the brittle deformed sample. The build up and sudden decrease in stress is repeated over the entire time of the sample deformation. This was the case throughout all brittle predictions of the sample with similar bonding properties as shown in fig. 6.11. Fukue (1977) also observed this behaviour in his unconfined compression tests specifically for moderately bonded snow.

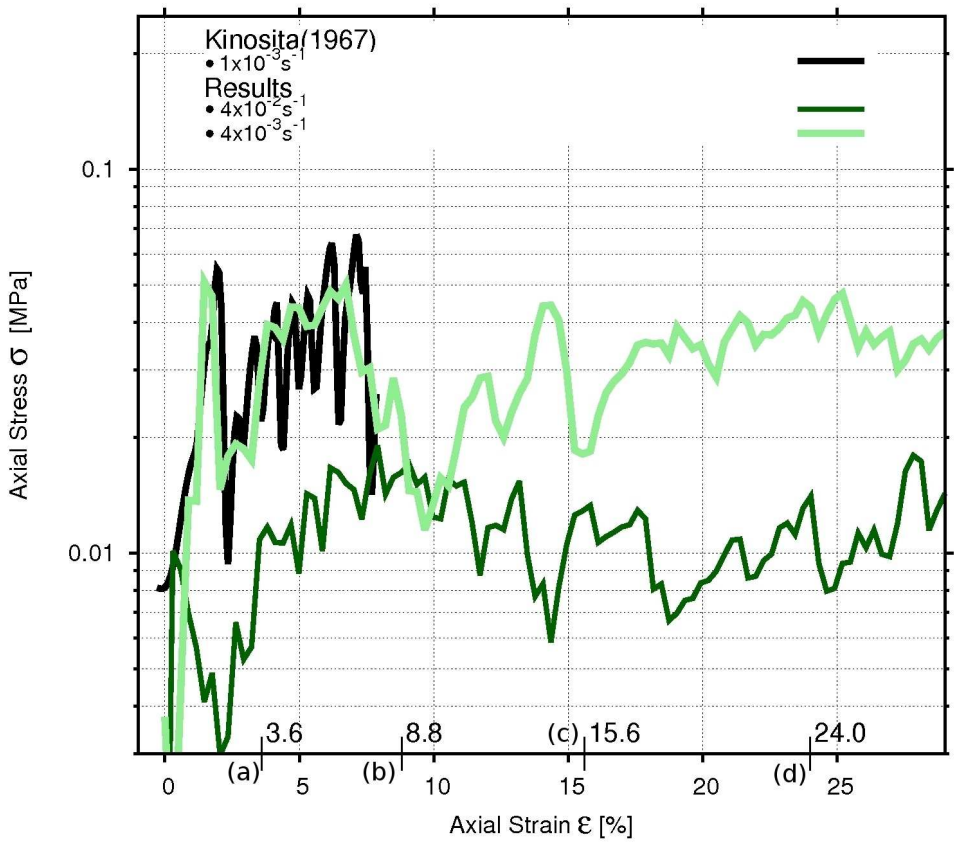


*Figure 6.11: Unconfined compression of a cylindrical snow sample with brittle loading rates. The green lines are the predicted results of the initial sample density is* 408 kg/m$^3$ *at different brittle rates. The black curve is a unconfined compression test of Kinosita (1967) at the brittle rate of about* $10^{-3}$ s$^{-1}$.

In fig. 6.12, the deformed sample of the curve corresponding to a strain rate of $\dot{\varepsilon}_l = 4 \cdot 10^{-2}$ s$^{-1}$ in fig. 6.11 is shown at four progressing strain states. The four states are labelled with (a),(b),(c) and (d) on the $\varepsilon$ axis of fig. 6.11. The snow sample is compressed at a temperature of $-16$ °C and has initial bonding properties of $N_b = 3.0$ and $\frac{r_b}{\overline{r}_g} = 0.5$. Fig. 6.13 visualises the bond structure at the selected states of deformation. Thereby, the bond structure is coloured by its normal stress component. Only half of the sample is shown to allow an inside view. Negative normal stress is thereby defined as stress developed due to compression while positive stress indicates the tension of a bond.
The continuous build up of stress peaks is caused several mechanism interacting. After each rupture loose grains re-arrange and re-bond and thereby forming new force, i.e. stress, chains. Also the remaining bond structure builds up a new stress distribution and forms new bonds and contacts with the re-arranged grains.

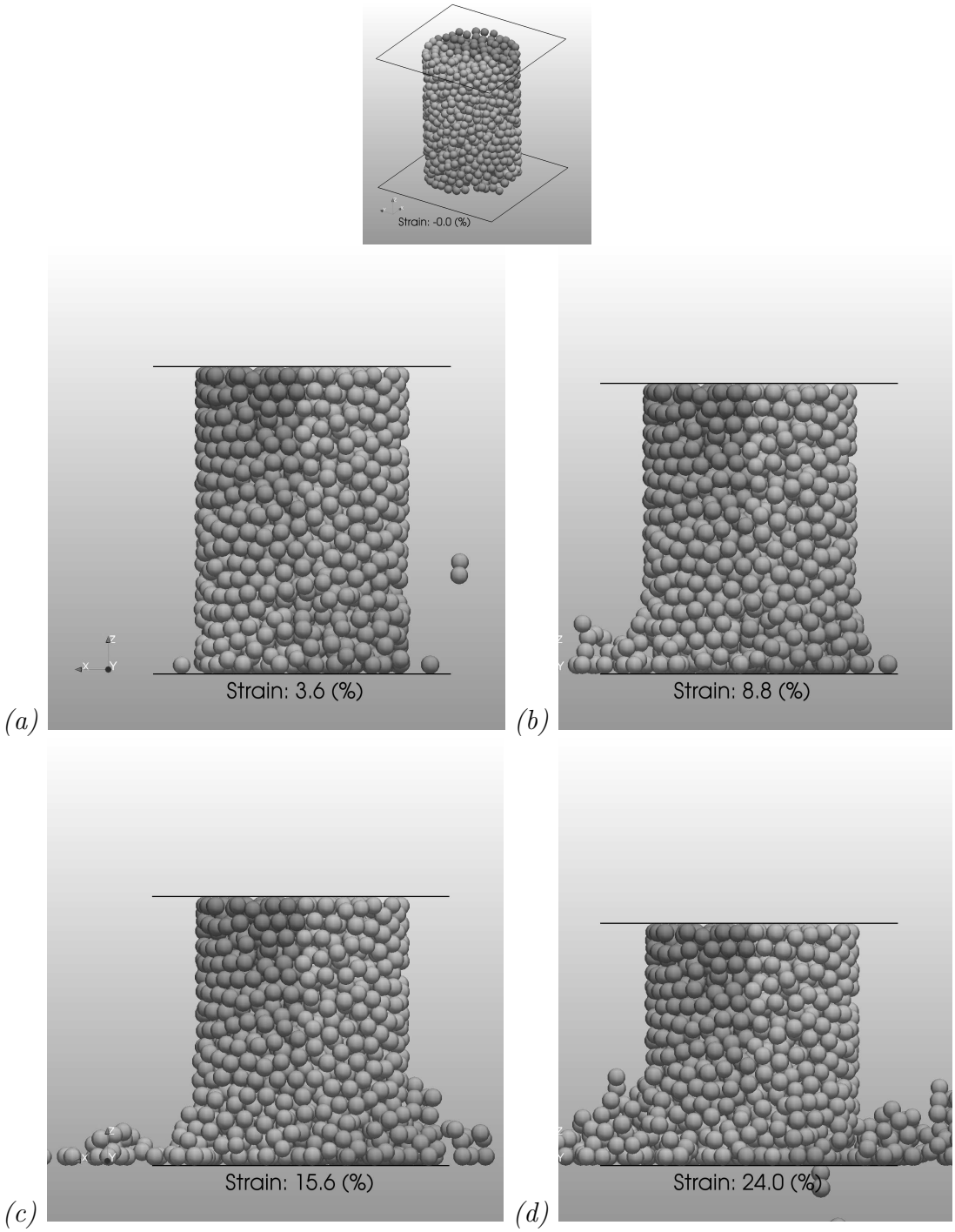


*Figure 6.12: Unconfined compression of a cylindrical snow sample by a brittle compression rate of* $4 \cdot 10^{-2}$ $\mathrm{s}^{-1}$. *The initial sample density equals* 408 $\mathrm{kg/m^3}$. *The temperature is* $-16$ °C *and the initial bonding parameters are* $N_b = 3.0$ *and* $\frac{r_b}{\overline{r}_g} = 0.5$.

The continuous rupture of the brittle strain-stress curve about an almost constant magnitude is caused by a pure surface fracture close to the ends of the snow sample. This

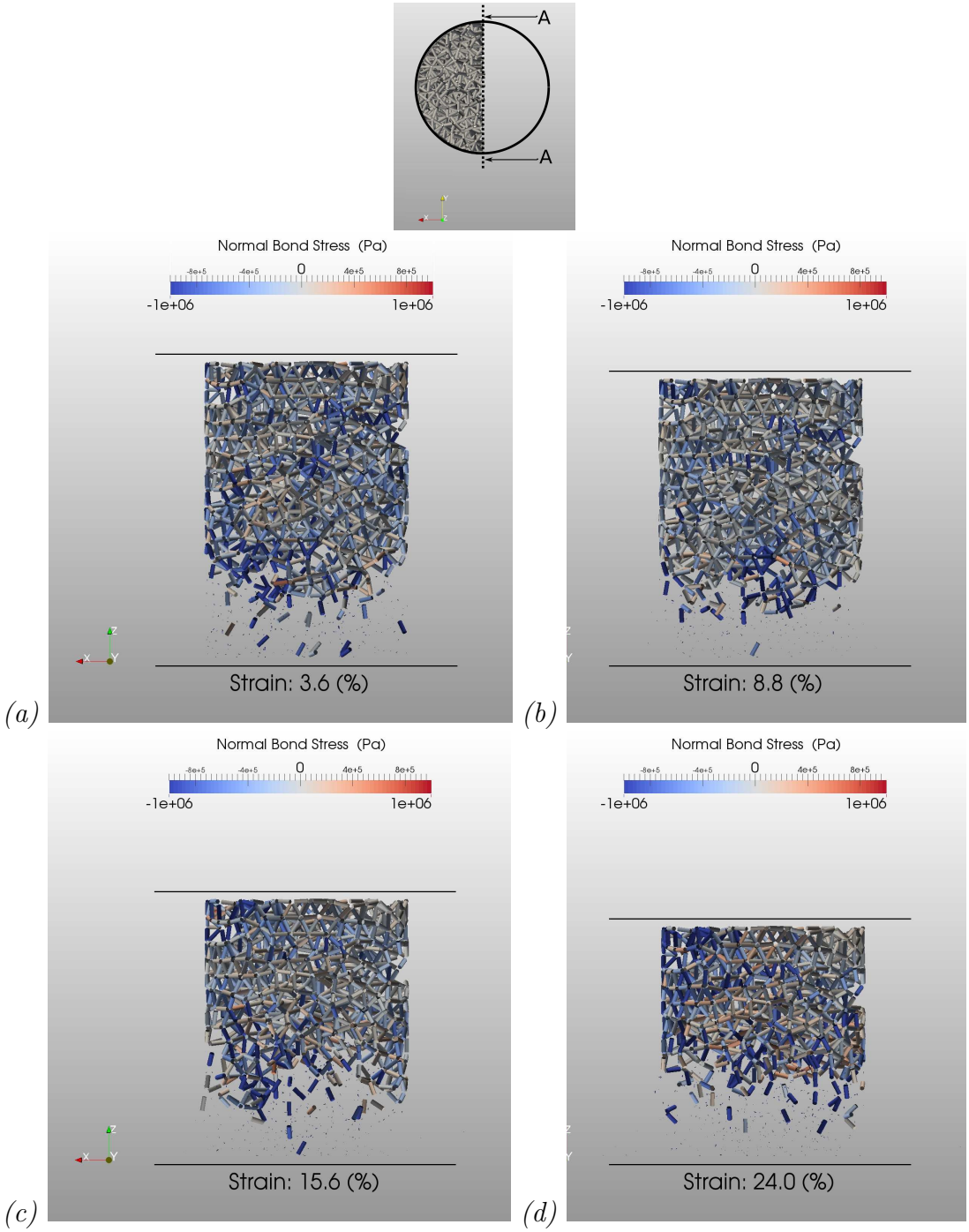


*Figure 6.13: Unconfined compression of a cylindrical snow sample by the pure brittle compression rate of* $4 \cdot 10^{-2}$ $\mathrm{s}^{-1}$. *The bond structure of the sample is depict at increasing strain states and coloured by the normal stress component (- compression / + tension). The initial sample density equals* 408 $\mathrm{kg/m^3}$. *A temperature of* $-16$ °C *is applied and the initial bonding parameters are* $N_b = 3.0$ *and* $\frac{r_b}{\overline{r}_g} = 0.5$.

surface fracture is depicted in fig. 6.12.
Kinosita (1967) described this type of brittle fracture as a non-uniform contraction with break downs concentrated at the sample end. The failure is taking place at the top or bottom of the snow cylinder. In fig. 6.12, the snow sample starts to rupture at its bottom part. Several small portions and single grains are breaking off. The fracture progresses into the sample with progressing strain while the upper portion remains unchanged by the brittle deformation. The bonds between grains, in fig. 6.13, rupture and the grains are either ejected or packed into the center between sample and end surface. The same behaviour was observed by Kinosita (1967) in his brittle compression tests of unconfined snow samples which are depicted in fig. 2.18. In fig. 6.13, it has to be noted that exclusively the bonds near the end of the sample are broken. The upper or remaining part of the bonds are almost entirely unaffected by the brittle deformation. The majority of bonds in the remaining portion of the sample develops minor or no stress as depicted by the normal component in fig. 6.13. Under the high strain rate applied, this and the almost linear stress increase of the curves indicate that the bonds have no time to relax stress. Thus, the creep of ice employed by the models of eq. 3.57 and 3.63 does not play a significant role in this deformation mechanism.
The phenomenon of no bond stress in the remaining sample portion is even more apparent with higher strain rates and denser samples as exemplified in fig. 6.14.

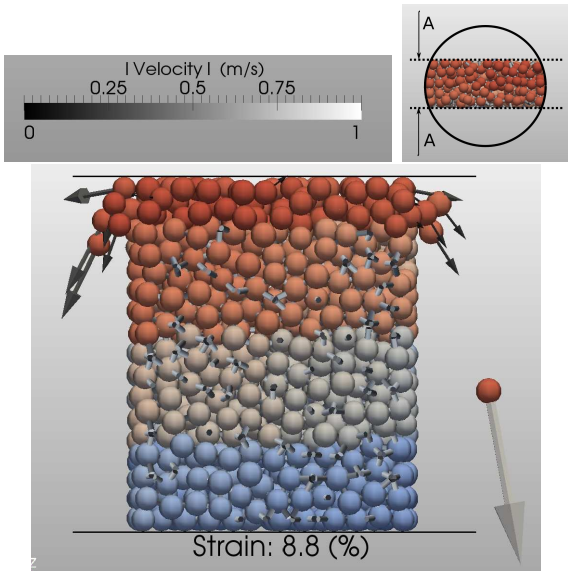


*The snow grains are coloured to allow visual tracking.*

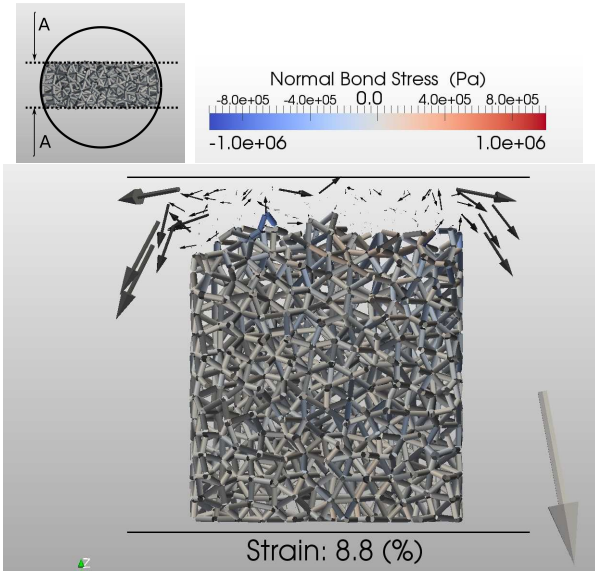


*The bond structure is coloured by the normal stress component.*

*Figure 6.14: Unconfined compression at* 8.8% *strain of a cylindrical snow sample by a brittle compression rate of* $4 \cdot 10^{-1}$ $s^{-1}$. *The initial sample density equals* 511 $kg/m^3$. *A temperature of* $-10$ °C *is applied and the initial bonding parameters are* $N_b = 3.5$ *and* $\frac{r_b}{\overline{r}_g} = 0.5$. *The arrows indicate the particle velocity.*

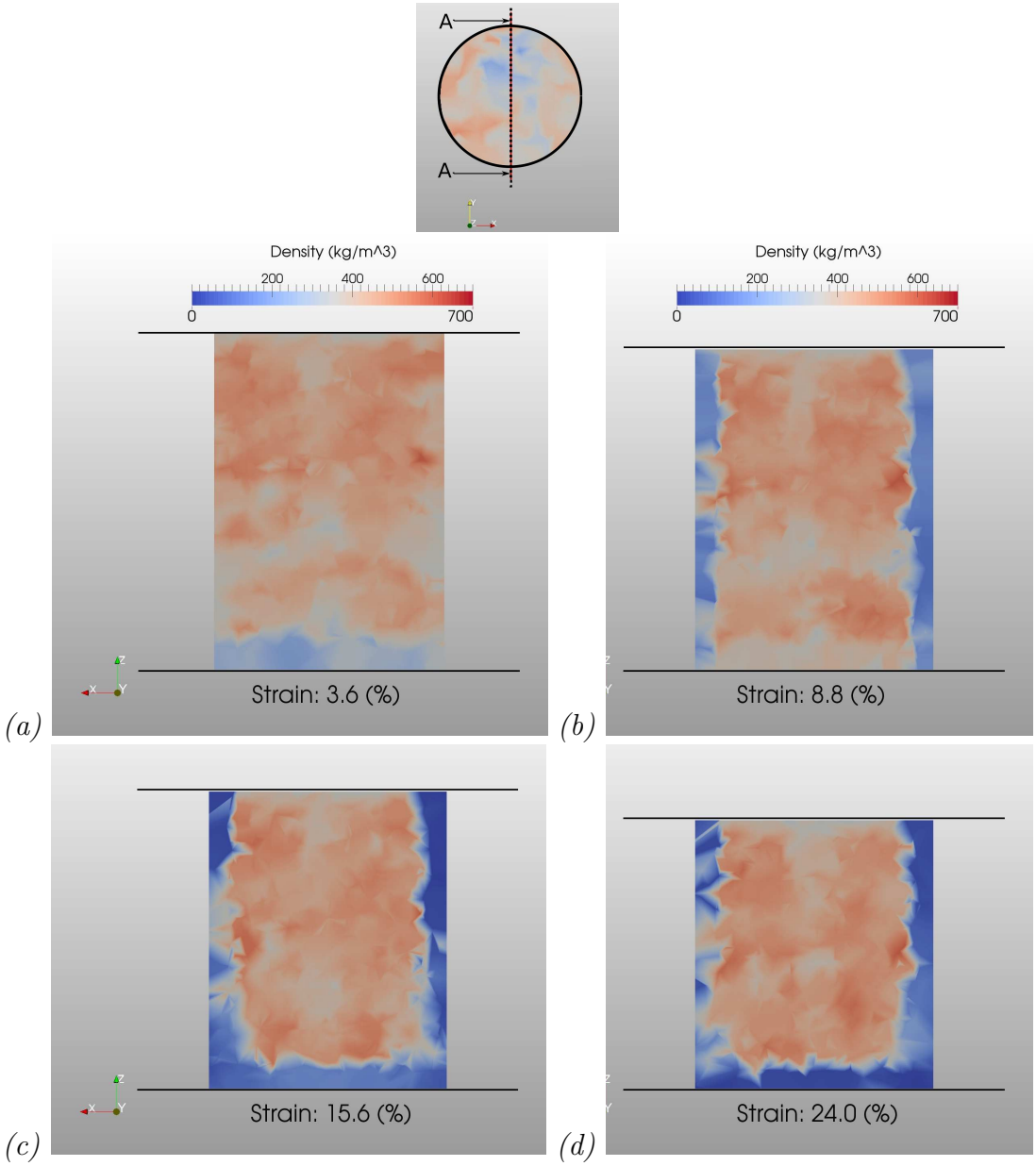


*Figure 6.15: The density distribution of the sample is depicted at increasing strain states for an unconfined compression of a cylindrical snow sample by a brittle compression rate of* $4 \cdot 10^{-2}$ $\mathrm{s}^{-1}$. *The initial sample density equals* 408 $\mathrm{kg/m^3}$. *A temperature of* $-16$ °C *is applied and the initial bonding parameters are* $N_b = 3.0$ *and* $\frac{r_b}{\overline{r}_g} = 0.5$.

The snow sample depicted has an initial density of 511 $\mathrm{kg/m^3}$ and is loaded with a rate of $4 \cdot 10^{-1}$ $\mathrm{s}^{-1}$. The snow grains and bond structure are shown at a strain state of 8.8% together with the velocity field of the particles.
In fig. 6.14, the sample fracture onsets at the upper load plate and progresses with increasing strain. In this case the remaining part is the lower portion of the sample. The velocity field visualises the break off of the upper snow grains. For the higher density and rate

compression of fig. 6.14, the remaining bond structure carries almost no load. Under high rate loading almost all deformation energy is released by the surface fracture mechanism. As mentioned, Kinosita (1967) observed the fracture behaviour on either end of the snow samples. Also in the predictions of this study the samples fractured brittle on one of the ends of the cylindrical samples which is already exemplified by the two samples in fig. 6.12 and 6.14, respectively. The predictions showed that the onset of the fracture surface correlates with lower density end of the sample. Fig. 6.9a and 6.9b show the initial density distributions of the represented 408 kg/m$^3$ and 511 kg/m$^3$ snow sample, respectively. The sample with initial density of 408 kg/m$^3$ shows a slight decrease in density towards the bottom while the sample of 511 kg/m$^3$ is weakest at the top end. In both cases this is the location of the onset of brittle fracture. A lower density causes less bonding possibilities and thus results in a weaker snow layer compared to the rest of the sample.
Fig. 6.15 shows the density field of the snow sample of 408 kg/m$^3$ used in fig. 6.12 at the selected strain states. The figure shows a slice through the center over the sample height. The density fields remain almost constant in the unfractured upper part of the snow sample at the increasing strain states.

### Transitional Deformation Behaviour

Three typical strain-stress curves of unconfined compression tests at the transition rate of $4 \cdot 10^{-4}$ s$^{-1}$ are shown in fig. 6.16. The profiles shown in fig. 6.16 are predicted at equal initial densities of 408 kg/m$^3$, but at the three temperatures $-4$ °C, $-10$ °C and $-16$ °C, respectively. Fig. 6.16 also contains experimental predictions by Chandel et al. (2014) at similar strain rates of $4.8 \cdot 10^{-4}$ s$^{-1}$ and $7.2 \cdot 10^{-3}$ s$^{-1}$.
The strain-stress curves predicted in transition regime between brittle and ductile behaviour lack any abrupt rupture. The stress increases viscoelastic with strain, until the yield stress is reached, followed by a strain-softening behaviour. The viscous stress build up and decrease, i.e. subsequent strain hardening and softening phases, can re-occur similarly once or twice after the first stress decrease with progressing compression as shown fig. 6.16. Eventually, all predicted curves in the transition regime show a decrease in stress with ascending strain caused by strain-softening of the samples. The measurements by Chandel et al. (2014) identified a rate of $2 \cdot 10^{-4}$ s$^{-1}$ as the strain rate of snow at which the softening effect is mainly observed. This coincides very well with the predicted results in this study. The strength $\sigma_y$ of the snow sample deformed under a transition rate is defined as the maximum stress reached over the entire deformation.
Fig. 6.17 visualizes the sample at the temperature of $-10$ °C of fig. 6.16. The bond structure of the sample has a coordination number of $N_b = 3.5$ and a bond radius of $\frac{r_b}{\overline{r}_g} = 0.5$. The deformed sample is shown with an axial strain of 1.6%, 5.2%, 20.8% and 27.6%. The bond structure of the same snow sample is depict in fig. 6.18 at the same states of deformation. The sample is again cut along its length to depict the bond structure coloured by its normal stress component. Negative normal stress is thereby defined as stress developed due to compression while positive indicates tension of the bond. Fig. 6.19 shows the density field of the snow sample of 408 kg/m$^3$ used in fig. 6.17 at the same strain states.
Fig. 6.17a at the strain state of 1.6% shows the deformed sample during the phase of

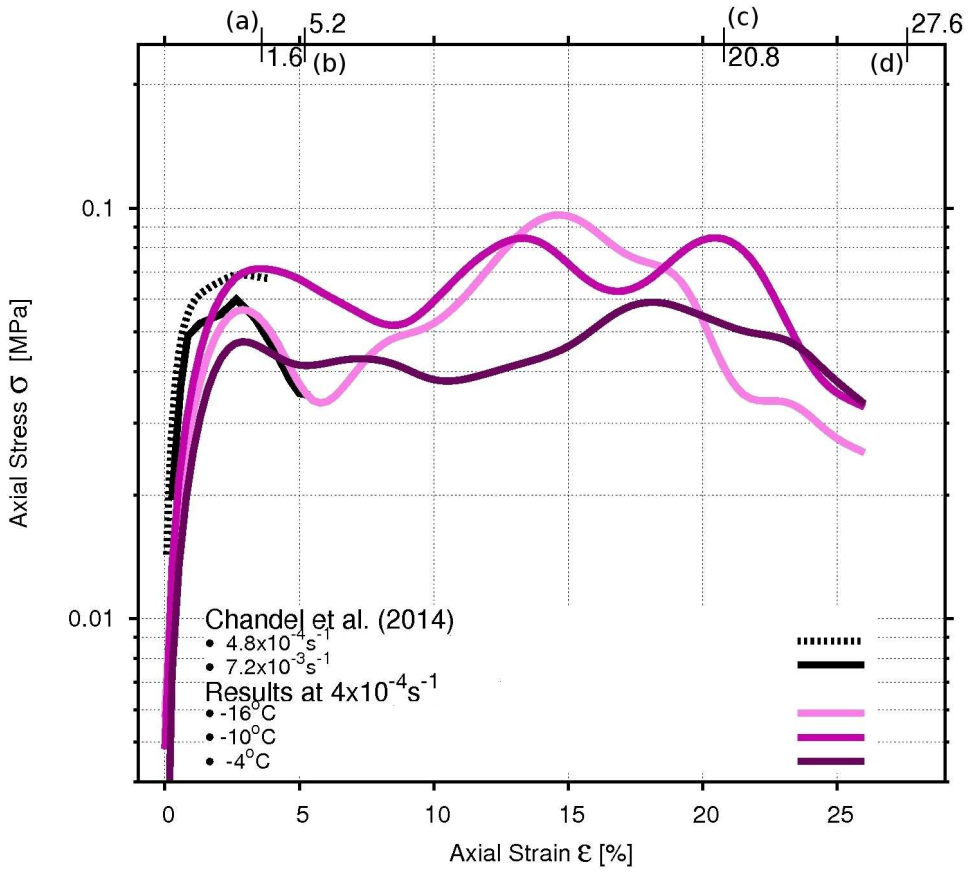


*Figure 6.16: Unconfined compression of a cylindrical snow sample of* 408 kg/m$^3$ *in the transition regime between ductile and brittle behaviour. The purple curves show the predicted results at different temperatures. The black curves depict unconfined compression tests of Chandel et al. (2014) at transition rates.*

the initial viscoelastic stress increase. At this state the sample in fig. 6.17 is contracted uniformly with no change in shape. The bond structure at the strain state of 1.6% in fig. 6.18a has not experienced any fracture. Further, the bonds developed a stress state in accordance to the deformations undertaken by the sample. Under the lower strain rate in contrast to brittle rates, the developed bond stress and the non-linear stress increase of the curves reveal that the bonds have time to grow and relax stress due to the creep models employed, eq. 3.57 and 3.63. However, the bonds can still not avoid failure entirely. These circumstances result in the subsequent strain hardening and softening phases observed in fig. 6.16.
The strain states of 5.2% and 20.8% depict the sample at the first and final onset of strain-softening identified in fig. 6.16. In fig. 6.17b at the strain of 5.2%, the snow sample apparently still holds the cylindrical shape while at 20.8% a non-uniform deformation is

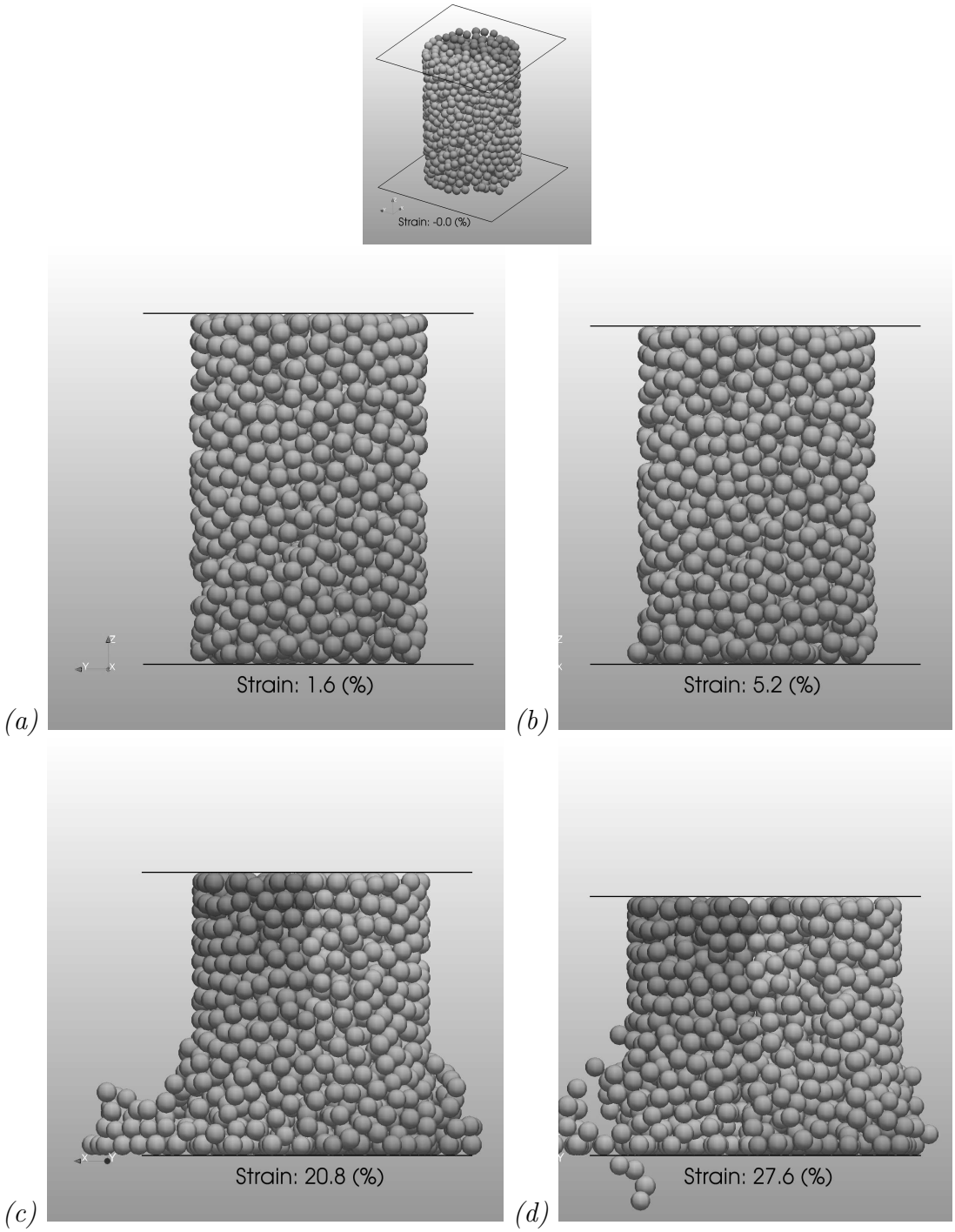


*Figure 6.17: Unconfined compression by a transition rate of* $4 \cdot 10^{-4}$ $\mathrm{s}^{-1}$. *The initial sample density equals* 408 $\mathrm{kg/m^3}$. *The temperature is* $-10$ °C *and the bonding parameters are* $N_b = 3.5$ *and* $\frac{r_b}{\overline{r}_g} = 0.5$.

observable. At the strain state of 20.8%, fig. 6.17c shows major pieces, i.e. grain agglomerations, of the sample have broken off. In fig. 6.18 both strain states show the same failure

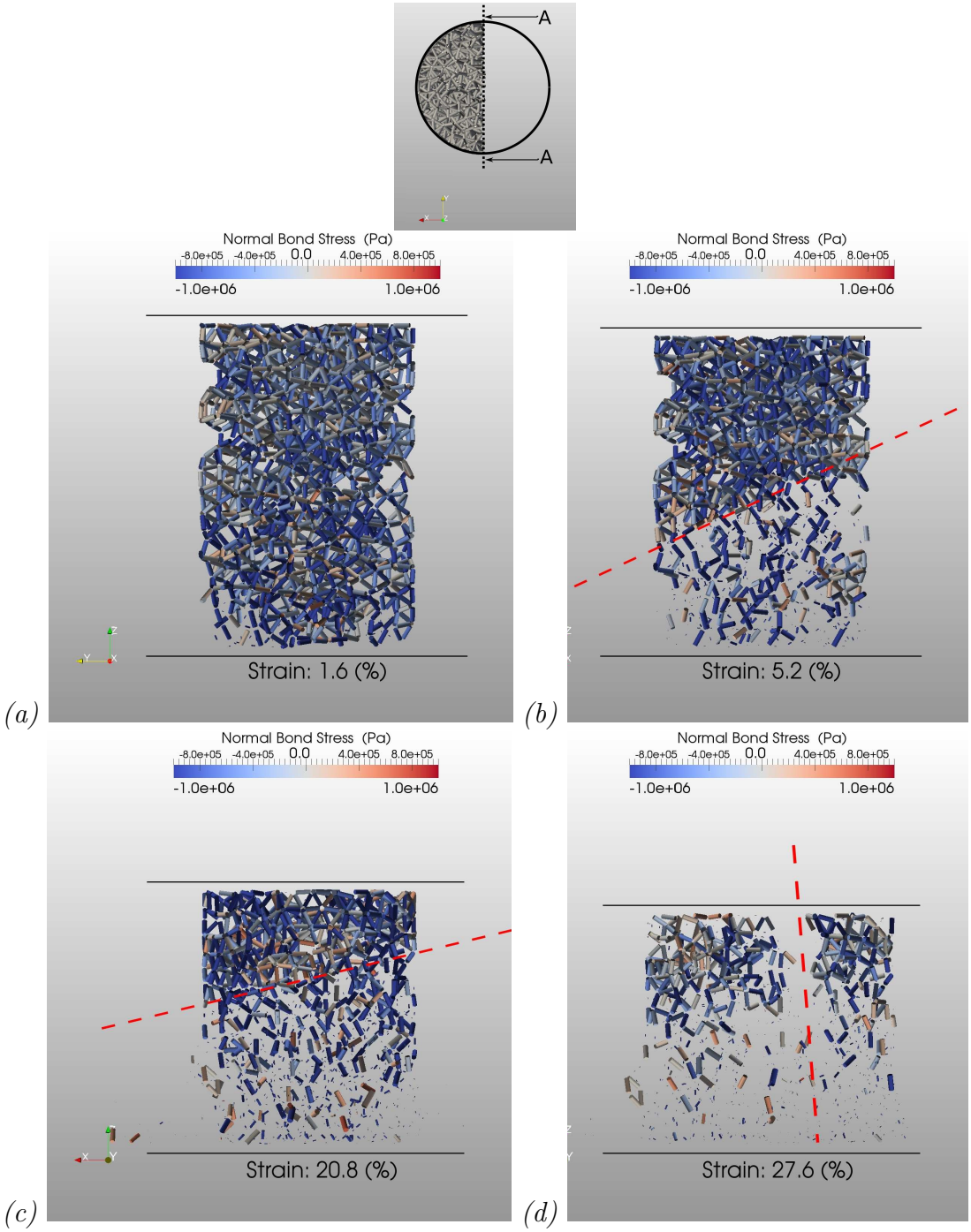


*Figure 6.18: The bond structure is depicted at increasing strain states and coloured by the normal stress component (- compression / + tension). An unconfined compression rate of* $4 \cdot 10^{-4}$ $\mathrm{s}^{-1}$ *is applied. The initial sample density equals* 408 $\mathrm{kg/m^3}$*. The temperature is* $-10$ °C *and the bonding parameters are* $N_b = 3.5$ *and* $\frac{r_b}{\overline{r}_g} = 0.5$*. A red dashed line indicates a fracture surface.*

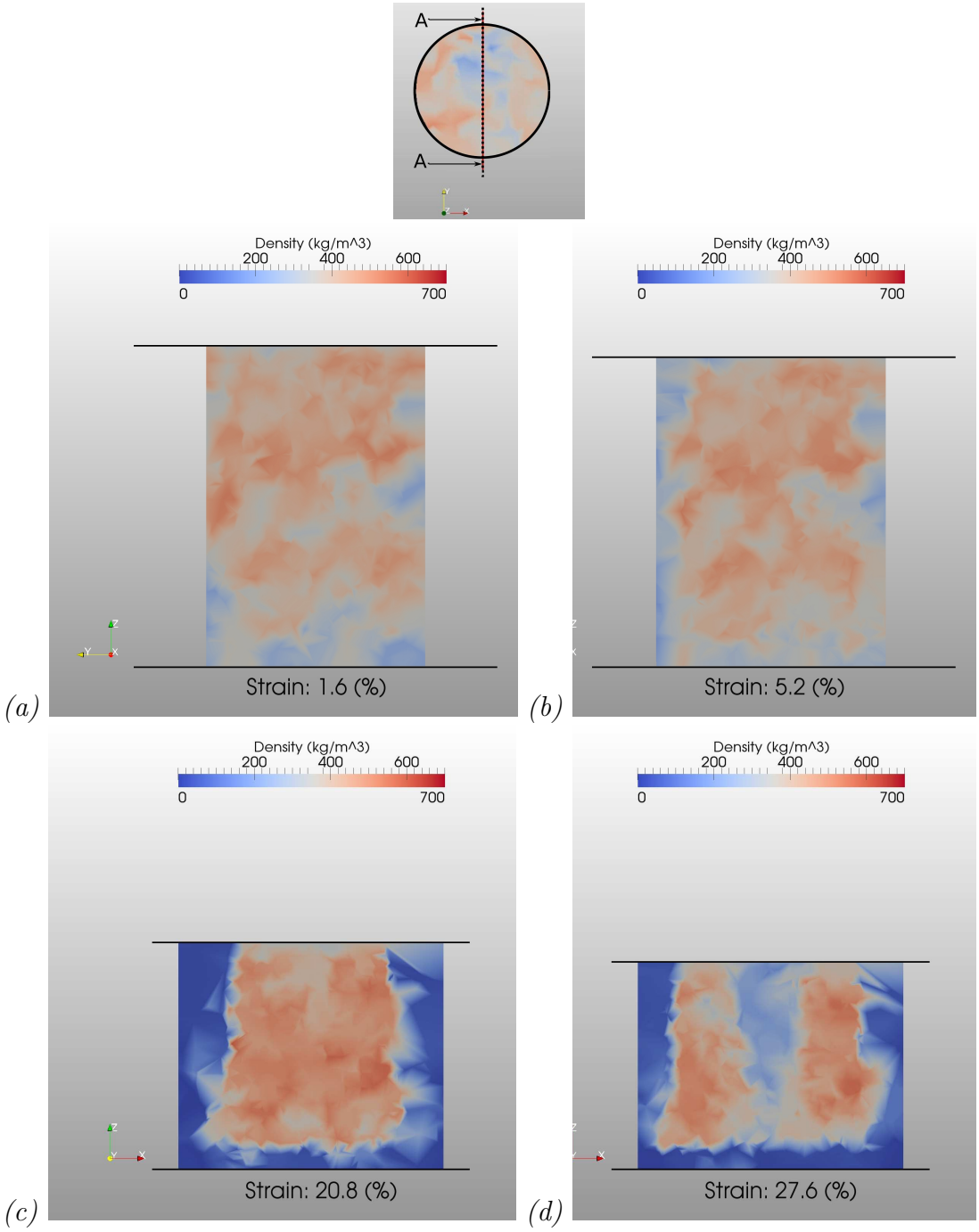


*Figure 6.19: The density distribution is depicted at increasing strain states. An unconfined compression rate of* $4 \cdot 10^{-4}$ $\mathrm{s}^{-1}$ *is applied. The initial sample density equals* 408 $\mathrm{kg/m^3}$. *The temperature is* $-10$ °C *and the bonding parameters are* $N_b = 3.5$ *and* $\frac{r_b}{\overline{r}_g} = 0.5$.

patterns. The majority of bonds beneath a certain fracture plane vanished. The fracture surface is identified as an inclined plane through the sample which is indicated by the red

dashed lines in fig. 6.18b and 6.18c. After each stress build up a new fracture surface develops due to the rupture of the majority of bonds between the new and the previous surface. Fukue (1977) observed a similar fracture type which is shown as type 2 in fig. 2.28. He described this type of fracture as multiple plane failure. The remaining bonds between the grains above and below any fracture surface still develop stress in accordance to the sample deformation. Within the volume of fracture below the fracture surfaces a certain portion of bonds remained. These bonds are mainly oriented into the direction of loading. This indicates the rupture of bonds was caused by the shear stresses developed.
The strain state of 27.6%, in fig. 6.16, indicates that the sample during the final period of strain-softening breaks apart gradually. Due to the decreasing number of bonds, particularly in the direction perpendicular to the loading direction, the sample weakens gradually. Major cracks develop along the length of the sample which are also visible in the final density distribution of fig. 6.19.
At any stage of the deformation of an unconfined snow sample by a transition rate the intra- and inter-granular creep models of ice employed, by eq. 3.2, play a major role for the macroscopic observed behaviour. Under a slower sample deformation, the bonds between grains are able to relax portions of the stress due to creep but can still not avoid failure entirely. Hence, the employed bond growth of eq. 3.63 has time to act at the transition strain rate. New bonds have time to develop under stress between compressed grains, but they do not reach enough strength to prevent failure of the sample.

### Ductile Deformation Behaviour

Two typical strain-stress curves predicted by the unconfined compression tests at the ductile strain rate of $4 \cdot 10^{-6}$ s$^{-1}$ are shown in fig. 6.20. The numerical samples are of equal initial densities 408 kg/m$^3$ but different initial bonding properties, i.e. the coordination numbers $N_b = (3.0; 4.0)$ and the bond radii $\frac{r_b}{\overline{r}_g} = (0.5; 0.9)$. Fig. 6.20 also includes experimental results by Scapozza and Bartelt (2003), von Moos (2001) and Chandel et al. (2014) at similar strain rates and temperatures.
In fig. 6.20, the strain-stress curves predicted under ductile deformation demonstrate an initial viscous-elastic stress increase with a high stiffness. The increase vanishes when the ductile yield stress $\sigma_y$ is reached. Thereafter the simulated curves show almost no change in stress, i.e. hold the yield value, with increasing strain. The initial stiffness of the ductile simulated curves increases with increasing bonding properties, i.e. $N_b$ and $\frac{r_b}{\overline{r}_g}$. This matched well with the observations of Fukue (1977) shown in fig. 2.21, which states that the strength and stiffness increases with increasing sintering time for similar density samples. Also von Moos (2001) observed an increase of the stiffness but related it to an increase in density. The increase of the stiffness can also be observed in the experimental curves depicted in fig. 6.20.
After yield strength is reached, the experimental curves show a change in slope. But the predictions don't change in strength after yielding. This work-hardening behaviour of snow after the yield point is reported by several authors, e.g. Fukue (1977),von Moos (2001) and Scapozza and Bartelt (2003). The predicted curves did not show any work-hardening with

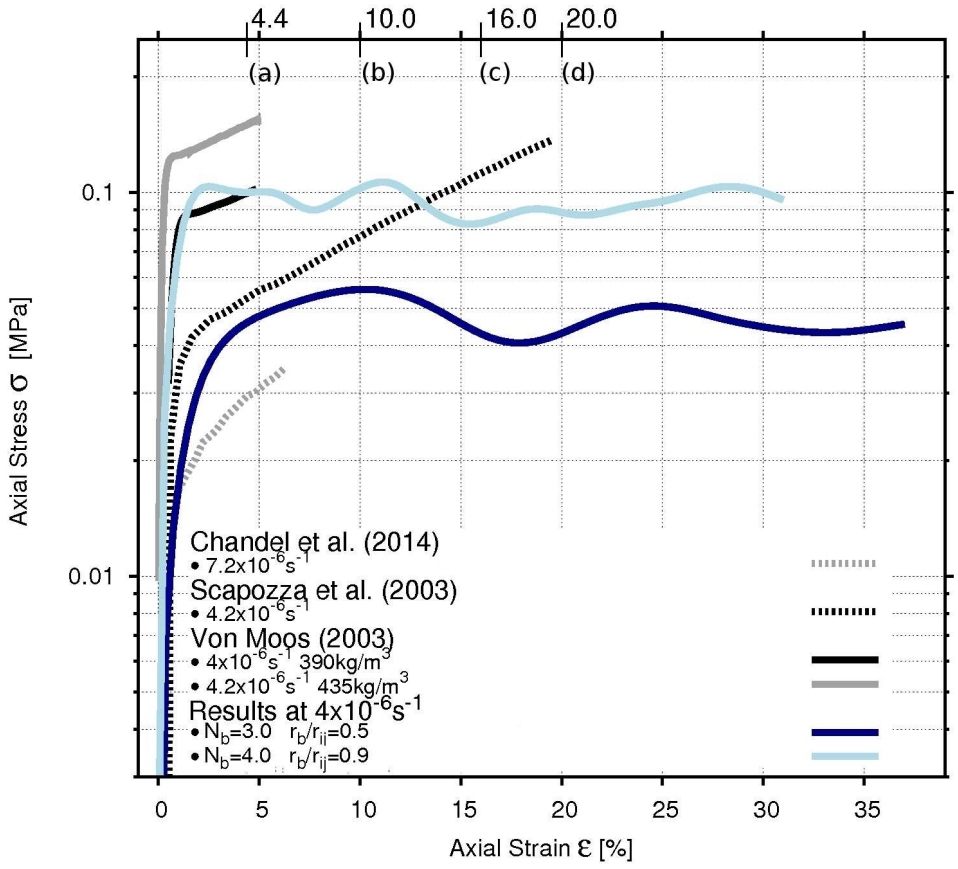


*Figure 6.20: Unconfined compression of a cylindrical snow sample by ductile rates at different temperatures. The blue curves are the predicted results for a sample of an initial density of* 408 kg/m$^3$. *The grey and black curves are unconfined compression measurements by Scapozza and Bartelt (2003), von Moos (2001) and Chandel et al. (2014).*

progressing plastic deformation. This effect shows that the creep of a bond under stress, by eq. 3.2, is too strong. This has to be investigated in future studies as the mechanism of the work-hardening remains unknown.
Fig. 6.21 visualises the sample of the dark-blue curve in fig. 6.20. The deformed sample is shown at the axial strain of yield of 4.4% and at three further states, i.e. 10.0%, 16.0% and 20.0%, during the plastic deformation phase. The corresponding bond structure is depicted in fig. 6.22 at the indicated states of deformation. The bond structure of the sample is again shown in the half open view and coloured by its normal stress component. Under ductile deformation the bond structure of the snow sample experiences no bond failure as depicted in fig. 6.22. During the entire deformation process, the majority of bonds develops stress . The strain state of 4.4% in fig. 6.21a shows the deformed sample at the point of yield. The yield point, i.e. the yield strength is thereby the point at the onset

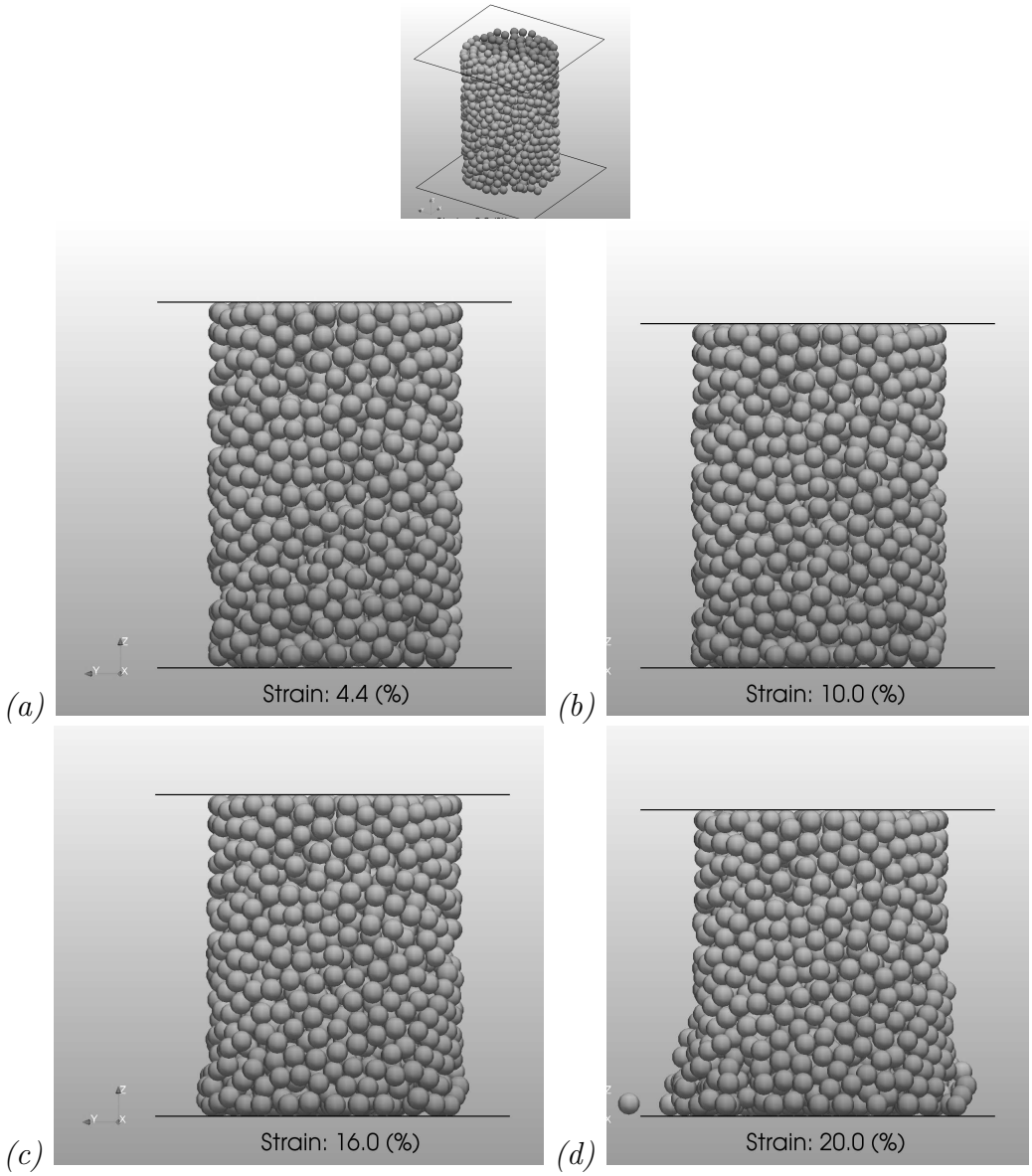


*Figure 6.21: Unconfined compression of a cylindrical snow sample for a ductile compression rate of* $4 \cdot 10^{-6}$ $\mathrm{s}^{-1}$. *The initial sample density equals* 408 $\mathrm{kg/m^3}$. *The temperature is* $T = -4$ °C *and the bonding parameters are* $N_b = 3.0$ *and* $\frac{r_b}{\overline{r}_g} = 0.5$.

of change in slope. At the strain state of 4.4% the sample is compacted uniformly with no change in shape. With ongoing plastic deformation the sample keeps compacting almost uniformly. But at higher strain states, i.e. 20% of deformation, a larger radial deformation towards the bottom of the sample can be observed. This causes an inhomogeneous distribution of stress throughout the bond structure whereby the stress increases towards the bottom of the sample. Also, an increasing number of bonds, oriented perpendicular to the loading direction, experiences tension due to the higher radial deformation towards the sample bottom. Under the low strain rate, the bonds are able to relax the stress and

thus avoid failure due to creep of ice described by eq. 3.2.

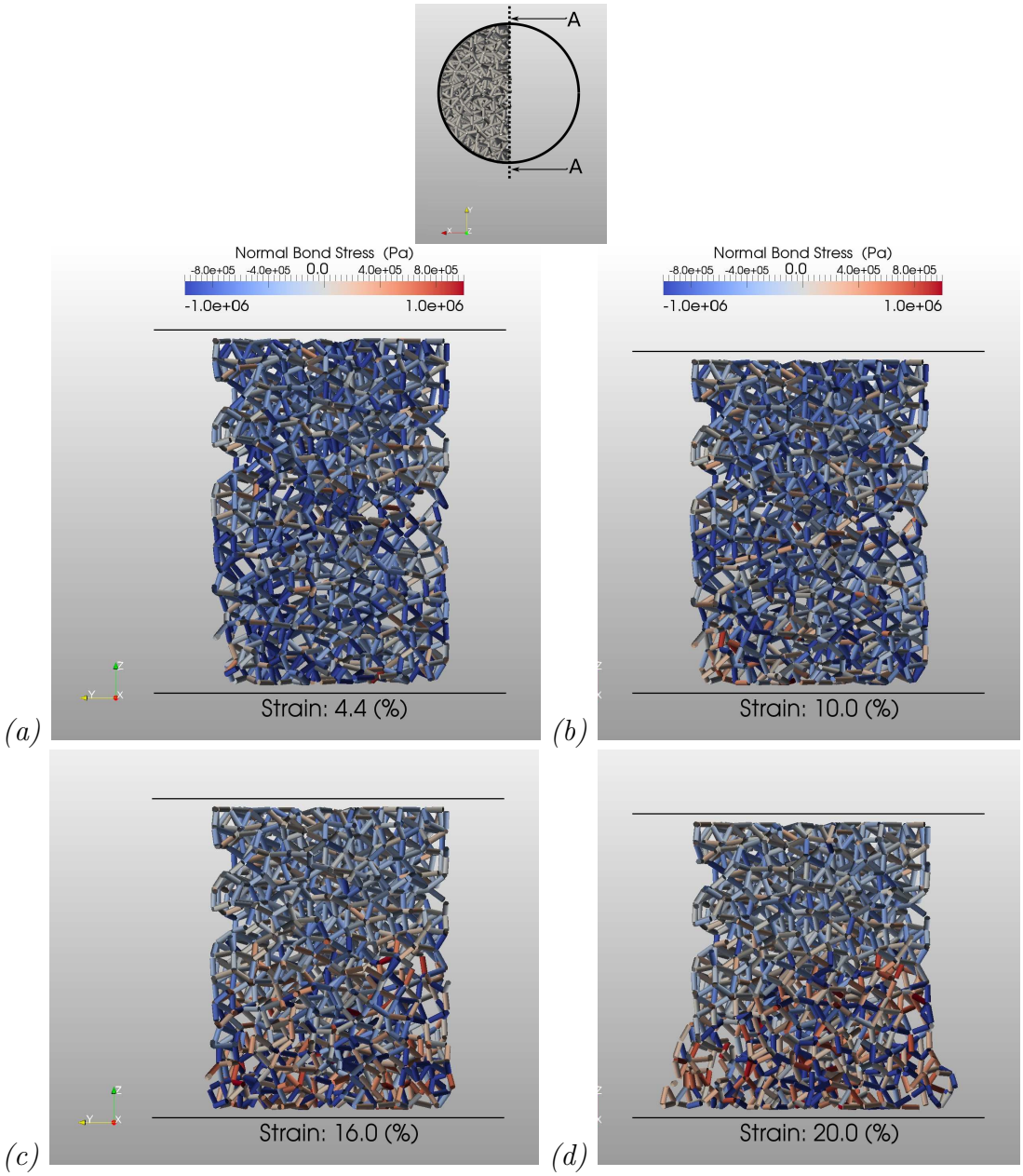


*Figure 6.22: The bond structure of the sample is depicted at increasing strain states and coloured by the normal stress component (- compression / + tension). Unconfined compression of a cylindrical snow sample under the ductile compression rate of* $4 \cdot 10^{-6}$ $\mathrm{s}^{-1}$. *The initial sample density equals* 408 $\mathrm{kg/m^3}$. *The temperature is* $T = -4$ °C *and the bonding parameters are* $N_b = 3.0$ *and* $\frac{r_b}{\overline{r}_g} = 0.5$.

### Snow Strength - Strain Rate Relationship

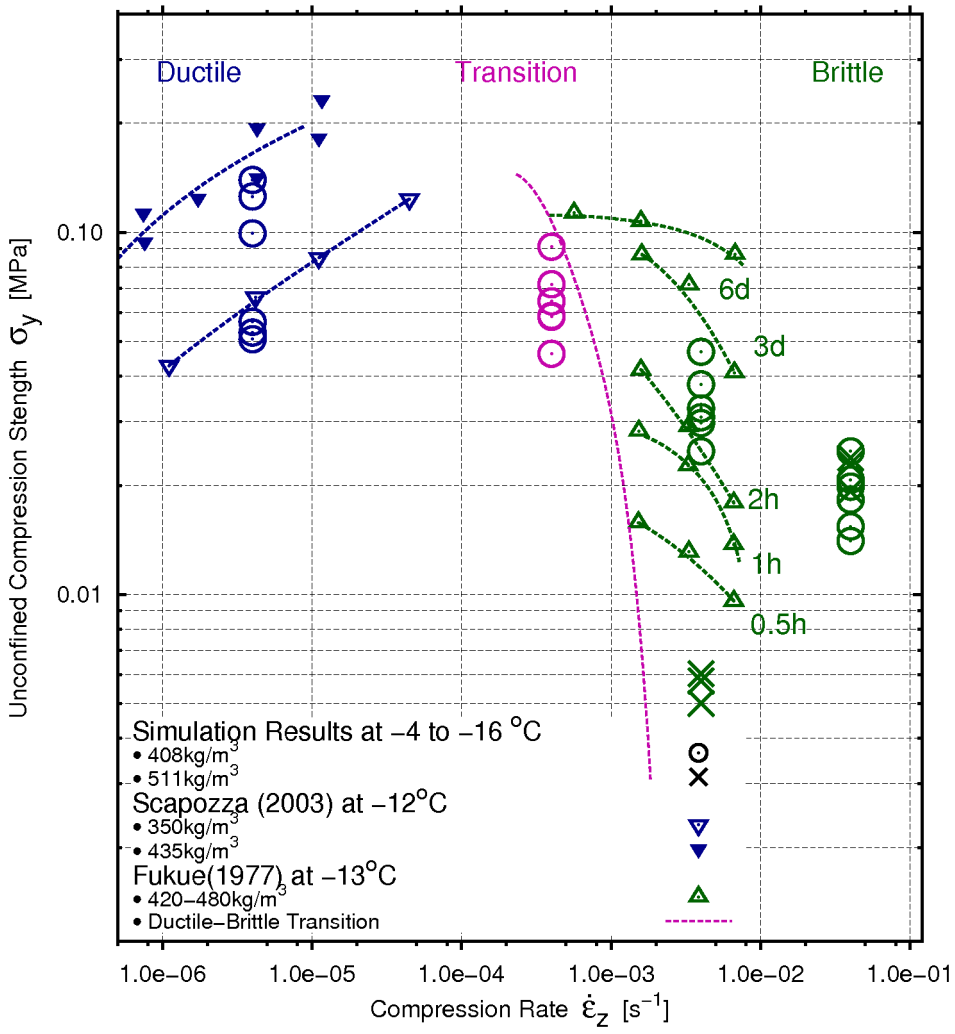


*Figure 6.23: Unconfined compression strength versus strain rate for snow densities of* 400 *to* 500 kg/m$^3$. *The lines fit the measurements by Fukue (1977) and Scapozza and Bartelt (2003). The distribution of the predicted results are indicated by the symbols.*

Fig. 6.23 gives an summary of the strength - loading rate relationship of snow in unconfined compression tests. The experimental and simulated data depicted are coloured by the mechanical behaviour of snow, i.e. ductile, transient and brittle. This highlights the regimes and shows the behaviour of snow observed at the different strain rates.
In fig. 6.23, unconfined compression tests under brittle compression rates conducted by Fukue (1977) are depicted at a temperature of −13 °C. His investigation focused on the dependence of the brittle strength in relation to the sintering age of snow, i.e. bonding

properties. Thus, the prediction of Fukue (1977) are marked with the sintering time, i.e. hours and days the sample spent under isothermal conditions before the compression test were conducted. The bonding properties in the predictions and thus the sintering age in the experiments have shown to be the most significant factors influencing the strength of a snow pack. Hence, the curves of Fukue (1977) are chosen with the purpose to visualise the spread in strength depending on the history of snow.
Fig. 6.23 also includes a curve of Fukue (1977) identifying the ductile to brittle transition rate. This curve shows the transition rate as a function of the isothermal sintering time of snow. Fukue (1977) showed that the transition rate increases with decreasing sintering time while Kinosita (1967) observed a decrease with decreasing temperature.
Fig. 6.23 further includes measurements of Scapozza and Bartelt (2003) of unconfined compression tests under ductile compression rates at a temperature of −12 °C. The data is shown for two densities of snow, i.e. 350 and 435 kg/m$^3$, similar to the densities used in the predictions of this study. As Scapozza and Bartelt (2003) used naturally sintered snow in their investigation the increase in density is an indicator for a longer sintering time.
The yield strength of snow predicted in the unconfined tests of this study is depicted as symbols for two densities, i.e. 408 and 511 kg/m$^3$. The predicted data in fig. 6.23 demonstrates the strength of the snow samples at temperatures from −4 °C to −16 °C and bonding properties of $N_b = 3.0 - 4.0$ and $\frac{r_b}{\overline{r}_g} = 0.3 - 0.9$. The variations of the temperatures and bonding properties are chosen from the micro-scale measurements of von Moos (2001).
Strength and behaviour of snow are clearly a function of the strain rate applied which is apparent in fig. 6.23. The unconfined brittle strength of snow increases with decrease of the rate applied to deform the snow sample. At the maximum brittle strength the brittle behaviour converts into the ductile behaviour of snow. This transition zone can be defined by a critical strain rate. However, the critical strain rate was shown to be dependent on temperature and sintering age itself by several investigators. Further decrease of the strain rate decreases the unconfined ductile strength as well and the snow sample is deforming purely ductile.
The yield strength extracted from the simulated data fits quite well into the overall strength - rate relationship of snow. Also the different mechanical behaviours of snow dependent on the strain rate have been observed.

### Snow Strength dependent on Initial Bonding

The sintering process in a snow strengthens the bonding structure between grains due to an increase in size and number of bonds. Thus an increase in sintering time, i.e. age of snow, equals an increase in the bonding properties, i.e. coordination number $N_b$ and bonding radius $\frac{r_b}{\overline{r}_g}$. In natural snow a higher density is often an indicator for longer sintering times. But this indicator might be misleading as a higher density is not necessarily a link to a stronger bonding structure.
In order to investigate into the dependence of the sintering time on the strength of a snow sample, the sample has to sinter in sealed isothermal conditions before the unconfined

compression tests are conducted. Fukue (1977) used a sealed container to avoid density changes. Fukue (1977) performed investigations with loading rates of the brittle and transition regime. Fig. 6.24 shows his measurements at four different sintering times, i.e. at 0.5, 1 and 2 hours and at 3 days, and at three increasing strain rates. The experimental data is approximated by black solid lines, calculated with cubical-splines.
The brittle compression strength of unconfined snow samples extracted from the predicted data is presented at the three brittle strain rates 0.4, $4 \cdot 10^{-2}$ and $4 \cdot 10^{-3}$ $s^{-1}$ and at the transition rate $4 \cdot 10^{-4}$ $s^{-1}$. The predicted results are further depicted for the following three bonding configurations:

| | | | |
|---|---|---|---|
| $\frac{r_b}{\overline{r}_g}$ | 0.3 | 0.5 | 0.9 |
| $N_b$ | 2.5 | 3.0 | 4.0 |

The different bonding configurations are identified by different symbols and their trend is indicted through dashed lines.
In fig. 6.24, the predicted and measured results of snow show an increase of the unconfined compression strength with increasing bonding properties or sintering age, respectively. Both results further describe an increase in strength with decreasing strain rate which is very uncommon to other brittle material.
Further, it can be observed that the differences in strength between different bonding properties grows significantly larger with small loading rates. This is another similarity to the experimental curves which show the same difference between different sintering ages of snow. Due to longer deformation time, the bonds are able to relax the developed stress. This is predicted by the elastic - viscoplastic bond model eq. 3.57, which employs the creep model of ice described by eq. 3.2. Yong and Metaxas (1985) described this effect as a 'healing' process of snow.
For engineering applications of high velocities, it is useful to notice that the strength of the snow may decrease with increasing brittle rates, but the strength does not decline below a certain value. This effect has been described by Kinosita (1967) as the second kind of brittle behaviour. His investigations revealed that the strength of snow does not change any more above a certain strain rate. Also the confined compression tests by Yong and Metaxas (1985) demonstrate this phenomena as shown in fig. 2.34.
According to the predictions of Kinosita (1967), the transition between from brittle to second kind of brittleness takes place at a rate of about $5 \cdot 10^{-2} s^{-1}$ for temperatures of about $-7$ to $-8$ °C. This matches quite well with the trend seen in the predicted curves in fig. 6.24. Above this rate the strength does barely change with increasing rate, temperature and bonding properties.
Finally, it has to be noticed that the predictions and the experiments show that below a certain size in bonding properties, i.e. sintering time, the bonding structure of a sample loses its influence on the strength almost entirely.

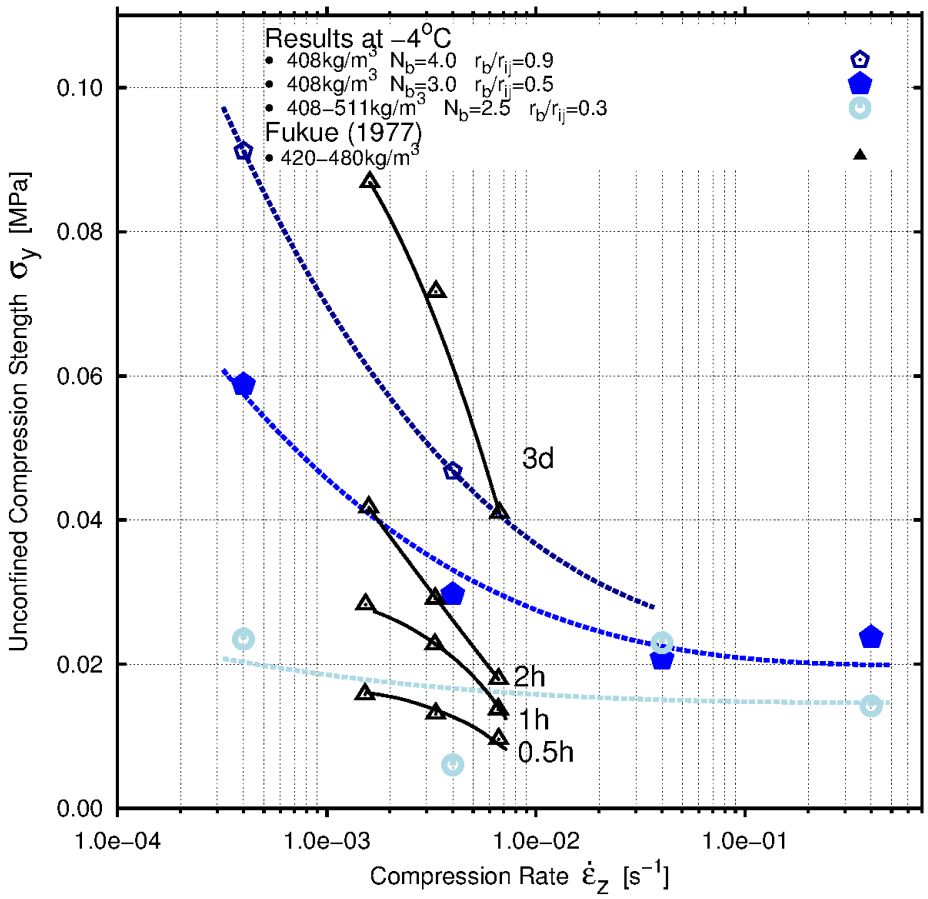


*Figure 6.24: Unconfined compression strength versus the bonding strength, i.e. sintering age, and strain rate. The solid lines are the measurements by Fukue (1977). A dashed line indicates a predicted result. The different bonding strengths are indicated by colour and the different sintering ages of snow within the measurements are noted next to the curves.*

For future engineering applications of the bonding models of this study it would be very useful to investigate into a mathematical relation between natural sintering time $t_s$ and the bonding properties, i.e. $N_b$ and $\frac{r_b}{\overline{r}_g}$.

### Snow Strength - Temperature Relationship

Kinosita (1967) conducted compression tests on unconfined cylindrical samples of natural snow with initial lengths from 1 to 14 cm and initial densities from 370 to 400 kg/m$^3$. His investigation focused on a temperature range from 0 to −30 °C. His results for the compressive strength of snow at ductile straining of 5% are shown as blue lines of constant stress in fig. 6.25. The green lines show the brittle strength of snow, i.e. the maximum

stress value measured. Further, the transition regime between ductile to brittle behaviour of 300 to 500 kg/m$^3$ snow is depicted as dashed purple lines. Finally, the transition between brittle to second kind of brittleness is plotted as a solid line coloured similar to the first transition regime. Kinosita (1967) and Yong and Metaxas (1985) observed that the strength of a snow sample above the second transition rate does not change with increasing strain rate. The different regimes, i.e. ductile, transitional, brittle and brittle second kind, are identified by different colours.
In fig. 6.25, the unconfined brittle strength of snow predicted for the initial density of 408 kg/m$^3$ is shown by symbols. The strength is illustrated at the three strain rates $4 \cdot 10^{-1}$ s$^{-1}$, $4 \cdot 10^{-2}$ s$^{-1}$ and $4 \cdot 10^{-3}$ s$^{-1}$ and for the three temperatures $-16$ °C, $-10$ °C and $-4$ °C, respectively. The strength is depicted for samples with the initial bonding properties $N_b = 4.0$ and $\frac{r_b}{\overline{r}_g} = 0.9$.

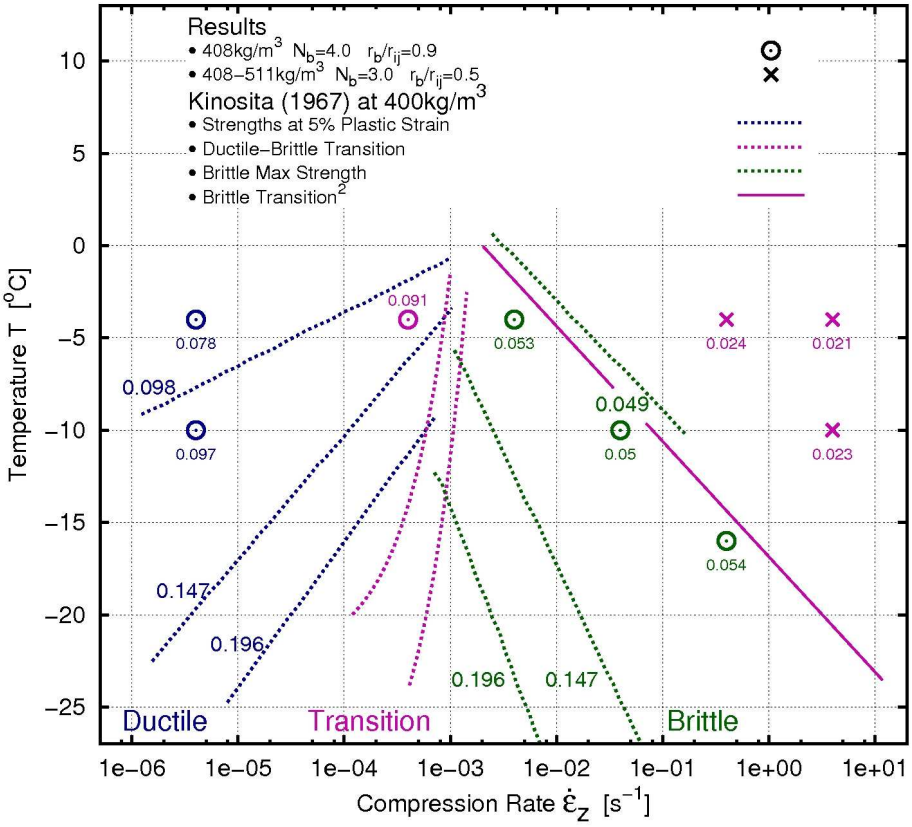


*Figure 6.25: Relations of unconfined compression strength, temperature and strain rate of snow under load. The dotted lines are iso-lines of constant strength predicted by Kinosita (1967) and the symbols are the predicted results. All values are presented in* MPa. *The different regime, ductile, transitional, brittle and brittle second kind, are indicated by different colours.*

The transitional and ductile strength of snow in fig. 6.25 is presented at the strain rates $4 \cdot 10^{-4}$ s$^{-1}$ and $4 \cdot 10^{-6}$ s$^{-1}$ for the temperatures $-4$ °C and $-10$ °C, respectively. The predicted strength of snow in fig. 6.25 aligns well with the lines of constant strength values measured by Kinosita (1967). The ductile strength of snow is also presented at the strain rate of $4 \cdot 10^{-6}$ s$^{-1}$ for the temperature of $-4$ °C.
In fig. 6.25, the predicted brittle strength of second kind is shown for the initial densities 408 kg/m$^3$ and 511 kg/m$^3$ and initial bonding properties of $N_b = 3.0$ and $\frac{r_b}{\overline{r}_g} = 0.5$. The results are shown for different initial densities to emphasis the fact stated by Kinosita (1967) that the strength above the second brittle transition rate does not change anymore with strain rate and temperature.
In fig. 6.25, it can be observed that the measurements and predictions show an increase in strength in the ductile, transition and brittle regime with decreasing temperature. Further, it can be observed that the brittle strength of snow increases with decreasing strain rate while the transitional to ductile strength decrease with decreasing strain rate.
The experimental curves show an increase of the transition rate between ductile and brittle behaviour with increasing temperature $T$. Hence, with increasing temperature the brittleness of snow decreases.
Fig. 6.16 also demonstrates this behaviour in the predicted transition curves. The compression curve predicted at $-4$ °C shows the lowest fluctuations about its average value. This is a characteristic of ductile deformation behaviour. However, the curve of $-16$ °C shows the highest fluctuations. This is a characteristic of brittle deformation behaviour.
This characteristic of snow is inherited from its ice matrix on the micro-scale. The closer the temperature raises to the melting point of ice the stronger becomes the creep behaviour of ice. Increasing temperatures also cause a softening of the ice. Hence, in the applied creep model of ice, eq. 3.2, the creep rate increases with increasing temperature. Further, the hardness of ice predicted by eq. 3.5 decreases with increasing temperature.
Another very unique characteristic to investigate in future works is the sudden jump in strength at the transition rate. Due to the increase of the transition rate with increasing temperature, it is possible that a higher temperature sample can show a higher strength compared to a lower temperature sample compressed under the same strain rate. Parallel to Kinosita (1967), this has also been observed in the tension tests conducted by Narita (1984).

#### 6.2.1.4 Confined Density-Stress Relationship of Snow

In confined compression tests, the cross section of the sample stays constant. Therefore, the strain state $\varepsilon_l$ and the current density $\rho_t$ of a sample during compression can be directly related as follows:

$$\rho_t = \rho_0 \cdot (1 - \varepsilon_l)^{-1}$$

where $\rho_0$ describes the initial density and $\varepsilon_l$ the strain state of compressed sample. Hence, the strain - stress and density - stress performances describe the same behaviour of snow in confined compression tests. However, the initial density plays a significant role in confined

brittle compression tests of snow as already shown by Abele and Gow (1975), Yong and Fukue (1977), Yong and Metaxas (1985) and Fukue (1977).

### Stress - Initial Density Relationship

Abele and Gow (1975) conducted confined compression tests on isothermally sintered snow with a brittle strain rate of 4 $s^{-1}$ and at temperatures of −1 °C, −4 °C, −10 °C and −32 °C. The measurements were performed on a wide range of initial densities and are represented as grey curves in fig. 6.26 for temperatures above −10 °C. The measurements are shown for sintering times of 3 to 7 days.

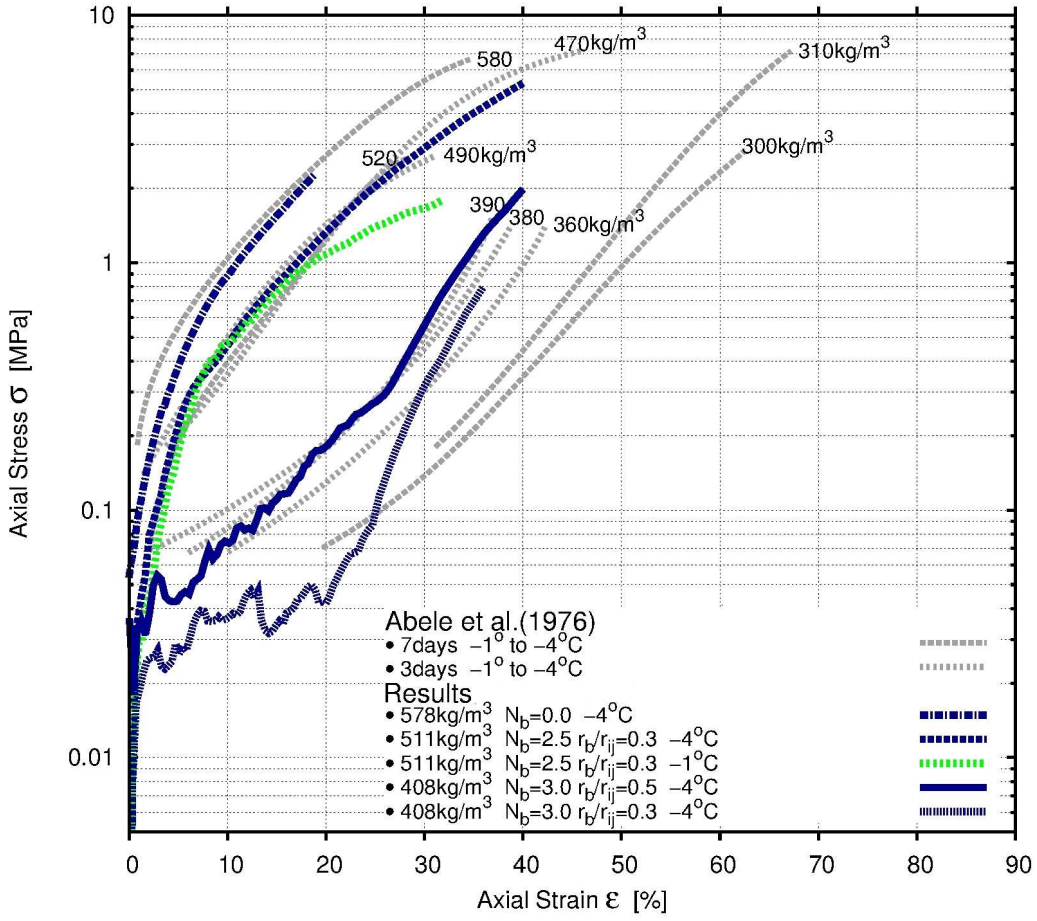


*Figure 6.26: Confined compression of a cylindrical snow sample at $T > -10$ °C. Different initial densities are compressed under a high rate of 4 $s^{-1}$. The grey curves are confined compression measurements by Abele and Gow (1975).*

The predicted results of the performed brittle compression tests of confined snow samples in fig. 6.26 are depicted as blue and green curves for the initial densities of 408 kg/$m^3$, 511 kg/$m^3$ and 578 kg/$m^3$. The predicted curves are shown for different initial bonding

properties which are emphasised in the figure legend. The predictions are conducted at a strain rate of 4 $s^{-1}$.
Fig. 6.27 shows the predicted results of confined compression tests at and below −10 °C. The initial densities, initial bonding properties and the strain rates are similar to fig. 6.26. Fig. 6.27 also shows the measurements of Abele and Gow (1975) conducted at temperatures of −10 °C and −32 °C. The measurements are also shown for sintering times of 3 to 7 days.

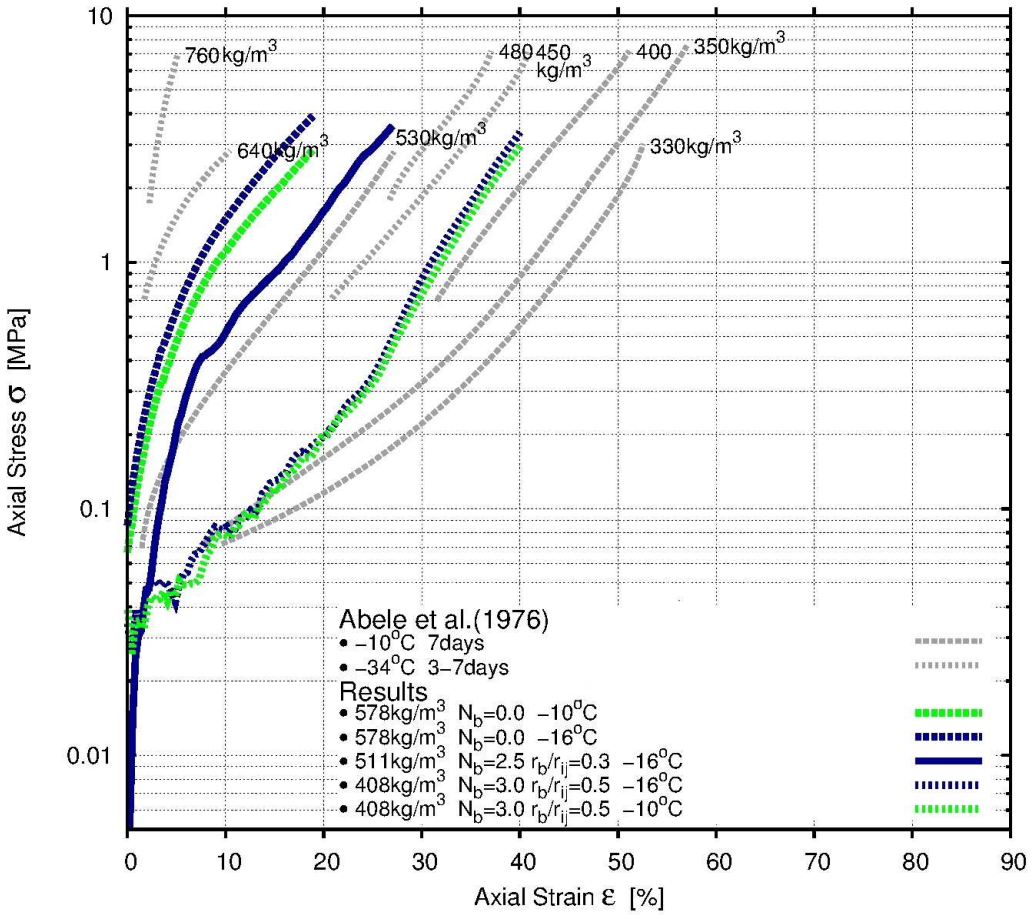


*Figure 6.27: Confined compression of a cylindrical snow sample at $T \leq -10$ °C. Different initial densities are compressed under a high rate of 4 $s^{-1}$. The grey curves are confined compression experiments by Abele and Gow (1975).*

Independent of the temperature, the predicted curves in both figures agree well with the experimental curves of the different initial densities. Experiments and predictions illustrate that the strength at any fixed strain state increases significant with increasing initial density.
In fig. 6.26 and 6.27, the curves of the high initial density 578 kg/$m^3$ show a continuous stress increase with increasing strain. After an initially high increase the slope of the curves

decreases continuously, without any abrupt change.
The confined curves for the initial density of 511 kg/m$^3$ also start with a high stiffness and increase continuously in stress with increasing strain. But the slope of the curve changes abruptly when it reaches the yield value. Thereafter, the stress continues to increase under a smaller slope.
The predicted results for the lower initial density of 408 kg/m$^3$ present an entirely different shape of the curve which has also been reported by Fukue (1977) and Abele and Gow (1975). The first part of the curves demonstrates the saw-tooth shape which is a typical characteristic of the brittle deformation behaviour. The initial part of the curve is constructed of a subsequent stress build-up and stress release whereby the mean stress value ascends with increasing strain. This saw-tooth effect is caused by a progressing bond fracture through the snow sample with increasing strain. Each subsequent stress build-up thereby reaches to a higher strength then its predecessor. With increasing densification beyond the initial phase of bond fracture the previous continuous growth of the higher density samples is reproduced.
Fukue (1977) investigated in detail this effect. A schematic representation of the described effect by Fukue (1977) is shown in fig. 2.32. In his investigation he projected the continuous part of the curve backward on the strain axis. Thereby, he predicted the threshold density at which the saw-tooth shape of the lower initial density curve turns into the continuous increase. The investigations of Fukue (1977) revealed the dependence of the threshold density on the strain rate and grain size as shown in fig. 2.33.
For a brittle strain rate of 4 s$^{-1}$, Fukue (1977) measured threshold densities between 420 and 460 kg/m$^3$. The threshold density predicted from the predicted curve of 408 kg/m$^3$ in fig. 6.26 and 6.27 is about 450 kg/m$^3$ for $N_b = 3.0$ and $\frac{r_b}{\overline{r}_g} = 0.5$. Such a unique and general consistency between measurements and predictions is a very good indicator for the reliability of the developed snow models.
Abele and Gow (1975) also reported the threshold effect for samples with initial densities of 300 to 400 kg/m$^3$. They observed a change in curvature at densities of 400 to 500 kg/m$^3$ which equals about 20 to 40% in strain. This change in curvature in the experimental curves can also be seen in fig. 6.26 and 6.27.

### Stress - Temperature Relationship

The difference in temperature dependent behaviour in confined brittle compression tests is again a result of the creep of ice on the micro-scale. The ice on the grain-scale becomes softer and more viscous with higher temperature.
In fig. 2.31a and 2.31b, Abele and Gow (1975) showed that the brittle compression behaviour can be divided into a behaviour for $T > -10$ °C and $T \leq -10$ °C. The temperature dependent behaviour is apparent at the high strains as seen in fig. 6.26 and 6.27. In fig. 6.26 where snow is compressed at temperature $> -10$ °C, experiments and predictions demonstrate a continuous decrease of the gradient of the curves with increasing strain. This is particularly apparent for the predicted curve of $-1$ °C as this temperature is the closest to the melting point of ice. In fig. 6.27 where snow is compressed at temperatures $\leq -10$ °C,

experiments and predictions increase in stress by a constant gradient at high straining portion of the curves.

### 6.2.2 Blade Scratch Tests

As shown in fig. 2.44 the motion of a tread block in the contact patch of a rolling tire is composed of penetration and scratch phases through the snow surface. Therefore, the predictions in this section approximate the procedure by penetrating and scratching through snow with a rigid metal blade. The blade proceeds through the snow by different velocities, at different temperatures and for different bonding properties. The penetration and scratch force exerted on the blade by the snow grains are recorded within the predictions. Thin blade penetrations are commonly conducted in the field of snow mechanics as shown in fig. 2.36. The predicted snow behaviour is studied and compared to these measurements. Further, the computed forces are validated with the experimental data by Borstad and McClung (2011) and Fukue (1977).

#### 6.2.2.1 Experimental Setup

The predictions are composed of two phases of controlled blade motion which are an initial penetration and a subsequent scratch phase as depicted in fig. 6.28. The blade

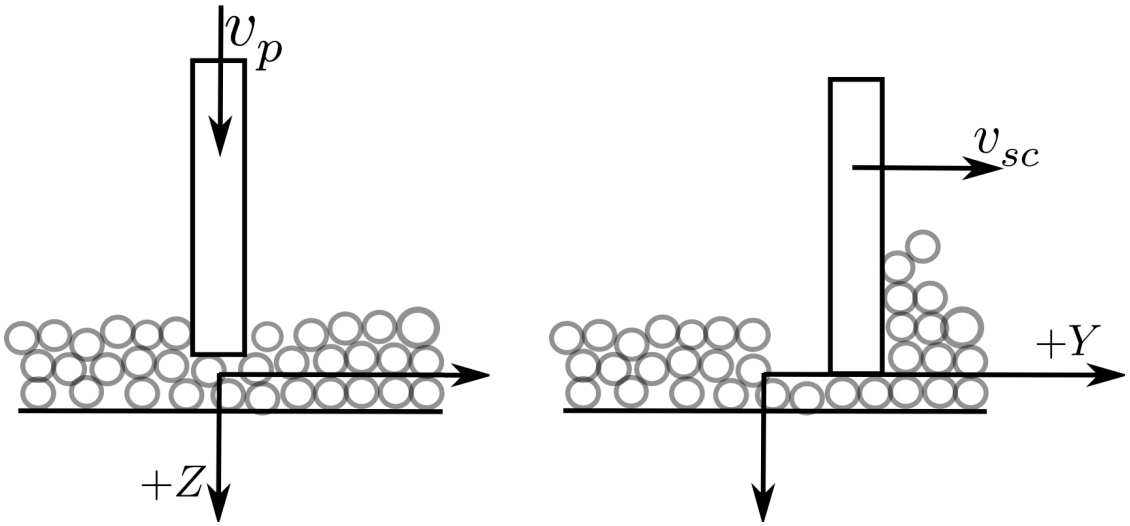


*Figure 6.28: Penetration and scratch phase of the metal blade through the snow surface.*

is initially positioned above the snow surface. During the initial penetration phase the blade penetrates the snow surface under the constant penetration velocity $v_p$. It stops the penetration after 12 mm, which equals the penetration depth of 10 mm, used by Fukue (1977), plus the maximum grain diameter.
After the penetration phase, the blade scratches through the snow surface at the constant penetration depth with the scratch velocity $v_{sc}$ over a distance of 30 mm.
Table 6.6 composes all properties describing the blade motion through the snow. The penetration and scratch tests are conducted with two different velocities.

*Table 6.6: Kinetic Properties*

| | | |
|---|---|---|
| Penetration Velocity $v_p$ [mm/s] | 10.0 | 20.0 |
| Scratch Velocity $v_{sc}$ [mm/s] | 10.0 | 20.0 |
| Penetration Depth $+Z$ [mm] | $\approx 12.0$ | |
| Scratch Distance $+Y$ [mm] | 30.0 | |

Fig. 6.29 shows the initial configuration of the metal blade and the prepared strip of the snow surface as well as the initial density distribution of the strip.

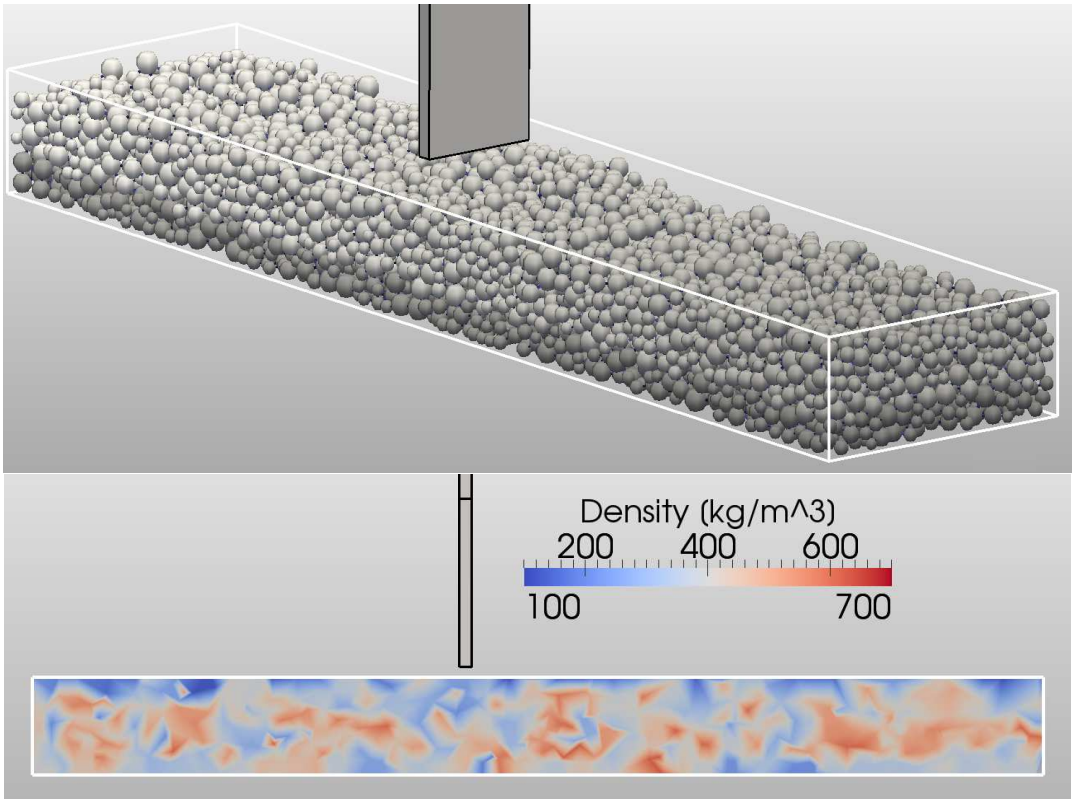


*Figure 6.29: Initial snow and blade configuration as well as initial density distribution.*

The spatial dimensions of the blade and the snow strip are documented in table 6.7. The snow strip contains spherical particles of random radii generated by the method in section 3.5. The minimum and maximum radius of the grains are presented in table 6.7 as well. In a previous simulation the grains were settled to approximate a natural distribution. Two different temperatures and three different bonding configurations are used for the snow strip of 410.0 kg/m$^3$. The snow strip is confined by rigid side and bottom walls, which are

assumed to be of the material snow as well. The bottom wall describes a hard layer of snow beneath the looser top layer of snow. The contacts between grains as well as the contacts between grains and confining walls are described by the models developed in section 3.4. The collision forces developing during the interaction between the snow grains and the

*Table 6.7: Metal Blade and Snow Strip Properties and Dimensions*

| | | | |
|---|---|---|---|
| **Metal Blade** | | | |
| Blade Width [mm] | 20.0 | | |
| Blade Thickness [mm] | 1.7 | | |
| Young's Modulus $E$[GPa] | 200.0 | | |
| Shear Modulus $G$[GPa] | 78.125 | | |
| Friction Coefficient $\mu$ | 0.1 | | |
| **Snow Strip** | | | |
| Initial Density [kg/m$^3$] | 410.0 | | |
| Temperature [°C] | $-1.0$ | $-16.0$ | |
| Strip Length [mm] | 210.0 | | |
| Strip Width [mm] | 46.0 | | |
| Strip Height [mm] | $\sim 20.3$ | | |
| No. Grains | 7862 | | |
| Grain Radius [ mm] | $> 1.0$ | $< 0.19$ | |
| Bond Size $\frac{r_b}{\overline{r}_g}$ | 0.1 | 0.3 | 0.5 |
| Number of Bonds per Grain $N_b$ | 2.5 | 3.0 | 3.5 |

blade are predicted by the Hertz Mindlin model, described in appendix A.1.5. The blade is assumed to be of the material steel and its material parameters are also shown in table 6.7.

#### 6.2.2.2 Penetration and Scratch Performance

Fig. 6.30 illustrates the penetration force experienced by the blade during the penetration and scratch phase of $v_p = v_{sc} = 20$ mm/s. The force is presented for the two different temperatures and the three increasing bonding configurations. Similar, fig. 6.31 depicts the corresponding resistance force in $+Y$ - direction.

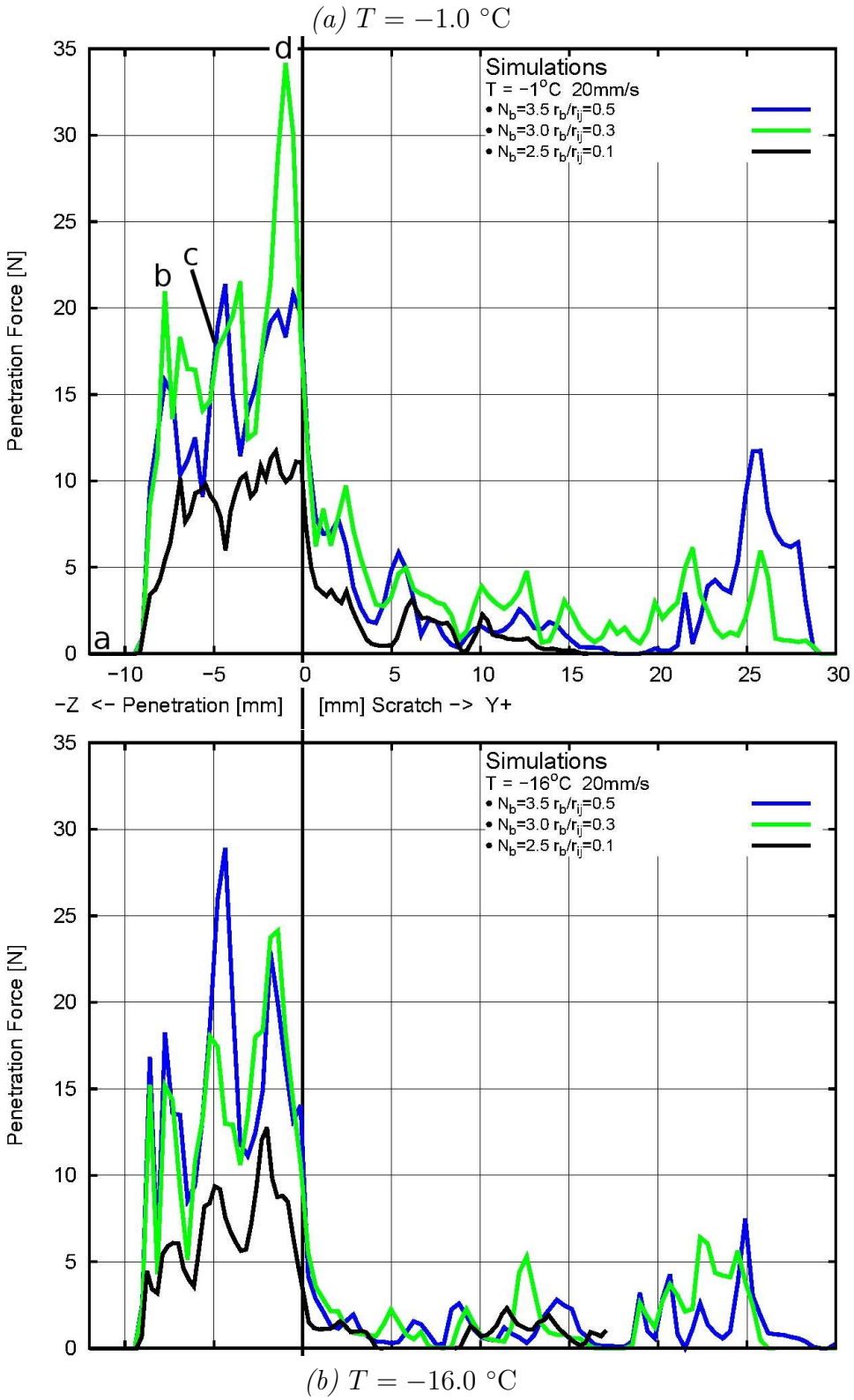


*Figure 6.30: Penetration force versus penetration depth and scratch distance for a velocity of* 20 mm/s *and at different temperatures and bonding configurations of the snow.*

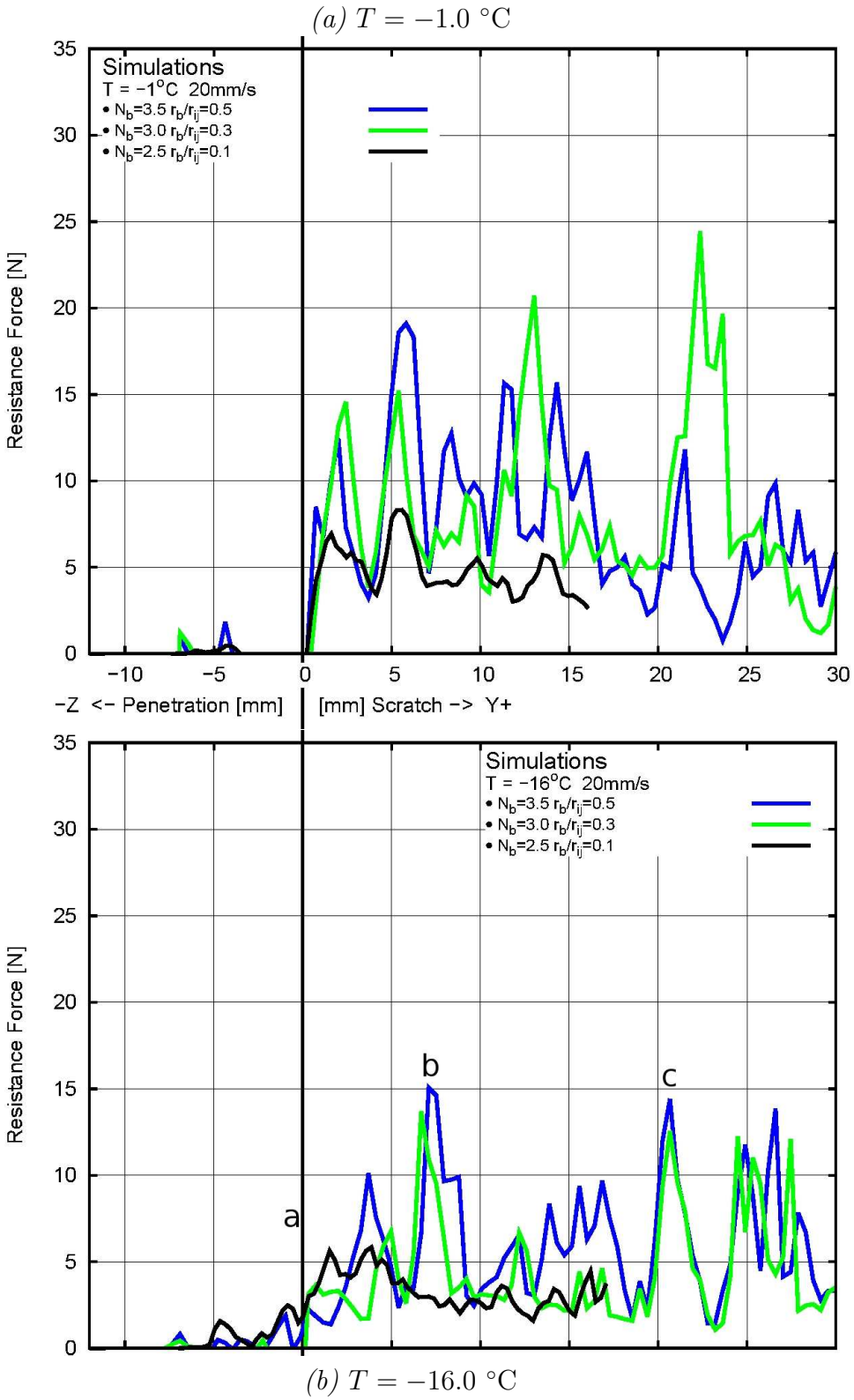


*(a)* $T = -1.0$ °C

*(b)* $T = -16.0$ °C

*Figure 6.31: Resistance force versus penetration depth and scratch distance for a velocity of* 20 mm/s *and at different temperatures and bonding configurations of the snow.*

During the penetration phase in fig. 6.30, the penetration force increases with penetration depth. The resistance force in fig. 6.31 shows no influence during the penetration phase. During the scratch phase the penetration force decreases to its minimum and a resistance force is exerted on the blade by the snow surface.
The velocities of the blade are identified by Fukue (1977) as velocities of the completely brittle regime in fig. 2.36. At these velocities the force curves in fig. 6.30 and 6.31 present the typical saw-tooth shape as already observed in the previous compression test under brittle strain rates. Within the force curves it is obvious that the resistance and penetration force increase with increasing bond number $N_b$ and size $r_b/\overline{r}_g$. Also the difference between peak and drop of the curves increases with increasing bond number $N_b$ and size $r_b/\overline{r}_g$.
The maximum force value reached during penetration was defined as the blade hardness index or the blade penetration force (BPF) by Borstad and McClung (2011) and Fukue (1977), respectively.
Fig. 6.32 illustrates the blade penetration tests in the field conducted by Borstad and McClung (2011). The thin blade penetration force reflects the bonding strength of snow due to the low influence of snow compression.

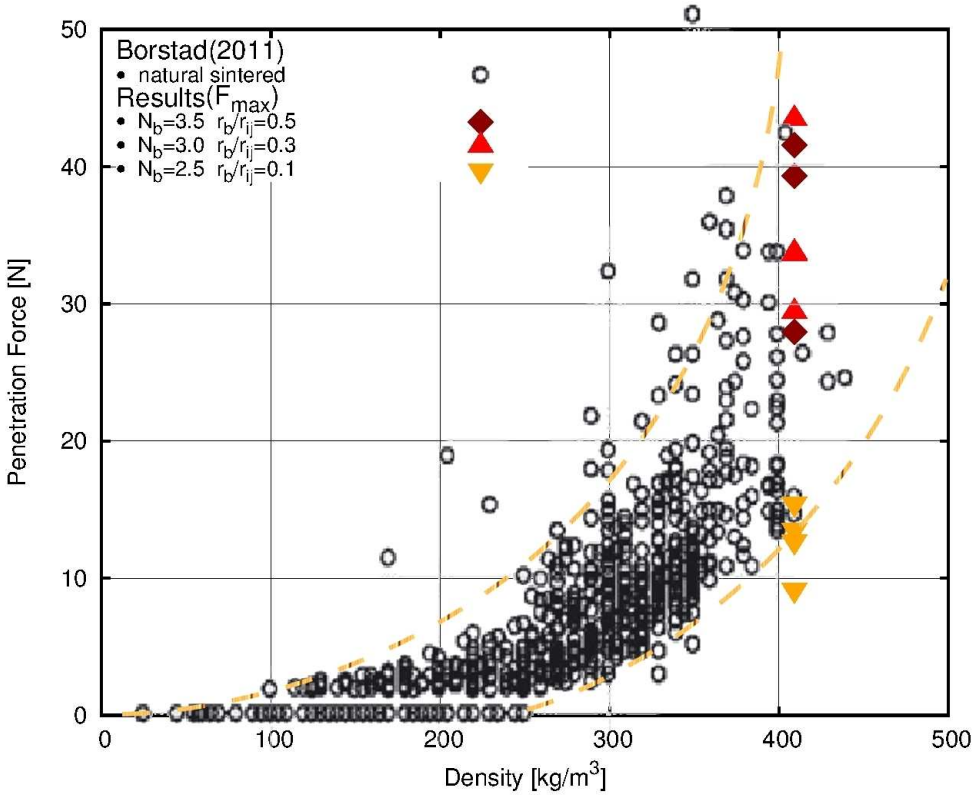


*Figure 6.32: Penetration force versus snow density. The predicted penetration force is shown for all three bond configurations.*

With increasing density one can observe an increasing variation between the measured

forces in fig. 6.32. Due to the increase in density the bonding possibilities multiply. Together with the increase in possibilities the variation in bonding strength increases as well. Fig. 6.32 also includes the predicted results of all three bond configurations. The differences between the penetration forces of the different bonding configurations agree well with the variation of the measured forces by Borstad and McClung (2011).
Fig. 6.33 illustrates the maximum penetration force for velocities of the ductile, brittle and completely brittle regime of snow behaviour. The measured force of Fukue (1977) is depicted for sintered snow of 350.0 to 480.0 kg/m$^3$ and at $-13$ °C. The maximum penetration force of the predictions is represented in the figure as well. The results shown are the predictions of the bonding configuration $N_b = 2.5$ and $r_b/\overline{r}_g = 0.1$ which corresponds to a snow sintered for several hours as shown in fig. 6.24.

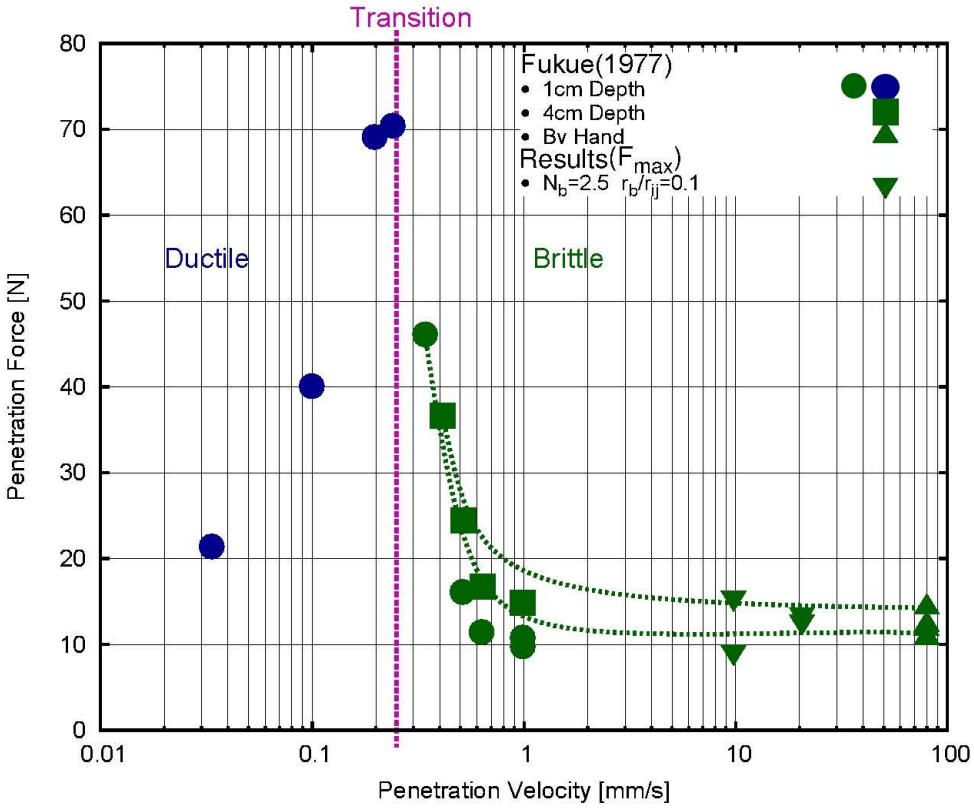


*Figure 6.33: Penetration force versus penetration velocity $v_p$.*

Fig. 6.34 illustrates four subsequent times during the blade penetration phase. The four times are marked in fig. 6.30 by the respective subfigure labels (a),(b),(c) and (d). In fig. 6.34, a slice of the snow surface beneath the blade is viewed in the $Y - Z$ plane. The whole snow structure and the bond structure only are depicted for each subsequent time. The four times selected are the initial configuration, the first penetration force build up and two subsequent force build ups, as marked in fig. 6.30. The bond structure is coloured by the normal stress component.

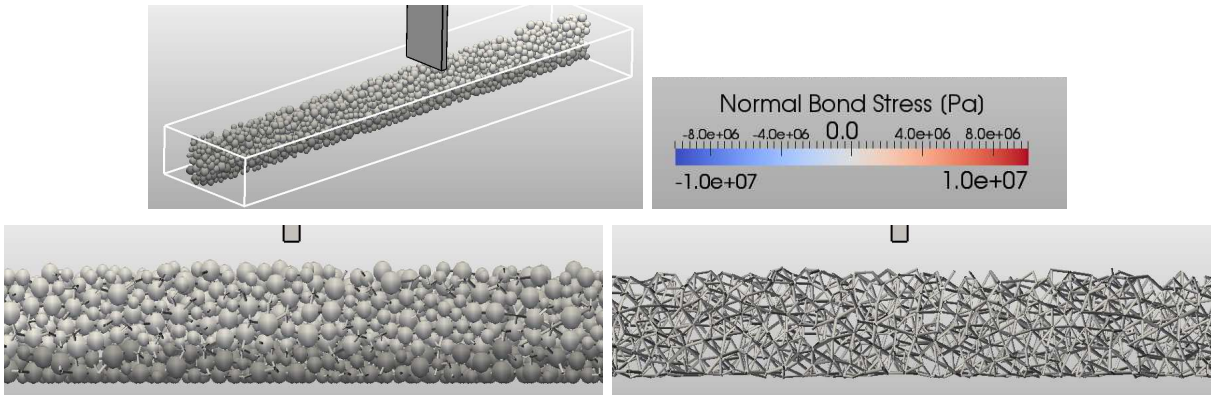


*(a) At $t = 0$ s and $Z = -12$ mm.*

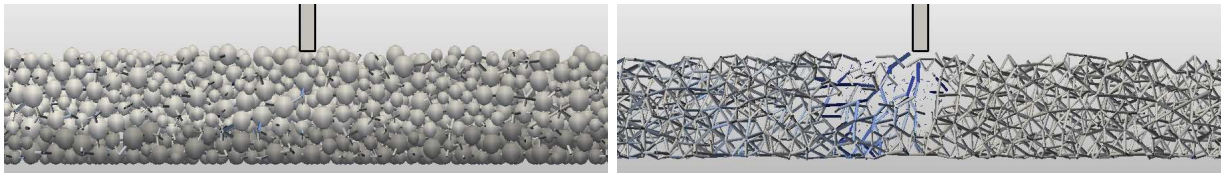

*(b) At $t = 0.2$ s and $Z = -8$ mm.*

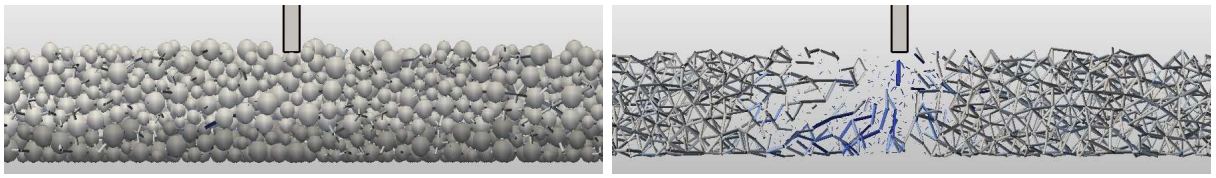

*(c) At $t = 0.25$ s and $Z = -5$ mm.*

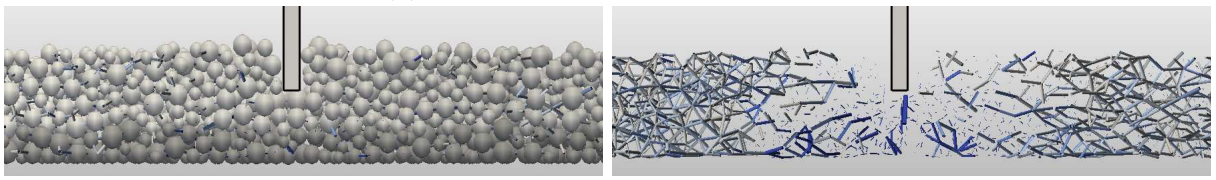

*(d) At $t = 0.54$ s and $Z = -1.25$ mm.*

*Figure 6.34: Grain and bond structure at selected penetrations depths marked in fig. 6.30. The snow has an initial bond configuration of $N_b = 3.0$ and $r_b/\overline{r}_g = 0.3$ and a temperature of $-1$ °C. The bonds are coloured by the normal stress component.*

Fig. 6.34 presents how the grains are pushed aside and are partially compressed beneath the blade. At the penetration velocity applied the initial bond structure fractures and reduces subsequently after each force build up. Therefore, new contacts and new bonds form which carry an increasing portion of the load with each subsequent reduction of the initial bond structure. The new contacts and bonds also fail after each force build up recorded in fig. 6.30. In fig. 6.34b at the penetration depth of the initial force build up, the initial bond structure experienced only a few failures so far. The biggest portion of the penetration is loaded onto the initial bond structure. In this view, the stress propagates mainly into the right part of the structure as the blade contacts the snow surface with its right edge first. After the initial build up, the initial bond structure experiences the first

major failure and reduces to the structure depicted in fig. 6.34c. An increasing portion of the penetration load is now also carried by new bonds and contacts. However, the initial bond structure also rebuilds stress due to the loading and keeps failing subsequently as illustrated by the differences between fig. 6.34c and fig. 6.34d. In fig. 6.34d at the last penetration force build up of fig. 6.30, the initial bond structure fails in all directions around the tip of the blade.
Fig. 6.35 illustrates three subsequent times during the scratch phase of the blade. The times are marked in fig. 6.31 by the respective subfigure labels (a),(b) and (c). The grains and bonds are illustrated in the same way as in the previous figure. The three times selected are the onset of scratch and two subsequent build ups of the resistance force, as marked in fig. 6.30.

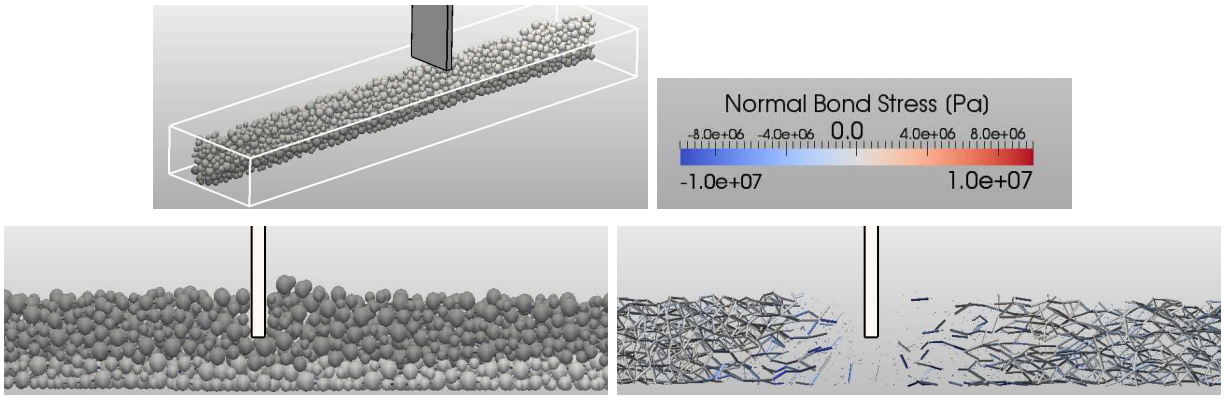


*(a) At $t = 0.6$ s and $Y = 0$ mm.*

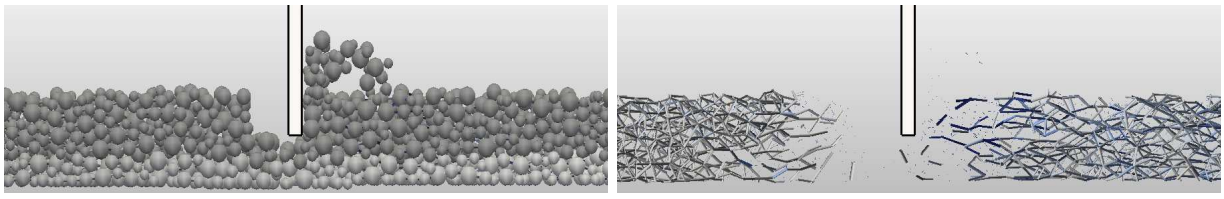

*(b) At $t = 0.95$ s and $Y = 7$ mm.*

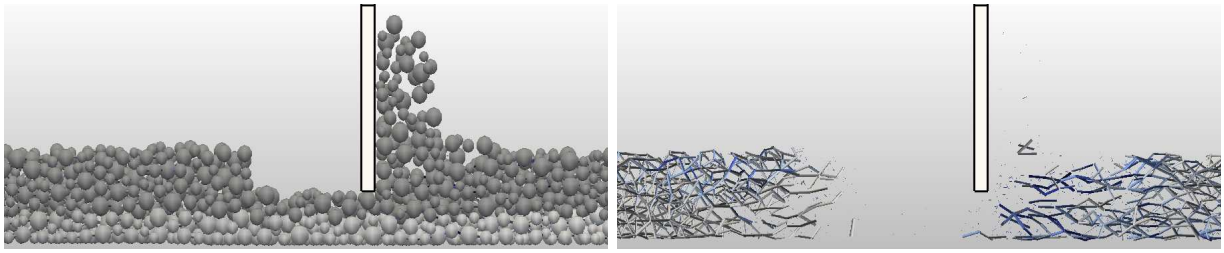

*(c) At $t = 1.64$ s and $Y = 20.75$ mm.*

*Figure 6.35: Grain and bond structure at selected scratch distances marked in fig. 6.31. The snow has an initial bond configuration of $N_b = 3.5$ and $r_b/\overline{r}_g = 0.5$ and a temperature of $-16$ °C. The bonds are coloured by the normal stress component.*

Fig. 6.35 illustrates that also at the scratch velocity applied the initial bond structure

fractures subsequently after each build up of the resistance force. With progression through the snow surface the initial bond structure fails in front and beneath the blade. The portions of the snow which failed in front of the blade pile up. These portions of the snow show a cohesive behaviour due to the formation of new bonds. They are piled up between the progressing blade and the non-fractured snow portion in $+Y$ - direction.
Finally, a rectangular trace is shaped into the snow reflecting the progression of the blade through the surface. The snow wall of the backside of the trace in $-Y$ - direction is held up by the bond structure remaining after the penetration phase. The snow layer beneath the trace of the blade remains in position with its initial bond structure fractured entirely.

## 6.3 XDEM - FEM Predictions of Tire Tread - Terrain Interaction

### 6.3.1 Tread Block - Snow Interaction

The motion of a tread block in the contact patch of a rolling tire is composed of penetration and scratch phases as already illustrated in fig. 2.44. The penetration and scratch performance of a tread block through a snow surface are predicted. The predictions are conducted similar to the blade penetration and scratch test of section 6.2.2. However, the tread block is able to deform during the interaction.

#### 6.3.1.1 Experimental Setup

The predictions are composed of two phases of constant velocities of the tread block. Initially the block penetrates the snow surface followed by a horizontal scratch as depicted in fig. 6.36. The tread block is initially placed above the snow surface. The coordinate

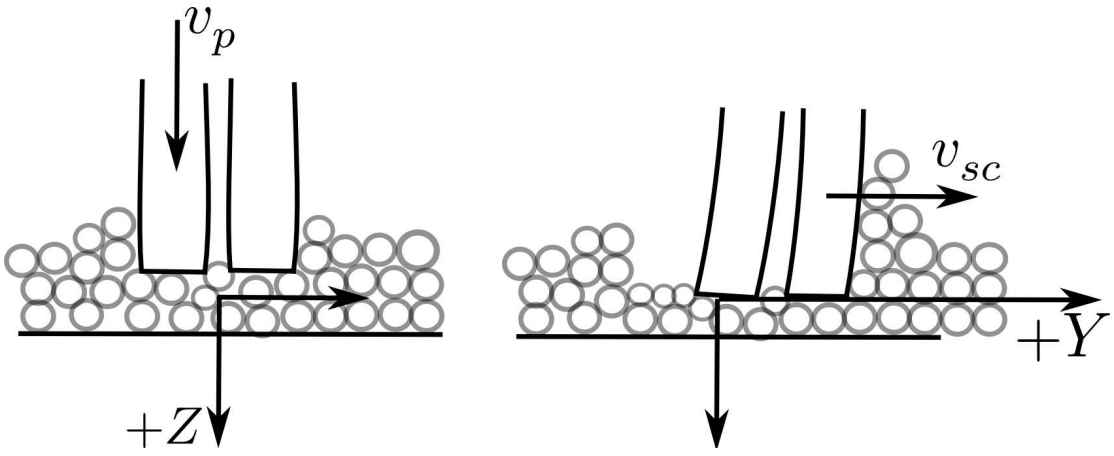


*Figure 6.36: Penetration and scratch phase of the tread block through the snow surface.*

origin aligns about 12 mm beneath the block. During the penetration phase the block moves down under the constant velocity $v_p$. It stops the penetration after 12 mm. In the

subsequent scratch phase the block moves horizontally by the scratch velocity $v_{sc}$. It stops after a distance of 30 mm.
Table 6.8 summarises the properties of the procedure.

*Table 6.8: Kinetic Properties*

| | |
|---|---|
| Penetration Velocity $v_p$ [mm/s] | 20.0 |
| Scratch Velocity $v_{sc}$ [mm/s] | 20.0 |
| Penetration Depth $+Z$ [mm] | $\approx 12.0$ |
| Scratch Distance $+Y$ [mm] | 30.0 |

Fig. 6.37 shows the initial configuration of the tread block and the snow strip. The initial density distribution of the strip is presented below.

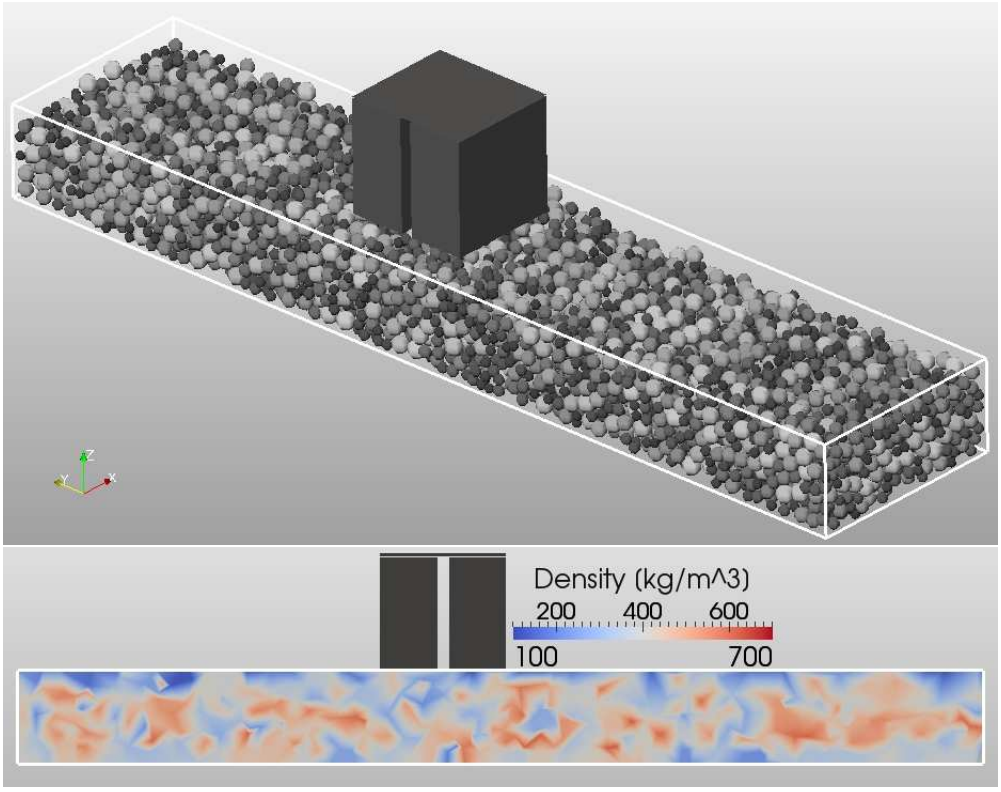


*Figure 6.37: Initial snow and tread block configuration and initial density distribution.*

The tread block is composed of two rectangular rubber blocks leaving a gap between them. The gap describes the sipe between two block on a winter tire tread. The sipe is aligned

in the $X - Z$ plane perpendicular to the scratch direction. The dimensions and material parameters of the tread block are presented in table 6.9.

*Table 6.9: Tread Block Properties and Dimensions*

| **Tread Block** | | | |
|---|---|---|---|
| Block Width [mm] | 25 | | |
| Block Length [mm] | 27.5 | | |
| Block Height [mm] | 25 | | |
| Sipe Size [mm] | 2.5 | | |
| Young's Modulus $E$[MPa] | 0.31 | 3.05 | 5.38 |
| Poisson's Ratio $\nu$ | 0.499 | | |
| Density $\rho_{rubber}$ | 1100 | | |

Within the predictions three different Young's Moduli are used. The moduli describe a hard, a soft and a very soft rubber to study the influence of the rubber composition. The deformation of the tread part is predicted by the linear elastic FEM model of chapter 4.1. The interaction between the snow and the tread block is accounted by the coupling method of chapter 5. The collision forces generated between the snow grains and the tread block are predicted by the Hertz Mindlin model, described in appendix A.1.5.
The spatial dimensions and properties of the snow strip are documented in table 6.10.

*Table 6.10: Snow Strip Properties and Dimensions*

| **Snow Strip** | | |
|---|---|---|
| Mean Initial Density [kg/m$^3$] | 410.0 | |
| Temperature [°C] | $-1.0$ | $-16.0$ |
| Strip Length [mm] | 210.0 | |
| Strip Width [mm] | 46.0 | |
| Strip Height [mm] | $\sim 20.3$ | |
| No. Grains | 7862 | |
| Grain Radius [ mm] | $> 1.0$ | $< 0.19$ |
| Bond Size $r_b/\overline{r}_g$ | 0 | 0.5 |
| Number of Bonds $N_b$ | 0 | 3.5 |

Thus, the snow strip contains spherical particles of random radii generated by the method in section 3.5. The minimum and maximum radius of the grains are presented in table 6.10. In a previous prediction the grains settled to approximate a natural distribution.

Two different temperatures, i.e. $T = -1$ °C and $T = -16$ °C, are used for the snow strip with a density of $\rho_0 = 410.0$ kg/m$^3$. The predictions were conducted with two different bonding configurations. The first configuration was initially unbonded, i.e. granular snow, which is allowed develop bonds during the prediction. The second configuration was a strong bonded snow structure. The large difference in initial bonding is applied to study the influence on the brittle behaviour of the snow at the high velocity. The snow strip is confined by rigid side and bottom walls which are assumed to be of the material snow as well. They describe the hard layer beneath the looser top layer of snow. Grain - grain and grain - wall contacts are described by the models developed in section 3.4.

#### 6.3.1.2 Penetration and Scratch Performance

Fig. 6.38 shows the force experienced by the tread block during penetration. The penetration force is shown for the initially non-bonded and strongly bonded snow at two different temperatures.

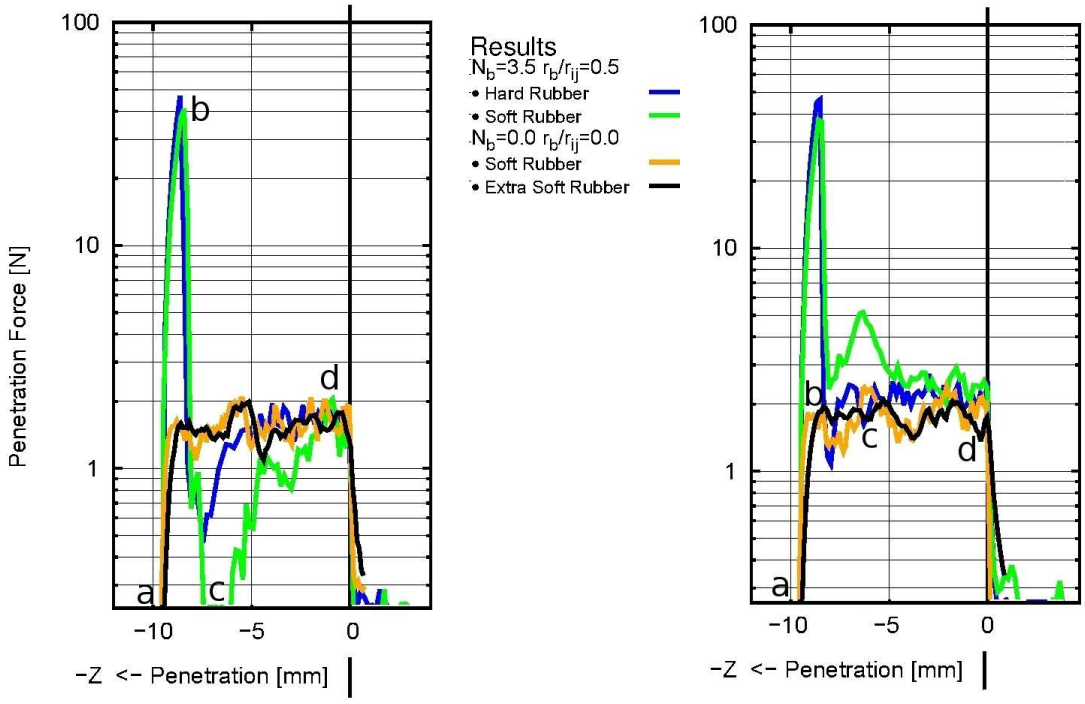


*(a)* $T = -1$ °C *(b)* $T = -16$ °C

*Figure 6.38: Penetration force versus penetration depth and scratch distance for a velocity of* 20 mm/s *and different temperature at different elastic moduli of the rubber and bonding configurations of the snow.*

The curves show the increase of the penetration force with ascending penetration depth and the decrease of the force with onset of the scratch phase. The predicted results in fig. 6.38 reveal that the influence of the elastic modulus of the rubber is negligible compared to the influence of the initial bonding strength of the snow. The initial bonding strength changes

the force response significantly. Shape and maximum force of the penetration curve are strongly dependent on the snow type.
The strong influence on the maximum penetration force was already recognised in the thin blade penetrations in fig. 6.30. But in the tread block penetrations the large contact area and the deformation of the block have an increasing influence on the shape of the curve with increasing initial bonding strength.
Despite the saw-tooth shape of the curves, the curves in fig. 6.38 of no initial bonding represent an almost ideal plastic progression with increasing penetration depth. The force builds up onto a rather low force value. With further penetration depth the curves show the common saw-tooth shape of brittle behaviour but in average they keep the low force value.
In fig. 6.38, the curves of the strong initial bond configuration show a strong initial increase followed by a sudden failure. During the release, the force can drop to zero before it builds up again, which is for instance the case for the green curve in fig. 6.38a. The maximum penetration force thereby correlates well with the unconfined brittle compression strength predicted in fig. 6.24.
Fig. 6.39 represents four penetration times of the black curve in fig. 6.38b. The four times

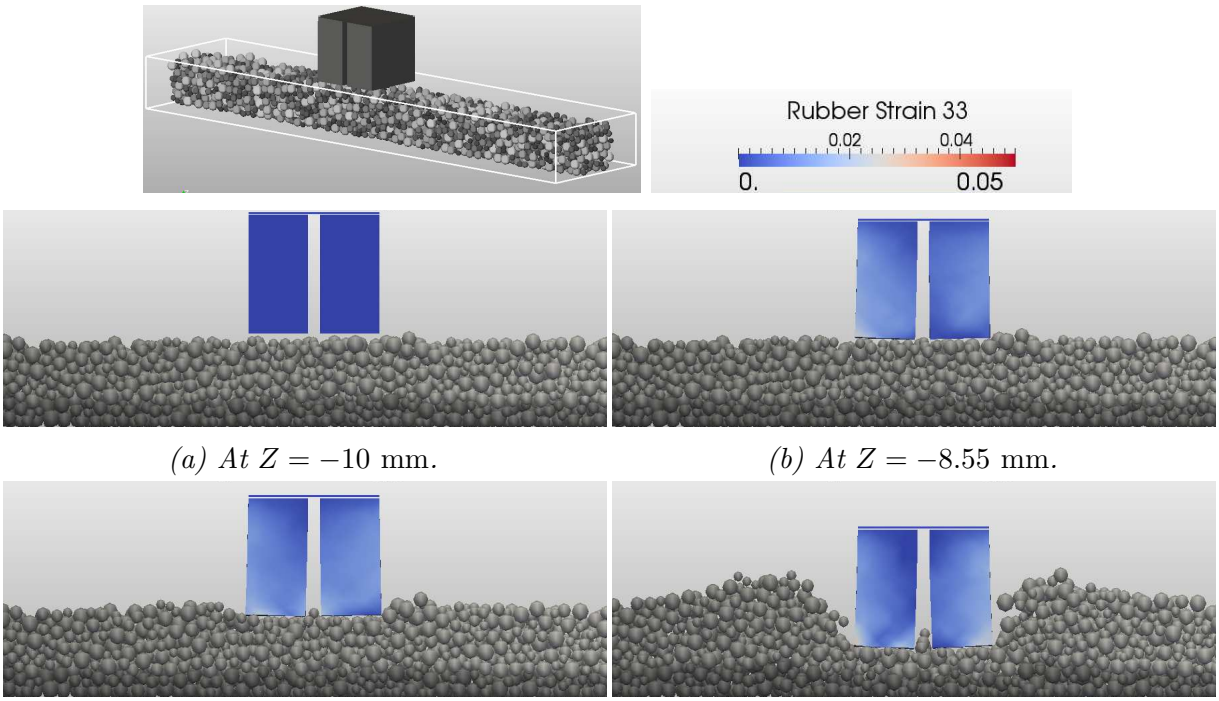


*(a) At $Z = -10$ mm.* *(b) At $Z = -8.55$ mm.*

*(c) At $Z = -7.2$ mm.* *(d) At $Z = -1.6$ mm.*

*Figure 6.39: Grain and bond structure at selected penetrations depths marked in fig. 6.38b. The snow has no initial bonding and a temperature of $-16$ °C.*

are marked in fig. 6.38b by the respective subfigure labels (a),(b),(c) and (d). The figure shows a slice of the snow surface beneath tread block in the $Y - Z$ plane. Each subsequent

time depicts the snow structure with grains and bonds. The selected times are an initial time step with no interaction at $Z = -10$ mm, the initial build up of the penetration force at $Z = -8.55$ mm and two subsequent times at increase penetration depth. The tread block is coloured by its strain component $\varepsilon_{33} = \varepsilon_{ZZ}$ in the direction of penetration.
Fig. 6.39a illustrates the penetration step when the tread touches the snow surface for the first time. In the second figure, fig. 6.39b, the penetration force is fully built up for the first time. Between this two steps the tread block develops a strain and stress state which does not change much in magnitude during the rest of the penetration. This of course correlates with the almost constant force in fig. 6.38.
During the entire penetration of the tread block into the initially unbonded snow the grains are continuously compressed beneath the tread block. Due to the progressing compression of the grains into the hard ground they are forced to escape into the looser snow sideways to the tread block. This lifts the snow surface next to the tread blocks. The side flow of the grains continuously deforms each single rubber block into $+Y$ and $-Y$ direction, respectively. Consequently, the gap between the rubber blocks widens and grains are increasingly compressed into the tread sipe with increasing penetration depth.
However, the penetration of the initially strong bonded snow, see fig.6.40 and the related green curve in fig. 6.38a, does not show the almost continuous plastic deformation of the initial unbonded snow.
Fig. 6.40 represents four subsequent time steps of the green curve in fig. 6.38a during the penetration phase. The first step shows again the initial configuration with no interaction between tread and snow at $Z = -10$ mm. Fig. 6.40b shows the tread block at the penetration position $Z = -8.55$ mm which correlates with the peak point of the maximum penetration force of the green curve in fig. 6.38a. Fig. 6.40c illustrates the drop of the penetration force in the curve. The final build up of the force is shown by fig. 6.40d.
Together with the initial strong increase of the penetration force, in the green curve in fig. 6.38a, the tread block develops a distinct strain state presented in fig. 6.40b. Due to the high bonding strength of the snow, the rubber blocks deform distinctively along the shape of the surface. Along with the strain concentrations developing in the tread block, the bonds of the grains in contact with the rubber build up high stress values.
When the strength limit of the ice bonds is reached they break and the deformation energy is suddenly released into the remaining snow grains and bond structure. This results into a total failure of all bonds beneath the tread block and a fracture of the surrounding bond structure into large individual snow pieces as shown in fig. 6.40c. The figure also shows that a large portion of the deformation energy is converted into kinetic energy. The unbonded snow grains are partially ejected off the snow surface.
After the fracture of the entire initial bond structure beneath the tread block the penetration progresses similar to the penetration of the initially unbonded snow. Fig. 6.40d illustrates the penetration into the remaining granular snow beneath the tread block. This observation also explains the re-build of the penetration force onto the force value of the unbonded snow in fig. 6.38.

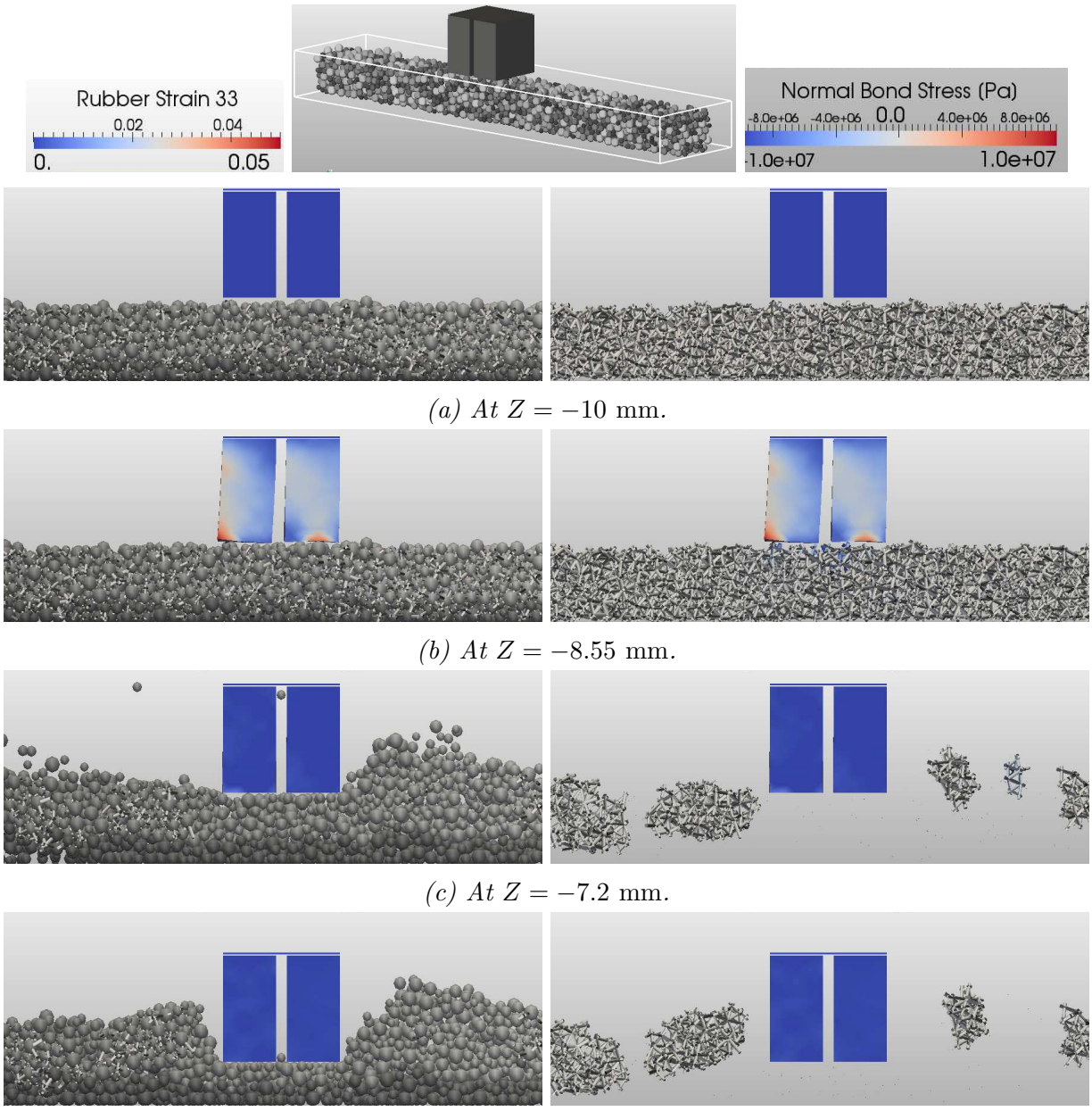


*(a) At $Z = -10$ mm.*

*(b) At $Z = -8.55$ mm.*

*(c) At $Z = -7.2$ mm.*

*(d) At $Z = -1.6$ mm.*

*Figure 6.40: Grain and bond structure at selected penetrations depths marked in fig. 6.38a. The snow has an initial bond configuration of $N_b = 3.5$ and $r_b/\overline{r}_g = 0.5$ and a temperature of $-1$ °C. The bonds are coloured by the normal stress component.*

### 6.3.2 Tire Tread - Soil Interaction

The coupling approach between XDEM and FEM described in chapter 5 is employed to predict the tractive performance of a rubber tire in interaction with soil terrain. This allows to resolve the response of the rolling tire during the interaction with the terrain as

well as the reaction of the soil bed on the tread. The prediction is set up according to the measurements of Shinone et al. (2010) for later comparisons with the numerical results.

#### 6.3.2.1 Experimental Setup

The prediction is composed of two phases which are a phase of vertical tire sinkage followed by the horizontal motion of the tire through the granular terrain by the angular velocity $\omega_t$ and translational velocity $v_t$. Fig. 6.41 depicts the two phases of tire travel schematically. During the sinkage phase the tire sinks into the soil bed under the constant velocity $v_s$

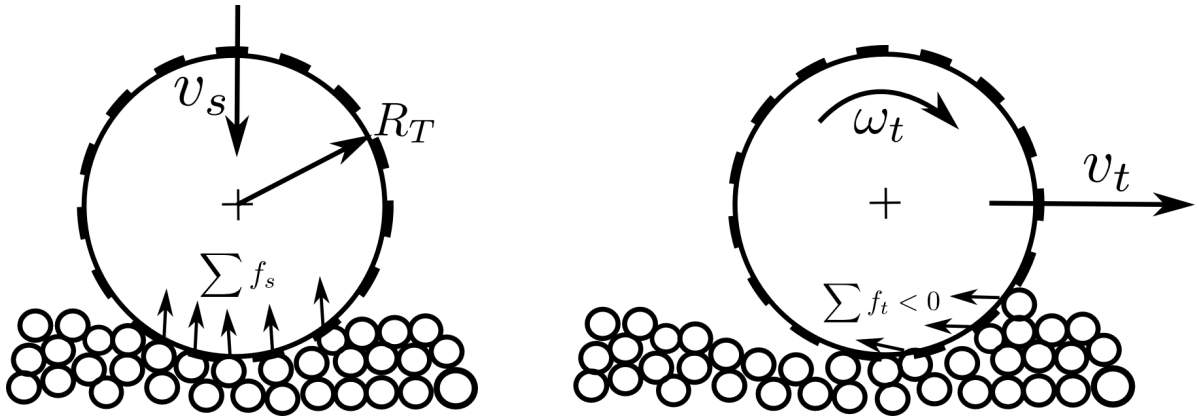


*Figure 6.41: Sinkage and travel phase of tire - soil interaction*

until the contact force $F_s$ is reached. $F_s$ is thereby the sum of all vertical forces.
Thereafter the tire rolls through the soil bed in horizontal direction with a predefined tire slip $s_T$.

$$s_T = \frac{(\omega_t \cdot R_T - V_t)}{\omega_t \cdot R_T}$$

During the horizontal motion of the tire through the soil bed, the running resistance $T_R$, gross tractive effort $T_H$ and drawbar pull $T_P$ are recorded for later comparison with the experimental results. The running resistance $T_R$ is predicted as the sum of all forces opposite to the direction of travel which develop between the tire surface and the grains in contact. This is indicated in fig. 6.41. The gross tractive effort $T_H$ is the counter part of the resistance $T_R$, which are computed as follows:

$$T_H = \sum f_t > 0 \qquad T_R = \sum f_t < 0$$

Finally the drawbar pull is calculated using the $T_R$ and $T_H$ as follows:

$$T_P = T_H - |T_R|$$

All properties describing the tire motion through the soil bed are composed in table 6.11. The spatial dimensions of the tire tread and the soil bed are documented in table 6.12.

*Table 6.11: Tire Travel Properties Dimensions*

| | |
|---|---|
| Sinkage Velocity $v_s$ [m/s] | 0.1 |
| Contact Force $F_s$ [N] | 5000 |
| Horizontal Velocity $v_t$ [m/s] | 0.976 |
| Angular Velocity $\omega_t$ [rad/s] | 1.80 |
| Tire Slip $s_T$ [%] | 5.0 |

*Table 6.12: Tire Tread and Soil Bed Dimensions*

| **Tire Tread** | |
|---|---|
| Tire size | $165/65R13$ |
| Radius $R_T$ [m] | 0.544 |
| Tread Width [m] | 0.165 |
| Wall Thickness [m] | 0.016 |
| Groove Depth [m] | 0.015 |
| Inflation Pressure [MPa] | 0.14 |
| No. Elements | 24287 |

| **Soil Bed** | |
|---|---|
| Bed Length [m] | 1.0 |
| Bed Width [m] | 1.0 |
| Bed Height [m] | $\sim 0.14$ |
| No. Grains | 21812 |
| Grain Diameter [ mm] | 15.6, 7.8, 6.9 $\pm 0.345$ |

Fig. 6.42 shows the initial configuration of the meshed tire volume and the settled soil bed. The soil bed contains three layers of spherical particles of different radii. The biggest radius is initially positioned at the bottom of the soil bed. The top layer consists of particles with the smallest radius which have been randomly distributed and settled in a previous prediction to approximate a natural terrain environment. The bed is confined by rigid walls with the same material properties as the soil particles. Thus, the soil bed bottom is approximated as hard soil ground.
The tire tread consist of a lug pattern whereby the lugs are arranged in a alternating apposition. Further, the tire tread is approximated by tetrahedral finite elements with linear shape functions. However, the displacements at the nodes of the tire tread contacting the rim are fixed. The inner surface of the tread experiences the normal stress resulting from the inflation pressure.
The element of the outer surface of the tire tread are allowed to interact with soil grains according the coupling procedure described in chapter 5.
The deformation of the tire is predicted by the linear elastic finite element description of chapter 4.1. Further, the soil bed motion is computed by the discrete element method described in chapter 3. During the interaction, forces developing between a soil grain and a finite element are computed based on the representative overlap. Thus, the collision forces developing during the interaction between soil grains as well as between a soil grain

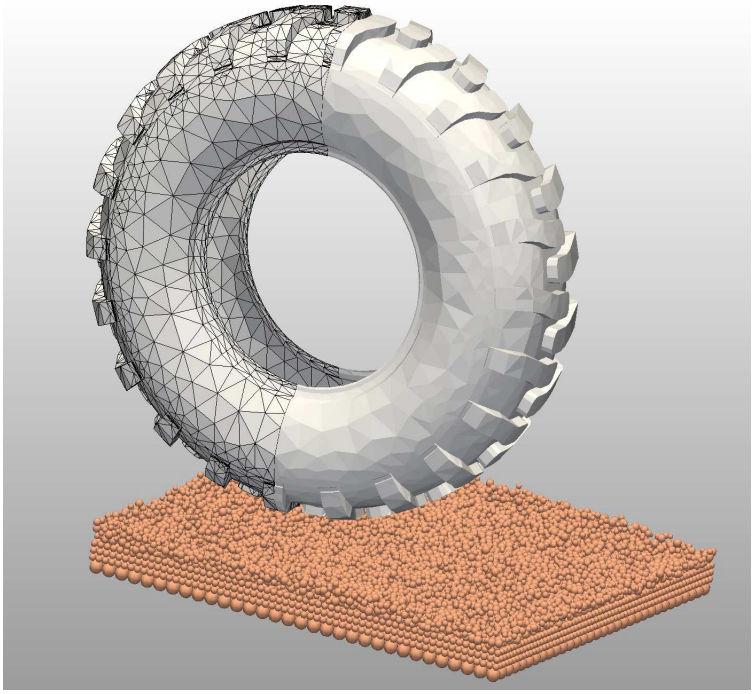

*Figure 6.42: Initial soil bed and and tire configurations.*

and a tire element are predicted by the Hertz Mindlin model, described in appendix A.1.5. The material properties used in the FEM, DEM and coupled predictions are stated in table 6.13. The tread and soil properties were taking from 2D FEM-DEM predictions by Nakashima et al. (2009). In their predictions they found the material parameters in correlation with the experiments of Shinone et al. (2010).

*Table 6.13: Material and Contact Parameters*

| | | **Tire Tread** | **Soil Grains** |
|---|---|---|---|
| Density | $\rho$ [ kg/m$^3$] | 1100.0 | 2600.0 |
| Young's Modulus | $E$ [kPa] | 20000.0 | 57.0 |
| Poisson Ratio | $\nu$ | 0.45 | 0.3 |
| Shear Modulus | $G$ [kPa] | 27586.2 | 78.6 |
| Friction Coefficient | $\mu$ | 0.3 | 0.6 |

#### 6.3.2.2 Traction Performance and Deformation

Shinone et al. (2010) measured the drawbar pull and torque of lugged tire treads at different slip configurations. The investigations were conducted with a single-wheel tester composed of a soil bin and a driving unit of the tire. The tires measured had a similar nominal size as the numerical tire tread, i.e. 165/60$R$13, with 535 mm diameter and 170 mm width. The

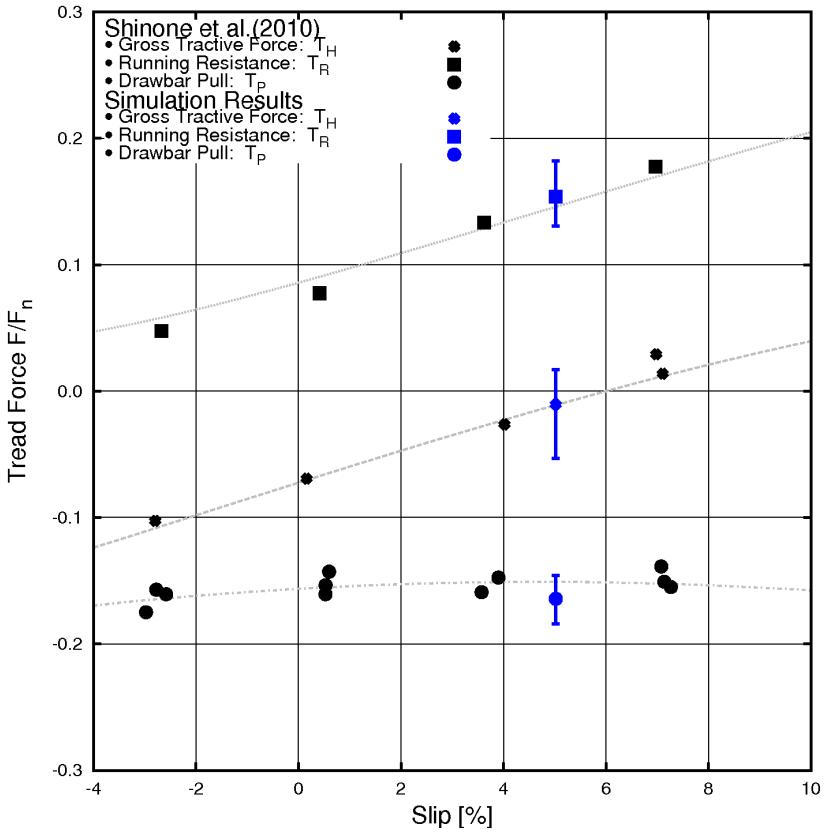


*Figure 6.43: Gross Tractive Force, Running Resistance and Drawbar Pull versus tire slip. The black symbols indicate the measurements by Shinone et al. (2010) of lugged tire treads at different slip values. The blue symbols and error bars show the mean, min and max of the predicted results at a slip of 5%.*

measured torque of the tire was used to predict the gross tractive effort $T_H = M/R_T$. The running resistance R was then predicted from the difference of gross tractive effort and drawbar pull $|T_R| = T_H – T_P$. The measurement results for lugged tire treads are shown as black symbols in fig. 6.43 for different slip values.

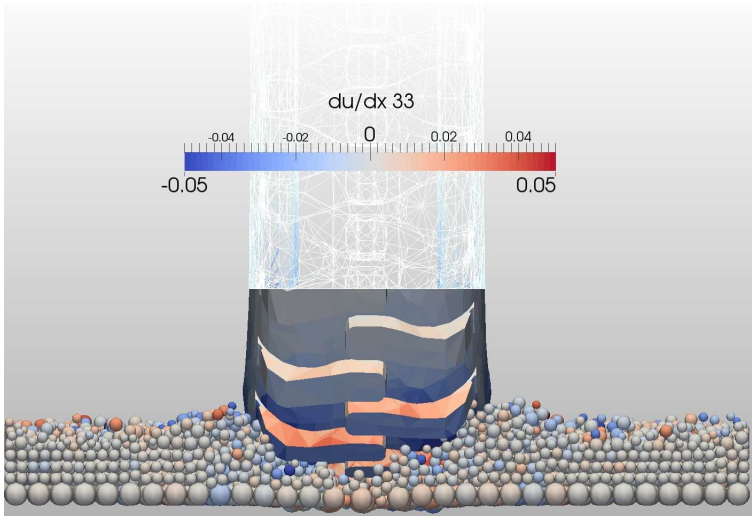


*(a) Final position after penetration*

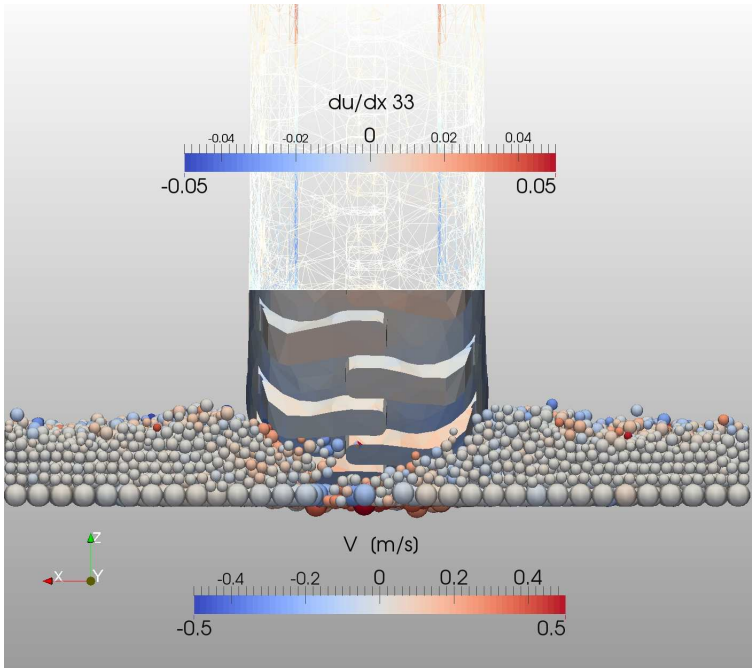


*(b) The tire during travel through the soil bed*

*Figure 6.44: Back view in travel direction of the tire during interaction with soil. The deformed tire is depicted and coloured by the strain component $\varepsilon_{33}$ in the direction of sinkage. The soil grains are coloured by their velocity in the direction of travel.*

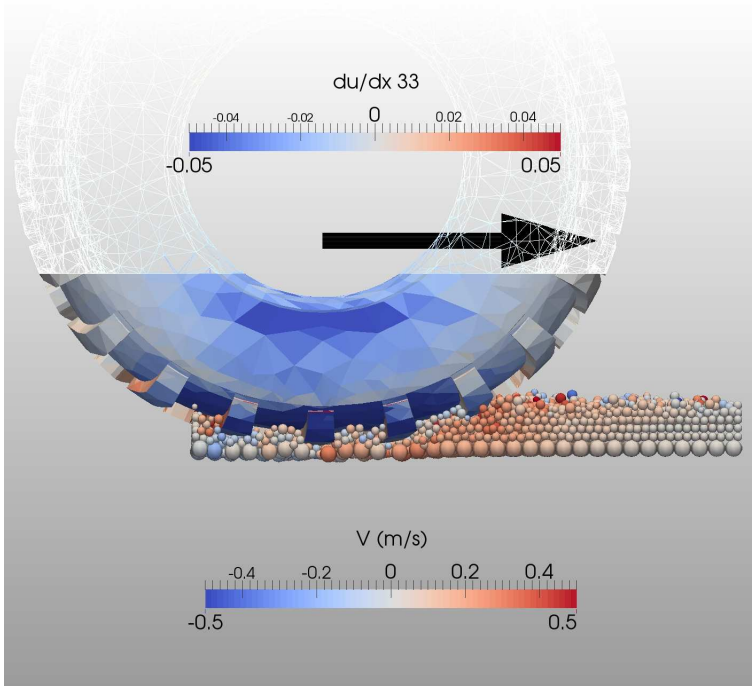


*(a) Final position after penetration*

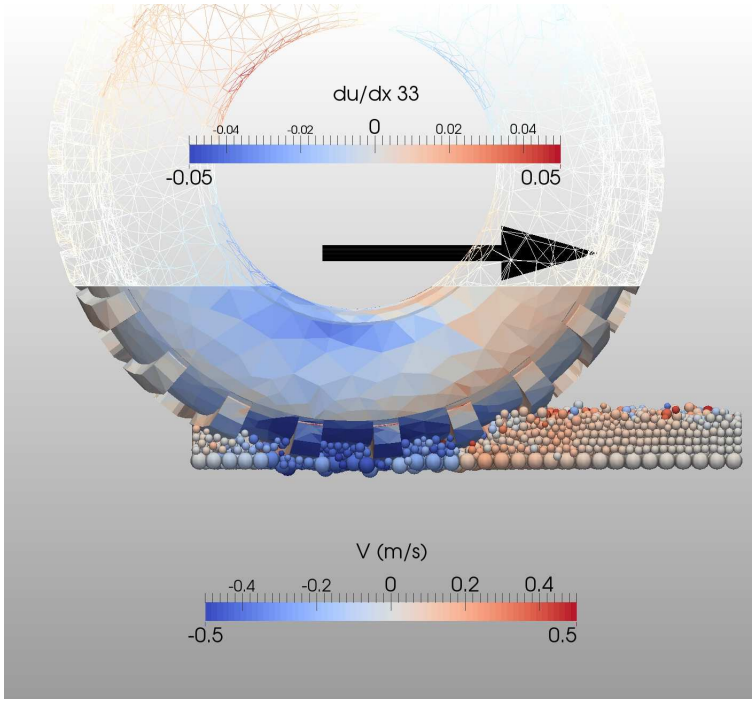


*(b) The tire during travel through the soil bed*

*Figure 6.45: Side view perpendicular to the travel direction of the tire during interaction with soil. The deformed tire is depicted and coloured by the strain component $\varepsilon_{33}$ in the direction of sinkage. The soil grains are coloured by their velocity in the direction of travel and the bed is depict clipped beneath the tread.*

Fig. 6.43 also contains the results of the coupled XDEM - FEM prediction at the slip value of 5.0%. The predicted results are shown as blue symbols of the mean value together with the min and max bars. The overall traction performance has been predicted very successfully even though the tire mesh and soil resolution are rather coarse. This proves the validity of the method for the application of tire traction performance.
Fig. 6.44 shows the tire from the backward position in the direction of travel. The soil grains are coloured by the velocity component in the direction of travel. Due to the interaction with the tire tread, the soil grains are compacted below and displaced onto the side of the tire. Two progressing time steps are shown in fig. 6.44. The first depicts the tire at the final sinkage position and the second during travel through the soil bed. The tire is represented in its deformed state and coloured by the strain component $\varepsilon_{33}$ in sinkage direction. The displacement of the soil next to the tire is clearly visual as well as the deformation of the tire wall due to the interaction forces.
Fig. 6.45 represents the same two timesteps shown in fig. 6.44 but in a side view. The soil bed is thereby cut open beneath the tire tread to allow an interior view. The colouring of the soil and tire is still by travel velocity and sinkage strain, respectively. This view visualizes clearly the maximum strain of the tire at the upper portion of the side wall due to the compression of the tread into the soil bed. Further, the acceleration of the soil grains beneath the tread against the direction of travel is visible when one compares the two timesteps depicted. The increase in velocity of the grains results from the grip of the tire into the bed during forward motion.
This grip of the footprint of the tire tread into soil bed is even more apparent in fig. 6.46. Fig. 6.46 shows a layer of the soil bed at the height of the tire lugs. With the motion of the tire into the direction of travel the majority of particles beneath the tread experiences an acceleration against the travel direction of the tire under the applied slip. This portion of the particles causes the gross tractive effort predicted. A minor portion of the soil grains is pushed ahead of the tread. These grains develop forces against the travel direction of the tire and thus cause the running resistance. Also, under the rolling of the tire tread through the bed the lugged tread patterns are pressed into the soil due to the traction developed.
Fig. 6.47 depicts the bottom view of the tire tread at the same two timesteps. The tire is coloured by the strain component $\varepsilon_{33}$ in direction of sinkage and the component $\varepsilon_{22}$ in the direction of travel. The arrow in fig. 6.47 indicates the travel direction. Component $\varepsilon_{33}$ indicates the maximum deformation on the tread shoulder under the load pressure developed between tire and soil during sinkage. The first moment shows a symmetric distribution of the strain at the end of the sinkage phase. For the component $\varepsilon_{22}$ the maximum of the strain develops at the front part of the footprint due to the soil grains producing the running resistance.

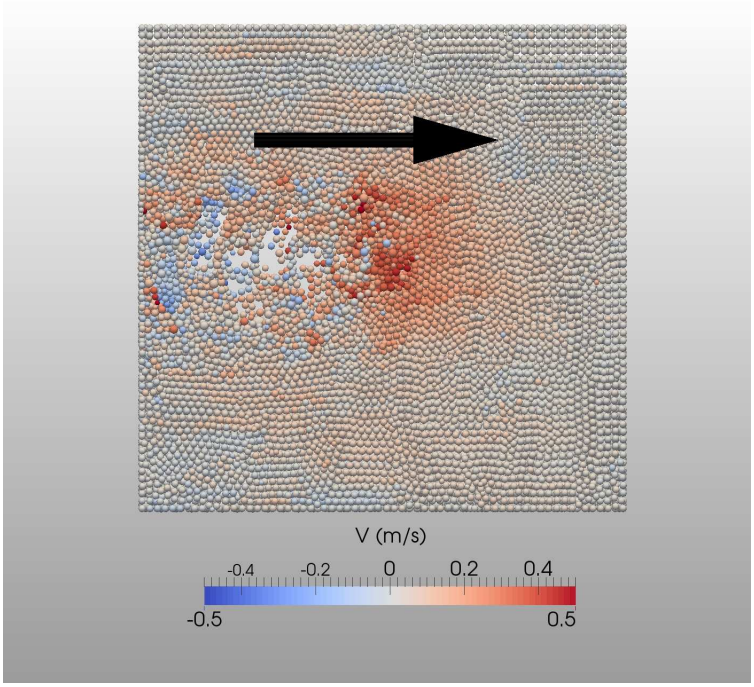


*(a) Final position of the tire after penetration*

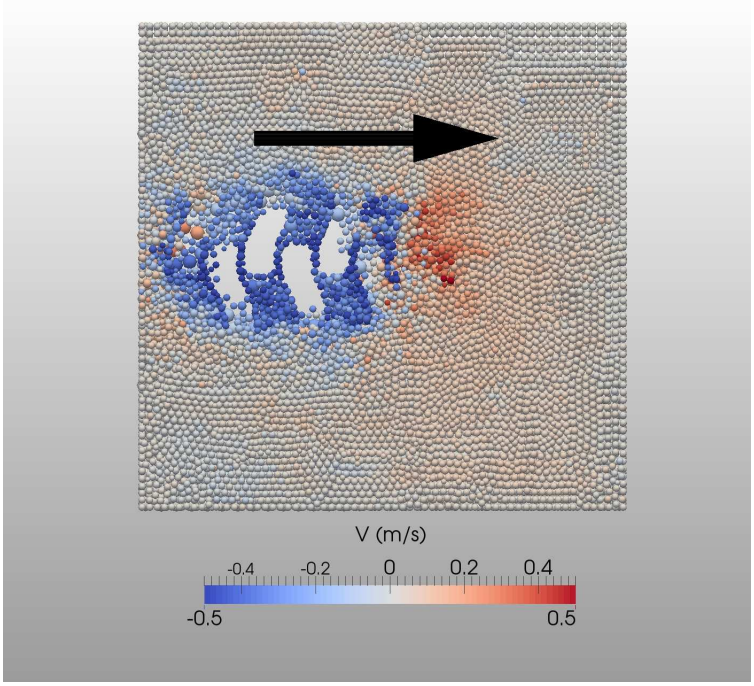


*(b) Tire during travel through the soil bed*

*Figure 6.46: Top view of soil bed during interaction with the tire. The soil grains are coloured by their velocity in direction of travel.*

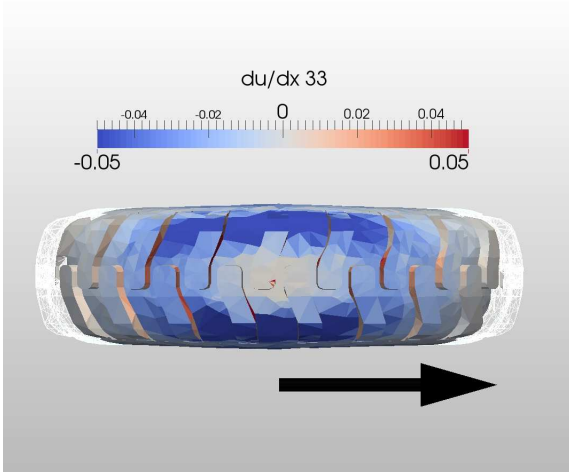


*(a) Final position after penetration*

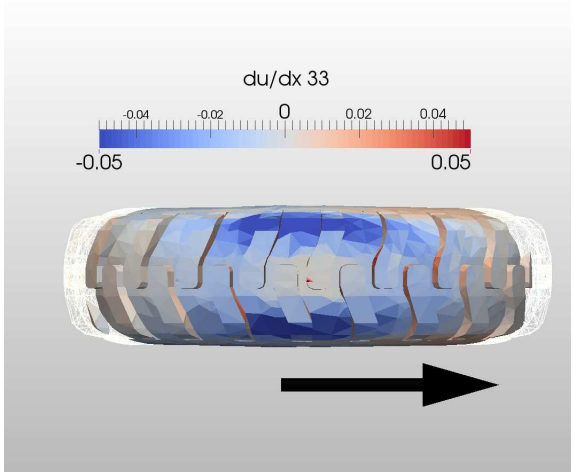


*(b) Final position after penetration*

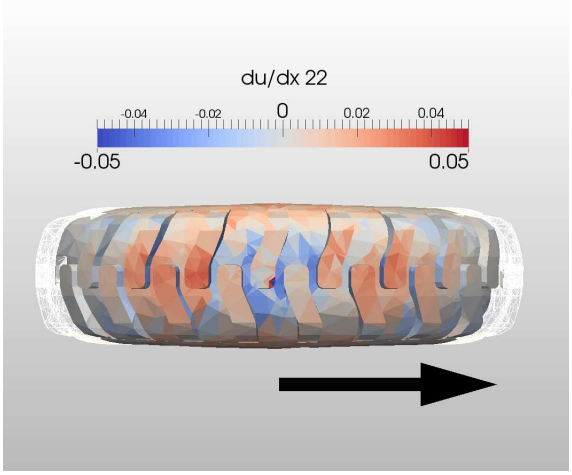


*(c) Tire during travel through the soil bed*

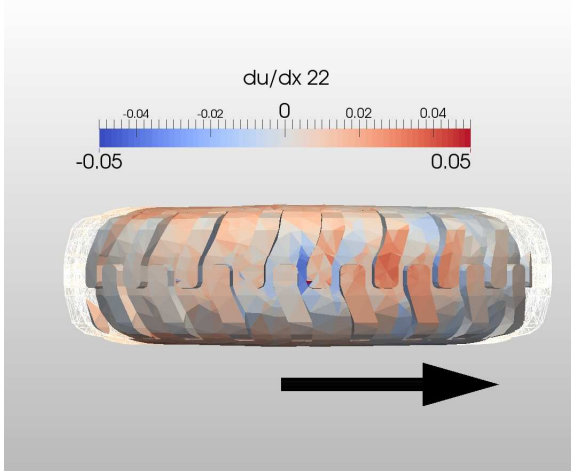


*(d) Tire during travel through the soil bed*

*Figure 6.47: Bottom view of the tire during interaction with soil. The deformed tire is depicted and coloured by the strain components $\varepsilon_{22}$ of direction of travel and $\varepsilon_{33}$ of direction of sinkage.*

# Chapter 7

# Conclusions

Within this thesis a simulation technique has been successfully developed to describe the interaction between a tire tread and a snow covered road. It supports understanding the nature of traction which consequently reveals measures to improve both traction and driving safety. Among the measures addressed can be form, orientation and geometry of a tire tread.

The Extended Discrete Element Method (XDEM) is employed to describe the mechanical behaviour of snow. Contrary to a continuum mechanics approach snow is considered to exist of discrete ice grains that are allowed to bond and collide with each other. Thereby, the individual grains and bonds build up an open-foam like structure. Snow behaves very complex during deformation due to its heterogeneity on micro-scale. Therefore, micro-mechanical models are developed to account for the micro-structural aspects of snow and in order to describe the interaction between snow and a tire tread. The micro-mechanical response of each snow grain in contact with the tire surface is transferred to the tread by means of an interface coupling. The interface couples the micro-scale nature of snow grains to the macro-scale of the tread surface. Due to the response forces the tire tread develops deformations which are described by a continuum description. Therefore, the tire tread itself is described by the Finite-Element-Method (FEM), in chapter 4, which evaluates the elastic deformation due to contact forces of the terrain.
Hence, the two key developments of this study are:

- the DEM - FEM interface coupling
- the discrete approach for snow behaviour

The first key development of the DEM – FEM interface, in chapter 5, meant to derive a coupling algorithm which enabled to connect the two domains efficiently. These developments first allowed the efficient detection of contact between the grains and the tread surface They also enabled the transfer of forces and geometrical information between the

DEM and FEM domain. The coupling algorithm transfers the forces caused by the impacting grains onto the appropriate finite elements. Thereafter, it updates the surface of the tire tread in accordance to the deformation predicted by the finite element solver. In order to describe the complex surface of a tire tread, the DEM software needed to be extended by a triangulated surface approximation. These triangular elements of the surface reflect the surface elements of a FEM mesh. A binary tree based algorithm has been developed and successfully employed for an efficient detection of contacts between the grains and the complex FEM surface.
The second key development of the discrete approach of snow, in chapter 3, included the implementation of a hierarchical algorithm into the employed software environment. The algorithm accounts for the inter-granular forces and moments within a loaded snow pack resulting from grain collisions, bond generations, deformations and fractures.
Based on the hierarchical algorithm, the material models for bond deformation and grain collision have been developed on the assumption that a snow pack is an ensemble of individual ice grains connected by cylindrical bonds. As snow behaviour is strongly dependent on its micro-structure, the material models had to be derived in order to describe the grain-scale features. The features implemented are:

- elastic-plastic grain collision
- inter-granular friction
- bond growth due to creep of ice
- elastic viscous-plastic bond deformation
- bond fracture

Additionally, these features account for the dependence on pressure, temperature and loading rate. The micro-scale models of bond formation and growth were thereby derived based on the ice-ice sintering measurements of Szabo and Schneebeli (2007), the contact theory of Hertz (1881) and the creep models of ice developed by Barnes et al. (1971). The models describing the bond deformation are set up to account for tension, compression, bending and torsion of the cylindrical ice neck between two adjoining snow grains.

In chapter 6.1, the developed snow models were validated in accordance to describe the grain-scale behaviour of snow and ice. The fracture and compressive response of a bond were accurately described by the models in comparison to the deformational behaviour of ice measured by Schulson (1990). Also the bond growth description predicted the time, pressure and temperature dependent relationship measured by Szabo and Schneebeli (2007) successfully. Further in appendix B.1, the elastic plastic behaviour during ice-ice collision was implemented into the micro-scale description of snow. The predictions by means of this model correlated very well with measurements of the coefficient of restitution of ice grains conducted by Higa et al. (1998).

In chapter 6.2, the validation of the discrete approach was undertaken to describe accurately the macroscopic behaviour of snow under load. Predictions of confined and unconfined compression tests of snow were conducted in relation to the measurements by Kinosita (1967), Von Moos et al. (2003), Abele and Gow (1975), Fukue (1977) and Yong and Metaxas (1985). These common experiments from the field of snow mechanics were predicted to show the validity of the developed models and to predict the dependencies of the snow behaviour in relation to several mechanical parameters. The parameter dependencies studied included micro-structural and mechanical properties and macroscopic dimensions. The studied parameters have been the bond and grain size, mechanical properties of ice, temperature of ice, coordination number, initial sample density, sample dimension, strain rate and grain distribution.
The strain-stress relation was captured accurately in the predictions of unconfined compression tests of snow samples at strain rates equal to and larger then $4 \cdot 10^{-3} s^{-1}$. The typical saw-tooth shape of the strain-stress curve of a brittle failing sample was re-captured as described by several authors. Also the predicted brittle strength of snow in dependence of the temperature, strain rate and sintering age correlated well with the measured dependencies.
Furthermore, the transition and ductile deformation of unconfined snow samples at strain rates about and smaller then $10^{-4} s^{-1}$ were predicted successfully by the developed approach. The strain softening behaviour of the transition regime was shown by the predicted strain-stress curves in comparison to the measurements. Although the ductile behaviour lacked the work-hardening effect under unconfined conditions, as found by several experimental investigators, the particular dependencies and characteristics related to the initial density and temperature could be described accurately. The strain rate - strength relationship in the transition and ductile regime agreed rather well with the measured relationship.
In the confined compression tests the grain-scale models managed to predict the density and temperature dependent mechanical behaviour of snow in accordance to the measured behaviour. The predictions and measurements followed the same strain-stress relation in dependence of the initial sample density.
The strong dependence of the strength of snow on the sintering age, as measured by Fukue (1977), was accurately described by the developed models of snow behaviour. The strain rate and the sintering age, i.e. the history, were shown to be the most influential parameters on the strength of a snow pack in the experiments and predictions. The strength - strain rate relationship of snow was captured properly in almost all conducted predictions compared to the strength measurements of Kinosita (1967).
In future developments of the snow models, the lack of work-hardening under ductile unconfined conditions should be addressed. For future engineering applications of the bonding model, a mathematical relation between natural sintering time and the bonding properties should be derived.

In chapter 6.3, the simulation technique proves to be able to predict accurately the traction behaviour of tire tread -terrain interactions. The gross tractive effort, rolling resistance and draw-bar pull have been compared successfully to measurements by Shinone et al. (2010). The principal deformations of the tire tread and the granular terrain could be described by

the DEM - FEM coupling method. However, the linear elastic description of the tire tread and the approximation as a whole rubber body are a very coarse approach. For future works the tire model should be extended to non-linear deformations. The different layers and compounds of a modern high-tech tire have to be accounted for in future predictions.

# List of Figures

# List of Tables

# References

Gunars Abele and Anthony Gow. Compressibility Characteristics of Compacted Snow. Technical report, CRREL, 1975. 33, 34, 42, 118, 120, 146, 147, 148, 176, 179, 184

M Akkok, C. M. Ettles, and S. J. Calabrese. Parameters Affecting the Kinetic Friction of Ice. *Journal of Tribology*, 109:552–559, 1987. 21, 22, 61, 62, 78, 180

Henri Bader. *The Physics and Mechanics of Snow as a Material*. CRREL, 1962. 22

P. Barnes, D. Tabor, and J. Walker. The Friction and Creep of Polycristaline Ice. In Barnes, editor, *Proceedings of the Royal Society of London*, volume 324 of *A*, 1971. 17, 18, 19, 59, 60, 61, 73, 175, 179, 180

P. Bartelt, M. Christen, and S. Wittwer. Progam hafeleli - two dimensional numerical simulation of the creeping deformatino and temperature distribution in a phase changing snow pack. In *Snow Engineering: Recent Advances and Developments*, 2000. 42

Klaus-Juergen Bathe. *Finite Element Procedures in Engineering Analysis*. Prentice-Hall Inc., New Jersey, 1982. 94

S.R. Beissel, C.A. Gerlach, and G.R. Johnson. Hypervelocity impact computations with finite elements and meshfree particles. *International Journal of Impact Engineering*, 33 (1-12):80–90, 2006. ISSN 0734-743X. doi: 10.1016/j.ijimpeng.2006.09.047. Hypervelocity Impact Proceedings of the 2005 Symposium. 52

M. J. Berger and S. H. Bokhari. A partitioning strategy for nonuniform problems on multiprocessors. *IEEE Transactions on Computers*, 36(5):570–580, 1987. 205

Josef Betten. *Finite Elemente fuer Ingenieure 2*. Springer Verlag, 2003. 94

Jane R. Blackford. Sintering and microstructure of ice: a review. *Journal of Physics D*, 40:R355–R385, 2007. 5, 6, 178

C.P. Borstad and D.M. McClung. Thin-blade penetration resistance and snow strength. *Journal Of Glaciology*, 57:325, 2011. 38, 39, 149, 154, 155, 180

L. Brendel, Y. Pengiran, M. Röck, U. Wahl, and U. Bröckel. Modelling of caked contacts in dems. *Chemical Engineering Technology*, 29:1355–1359, 2006. 44, 58, 88

C.S. Campbell. *Shear flows of granular materials*. PhD thesis, California Institute of Technology, 1982. 56

Chaman Chandel, Praveen K. Srivastava, and P. Mahajan. Micromechanical analysis of deformation of snow using x-ray tomography. *Cold Regions Science and Technology*, (0):–, 2014. ISSN 0165-232X. doi: http://dx.doi.org/10.1016/j.coldregions.2014.01.005. 29, 30, 33, 131, 132, 136, 137, 179, 183

Samuel C. Colbeck. A Review of Sintering in Seasonal Snow. Technical report, CRREL US Army Corps of Engineering, 1997. 7, 8, 10, 58, 178

Silene Cresseri, Francesco Genna, and Cristina Jommi. Numerical integration of an elastic–viscoplastic constitutive model for dry metamorphosed snow. *International Journal for Numerical and Analytical Methods in Geomechanics*, 34(12):1271–1296, 2010. ISSN 1096-9853. doi: 10.1002/nag.864. 41

P.A. Cundall and O. D. L. Strack. A discrete numerical model for granular assemblies. *Geotechnique*, 29:47–65, 1979. 56, 198

Algis Dziugys and Bernhard Peters. An approach to simulate the motion of spherical and non-spherical fuel particles in combustion chambers. *Granular matter*, 3:231–265, 2001. 70

Sergey V. Ershkov. Exact solution of viscous-plastic flow equations for glacier dynamics in 2-dimensional case. online, 2000. 3, 178

A. Estupinan, F. Hoffmann, and B. Peters. extended discrete element method used for convective heat transfer predictions. *International Review of Mechanical Engineering (I.R.E.M.E)*, 7(2):(in press), 2013. 201

X Fan, P Ten, C Clarke, A Bramley, and Z Zhang. Direct measurement of the adhesive force between ice particles by micromanipulation. *Powder Technology*, 131:105–110, 2003. ISSN 0032-5910. doi: 10.1016/S0032-5910(02)00339-X. 20, 210

Carlos A. Felippa. Introduction to Finite Element Methods. Lecture Notes, Department of Aerospace Engineering Sciences and Center for Aerospace Structures, University of Colorado, 2004. 94

Masaharu Fukue. *Mechanical performance of snow under loading*. PhD thesis, Department of Civil Engineering and Applied Mechanics, McGill, 1977. 8, 9, 25, 28, 29, 30, 31, 36, 37, 38, 39, 90, 118, 125, 136, 140, 141, 142, 143, 146, 148, 149, 154, 155, 176, 178, 179, 180, 181, 184

N. Fukuoka. Advanced technology of the studless snow tire. *JSAE Review*, 15:59–66, 1994. 48

P. H. Gammon, H. Kiefte, and M. J. Clouter. elastic constants of artificial and natural ice samples by breillouin spectroscopy. *Journal Of Glaciology*, 29, 1983. 58, 59, 83, 84, 198

J. Gaume, G. Chambon, M. Naaim, and N. Eckert. Influence of the weak layer's heterogeneity on slab avalanches releases using a finite element method. In Bonelli S., Dascalu C., and Nicot F., editors, *Advances in Bifurcation and Degradation in Geomaterials*, volume 11 of *Springer Series in Geomachanics and Geoengineering*, pages 261–266, 2011. 42

M. Gießler, F. Gauterin, B. Hartmann, and B. Wies. Influencing factors on force transmission of tires on snow tracks. Technical report, VDI - Bericht, 2007. 2, 45, 48, 49, 178

Martin Gießler, Frank Gauterin, Klaus Wiese, and Burkhard Wies. Thermographische laboruntersuchungen der kraftübertragung von reifen auf winterlichen fahrbahnen. In *19. Aachener Kolloquium Fahrzeug- und Motorentechnik*, 2010. 48, 49, 50, 180

I. Goldhirsch and G. Zanetti. Cluster instability in dissipative gases. *Physical Review Letter*, 70:1619–1622, 1993. 56

Robert B. Haehnel and Sally A. Shoop. A macroscale model for low density snow subjected to rapid loading. *Cold Regions Science and Technology*, 40(3):193–211, 2004. ISSN 0165-232X. doi: 10.1016/j.coldregions.2004.08.001. 40, 41, 50

Pascal Hagenmuller. Experiments and simulation of the brittle failure of snow. Master's thesis, WSL Institute for Snow and Avalanche Research SLF, 2011. 10, 42, 43, 89, 180

Heinrich Hertz. Ueber die beruehrung elastischer koerper. *Journal für die reine und angewandte Mathematik*, 92:156–171, 1881. 20, 76, 79, 85, 116, 175, 200

Michiya Higa, Masahiko Arakawa, and Norikazu Maeno. Size Dependence of Restitution Coefficients of Ice in Relation to Collision Strength. *Icarus*, 133(2):310–320, 1998. ISSN 0019-1035. doi: 10.1006/icar.1998.5938. 19, 20, 28, 175, 179, 185, 186, 196, 197, 209, 210

P. V. Hobbs. *Ice Physics*, volume 6. Oxford University Press, 1974. 16, 59

F. Hoffmann and B. Peters. An integrated approach to model blast furnaces. In *Proceedings of METEC InSteelCon 2011, 4th International Conference on Modelling and Simulation of Metallurgical Processes in Steelmaking (STEELSIM)*, 2011. 201

David A. Horner, John F. Peters, and Alex Carrillo. Large Scale Discrete Element Modeling of Vehicle-Soil Interaction. *Journal of Engineering Mechanics*, 127(10):1027–1032, 2001. 53, 110

S. Idelsohn, E. Onate, F. Del Pin, and N. Calvo. Fluid Structure Interaction Using the Particle Finite Element Method. *International Center for Computational Methods in Engineering*, 195:2100–2123, 2006. 52

Jerome B. Johnson and Mark A. Hopkins. Identifying microstructural deformation mechanics in snow using discrete-element modeling. *Journal of Glaciology*, 51, 2005. 43, 44, 58

Jerome B Johnson, Daniel J Solie, Joseph A Brown, and Edward S Gaffney. Shock response of snow. *Journal of Applied Physics*, 73(10):4852, 1993. 40

Th. U. Kaempfer and M. Schneebeli. Observation of Isothermal Metamorphism of New Snow and Interpretation as a Sintering Process. *Geophysical Research Letters*, 112, 2007. 11, 12, 13, 73, 178

F. E. Kennedy, E. M. Schulson, and D. E. Jones. The friction of ice on ice at low sliding velocities. *Philosophical Magazine A*, 80(5):1093–1110, 2000. 21, 62, 179, 180

Sun-Young Kim and Yasushi Sasaki. Simulation of Effect of Pore Structure on Coke Strength Using 3-dimensional Discrete Element Method. *ISUJ International*, 50:813–821, 2010. 44, 58

Seiiti Kinosita. Compression of Snow at Constant Speed. *Physics of Snow and Ice*, 1(2): 911–927, 1967. 20, 23, 24, 25, 26, 27, 28, 30, 33, 37, 39, 73, 118, 119, 125, 126, 129, 131, 141, 142, 143, 144, 145, 176, 179, 182, 184

H. O. K. Kirchner, G. Michot, H. Narita, and T. Suzuki. Snow as a foam of ice: plasticity, fracture and the brittle-to-ductile transition. *Philosophical Magazine, Part A*, 81:2161–2181, September 2001. doi: 10.1080/01418610010029043. 40

Vitaly A. Kuzkin and Igor E. Asonov. Vector-based model of elastic bonds for simulation of granular solids. *Phys. Rev. E*, 86:051301, Nov 2012. doi: 10.1103/PhysRevE.86.051301. 44

T. J. LaClair. *The Pneumatic Tire*, chapter Rolling Resistance, pages 476–529. NHTSA, 2005. 48, 49, 180

Theodore E. Lang and Richard Sommerfeld. The modeling and measurements of the deformation of a sloping snow pack. *Journal of Glaciology*, 19(81):153–163, 1977. 41

W.F. St. Lawrence and T.E. Lang. A constitutive relation for the deformation of snow. *Cold Regions Science and Technology*, 4(1):3–14, 1981. ISSN 0165-232X. doi: 10.1016/0165-232X(81)90026-4. 40

Jonah H. Lee. A new indentation model for snow. *Journal of Terramechanics*, 46(1):1–13, 2009. 50

B. E. Lindenmuth. *The Pneumatic Tire*, chapter An overview of tire technology, pages 2–27. NHTSA, 2005. 46, 180

Jacques Meyssonnier, Armelle Philip, Laura Capolo, and Philippe Mansuy. Experimental studies of the viscoplasticty of ice and snow. In Dimitrios Kolymbas and Gioacchino Viggiani, editors, *Mechanics of Natural Solids*, pages 203–221. Springer Berlin Heidelberg, 2009. ISBN 978-3-642-03578-4. 7, 10, 11, 22, 58, 178

M. Michael, B. Peters, and F. Vogel. Resolution of Different Length Scales by an Efficient Combination of the Finite Element Method and the Discrete Element Method. In B. H. V. Topping, editor, *Proceedings of the Eleventh International Conference on Computational Structures Technology*, Stirlingshire, United Kingdom, 2012. Civil-Comp Press. paper 249. 201

R.D. Mindlin. Compliance of elastic bodies in contact. *Applied Mechanics*, 16:259–268, 1949. 200

Gordon Moore. Cramming more components onto integrated circuits. *Electronics Magazine*, 38(8), April 1965. 56

J.P. Morris, M.B. Rubin, G.I. Block, and M.P. Bonner. Simulations of fracture and fragmentation of geologic materials using combined FEM/DEM analysis. *International Journal of Impact Engineering*, 33(1-12):463–473, 2006. ISSN 0734-743X. doi: 10.1016/j.ijimpeng.2006.09.006. Hypervelocity Impact Proceedings of the 2005 Symposium. 52

H. Nakashima and A. Oida. Algorithm and implementation of soil-tire contact analysis code based on dynamic FE-DE method. *Journal of Terramechanics*, 41:127–137, 2004. 53, 110

Hiroshi Nakashima, Yuzuru Takatsu, Hisanori Shinone, Hisao Matsukawa, and Takahiro Kastani. FE-DEM Analysis of the Effect of Tread Pattern on the Tractive Performance of Tires Operating on Sand. *Journal of Mechanical Systems for Transportation and Logistics*, 2(1):55–65, 2009. 53, 167

Hideki Narita. An experimental study on tensile fracture of snow. *Contributions from the Institute of Low Temperature Science*, A32:1–37, 1984. 32, 33, 125, 145, 179

Francios Nicot. *Modélisation multi-échelles des solides, géomatériaux, contribution au traitement des risques naturels*, volume Habilitation. Institut National Polytechnique de Grenoble, 2003. 4, 178

Francois Nicot. Constitutive modelling of snow as a cohesive-granular material. *Granular Matter*, 6:47–60, 2004a. 42, 58

Francois Nicot. From constitutive modelling of a snow cover to the design of flexible protective structures Part 1 – Mechanical modelling. *International Journal of Solids and Structures*, 41:3317–3337, 2004b. 22, 42

Michal Nitka, Gabriela Bilbie, Gael Combe, Cristian Dascalu, and Jacques Desrues. A DEM—FEM two scale approach of the behaviour of granular materials. *AIP Conference Proceedings*, 1145(1):443–446, 2009. doi: 10.1063/1.3179957. 52

B. Peters. Classification of combustion regimes in a packed bed based on the relevant time and length scales. *Combustion and Flame*, 116:297–301, 1999. 201

B. Peters and C. Bruch. Drying and pyrolysis of wood particles: experiments and simulation. *Journal of Applied and Analytical Pyrolysis*, 70:233–250, 2003. 201

V F Petrenko and R W Whitworth. *Physics of ice*. Oxford University Press, USA, 1999. 87

Thorsten Poeschel and Thomas Schwager. *Computational Granular Dynamics*. Springer, Berlin, 2005. 56, 70

M. G. Pottinger. *The Pneumatic Tire*, chapter Contact Patch (Footprint) Phenomena, pages 233–281. NHTSA, 2005. 47, 180

F Radjai and F Dubois. *Discrete element modeling of granular materials*, volume 41. ISTE Ltd and John Wiley & Sons, Inc, 2011. 56, 62, 70

Vincent Richefeu, Moulay Saïd El Youssoufi, Emilien Az'ema, and F Radjaï. Force transmission in dry and wet granular media. *Powder Technology*, 190(1-2):258–263, 2009. 44

Chris H. Rycroft. *Multiscale modeling in granular flow*. PhD thesis, MIT, 2007. 112, 121

Kasra Samiei. *Assessment of Implicit and Explicit Algorithms in Numerical Simulation of Granular Matter*. PhD thesis, University of Luxembourg, 2012. 66, 201

C Scapozza and P Bartelt. Triaxial tests on snow at low strain rate. Part II. Constitutive-behaviour. *Journal Of Glaciology*, 49(164):91–101, 2003. 26, 28, 41, 118, 136, 137, 140, 141, 179, 183, 184

M Schneebeli. Numerical simulation of elastic stress in the microstructure of snow. *Annals Of Glaciology*, 38(1):339–342, 2004. 10, 42

E.M Schulson. The brittle compressive fracture of ice. *Acta Metallurgica et Materialia*, 38 (10):1963–1976, 1990. ISSN 0956-7151. doi: 10.1016/0956-7151(90)90308-4. 15, 16, 73, 83, 86, 87, 117, 118, 175, 179, 182

Erland M. Schulson. Brittle failure of ice. *Engineering Fracture Mechanics*, 68(17–18): 1839–1887, 2001. ISSN 0013-7944. doi: 10.1016/S0013-7944(01)00037-6. 15, 16, 87

Juerg Schweizer. The influence of the layered character of snow cover on the triggering of slab avalanches. *Annals of Glaciology*, 18:193–198, 1993. 41

Eisuke Seta, Tatsuya Nakai, Martin Heggli, Matthias Jaggi, Henning Loewe, Martin Schneebeli, and Denes Szabo. Prediction of tire traction on compacted snow road. pages 45–49, 2011. 51

Lewis.H. Shapiro, Jerome B. Johnson, Matthew Sturm, and George L. Blaisdell. Snow Mechanics - Review of the State of Knowledge and Applications. Technical report, US-Army CRREL, 1997. 41

Hisanori Shinone, Hiroshi Nakashima, Yuzuru Takatsu, Takahiro Kasetani, Hisao Matsukawa, Hiroshi Shimizu, Juro Miyasaka, and Katsuaki Ohdoi. Experimental Analysis of Tread Pattern Effects on Tire Tractive Performance on Sand using an Indoor Traction Measurement System with Forced-slip Mechanism. *EAEF*, 3 (2):61–66, 2010. 165, 167, 168, 176, 185

F. W. Smith. Elastic stresses in layered snow packs. *Journal of Glaciology*, 11(63):407–414, 1972. 41

Martin Stoffel and Perry Bartelt. Modelling snow slab release using a temperature-dependent viscoelastic finite element model with weak layers. *Survey in Geophysics*, 24:417–430, 2003. 41

Alexey Stomakhin, Craig Schroeder, Lawrence Chai, Joseph Teran, and Andrew Selle. A material point method for snow simulation. In *Proceedings of Siggraph 2013*, 2013. 44

D. Szabo and M. Schneebeli. Subsecond sintering of ice. *Applied Physics letters*, 90, 2007. 13, 14, 20, 83, 85, 86, 114, 115, 175, 178, 181, 182, 210

J. B. Tatum. Classical mechanics. http://orca.phys.uvic.ca/ tatum/classmechs.html, 2010. 70

Testworld. International testing service. Ivalo, Finland. 2, 178

The HDF Group. Hierarchical data format version 5. 2000-2013. 202

T. Theile, H. Loewe, T. C. Theile, and M. Schneebeli. Simulating creep of snow based on microstructure and the anisotropic deformation of ice. *Acta Materialia*, 2011. 10, 43

Y. Tsuji, T. Tanaka, and T. Ishida. Lagrangian numerical simulation of plug flow of cohesionless particle in a horizontal pipe. *Powder Technology*, 71:239–250, 1992. 200

Y. Tsuji, T. Kawaguchi, and T. Tanaka. Discrete particle simulation of two-dimensional fluidized bed. *Powder Technol.*, 77(79), 1993. 52, 79

Stefan van Baars. Discrete Element Analysis of Granular Materials. *Heron*, 41:2–, 1996. 56

S. Varrette, P. Bouvry, H. Cartiaux, and F. Georgatos. Management of an Academic HPC Cluster: The UL Experience. In *Proc. of the 2014 Intl. Conf. on High Performance Computing & Simulation (HPCS 2014)*, Bologna, Italy, July 2014. IEEE. 2

Veritasium. Regelation of ice. Science Blog, 2011. 4, 178

Loup Verlet. Computer "experiments" on classical fluids. i. thermodynamical properties of lennard-jones molecules. *Phys. Rev.*, 159:98–103, Jul 1967. doi: 10.1103/PhysRev.159.98. 67

P Villard, B Chevalier, B Le Hello, and G Combe. Coupling between finite and discrete element methods for the modelling of earth structures reinforced by geosynthetic. *Computers and Geotechnics*, 36(5):709–717, 2009. 52

Markus von Moos. *Untersuchungen "uber das visko-elastische verhalten von Schnee auf der Grundlage von triaxialen Kriechversuchen.* PhD thesis, ETH Z"urich, 2001. 41, 136, 137, 141, 183

Markus Von Moos, Perry Bartelt, Adrian Zweidler, and Erst Bleiker. Triaxial tests on snow at low strain rate. Part I. Experimental device. *Journal Of Glaciology*, 49(164): 81–90, 2003. 8, 9, 10, 26, 33, 41, 90, 118, 119, 176, 178, 181

Gorow Wakahama. On the plastic deformation of single crystal of ice. In *Physics of Snow and Ice*, pages 291–311. Institute of Low Temperature Science, Hokkaido University, 1967. 15

O. R. Walton and R. L. Braun. Viscosity, granular-temperatures, and stress calculations for shearing assemblies of inelastic, frictional disks. *Rheology*, 60(5):949–980, 1986. 76, 197

B. H. Xu and A. B. Yu. Comments on the paper "numerical simulation of the gas–solid flow in a fluidized bed by combining discrete particle method with computational fluid dynamics"-reply. *Chemical Engineering Science*, 53:2646–2647, 1998. 52

Raymond N. Yong and Ioannis Metaxas. Influence of age-hardening and strain-rate on confined compression and shear behaviour of snow. *Journal of Terramechanics*, 22(1): 37–49, 1985. ISSN 0022-4898. doi: 10.1016/0022-4898(85)90006-0. 13, 20, 35, 36, 37, 40, 73, 118, 142, 144, 146, 176, 179, 180

R.N. Yong and M. Fukue. Performance of snow in confined compression. *Journal of Terramechanics*, 14(2):59–82, 1977. ISSN 0022-4898. doi: 10.1016/0022-4898(77)90002-7. 35, 36, 118, 146, 180

# Appendix A

# Extended Discrete Element Method

## A.1 Discrete Collision Models

This chapter lists further collision models of discrete particles developed and used in this study.

### A.1.1 Coefficient of Restitution of Ice

The coefficient of restitution $e_{ice}$ of ice used in this study has been derived by Higa et al. (1998). The impact and rebound velocity of ice spheres on an ice plate was measured to define the coefficient of restitution of ice. Their investigations revealed the dependencies of $e_{ice}$ on the impact velocity, size and temperature of the ice spheres. They derived the following ideal relation:

$$e_{ice} = \begin{cases} \cong 1 & : v_i < v_c \\ \left(\frac{v_i}{v_c}\right)^{-\log \frac{v_i}{v_c}} & : v_i \geqq v_c \end{cases} \tag{A.1}$$

where $v_i$ stands for the component of the impact velocity normal to the plain and $v_c$ describes the critical velocity. The critical impact velocity distinguishes between elastic and plastic-brittle impact behaviour. In fig. A.1, both regimes are separated by the critical velocity of $v_c = 0.73$ m/s. The elastic regime is defined ideally by no energy lost during the impact. The plastic-brittle regime can be approximated by an exponential decrease with increasing velocity due plastic deformation and fracture during impact. Higa et al.

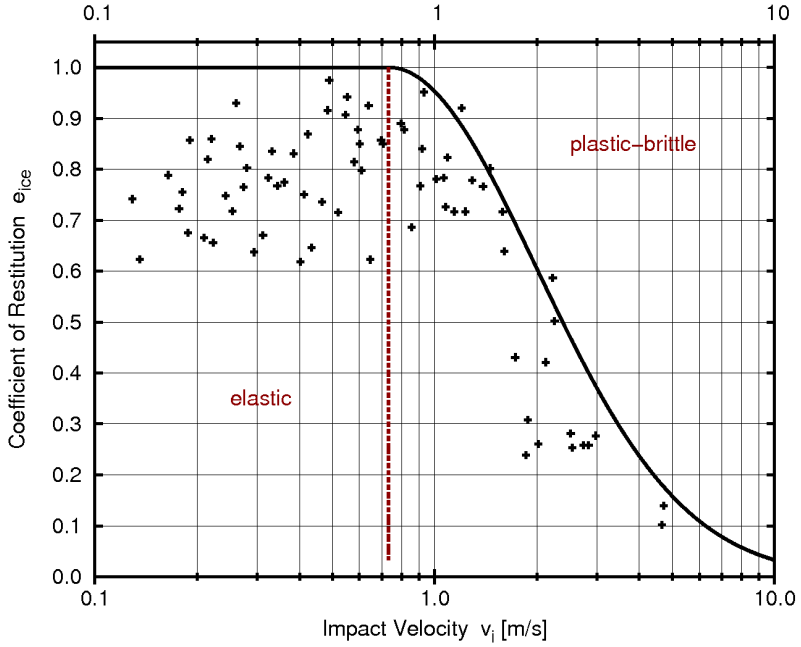


*Figure A.1: Coefficient of restitution of ice versus impact velocity for an ice sphere of* 15 mm *in diameter and a temperature of* $-12°$ *C. The line represents eq. A.1 and the symbols stand for the measurements by Higa et al. (1998)*

(1998) derived the following relation to predict the critical velocity:

$$v_c = \begin{cases} 5.72 \cdot 10^{-4} \cdot e^{\frac{Q}{2RT}} \cdot \dfrac{(1+\gamma^3)^{\frac{3}{4}}}{(1+\gamma)^{\frac{7}{4}}} \left(\dfrac{r_i}{0.015}\right)^{\frac{-1}{2}} & : T \geqq 229 \text{ K} \\ 180 \cdot \dfrac{(1+\gamma^3)^{\frac{3}{4}}}{(1+\gamma)^{\frac{7}{4}}} \left(\dfrac{r_i}{0.015}\right)^{\frac{-1}{2}} & : T < 229 \text{ K} \end{cases} \tag{A.2}$$

where $r_i$ denotes the radius of ice sphere $i$ and $\gamma = r_i/r_j$ is the ratio of the impacting ice spheres. The critical velocity $v_c = f(r_i, T)$ depends strongly on the size of the ice grains and on the temperature.

### A.1.2 Elastic Brittle-Plastic Model for Snow and Ice Grains

This grain collision model is based on the linear hysteretic model developed by Walton and Braun (1986). The model is well suited to describe the plastic to brittle collision behaviour of snow and ice grains at high deformation rates. This feature is inherited from the restitution coefficient of ice, eq. A.1, which accounts for the plasticity of this model. The responding normal force $\vec{F}_{ij}^{c,n}$ is also predicted by eq. 3.41. The loading part of the rheological model is still described as pure elastic. The stiffness is predicted by the Young's modulus of ice. But the unloading part is represented as an elastic plastic model, as depicted in fig. A.2, where the plastic part employs the restitution of ice derived by Higa et al. (1998).

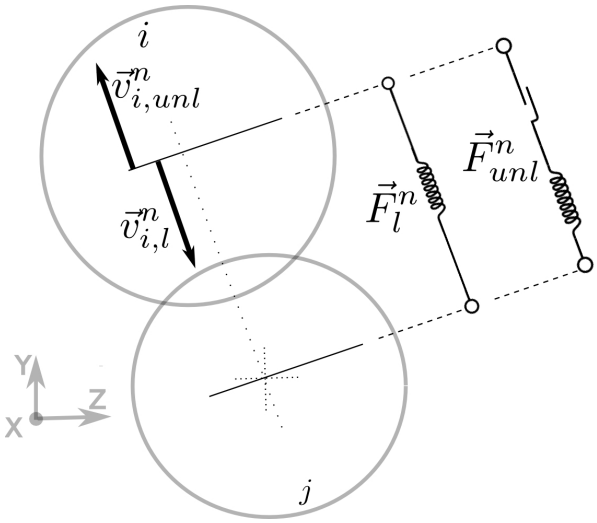


*Figure A.2: Schematic demonstration of the material law of the elastic plastic impact model*

Thus, in this model the loading stiffness $k_l^n$ is predicted as follows:

$$k_l^n = E_{ice} \cdot \sqrt{R_{ij} \cdot \delta_{ij}^n} \cdot (1 - \nu_{ice})^{-1} \tag{A.3}$$

where $R_{ij}$ denotes the effective radius, $\delta_{ij}^n$ the normal overlap, $E_{ice}$ is the Young's modulus and $\nu_{ice}$ denotes Poisson's ratio. The Young's modulus and Poisson's ratio of ice are given in table 3.1 by Gammon et al. (1983). The unloading stiffness is determined as follows:

$$k_{unl}^n = \frac{k_l^n}{e_{ice}} \tag{A.4}$$

Eq. A.4 employs the coefficient of restitution $e_{ice}$ according to eq. A.1. As already mentioned the coefficient of restitution $e_{ice} = f(T, R_{ij}, v_{imp})$ is a function of the temperature, the ratio of the radii and the impact velocity. The impact velocity is assumed to be the initial velocity, i.e. the velocity $v_{imp} = \vec{v^n}_{ij}(t_o^c)$ at the time of the first contact. The plastic overlap is than simply the relation of eq. A.5 between the loading $k_l^n$ and unloading stiffness $k_{unl}^n$ times the maximum normal overlap $\delta_{ij,max}^n$.

$$\delta_{ij}^{n,p}(t) = \frac{k_{unl}^n - k_l^n}{k_l^n} \cdot \delta_{ij,max}^n \tag{A.5}$$

### A.1.3 Linear Spring Dashpot I

This section presents a damped linear spring model for the prediction of a collision force derived by Cundall and Strack (1979). The normal collision force is composed of a linear spring force and a dashpot force. The spring results in an elastic repulsive force and the dashpot contributes as a damper which can be written as follows:

$$F_{ij}^n = m_{ij}\ddot{\delta}_{ij}^n = -(k_n \delta_{ij}^n + c_n \dot{\delta}_{ij}^n) \tag{A.6}$$

where $\delta_{ij}^n$ is the normal overlap and $m_{ij}$, $k_n$ and $c_n$ are the reduced mass, the normal spring stiffness and the normal dissipation coefficients, respectively.
The normal dissipation coefficient is predicted as follows:

$$c_n = \ln e \sqrt{\frac{4 m_{ij} k_n}{\pi^2 + \ln e^2}} \tag{A.7}$$

where $e$ denotes the coefficient of restitution.
The tangential force is computed by a static friction force which is limited by a dynamic friction force. The static friction is a viscous damping force and the dynamic friction is obtained from Coulomb's law of friction as follows:

$$F_{ij}^t = min(c_t \dot{\delta}_{ij}^t, \mu F_{ij}^n) \tag{A.8}$$

where $c_t$ is the tangential damping coefficient and $\mu$ is the Coulomb's friction coefficient whereas $\dot{\delta_{ij}^n}$ describes is the relative tangential velocity.

### A.1.4 Linear Spring Dashpot II

The second linear spring dashpot model presented in this section is an improved version of the previous model. In this model the normal stiffness is derived from the maximum strain energy of a Hertzian contact and can be written as follows:

$$k_n = \frac{16}{15} R_{ij}^{\frac{1}{2}} E_{ij} \left(\frac{15 m_{ij} v^2}{16 R_{ij}^{\frac{1}{2}} E_{ij}}\right)^{\frac{1}{5}} \tag{A.9}$$

where $R_{ij}$, $E_{ij}$ and $v_{ij}^n$ are the reduced radius, effective young modulus and the collision velocity respectively.
Therefore, the normal collision force can be written as:

$$F_{ij}^n = m_{ij} \ddot{\delta} = -\left(\frac{16}{15} R_{ij}^{\frac{1}{2}} E_{ij} \left(\frac{15 m_{ij} v^2}{16 R_{ij}^{\frac{1}{2}} E_{ij}}\right)^{\frac{1}{5}} \delta_{ij}^n + c_n \dot{\delta_{ij}^n}\right) \tag{A.10}$$

The tangential force is also composed of a static and dynamic friction part whereby the static part is based on a spring-dashpot model:

$$F_{ij}^t = min(k_t \delta_{ij}^t + c_t \dot{\delta}_{ij}^t, \mu F_{ij}^n) \tag{A.11}$$

where $\delta_{ij}^t$ is the tangential displacement.
The tangential dissipation coefficient is derived from the tangential stiffness similar to the normal dissipation coefficient as follows:

$$c_t = \ln e_t \sqrt{\frac{4 m_{ij} k_t}{\pi^2 + \ln {e_t}^2}} \tag{A.12}$$

where $e_t$ is the coefficient of tangential restitution.

### A.1.5 Hertz-Mindlin

The Hertz-Mindlin model is based on the theory of Hertz (1881). The normal elastic force and the normal energy dissipation are modeled based on the theory proposed by Mindlin (1949). The formula for the normal force can be written as follows:

$$F_{ij}^n = m_{ij}\ddot{\delta_{ij}^n} = -(\frac{4}{3}E_{ij}\sqrt{R_{ij}}\delta_{ij}^{t\,\frac{3}{2}} + c_n\delta_{ij}^{t\,\frac{1}{4}}\dot{\delta_{ij}^t}) \tag{A.13}$$

The equation for the normal dissipation coefficient $c_n$ is proposed by Tsuji et al. (1992) as follows:

$$c_n = \ln e\sqrt{\frac{5m_{ij}k_n}{\pi^2 + \ln e^2}} \quad \text{with} \quad k_n = \frac{4}{3}E_{ij}\sqrt{R_{ij}} \tag{A.14}$$

The tangential force is a function of static and dynamic friction whereby the static friction is modeled by a spring-dashpot model:

$$F_{ij}^t = min(k_t\delta_{ij}^t + c_t\dot{\delta_{ij}^t}, \mu F_{ij}^n) \tag{A.15}$$

where $\delta_{ij}^t$ is the tangential spring displacement which is defined as the total displacement in the tangential direction since the beginning of this contact. The tangential stiffness is estimated by eq. A.16.

$$k_t = 8G_{ij}\sqrt{R_{ij}\delta} \tag{A.16}$$

where $G_{ij}$ is the effective shear modulus defined in eq. A.17.

$$\frac{1}{G_{ij}} = \frac{2-\nu_i}{G_i} + \frac{2-\nu_j}{G_j} \tag{A.17}$$

The tangential dissipation coefficient is derived from the tangential stiffness using eq. A.18.

$$c_t = \ln e\sqrt{\frac{5(4m_{ij}k_t)}{6(\pi^2 + \ln e^2)}} \tag{A.18}$$

## A.2 Software Design

The software design DPM is organised as a C++ library and a set of simulation drivers designed to provide high quality and fast simulations of different physical phenomena in granular matter.
DPM supports multi-physics simulations via different simulation modules. Currently, two simulation modules for granular materials are available:

1. motion of a granular ensemble is available via the *Dynamics* module
2. chemical conversion between grains is provided by the *Conversion* module

The design is meant to be flexible so that additional simulation modules can be added easily. Predictions with only one module or in a coupled mode are possible. Fig. A.3 presents the two modules schematically.

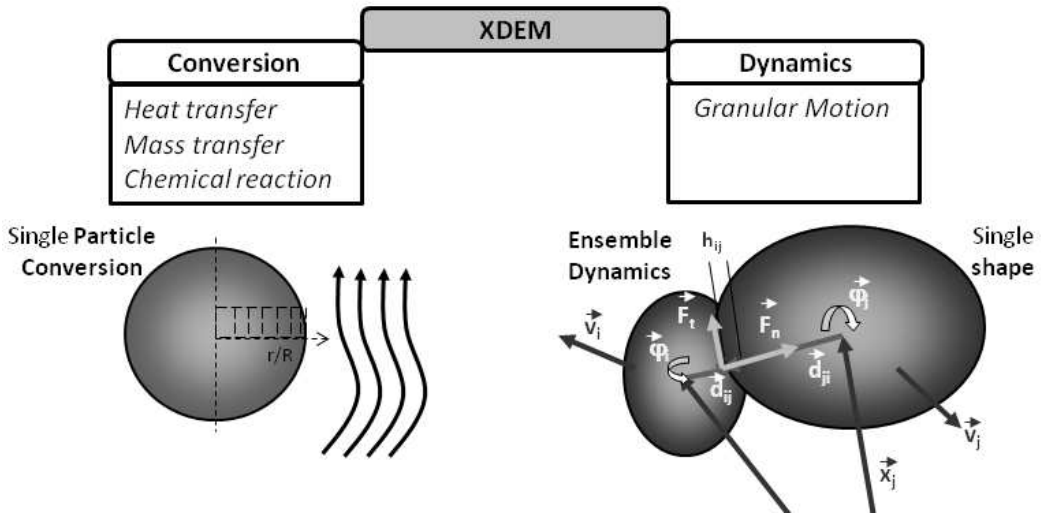


*Figure A.3: Conversion and motion module in DPM.*

DPM has been successfully used for the prediction of convective heat transfer by Estupinan et al. (2013) and combustion processes in packed beds by Peters (1999), drying and pyrolysis in particulated systems by Peters and Bruch (2003), iron ore reduction by Hoffmann and Peters (2011), particle motion and conversion processes on backward and forward acting grates by Samiei (2012) as well as to predict the interaction between bulk materials and deformable bodies by Michael et al. (2012).

### Workflow

A prediction operates on a set of particles and boundaries which can be of various shape and material. The initial state of a prediction is setup during the initialisation step and all the information required for this are read from the input file. The initial state of a

particle is defined, among of other values, by its position and orientation, its velocity and angular velocity, its shape , its material, its temperature. The input is stored in the flexible HDF5 file format, see The HDF Group, where the information is organised hierarchically. Particles sharing the same shape and material are grouped together into *piles*.
Boundaries are treated a special case of particles. In contrast to particles, boundaries do not accelerate do to forces experienced. Thus they are not accounted for when solving the equations of inertia.
After the state of the system has been initialized, the prediction starts which represents most of the computation. The prediction is an iterative loop in which each iteration corresponds to a timestep of the prediction. For each timestep $t$, the new state of the system at $t + \Delta t$ is computed. During a timestep, the computation is split in two phases:

1. the *interaction* step
2. the *integration* step

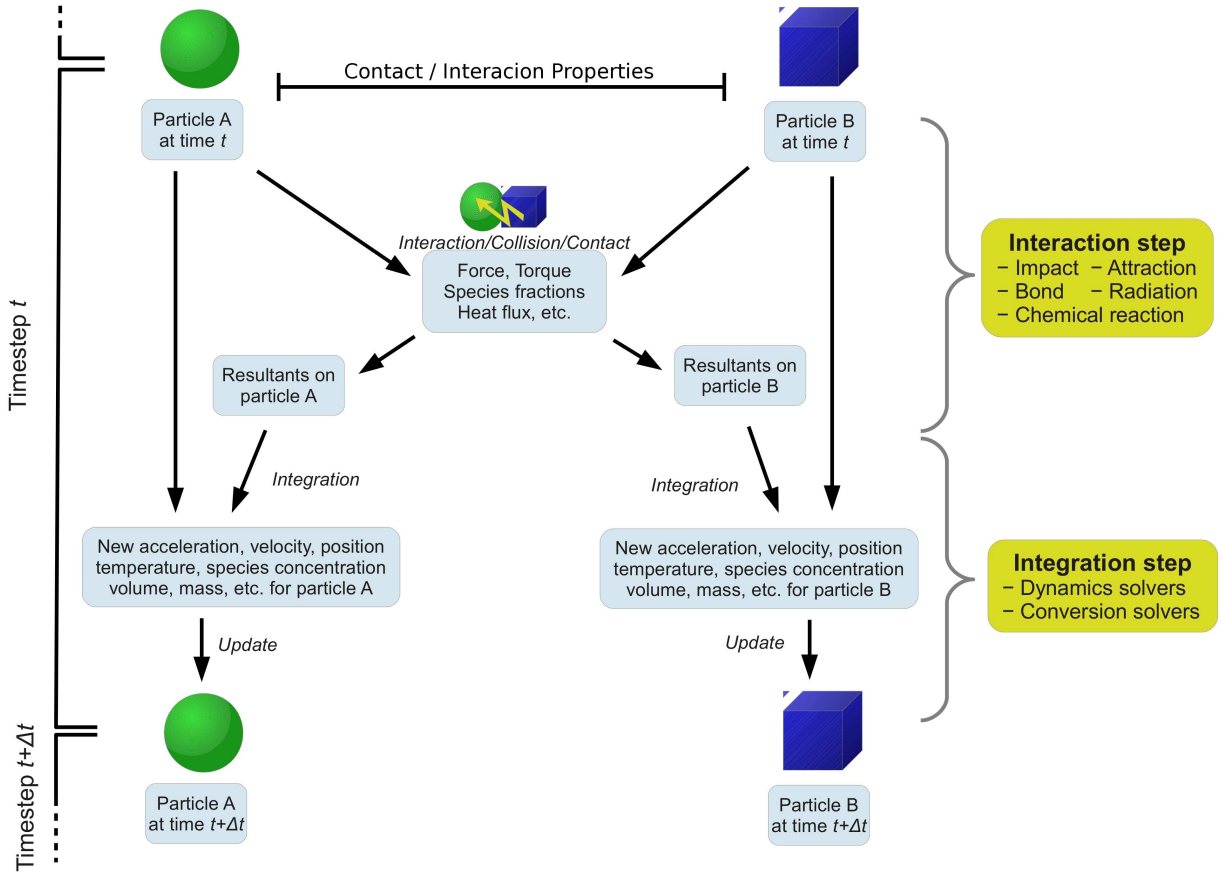


*Figure A.4: Computation phases during a timestep t: interaction and integration steps.*

Fig. A.4 illustrates the procedure during a single timestep of the time loop. At timestep $t$, all particle pairs are considered. During the *interaction* step, the contact properties between a particle pair are computed to predict the resultant interactions, e.g. force and

torque, between the particles. Thereafter, the *integration* step integrates to the new state of the particle system, such as position, velocity, temperature, by solving the respective partial differential equations in discrete formulation. These two steps are described in details in the following sections.

## Interaction step

In the model, different kinds of interactions are possibles between the particles. First, some are specific to a given simulation module, e.g. *impact/collision interactions* are only considered when the motion simulation module is enabled. Additionally some interactions depend on the materials of the particles interacting. Nevertheless, each interaction depends on the contact / interaction properties between the two particles. For instance, for collision or heat transfer between particles contact has to appear but radiation effects are considered over a particular distance between particles.
During the interaction step, the contact / interaction properties are evaluated for all particle pairs and then interactions are considered if the particles are able to influence each other depending on the inter-granular model employed. As a result, interactions will only take place between neighbouring particles. For two interacting particles, the resultants of the interaction are predicted. For instance, collision or bonding interactions result in forces and torques that are applied to the particles. But chemical reactions result in specie transfers and radiation results in heat flux.
Because a given particle can interact with many other particles during a single timestep, the contribution of all these interactions must be taken into account. Thus all the interaction resultants are accumulated for particles. The resultants are temporary values whose scope is limited to the current timestep. They are used to update the particle states during the *integration* step.

## Integration step

As shown in fig. A.4, the *integration* step computes the new state of each particle by taking into account the contributions of all interactions in which the single particle has been involved during the *interaction step*. Thus, this step can be performed independently for all the particles in the system as it only relies on single particles data.
The integration itself solves the respective equations of energy and/or inertia to gain the new states. New values for acceleration, velocity, position, are obtained for each particle. These values describe the new state of the particle system. Thereafter, the updated particles will be used in the next timestep at $t + dt$.

## A.3 Algorithms of Computational Efficiency

Computational efficiency is the major challenge when applying discrete element simulations to engineering applications. One challenge is the validity of the discrete approach with small time steps. The other challenge is that the number of particles involved can easily increase up to millions in engineering applications. Therefore, different approaches are implemented and presented in this section to increase the efficiency of the computational efforts.

### Link Cell Algorithm

On of the highest computational costs in a DEM simulation are caused by the detection of contact partners. At each time step $t$, all the contact partners for each particle have to be detected. To identify the contact partners of a certain particle, the simplest approach would be to loop over all other particles in the system and predict the overlap according eq. 3.37. This requires $n(n-1)/2$ evaluations of overlap $\delta_{ij}^n$ at each time step. The number $n$ thereby describes the total number of particles in the domain. This is inefficient for large systems.
However, the loop over all particles is not necessary as potential contact partners are in the neighbourhood of the particle. Therefore, checking contact with the neighbouring partners only is far more sufficient and reduces the number of contact evaluations significantly. This idea is implemented by the Link Cell Algorithm. Furthermore, the method is straight forward compatible with the parallelisation presented in the following section. The basic principle of the Link Cell Algorithm is to divide the domain into a number of rectangular cells. Each cell is identified by an index. Those indices represent location of a cell in the domain. By this approach the minimum cell size is limited to the largest particle size:

$$l_{cell} \geq 2 \cdot r_g \tag{A.19}$$

where $l_{cell}$ denotes the minimum length of the cell and $r_g$ is the maximum radius of a particle in the domain.
For a given simulation domain from ($x_{min}$, $y_{min}$, $z_{min}$) to ($x_{max}$, $y_{max}$, $z_{max}$) , the number of cells $n_x$ , $n_y$ and $n_z$ in spatial direction is computed as follows:

$$n_x = int\left(\frac{x_{max} - x_{min}}{l_{cell}}\right) \tag{A.20}$$

$$n_y = int\left(\frac{y_{max} - y_{min}}{l_{cell}}\right) \tag{A.21}$$

$$n_z = int\left(\frac{z_{max} - z_{min}}{l_{cell}}\right) \tag{A.22}$$

With the simulation domain divided into cells, the next step links particles to the containing cells. Therefore, each particle is referred by a unique integer and each cell is identified by the three integers ($i$, $j$, $k$) corresponding to the indexes of the cell. A particle in the

simulation domain can be contained by only one cell. Linking of particles to cells is handled by a linked-list associated with each cell. To be associated to a cell list the centroid of a particle has to align within the cell dimensions. For a particle with location ($x$, $y$, $z$), the containing cell ($i$, $j$, $k$) is predicted as follows:

$$\begin{aligned} i &= int\left(\frac{x - x_{min}}{l_{cell}}\right) \\ j &= int\left(\frac{y - y_{min}}{l_{cell}}\right) \\ k &= int\left(\frac{z - z_{min}}{l_{cell}}\right) \end{aligned} \tag{A.23}$$

During the detection of contact partners for a particle, the loop covers particles of the containing cell and the direct neighbouring cells. As each cell is described as a rectangle it has twenty six direct neighbour cells in the domain, except a cell at the domain boundaries which has less.

## Parallelization

Parallelization of the computational effort is increasingly applied in computer science to increase efficiency. The process of solving a problem can be usually divided into independent parts. Those parts of a prediction can be executed simultaneously under sufficient coordination. The performance and efficiency of the parallelization depends thereby mainly on the partitioning of the simulation domain onto different processors. A principal difficulty is the load balance and communication between processors. Hence, a appropriate decomposition or partitioning method is the challenge when targeting for more efficiency by parallelization.

### Orthogonal Recursive Bisection

In this study, the domain decomposition method by Berger and Bokhari (1987) called Orthogonal Recursive Bisection is used. This method considers the spatial coordinates of the particles for the distribution onto different processors. Thereby, particles that are close to each other are assigned to the same processor. Also the implementation of a ORB algorithm is based on a cell structure.
Two principal C++ objects enable an ORB algorithm:

1. the *domain* object which defines the simulation space, the simulation cells, the weight of the cells and the decomposition algorithm

2. the *sub-domain* object which stores the cells belonging to a processor after the decomposition

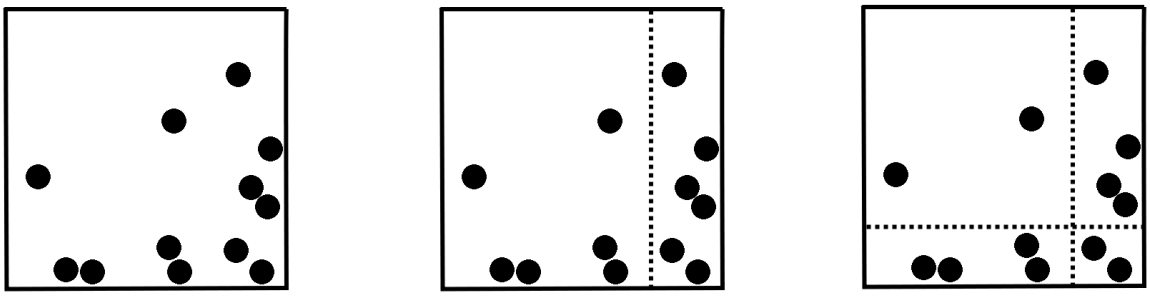

*Figure A.5: A simple particle arrangements with the rectangular domain follow by horizontal decomposition and finalised by a vertical, depicted from left to right respectively.*

The weight of a ORB cell is related to the number of particles contained by that cell. This assumes that all the particles are of similar computational load. By weighting the cells the ORB approach constructs domain partitions of higher quality compared to simple geometrical divisions. Fig. A.5 depicts the decomposition of a domain into sub-domains of similar weights for a simple particle arrangements. The decomposition of a domain into $N$ sub-domains thereby requires $N$-1 processes.

### Message Passing

Parallelisation onto distributed memory requires message passing. In this study the Message Passing Interface (MPI) is used. The MPI implementation provides low commu-

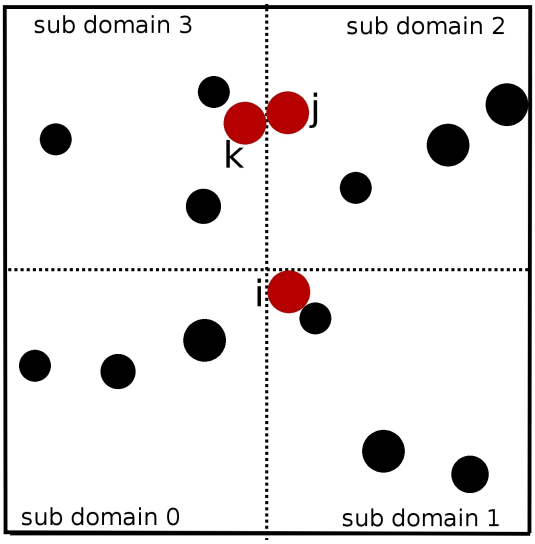


*Figure A.6: The rectangular particle domain is divided into four sub domains whereby the particles $i$, $j$, $k$ are seen as ghost particles by the according neighbouring sub domains.*

nication overhead and code portability for Linux and Windows operating systems. The message exchange between processes do thereby fulfil two informational purposes:

- particles crossing from one processor, i.e. partition, to a neighbouring partition
- updating of the neighbouring particles seen by a process

Ghost particles are a particles contacting the cell boundaries of different sub-domains as shown in fig. A.6. Hence, those particle are potential contact partners with particles of the other sub domains. Thus, any sub domain needs the information about the ghost particles bordering in addition to the sub domain they belong to.
An MPI interface class for message buffering is available by means of the MPI libraries. The buffer class controls all packing/unpacking and sending/receiving functionality. It further contains the functionality for buffer maintenance such as updating buffer pointers, setting buffer sizes and specifying data packing sizes. The buffer class packs or unpacks all C++ data types needed to send between the processors. It further aims to reduce redundant calls by packing all data first and sending it with a single call rather than sequentially.

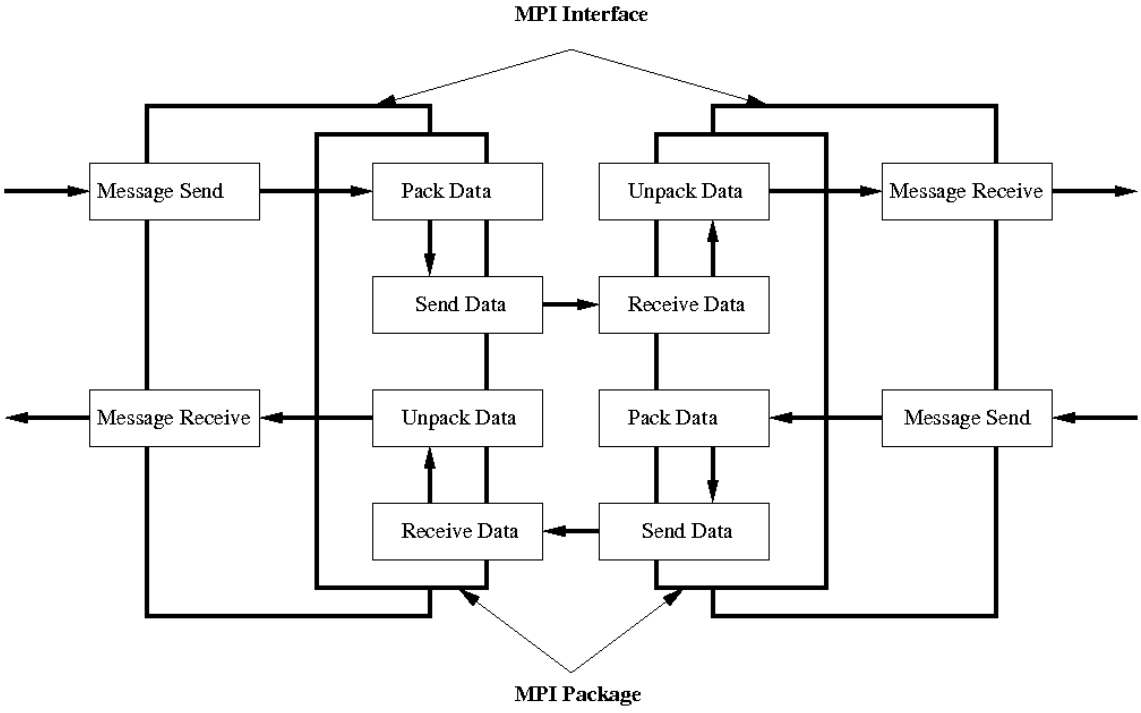


*Figure A.7: Conceptual message flows.*

Hence, for the purpose of data exchange, each C++ object contains a packing and unpacking function. Therefore, the message exchange between two sub-domains, illustrated in fig. A.7, proceeds as follows when sending an object:

- the sender sub domain creates a buffer object which calls the packing function of the object
- the object in turn calls the packing function of the buffer object for each data to be sent

- the sub domain calls the sending method of the buffer object

When receiving data of an object, the exchange proceeds as follows:

- the receiver sub domain creates an buffer object and calls its the receiving function
- this creates the object and calls the unpacking function of the object with the buffered data provided

# Appendix B

# Validations

## B.1 Validation on a Grain-Scale

### B.1.1 Grain Collisions

In here, the measurements of the coefficient of restitution of ice by Higa et al. (1998) have been numerically predicted. Within the measurements ice spheres were impacting on an ice plate in normal direction as shown in fig B.2. The impact and rebound velocity, $v_i$ and $v_r$, respectively, were measured and the coefficient $e_{ice}$ was predicted as follows:

$$e_{ice} = \frac{v_r}{v_i}$$

The investigation yielded the dependencies of the coefficient of restitution on the impact velocity, size and the temperature of the ice grains. From the measurements, Higa et al. (1998) derived the ideal relation of eq. 2.8, where $v_c$ describes the critical velocity dividing the elastic and the brittle-plastic regime of the relation.

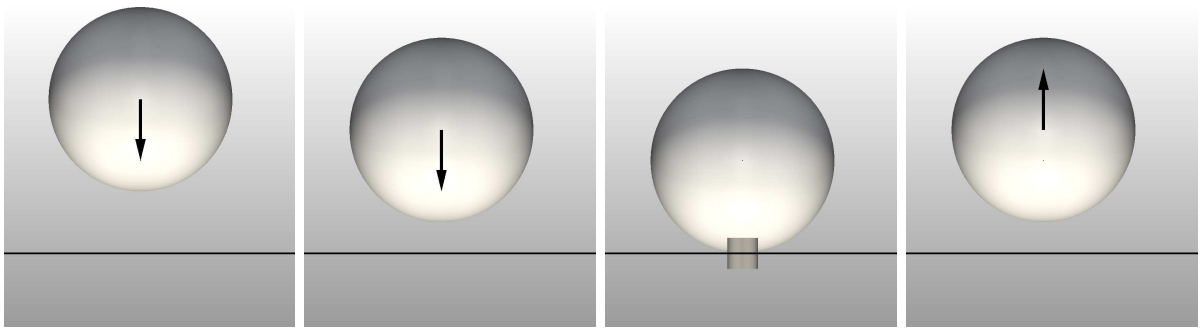


*Figure B.1: Ice grain approaching onto an ice plate by $v_i$ at $t_0$ and $t_1$, impacting and bonding at $t_2$ and rebounding by $v_r$ at $t_3$.*

The relation assumes no energy loss within the quasi-elastic regime and thus full recovering of the rebound velocity. Fig. B.3 depicts the prediction by the analytical relation of eq. 2.8. The experimental, analytical and numerical predictions illustrated in fig B.3 are conducted for ice spheres of a radius of 1.5 cm and a temperature of −12 °C. Fig. B.1 demonstrates a simulation sequence of a spherical ice grain approaching the ice plate by $v_i$, impacting and bonding with the plate and rebounding by $v_r$.

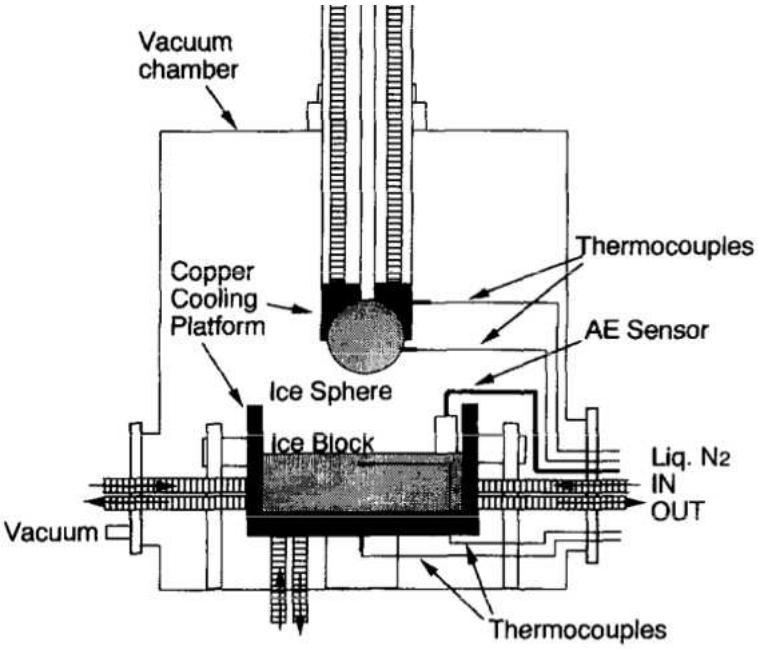


*Figure B.2: Measurement device of Higa et al. (1998).*

The experiments showed a critical velocity $v_c$ of 0.4 m/s for a grain radius of 1.5 cm and −12 °C. The predicted coefficient in fig B.3 describes the experimental results very well. In the quasi-elastic regime for $v_c < 40$ cm/s the restitution coefficient predicted by the ideal relation of eq. 2.8 does not change with velocity.
In the experimental predictions the potential energy is not entirely recaptured after impact during the quasi-elastic regime. Szabo and Schneebeli (2007) and Fan et al. (2003) observed instantaneous bonding between ice grains when contacting. The bonding model of section 3.4.3 used in this predictions also allows instantaneous creation of a bond.
Hence, the rebounding energy has to be less then the impact energy due to the necessary bond fracture. This is the case for the experimental and predicted results in fig. B.3. The predicted coefficient increases slightly with impact velocity in the elastic regime, because at lower velocities the bond has more time to grow and thus its fracture consumes a bigger portion of the rebound energy.
During the plastic/brittle regime in fig. B.3 for $v_c > 40$ cm/s, Higa et al. (1998) reported the observation of plastic deformations after the impact. At even higher impact velocity the fracture of the ice grains was observed. For the coefficient of restitution $e_{ice}$ in fig. B.3 this results in a decrease with increasing impact velocity. The applied collision model of section A.1.2 recaptures this behaviour very well.

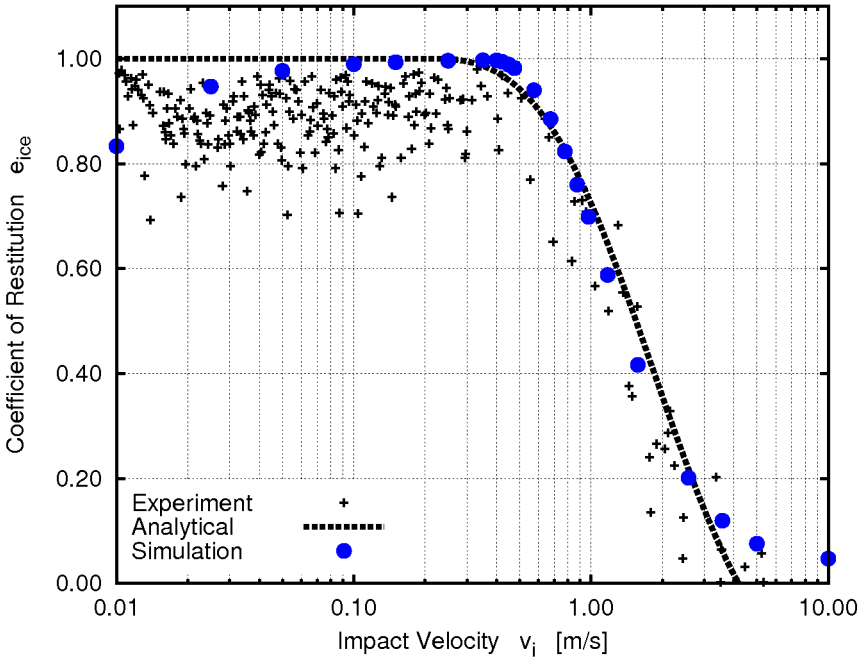


*Figure B.3: Experimental, analytical and numerical predictions of the coefficient of restitution $e_{ice}$ dependent on the impact velocity $v_i$. The ice sphere has a radius of* 1.5 cm *and was impacting the ice plate at* $-12$ °C.

## B.2 Validation of XDEM - FEM Coupling

### B.2.1 Elastic Sheet Enforcement of Granular Ensembles

In this section a benchmark case is used to study the influence of the resolution of the finite element mesh and the number of particles on the results of a DEM - FEM coupling simulation. The case chosen is an elastic sheet which served to enforce a granular ensemble and thus deforms under the mass of the ensemble. The analytical solution of an elastic sheet under constant area load is used as reference to study the influence and convergence of the parameters studied.

#### B.2.1.1 Experimental Setup

The bench mark case consists of a granular layer of spherical particles which settle on an elastic sheet.
The deformation of the sheet is predicted by the linear elastic finite element approach of chapter 4.1. The granular settling is computed by the discrete element method described in chapter 3. The interaction between both are accounted for by the coupling procedure of chapter 5.

The elastic membrane has a length of $l = 10$ m and a width of $b = 0.5$ m. The sheet has an free deforming section of 2 m in length as shown in fig. B.4. The origin of the

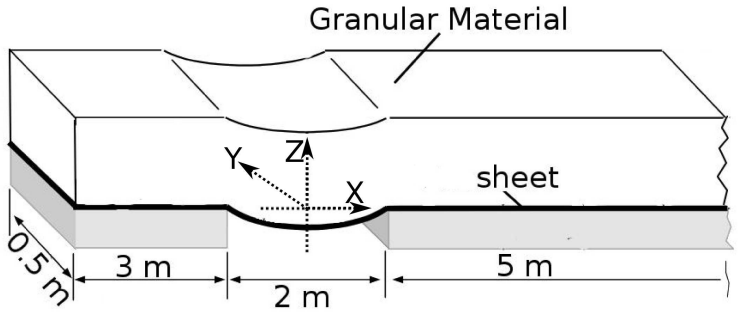


*Figure B.4: Configuration of bench mark case.*

coordinate system is aligned in the center of the free section at 4 m along the length of the sheet. The deformations $u_z$ in $Z$ - direction are fixed for $u_z(-4 \text{ m} < x < -1 \text{ m}) = 0$ and $u_z(1 \text{ m} < x < 6 \text{ m}) = 0$. In $X$ - direction the deformations $u_x$ are fixed for $u_x(-4 \text{ m}) = 0$. Also the deformations $u_y = 0$ in $Y$ - direction are fixed over the entire sheet area. This results in a free deforming sheet for $-1 \text{ m} < x < -1 \text{ m}$.
The mass of the granular ensemble is kept constant, thus the upper sheet area is always loaded by a constant stress of $q = 8.5$ kPa. The density of the sheet and grains as well as the contact and material properties are presented in table B.1.

*Table B.1: Material and Contact Parameters*

| | | Sheet | Grains |
|---|---|---|---|
| Density | $\rho$ [ kg/m$^3$] | 1270.0 | 1732.93 |
| Young's Modulus | $E$ [MPa] | 220.0 | 0.162 |
| Poisson Ratio | $\nu$ | 0.3 | 0.3 |
| Shear Modulus | $G$ [MPa] | 84.61 | 0.062 |
| Normal Stiffness | $k_n$ [N/m] | $1.1 \cdot 10^6$ | 13660 |
| Tangential Stiffness | $k_t$ [N/m] | $1.1 \cdot 10^6$ | 11612 |
| Friction Coefficient | $\mu$ | 0.6 | 0.6 |

In the following the resolution of the finite element mesh and the number of particles are the parameter studied in relation to the sheet deformation. This benchmark contains two simulation domains, i.e. the FEM and the DEM domain. To arrive at the proper solution the necessary resolution of both domains needs to be predicted.
Fig. B.5 exemplifies one configuration of 1000 settled particles on the sheet mesh of 60 nodes in $X$, 10 nodes in $Y$ and 2 nodes in $Z$ - direction. The particles are initially generated

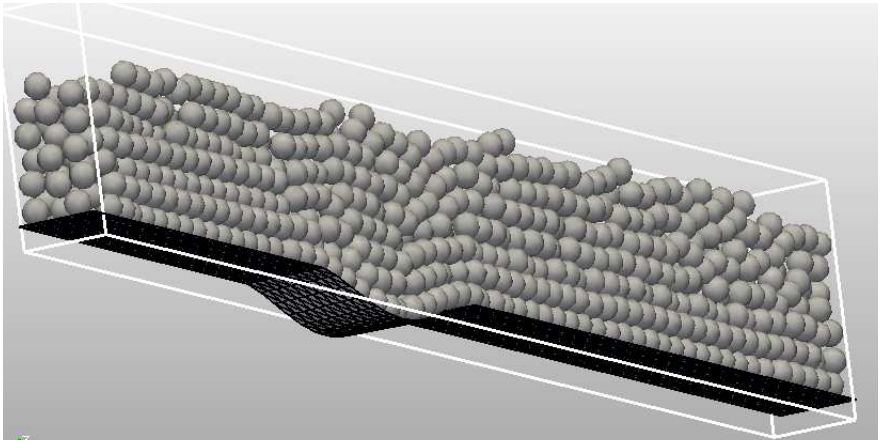

*Figure B.5: Example result.*

as an uniform rectangular grid before they settle on the sheet as shown in the fig. B.5. The contact model used in this prediction is the linear spring-dashpot model presented in section A.1.4. This configuration is used as the reference configuration for the following variations.
The predicted results are evaluated by the vertical displacement $u_z(x)$ in the free region $-1\ \text{m} < x < -1\ \text{m}$ of the sheet. The free region has a length of $l_f = 2$ m. As the displacements in $Y$ - direction are fixed over the entire sheet area, the analytical solution can be evaluated in one dimension by the beam theory. Assuming a beam fixed on both ends the vertical displacement $u_z(x)$ can be calculated as follows:

$$u_z(x) = \frac{q \cdot b \cdot l_f^4}{24 \cdot E \cdot I_y} \cdot \left( \left( \frac{x}{l_f} \right)^2 - 2 \cdot \left( \frac{x}{l_f} \right)^3 + \left( \frac{x}{l_f} \right)^4 \right) \tag{B.1}$$

where $I_y$ the moment of inertia, which is calculated as follows: $I_y = \frac{1}{12} \cdot b \cdot h^3$

#### B.2.1.2 Mesh Resolution

In this section, the resolution of the finite element mesh is studied. Therefore, in this section the resolution of the FEM domain will be modified. The resolution of the DEM domain is fixed at 1000 particles which is more than sufficient as concluded in the in next section. The resolution of the FEM mesh which matches the analytical solution needs to be predicted. Table B.2 presents the simulated mesh resolutions, scaled in relation to the reference configuration, by their number of nodes in $X$ and $Y$ - direction.

*Table B.2: Mesh Resolutions*

| | $X$ | $Y$ | $Z$ |
|---|---|---|---|
| 0.75x | 45 | 7 | 2 |
| 1.0x | 60 | 10 | 2 |
| 2.0x | 120 | 20 | 2 |
| 3.0x | 180 | 30 | 2 |

Fig. B.6 presents the vertical displacement along the longitudinal $X$ - direction for the four different mesh resolutions. The vertical displacements are normalised by the maximum displacement of the analytical solution.

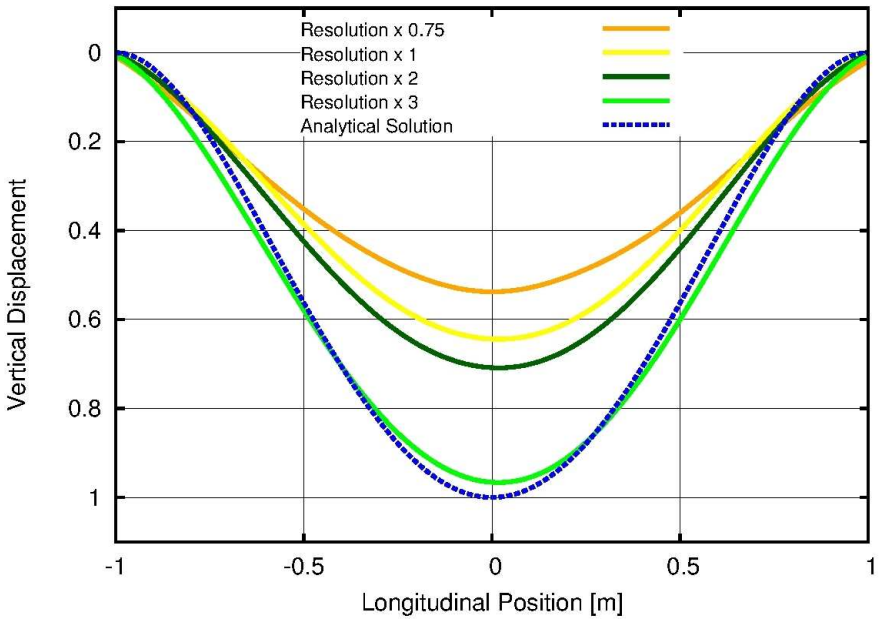


*Figure B.6: Influence of the mesh resolution.*

With increasing mesh resolution the displacement results converge to the analytical solution of eq. B.1. The fourth mesh resolution matches the analytical solution very well.
On one hand, a higher number of finite elements does result in a higher resolution of the FEM domain. On the other hand, the finer mesh results also in a finer resolution of the contact patch between both domains.
The benchmark case showed to converge to the analytical solution at a resolution of the FEM domain of 180 x 30 x 2 nodes.

### B.2.1.3 Number of Particles

The parameter varied in this section is the number of particles forcing the sheet to deform. The number of particles describes the load distribution on the elastic sheet. In this section, the resolution of the FEM domain is fixed while the resolution of the DEM domain will be modified. The resolution of the FEM domain is fixed at 180 x 30 x 2 nodes which is more than sufficient as concluded in the in previous section.
Table B.3 presents the three numbers of particles $N$ and the resultant grain radii $r_g$.

*Table B.3: Simulated numbers of particle*

| $N$ | 100 | 500 | 1000 |
|---|---|---|---|
| $r_g$ [mm] | 181 | 106 | 84 |

As the load on the upper face of the sheet is suppose to be constant, the grain density $\rho_g$ is used to predict the radius $r_g$ as follows:

$$r_g^3 = \frac{3}{4} \cdot \frac{q \cdot A_s}{N \cdot \pi \cdot \rho_g \cdot g}$$

where $A_s$ describes the upper face area of the sheet and $g$ is the gravity of the earth.
Fig. B.7 illustrates the free vertical displacement for the different numbers of particles. The vertical displacements are normalised by the maximum displacement of the analytical solution.

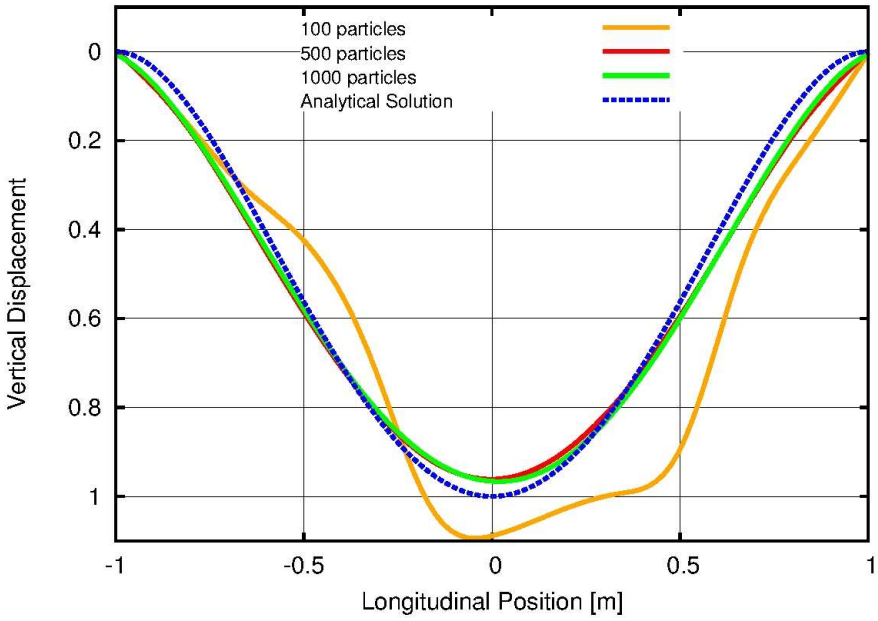


*Figure B.7: Influence of number of particles.*

The vertical displacement smoothens between 100 and 500 particles due to the more uniform distribution of the load. From 500 to the configuration of 1000 particles the vertical displacement of the sheet converges to one displacement. The analytical solution of eq. B.1 is matched by the higher number of particles. Hence, the load distribution is resolved properly at a number of 500 particle and higher in this benchmark case.